COAL CONVERSION EXPERIMENTAL METHODS FOR VALIDATION OF PRESSURIZED ENTRAINED-FLOW GASIFIER SIMULATION

by

David Ray Wagner

A dissertation submitted to the faculty of
The University of Utah
in partial fulfillment of the requirements for the degree of

Doctor of Philosophy

Department of Chemical Engineering

The University of Utah

December 2013

The University of Utah Graduate School

STATEMENT OF DISSERTATION APPROVAL

The dissertation of **David Ray Wagner**

has been approved by the following supervisory committee members:

Kevin J. Whitty	, Chair	**5/28/2013** Date Approved
N. Stanley Harding	, Member	**6/3/2013** Date Approved
Terry Ring	, Member	**5/28/2013** Date Approved
Mikhail Skliar	, Member	**5/28/2013** Date Approved
Philip J. Smith	, Member	**6/3/2013** Date Approved

and by **Milind D. Deo** , Chair of the Department of **Chemical Engineering**

and by David B. Kieda, Dean of The Graduate School.

ABSTRACT

Gasification of coal provides society with electricity, commodity chemicals, substitute natural gas, and consumer products. With the continued use of coal in the United States and abroad, the utilization of this fuel must be optimized with the aid of continued research on laboratory, pilot, and industrial scales in addition to responsible government regulation and legislation.

This study aims to forge a relationship between laboratory measurements and gas-phase data collected from a pressurized entrained-flow gasifier. Experiments utilizing a wire-mesh reactor and thermogravimetric analyzer lay the groundwork for extracting hot, pressurized gases from an entrained-flow gasifier by using a novel sampling system developed as part of the work presented here. Models for entrained-flow gasification of coal complement the experimental endeavors and aid in data analysis.

A novel pressurized wire-mesh reactor was used to determine the extent to which temperature, pressure, hold time, and heating rate influence coal devolatilization and associated char yields. Pressurized thermogravimetric studies were performed to determine the influence of pressure and gas composition on char conversion rates under a range of partial pressures of carbon monoxide and carbon dioxide. The resulting yields and devolatilization rates measured in the pressurized wire mesh heater and char conversion rates from the thermogravimetric analyzer were used to create a model for the entrained-flow gasifier and predict useful synthesis gas and gasification metrics. To

sample the reaction zone of the gasifier, a sample system was fabricated, allowing for radial measurements of gas composition at variable operating conditions.

Key laboratory-scale results indicate that volatiles yields increase with temperature and hold time (residence time), and decrease with pressure, but to a lesser degree. During char gasification, high pressures were concluded to decrease the gasification rate, which was further inhibited by higher carbon monoxide partial pressures. Pilot-scale data show that syngas compositions change with temperature and carbon monoxide and hydrogen yields decrease as temperature increases. Conversely, higher temperatures increase carbon dioxide yields. A significant conclusion is that gas concentrations do not change radially in the pilot-scale entrained-flow gasifier. Correlations of laboratory-scale data provide a context for data acquired during the pilot-scale gasifier operation in addition to modeling endeavors. A developed additive reaction model characterizes char burnout characteristics and extends to devolatilization behavior and drying. This model yields residence times that corresponds within an order of magnitude to a one-dimensional model that tracks syngas composition, residence time, and coal conversion as a function of gasifier length. These results agree within 50% of the experimental data acquired from the entrained-flow gasifier at temperatures above 2650 °F (1438 °C) and is recommended as a tool to predict gasifier behavior and metrics.

Dedicated to my father who taught me the importance of responsibility and the meaning of a strong work ethic, but above all, the benefit of immaturity.

TABLE OF CONTENTS

NOMENCLATURE

Symbol	Definition	Units
Ag	Grain area	m^2
Ap	Pellet area	m^2
AR	As received fuel basis	-
A_s	Surface area	m^2
c	Specific heat	kJ/kg·K
$C_{A_0}^n$	Initial gas concentration	mol/m^3
daf	Dry and ash-free fuel basis	-
De	Effective diffusivity	cm^2/s
dp	Particle diameter	m
Fg	Grain shape factor	-
Fp	Pellet shape factor	-
GM	Gasifiable material	mg
H	Hold time	Seconds
h	Convective heat transfer coefficient	$W/m^2·K$
k	Rate constant	1/s
k_{dash}	Ash film diffusion constant	$g/cm^2·atm·s$
k_{diff}	Gas-film diffusion constant	$g/cm^2·atm·s$
k_s	Surface reaction constant	$g/cm^2·atm·s$
P	Total or partial pressure	psig or bar
P_t	Reactor pressure in Equation 12	atm
R_{C-i}	Equation 13 reaction rate	
r_c	Uncreated-core radius	cm
r_p	As-layer particle radius	cm
Sc	Schmidt number	-
Sh	Sherwood number	-
T	Temperature	°F or ℃
t	Reaction time	seconds
t*	Dimensionless reaction time of Equation 16	-
V	Volumetric flow rate of Equation 14	SCFH of LPM
V	Equation 15 droplet volume	m^3
V_2, V_1	Volatiles yield in Equation 12	%

Symbol	Definition	Units
Vp	Pellet volume	m^3
V_R	Reactor volume of Equation 14	ft^3 or L
X	Conversion extent	-
θ	Temperature difference in Equation 15	-
ρ	Density	kg/m^3

ACKNOWLEDGMENTS

I would like to thank my advisor, Kevin Whitty, and my supervisory committee members, Stan Harding, Terry Ring, Mikhail Skliar, and Phil Smith. Their guidance, criticisms, and advice made the coherent chaos on the following pages possible. Stan Harding's help during the final stages of this thesis were an enormous help as well as his continued support of my postdoctoral endeavors. Glenn Shoaf and Paul Fanning of Eastman Chemical Company merit recognition as well for teaching me how to conduct research while thinking of how the results can aid industry. They are also two cool guys who still find nice ways to let me know I am wrong; "Well, I think what you meant to say, David, was…"

I would also like to thank the laboratory engineers at the University of Utah, Bob Cox and Dana Overacker, for essentially allowing me free reign to "procure" equipment and supplies and trusting that I knew what I was doing. In addition, many of the large-scale endeavors would have not been possible without the staff engineers at the Industrial Combustion and Gasification Research Facility, Andrew Fry, Ryan Okerlund, and Dave Wagner. The combined effort and persistent reminder of where my head was at and insisting that I put it somewhere else was a continual source of inspiration. Senior Engineer Dave Wagner deserves the highest echelon of thanks and gratitude for his pragmatic optimism and the extended efforts he spent continually improving existing systems and fabricating better ones.

Other students and staff members that deserve recognition are Chris Clayton for aide in BET analysis, Ben Silcox for initial wire-mesh reactor operation, Matt Delong for SEM/EDS operation, Dennis Romney and Ron the Welder for their work on the EFG probe, and Jessica "Duchess" Earl for her immense help with GC data analysis. Travis "Scoot" Waind deserves exceptional gratitude for tolerating me for the previous three years and for always being prepared for field trips in addition to operating the EFG and swapping turns as a scapegoat when necessary. I will never forget the Summer of Great Accomplishment, Scoot. Special thanks are extended to Sue Brady for correcting my thesis drafts and for being one cool landlady.

My friends Kevin "Gee" Erickson, Josh Nutter, Aaron Peterson, and Carl Shea deserve thanks for persistently reminding me of more enjoyable pursuits and allowing me to vent my frustrations even though they had no idea what I was talking about, and more often than not, didn't care. Finally, I would like to thank my other half, Rachel Hilton, brother, Connor, and parents, Geni and Dave, for their consistent support and reminding me that science and engineering are not the most important things in the world…but are still really close.

CHAPTER 1

INTRODUCTION

1.1 Background and Motivation

Gasification is the process of breaking down a fuel via thermal decomposition. Unlike combustion processes, gasification utilizes less oxygen per pound of fuel and essentially starves the fuel of continual rapid oxidation reactions. For coal gasification, the process can be viewed as four major steps: drying of the fuel, devolatilization of the fuel via thermal decomposition reactions, char gasification via fluid-solid reactions, and finally, a phase where gas species reach thermodynamic equilibrium and solids exit the reactor as ash or slag. Assuming the reactor has a sufficient residence time, these stages will occur allowing for complete conversion of the coal. With many systems, however, recirculation of the gases occurs and the drying and devolatilization stages can occur simultaneously and, depending on the geometry of the reactor, can occur in tandem with char gasification. The fluid-fluid thermodynamic equilibrium is continually taking place, but does not reach pseudo steady-state values until the solid fuel is essentially converted to gaseous species and ash. This final gaseous product stream is termed synthesis gas, or syngas, and primarily consists of carbon monoxide, hydrogen, carbon dioxide, and water vapor. Additional species produced are methane, hydrogen sulfide, and various cyanides, but at much lower quantities. Syngas is the direct product of gas-phase equilibrium and char oxidation and to a lesser degree, hydrogenation. These processes occur simultaneously in a gasifier so it is

vital to understand each one unaccompanied by the others in order to measure the significance of each process. This overall process is shown in Figure 1 for a slurry-fed system.

Three distinct gasifier reactors are used in larger-scale systems: fixed-bed, fluidized bed, and entrained-flow gasifiers. Fixed bed gasification takes place in a reactor that allows a bed of coal to be subjected to a continual flow of steam, air, or oxygen with the product gases exiting the top and ash exiting the bottom. For fluidized bed gasification, the flow of steam, air, or oxygen is at sufficient rates to fluidize a bed of coal and increase the overall heat transfer of the reactor. Again, the gases typically exit the top of the reactor and the ash and slag exit the bottom. The particle size must be small enough for fluidized bed gasification to allow the bed to fluidize and not slug, but also large enough for the bed to not channel and create uneven heat transfer. For entrained-flow gasifiers, the particle size must be smaller than both fixed bed and fluidized bed systems in order to feed the coal as either dry or wet. Common dry-feed technologies include Siemens and Shell and wet technologies, or slurry-fed systems as depicted in Figure 1, include the General Electric (GE) technology. Others technologies offer single or two-stage feeding where oxidant is fed at a secondary location to the primary to increase the target components of the syngas. Hydrogen and carbon monoxide ratios are optimized depending on the process and downstream use of the gas. Figure 2 shows a cross-sectional view of a GE-style gasifier coupled with a particle perspective of gasification as in Figure 1.

Synthesis gas is used in a variety of downstream technologies that include coal-to-liquids, coal-to-chemicals, electricity production through Integrated Gasification Combined Cycle, and coal-to-SNG (synthetic natural gas).

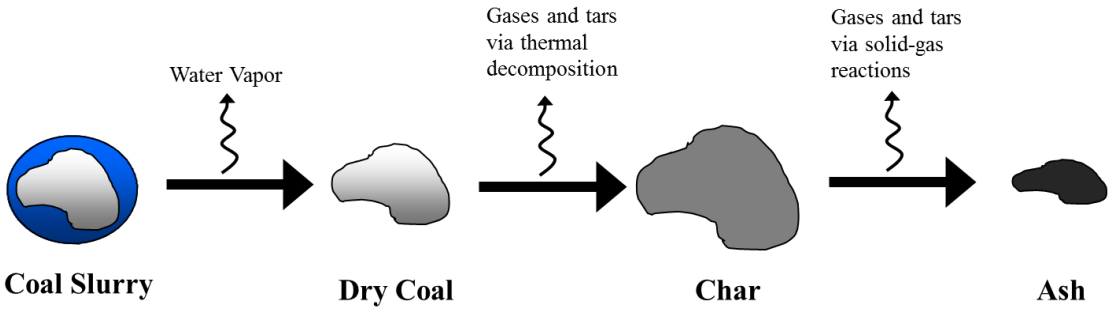

Figure 1: Gasification stages of coal slurry.

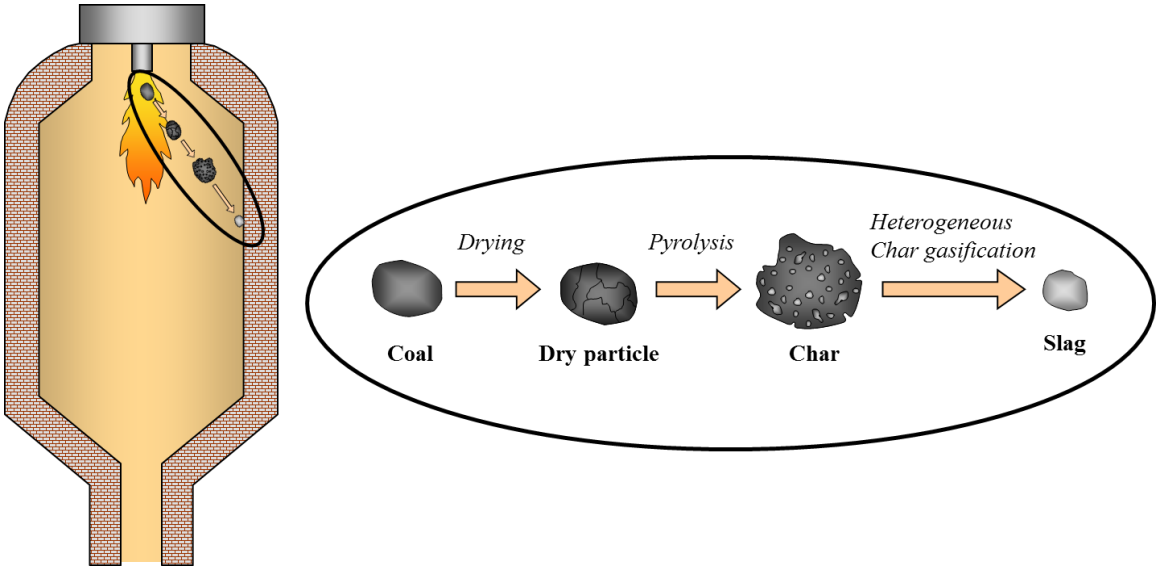

Figure 2: Cross-sectional view of an entrained-flow system.

1.2 Objectives

The aim of this study is to increase the understanding of the chemical processes that dictate high-pressure, entrained-flow coal gasification. Understanding how these processes work individually and how they function together and compete for the same resources (e.g. fuel-bound or gas-phase species) is vital to this aim. If a reasonable understanding of the physical and chemical processes is established, energy and economical resources can be preserved with advanced simulation techniques like reactive

flow computational fluid dynamics. The data acquired in bench- and pilot-scale systems can be used to validate comprehensive models and minimize cost and person-hours for industrial-scale production. With this in mind, the key objectives are listed below.

1. Develop a safe sample procedure for measuring gas-phase compositions within a pressurized gasifier and use this procedure to measure gas concentrations at various locations.
2. Develop a basic model to approximate gas compositions of entrained-flow gasifiers.
3. Extend bench-scale experimental findings to predict how pilot-scale testing will be conducted and how to determine key findings.
4. Expand the body of knowledge of coal gasification.

1.3 Outline of Thesis

This thesis follows a traditional format, presenting an introduction prior to a review of pertinent literature, Chapters 1 and 2, respectively. Chapter 3 details the three apparatuses utilized for experimentation with accompanied methods of data analysis and descriptions of approaches taken per apparatus. A discussion of experimental results follows in Chapter 4 where the findings are reviewed and scrutinized to determine valid conclusions in addition to Chapter 5 containing model results. A summary of these conclusions and recommendations for future work constitute Chapter 6. Supplemental calculations and experimental details comprise the Appendices.

CHAPTER 2

LITERATURE REVIEW

This chapter details previous gas-phase equilibrium and char oxidation studies as they pertain to coal and down-fired, entrained-flow gasification systems.

2.1 Pyrolysis and Devolatilization

Higman (*1*) defines pyrolysis as the heating of a feedstock without the presence of oxygen and devolatilization as the heating of a feedstock with or without oxygen and is used as a more general description of the thermal decomposition of a fuel. Volatile gases and tars are products of both processes and are affected by a number of factors. The most dominant of these influences are temperature, pressure, heating rate, particle size, and the gas environment in which pyrolysis and devolatilization take place. These influences are discussed individually in the following sections for bench-scale experiments and how the influences relate to larger gasification systems on the pilot- or industrial-scale. Significant directional effects are summarized at the end of this chapter.

2.1.1 Temperature Effects

It has been demonstrated that as temperature increases, volatile yields increase as well. Three distinct temperature regimes exist when pyrolyzing coal: kinetic-dependent, mass transfer-dependent, and an intermediate mode when these two compete (*2*). These three regimes are shown in Figure 3.

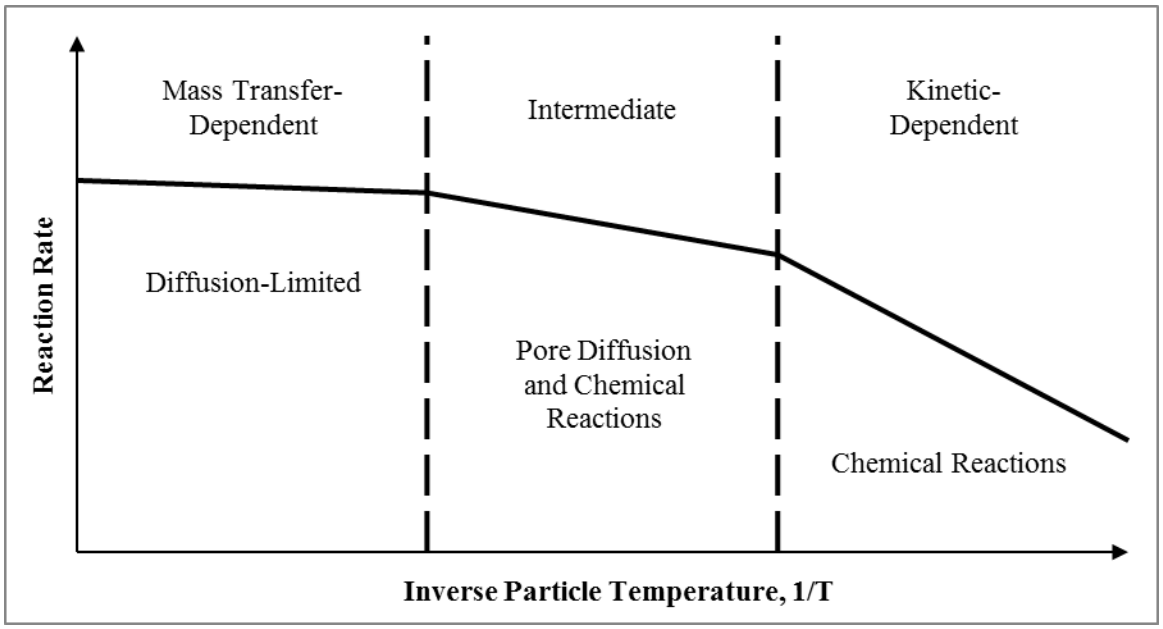

Figure 3: Effect of temperature on reaction rate.

Figure 3 illustrates that lower temperatures exhibit kinetic controlled reactions, while at higher temperatures, diffusion-limited rates dominate. As a system increases in temperature, it will transition from the kinetic-dependent to mass transfer-dependent regime with an increasing influence of pore and bulk diffusion. Many thermogravimetric studies utilize the kinetic regime, while drop-tube and large-scale studies attempt to approximate the high temperature of an entrained-flow gasifier by relying on mass transfer dependence.

In both thermogravimetric (*3*) and entrained-flow experiments (*4–6*), including drop-tube, higher fuel conversions are seen at higher temperatures. In addition, regardless of the geometry of the system, as temperature increases so do the levels of volatile yields. This is evident in wire-mesh reactors (*7–11*), thermogravimetric analyzers (*12*, *13*), and entrained-flow systems (*5*). Tar yields are also shown to increase with temperature in wire-mesh reactors (*14–16*). These increases in tar and volatile yields then account for the loss

in char surface area due to devolatilization and thermal decomposition. Trends have been acknowledged in both TGA (*12*) and entrained-flow (*17*) experiments.

Another association with operability of gasifiers is the residence time of the fuel particles. As with higher temperatures, a longer residence time will yield a higher conversion (*5*). This correlation is not dependent on geometry. Similarly, as residence time increases, volatile and tar yields increase (*18*), which will have a direct influence on the amount of char remaining. This char will decrease in surface area as residence time increases and more volatiles are emitted. This decrease in surface area is enhanced by higher temperatures, specifically for entrained-flow systems (*17*).

2.1.2 Pressure Dependence

Unlike temperature and residence time, most pressure effects are not as intuitive. While there is an increase in diffusion (*19*), tar yields can either increase or decrease depending on the heating rate of the sample. It was found that at low heating rates on the order of 10 K/min (*12*) and above five bar (*20*), tar yields increased. While this occurs in precise operating conditions, high heating rates are shown to decrease the tar yield for wire-mesh reactors (*14*, *15*, *20*, *21*), flat-flame burners (*22*), or entrained-flow apparatuses (*23*, *24*). Another seemingly special case is at low pressures, one to five bar, and slow heating rates (*20*), when the tar yield also decreases. There is a universal trend as pressure increases for the volatile yields to decrease, regardless of geometry (*5*, *7*, *10*, *11*, *14–16*, *18*, *22*, *25*). And while in many cases the tar yield decreases, one study (*18*) found that the hydrogen content of the tar increased with pressure.

Pressure and coal rank seem to have a competing influence on the swelling properties of coal. Flat-flame burner studies (*26*), (*27*) show that as coal rank increases,

particle swelling increases, perhaps due to the tars that are evolved (*27*), while within a coal rank or ranks, the swelling ratio will decrease (*26*). Swelling of the particles could also account for the decrease in available internal surface area on which reactions take place (*22*). Enlarged particles may eliminate routes to active surface sites for reactions by decreasing the pore size to the degree that gases cannot readily evolve to transport through the fissures.

As stated above, the general direction of volatile yields declines as pressure increases, but this does not extend to trends of individual species. As pressure increases, so does methane production (*21*), which could be a product of the increased devolatilization rate at lower temperatures, perhaps due to primary pyrolysis (*12*). The fate of sulfur is also pressure dependent as approximately 25% of fuel-bound sulfur remains in the fuel as pressure is increased from ambient conditions to 10 bar (*28*). This accounts for the reduction in SO_2 and CS_2 in entrained-flow gasifiers (*28*). In another study utilizing the same gasifier as in (*28*), it was found that H2 and CO yields increased with pressure (*29*). This increase in syngas products would then have a direct influence on the char yield. It was found that as pressure increased, conversion increased as coal rank decreased (*30*) and for O_2/coal ratios exceeding 0.8 from 1 to 5 bar (*29*).

The partial pressure of gas species also has an effect on the yields of wire-mesh reactor data. It was found that as the partial pressure of hydrogen increased, the volatile yields increased as well (*8*, *11*). Conversely, as the partial pressure increased, the tar yield decreased (*8*). This is from hydrogenation, readily breaking the bonds in the tar and producing volatiles, and interrupting the char formation process. No entrained-flow tests were found to correlate the relationship. If enough carbon dioxide were present, this excess

of hydrogen would push the CO-shift reaction, in reverse yielding higher quantities for CO and vapor-phase water.

2.1.3 Heating Rate Influence

The influence of the heating rate is primarily determined by comparing low heating experiments to those with high heating rates. The most common apparatus for low heating rates is a thermogravimetric analyzer, while the most common high heating rate apparatus is a wire-mesh heater. With a wire-mesh heater, the heating rate can be exactly determined from a computer that controls the current delivered to the sample. Other apparatuses that could be used in rapid heating of fuel samples are drop-tube furnaces and flat-flame burners where the rate of heating is on the order of 10^4 to 10^5 K/s.

As with high temperatures, rapid heating produces increased yields of volatiles and tar, but only to a certain threshold. Both tar and volatile yields were seen to increase at atmospheric and vacuum pressures (*8*, *11*, *16*, *25*, *31*), but decrease once the pressure was raised to approximately 10 bar (*20*) and above (*16*). This is evidence of mass transfer limitations within the coal particle and the presence of a junction between pore diffusion and bulk diffusion. The influence of pressure on heating rate can be seen in the swelling properties of coal during devolatilization. Zeng, et al. (*26*) showed that as heating rate increased, the level of swelling of the particles decreased, indicating that external forces kept the particle from expanding as it would at atmospheric pressure.

2.1.4 Particle Size Influence

Particle size plays an important role in the gasification of coal. It is desirable to have a larger particle for fluidized bed gasification, whereas entrained-flow gasification requires smaller particle sizes due to reactor transport and feeding issues. For entrained-

flow gasifiers (*32*) it was found that smaller coal particles increased the cold gas efficiency, defined below as Equation 1 (*33*).

$$Cold\ gas\ efficiency\ [\%] = \frac{Heating\ value\ in\ product\ gas\ [MW]}{Heating\ value\ in\ feedstock\ [MW]} \cdot 100 \qquad \text{Equation 1}$$

Concerning the syngas effects of particle size, it was found that as the particle size increased, there was a distinct decrease in the tar and volatile yields (*7*, *11*, *21*, *32*). This was particularly evident in the carbon monoxide yield in entrained-flow systems (*32*), but conversely, as the particle size increased, so did the methane yield (*21*). This could be related to the temperature at which the experiments were carried out since more methane is produced at lower temperatures. Intuitively, as the volatile yields decrease, the char yields increase as a function of particle size (*14*).

2.2 Char Gasification

The temperature, pressure, residence time, gas environment, and even particle physical characteristics influence the way coal becomes char. This section details the general behavior of coal becoming char and focuses less on the input parameters of temperature, pressure, etc., and more on the mechanism and how these parameters influence and depend on one another to produce char.

As with coal devolatilization, different parameters will have variable effects on the char gasification stage. With an increase in pressure, it was shown (*16*, *22*, *24*) that char reactivity decreased under high heating rates (>1000 ℃/s), while char reactivity increased with lower heating rates on the order of 10 ℃/s. The temperature at which the char was created also has a significant influence on the char reactivity. As the char formation

temperature increases, the reactivity decreases, which may be a result of thermal annealing of the coal, but a definite deactivation of the char as volatiles are evolved (*17*). This was shown to be the case in entrained-flow (*17*), wire-mesh (*8*) and thermogravimetric (*12, 34*) apparatuses. As the temperature was raised from 1200 ℃ to 1400 ℃, the reactivity was found to decrease by a factor of seven in entrained-flow systems (*17*).

In contrast to the aforementioned temperature trends, it was also found that as temperature increased, so did the char reactivity (*13, 35*). Comparing these studies, it was determined the only significant difference was the pressure at which the reactions were subjected. At atmospheric and near atmospheric pressure (*8, 12, 34*), a decrease in reactivity was shown for increasing reactor temperature, whereas at 450 psi with high heating rates, char reactivity increased with rising temperature. Other factors that affect char reactivity in similar studies show a decrease in reactivity as hold time at high temperatures increases (*8*) and a decrease as the particle porosity is increases (*36*).

Residence time has an important role in the reactivity of the char in addition to pressure and temperature. It was determined that as residence time increased, char reactivity decreased (*17, 35, 37*). This trend was shown to continue even as temperature was increased (*37*). The rationale as to why a prolonged residence time decreases the reactivity is that as a particle resides in a reactor for a longer period of time and is subjected to high temperatures, the solid-gas reactions become more important and may become more and more influenced by the geometry of the particle. This is the case even in reactive gas environments of pure carbon dioxide, that as the porosity of the particle increases and becomes less dense, the char reactivity decreases.

2.3 Overall Entrained-Flow Gasifier Performance

In large- or pilot-scale gasifiers, the number of parameters that can be changed is limited by the geometry or equipment. For this reason, many operations change the flows of steam, coal, and oxygen to the gasifier to obtain a specific temperature range. Azuhata, et al. (*32*) and Nichols, et al. (*28*) show that by increasing the oxygen-to-carbon feed ratio, conversion of the fuel is increased as well as the sulfur conversion from the parent coal. The fate of the coal-bound sulfur at higher temperatures will yield higher concentrations of hydrogen sulfide and carbon sulfide and potentially sulfur dioxide in more oxidative environments (*28*). By adding more steam and increasing the hydrogen-to-carbon ratio, instead of oxygen (as O_2), the yield of hydrogen can be increased in the syngas of an entrained-flow system (*38*). The addition of steam to a gasifier will also have an influence on other major gas species due to gas-phase equilibrium via the water-gas and CO shift reaction, seen as Reaction 1 and Reaction 2, respectively.

$$C + H_2O \rightarrow CO + H_2 \qquad \text{Reaction 1}$$

$$CO + H_2O \leftrightarrow CO_2 + H_2 \qquad \text{Reaction 2}$$

These two main reactions account for the increased production of hydrogen upon the addition of steam, but also account for a reduction in carbon monoxide in the syngas. Brown, et al. (*38*) and Skinner, et al. (*39*) showed that in entrained-flow, dry-feed systems, the addition of steam will decrease the ratio of CO to CO_2. The reactions above show this to be correct by utilizing the mole of CO produced from the water-gas reaction to yield one mole of CO_2 and one mole of H_2 when added to steam. It was also shown that the addition of steam decreased the levels of pollutants from the same gasifier with the assumption that

necessary particle and gas treatment facilities were attached the effluent syngas piping (*40*). Brown (*38*) also showed that with an increase of volatile matter in the proximate analysis, there would be more CO present in the effluent.

From an operability perspective, entrained-flow processes require the smallest particle size for gasification processes (*41*, *42*). This is because larger particles require more energy to transport through the reactor and the gasifier will lose efficiency. Higher reactor temperatures exist from more oxygen being present in entrained-flow processes, resulting in flame temperatures that can exceed 2000 ℃ (*43*). Excessively high temperatures then cause much higher heat losses than other gasifiers and lead to lower efficiencies (*42*). Ullmann's Encyclopedia of Industrial Chemistry (*43*) lists many advantages and disadvantages to entrained-flow processes summarized below.

Advantages of entrained-flow processes:

1. Multiple designs exist for commercial use
2. Gasification processes contain the highest capacity per unit volume
3. There are no moving parts, thus less maintenance
4. No particle fines are rejected due to entrainment
5. Product gas (syngas) is free of tars and heavy oils
6. Any rank of coal may be used for gasification processes
7. The process produces inert slag with a low carbon content

Disadvantages include:

1. Heat recovery is vital, especially in the presence of molten slag
2. Pulverization of gasifier feedstock is necessary
3. Drying of feedstock is required unless slurry feed system is used

4. High temperatures result in more heat loss and higher costs in materials

2.4 Modeling

Numerous gasifier and coal particle devolatilization models have been proposed. Many of these models are specific to a type of gasifier (i.e. entrained-flow, fluidized bed, or fixed-bed) and have their own set of assumptions. Both commercial and non-commercial codes exist to achieve accurate and precise simulations within a resolved error. This section does not aim to measure these models against one another and declare the pros and cons of each, but to show the myriad of possibilities of how the approach is altered to obtain a desirable means-to-an-end.

2.4.1 Gasifier System Models

The most well-known of these is perhaps the Pulverized Coal Gasification or Combustion (PCGC) models of Smoot and Smith in the late 1970s to early 1980s from Brigham Young University. Many experimental campaigns have been evaluated using the two-dimensional PCGC (PCGC-2) model in the 1980s (*4*, *44*, *45*). The precursor to this series of models is the 1-DICOG (1-Dimensional Combustion or Gasification) model introduced by Smith (*46*, *47*). Some of the key limitations that the 1-DICOG model experienced were the lack ability to predict the rates of mixing and recirculation, the inability to predict both axial and radial fluctuations, a lack of kinetic parameters stemming from empirical data, and the nature of additional assumptions that simplified the complex process of coal combustion or gasification (*47*). The PCGC-2 code was able to remedy many of these deficiencies through additional empirical data and computing power. A 3-dimentionsal (PCGC-3) model was created in the early 1990s, also at Brigham Young University. In addition to the model including a third dimension, it characterizes reactive

and nonreactive flows with particles by a set of fully coupled conservation equations, accounting for momentum, energy, and mass. A more rigorous treatment of the coal gasification and combustion models and subroutines is given by Smoot and Pratt (*47*), and Smoot and Smith (*48*).

Additional codes have been generated since the inception of PCGC-3, and with advances in computing power and empirical findings, become useful tools. With programs like Fluent, COMSOL MultiPhysics, and ASPEN, models ranging from simple to complex have been used to solve entrained-flow gasification systems. While simplified and 1-dimensional models have been generated for specific gasifiers or purposes (*49–55*), others are able to use advanced solution algorithms to solve the conservation equations and produce viable and robust conclusions. The Reynolds-Averaged Navier-Stokes method is able to solve turbulent gasifiers using variable time and length scales (*56–58*), while ANSYS has published commercial products via Fluent to solve these complex equations (*59*). The computational fluid dynamic (CFD) code CFX-4 was also published by ANSYS and is used by Watanabe and Otaka (*60*) to solve a three-dimensional gasifier via three processes: pyrolysis, char gasification, and gas-phase reactions. A more recent approach to simulate entrained-flow gasifiers utilized ASPEN Custom Modeler by creating a reduced order model, employing a reactor network model (*61*), (*62*). Essentially, the authors place a number of plug-flow reactors and well-stirred reactors in series and parallel to simulate an entrained-flow gasifier. These network models can account for reaction and quench zones as well as recirculation zones and even model one- and two-stage gasifiers. A rigorous validation and sensitivity analysis is presented by Monaghan and Ghoniem (*62*).

2.4.2 Coal Devolatilization Models

Models detailing coal reaction kinetics in a variety of circumstances are far more common than gasifier models. Review articles are useful in summarizing these models and finding the most suitable per application (*63–66*). Other sources delve into the processes of devolatilization and/or char gasification and kinetics to varying degrees (*7*, *23*, *67–79*). Some of the more prominent codes were developed by Solomon, et al. (*80*), Niksa (*81*, *82*), and Fletcher (*83*). Solomon presented a model called FG-DVC (functional group – depolymerization, vaporization, cross-linking) that considers functional groups to yield light gases, while depolymerization of a macromolecular network (coal particle) is subject to tar vaporization, cross-linking, and bridge breaking. Solomon's model sees the coal particle as a network of groups that devolatilize and undergo char gasification in stages. Niksa's model (*81*, *82*) is the combination of three submodels, DISCHAIN, DISARAY, and FLASHTWO, thus titled FLASHCHAIN (*84*). Unlike FG-DVC, no functional groups appear and the coal particles are modeled as chains with aromatic clusters that are interconnected by bridges and char links. The volatile species, upon devolatilization, are met with no mass transfer resistance. A third model is called CPD (chemical percolation devolatilization) and developed by Grant, et al. (*83*). CPD is able to describe rapid devolatilization using lattice statistics to describe tar evolution. The model also incorporates the FG model of Solomon (*80*) and requires nuclear magnetic resonance (NMR) data as input.

2.5 Summary

A large portion of the empirical findings presented above is pertinent to the remainder of this work. The conclusions from literature sources will be used by confirming

the data presented herein. These data will also widen the body of knowledge and contribute to the new findings. Major findings of this review are summarized in Table 1, Table 2, Table 3, and Table 4. As a gasification parameter is increased, the directional effects are tabulated with notes, if necessary. Table 2, Table 3, and Table 4 present directional effects for temperature, pressure, and other gasification parameters, respectively, while Table 1 contains definitions of abbreviations used in the others.

Table 1: Abbreviations for directional effect tables.

Abbreviation	Definition
TGA	Thermogravimetric Analyzer
WMR	Wire-Mesh Reactor
EF	Lab-Scale Entrained-flow
FFB	Flat-Flame Burner
TY	Tar Yield
VY	Volatiles Yield
CGE	Cold Gas Efficiency
VM	Volatile Matter

Table 2: Directional effects for an increase in reactor temperature.

Directional Effect	**Notes**	**Geometry**	**Ref.**
Decrease in reactivity	Decreases by a factor of 7 from 1200 ℃ to 1400 ℃ (*17*); P_{atm}; CO_2 atmosphere at 1000 K/min (*34*); at atmospheric pressure (*12*)	TGA (*12*, *34*); WMR (*8*)	(*5*, *8*, *12*, *17*, *34*)
Decrease in specific surface area of char			(*12*)
Decrease in surface area			(*17*)
Increase in carbon conversion		EF (*4–6*); TGA (*35*)	(*5*)
Increase in gasification reactivity	450 psi; CO_2 atmosphere at 500 to 1500 K/s (*13*)	TGA	(*13*, *35*)
Increase in H_2 and CO yields		EF	(*38*)
Increase in TY and VY	Helium atmosphere (*14*)	WMR	(*14–16*)
Increase in thermal deactivation of char	With increasing pressure	TGA	(*10*)
Increase in VY		TGA (*12*, *13*); EF (*5*); WMR (*7–11*)	(*5*, *7–13*, *25*)

Table 3: Directional effects for the increase of gasifier pressure.

Directional Effect	**Notes**	**Geometry**	**Ref.**
Decrease in char reactivity	Oxidation reactivities for bituminous and lignite coals (*26*)	EF (*24*); FFB (*22*); TGA (*26*)	(*22*, *24*, *26*)
Decrease in internal surface area of char		FFB	(*22*)
Decrease in reactions rates	Steam; worsens with temperature increase	TGA	(*85*)
Decrease in SO_2 and CS_2 yields		EF	(*28*)
Decrease in sulfur conversion from fuel	by ~25%	EF	(*28*)
Decreased swelling		FFB	(*26*)
Decrease in TY	By ~25% from 3 to 13 atm (*24*); High heating rates (*20*); Slow heating rates, 1 to 5 bar (*20*); Helium atmosphere (*14*)	EF (*24*); FFB (*22*); WMR (*14*, *15*, *20*, *21*); EF (*18*)	(*14*, *15*, *20–22*, *24*, *86*)
Decrease in VY	for lignite and bituminous at 1000 C (*5*); Helium atmosphere (*14*)	WMR (*5*, *7*, *10*, *11*, *16*); FFB (*22*); WMR (*14*, *15*); EF (*18*)	(*5*, *7*, *10*, *11*, *14–16*, *22*, *25*, *86*)
Increase in conversion	As coal rank decreases (*30*); For O_2/coal > 0.8 from 1 to 5 atm (*29*)	EF	(*29*, *30*)
Increase in gasification reactivity	At 800 Celsius		(*12*)
Increase in H_2 and CO yields		EF	(*29*)
Increase in tar hydrogen content		EF	(*18*)
Increase in methane yield		WMR	(*21*)
Increase in particle swelling		FFB	(*27*)
Increase in TY	Slow heating rates; above 5 bar	WMR (*20*); TGA (*12*)	(*12*, *20*)
Increase in the devolatilization rate	At low temperatures		(*12*)
Increase in the gasification rate	At high temperatures		(*10*)
Increase of diffusion influence		WMR	(*19*)

Table 4: Directional effects for the increase of various gasification parameters.

Increase In	Directional Effect	Notes	Geometry	Ref.
Heating Rate	Decrease in swelling	10^4 to 10^5 K/s	FFB	(*26*)
	Decrease in VY	70 bar	WMR	(*16*)
	Decrease in TY	Above 10 bar in hydrogen (*20*); 70 bar (*16*)	WMR	(*16*, *20*)
	Increase in char reactivity		WMR	(*8*)
	Increase in TY	Atmospheric pressure (*16*)	WMR (*8*), (*16*)	(*31*)
	Increase in VY	Atmospheric pressure (*16*)	WMR (*8*, *11*, *16*)	(*25*)
Particle Size	Decrease in TY		WMR	130
	Decrease in VY		WMR	(*7*, *16*)
	Increase in char yield	Helium atmosphere	WMR	(*14*)
	Decrease in CO yield		EF	(*32*)
	Decrease in CGE		EF	(*32*)
	Increase in methane yield		WMR	(*21*)
Particle Porosity	Decrease in char reactivity	CO_2 atmosphere	EF	(*36*)
Residence Time	Decrease in char reactivity	Trend continues as temperature increases (*37*)	TGA (*35*)	(*17*, *35*, *37*)
	Decrease in surface area	Enhanced by increasing temperature		(*17*)
	Increase in conversion		EF	(*5*)
	Increase in TY and VY		EF	(*18*)
Hold Time	Decrease in char reactivity		WMR	(*8*)
O/C Feed Ratio	Increase in conversion		EF	(*32*)
	Increase in sulfur conversion		EF	(*28*)
H/C Feed Ratio	Increase in H_2 yield		EF	(*38*)
Steam	Decrease in CO/CO2 ratio	Decrease of CO yield and Increase in CO_2 yield (*39*)	EF	(*38*, *39*)
Steam/Coal Ratio	Decrease in pollutants		EF	(*40*)
Partial Pressure of CO_2	Increase in the measured reaction rate		TGA	(*87*)
Partial Pressure of H_2	Decrease of TY		WMR	(*8*)
	Increase in VY		WMR	(*8*, *11*)
Proximate VM	Increase in CO yield		EF	(*38*)

CHAPTER 3

EXPERIMENTAL SPECIFICS

This section serves to clarify and illuminate all aspects related to the experimental apparatuses and procedures. It discusses various analysis methods as they pertain to each apparatus and provides a basis for subsequent sections. Fundamental fuel testing at the beginning of a campaign is necessary to appreciate the results and their implications. Second to this basic testing, the effects of temperature and pressure are tested via established thermogravimetric analysis methods and lesser-known wire-mesh heater methods. Figure 4 shows a flow diagram of this experimental layout and model relations.

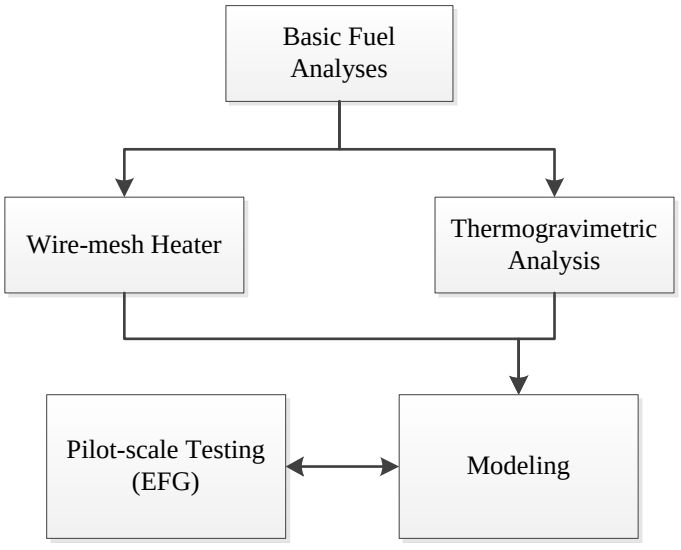

Figure 4: Diagram of experimental layout.

The effects of high temperature and high pressure are studied independently and dependently using thermogravimetric analyzers (TGAs), while wire-mesh heater methods will include the effects of high-pressure and rapid sample heating on the order of 1000 ℃/s with high final temperatures. Pilot-scale testing of the Institute for Clean and Secure Energy's entrained-flow gasifier (EFG) utilizes these data to run a campaign to confirm computer models.

3.1 Fuel Characterization

3.1.1 Description of Analyses

3.1.1.1 Ultimate Analysis

This analysis presents the percentages of carbon, hydrogen, nitrogen, oxygen, and sulfur on a mass basis, either dry or as received. To determine the percentages of these elements, the University of Utah sent samples to Huffman Laboratories in Golden, CO, for analysis. The methods used for these analyses were ASTM methods D5373, D5622, and D4239.

3.1.1.2 Proximate Analysis

This analysis reports percentages of moisture, ash, volatile material, and fixed carbon. Huffman Laboratories analyzed these samples using ASTM methods D3172 and D3175 for proximate analysis.

3.1.1.3 Heating Value

Also called 'calorific value', this analysis measures the thermal energy from a unit mass of fuel. Huffman Laboratories used ASTM method D5865 for the analysis.

3.1.1.4 Ash Composition

Huffman Laboratories performed this analysis using ASTM method D3174. The oxides detected were aluminum, calcium, iron (III), magnesium, manganese, phosphorus, potassium, silicon, sodium, sulfur, and titanium.

3.1.1.5 Brunauer, Emmett, and Teller (BET) Surface Area

This analysis to measure the specific surface area of a fuel has no specified ASTM method. Dr. Suhui Li wrote the method during his time at the University of Utah. MCE 2424 houses the BET manufactured by Micromeritics Instrument Corporation; model Tristar II 3020.

3.1.2 Physical and Chemical Fuel Data

Table 5 contains all data discussed in the previous section; ultimate and proximate analyses as well as BET surface area, heating value, and ash composition. The Sufco coal was received in one-ton super-sacks and presumed homogenous. The fuel was pulverized to 70% minus 200 mesh (70% of the fuel would pass through a 200 mesh screen [74 micron]). All data are presented on an 'as received' (AR) basis, unless otherwise noted. All experimentation and calculations described herein use the properties outlined in Table 5 unless otherwise stated.

3.2 Wire-Mesh Reactor Studies

This section outlines and discusses the wire-mesh reactor (WMR) and the experimental approach, including run conditions and experimental procedure, similar to previous work performed by the author (*88*). Data analysis methods are discussed.

Table 5: Physical and chemical coal data.

Fuel Name		Sufco
Fuel Rank		Bituminous
Heating Value (BTU/lb), AR basis		11899
BET Surface Area (m^2/g)		1.79 ± 0.139
Ultimate Analysis (wt%, Ash-free basis)	Carbon	67.87
	Hydrogen	5.45
	Nitrogen	1.09
	Oxygen	16.87
	Sulfur	0.36
Proximate Analysis (wt%, AR basis)	Loss-On-Drying	6.11
	Ash	8.36
	Volatile Material	38.49
	Fixed Carbon	47.04
Ash Composition (% of Ash)	Al as Al_2O_3	8.34
	Ca as CaO	18.21
	Fe as Fe_2O_3	5.25
	Mg as MgO	2.84
	Mn as MnO	0.05
	P as P_2O_5	0.01
	K as K_2O	0.33
	Si as SiO_2	48.85
	Na as Na_2O	3.09
	S as SO_3	5.96
	Ti as TiO_2	0.64

3.2.1 Pressurized Wire-Mesh Reactor Apparatus

3.2.1.1 Pressure Vessel and Grid Support

The pressure vessel of the wire-mesh apparatus is 8.5 inches in diameter and seven inches tall when fully assembled. It is constructed of 304L stainless steel with a 0.75 inch wall thickness and a 1 inch thick ceiling. The base of the system is mounted, while the lid is secured with eight lengths of 5/8-inch threaded rod for pressurized operation and the option of 0.625 inch, fine-thread socket-head bolts (5/8”-18) for ambient pressure operation. High-pressure Conax fittings on the underside of the vessel allow the feed-through of the copper studs for power delivery and thermocouple wires. Figure 5 shows the base of the pressure vessel with a 5/8”-18 bolt pattern, three 0.25 inch NPT ports for gas and thermocouple ports, and two 0.5 inch NPT ports for the copper stud feed-throughs for power delivery to the fuel sample.

The copper plates shown in Figure 5 hold the foil in place and do not allow movement via tightening them down with a 0.25 inch Allen-socket bolt on each copper plate pair. The top copper plate measures 1 inch by 0.5 inches and 0.25 inches thick with a 0.25 inch hole. The top plate measures 1.5 inches by 0.5 inches and 0.125 inches thick with two holes measuring 0.25 inches and 0.375 inches. Conax compression fittings secure the 0.375 inch diameter copper studs from underneath the base plate. Figure 6 shows isometric views of the base plate with the copper pieces and of the assembled pressure vessel.

The gasket material is Garlock BLUE-GARD® 3000 and has a torque specification of 120 ft-lbs and maximum temperature and pressure of 700 °F (371 °C) and 1000 psig (70 bar), respectively.

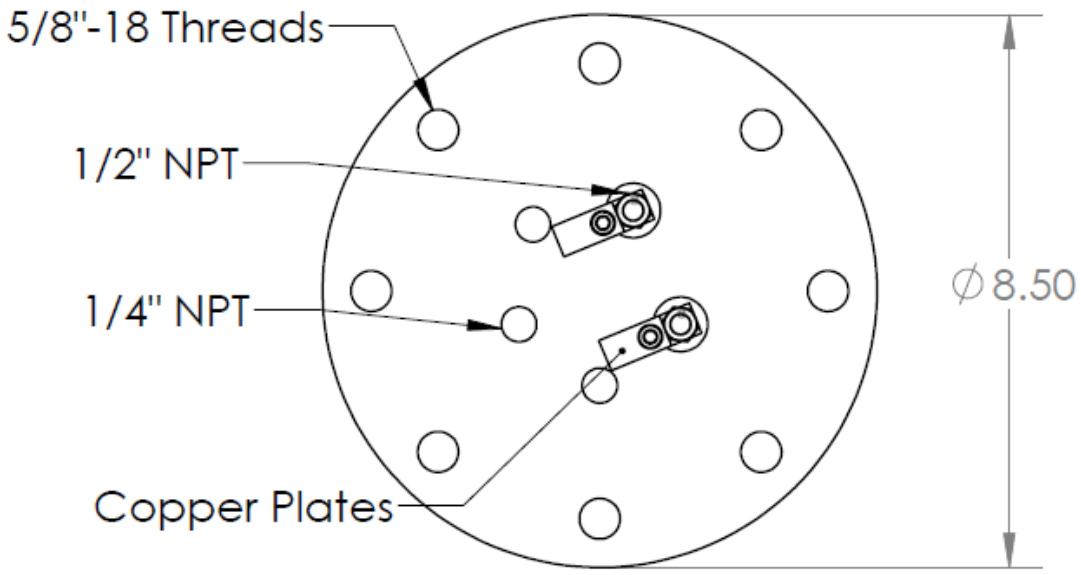

Figure 5: CAD drawing of the wire-mesh pressure vessel base.

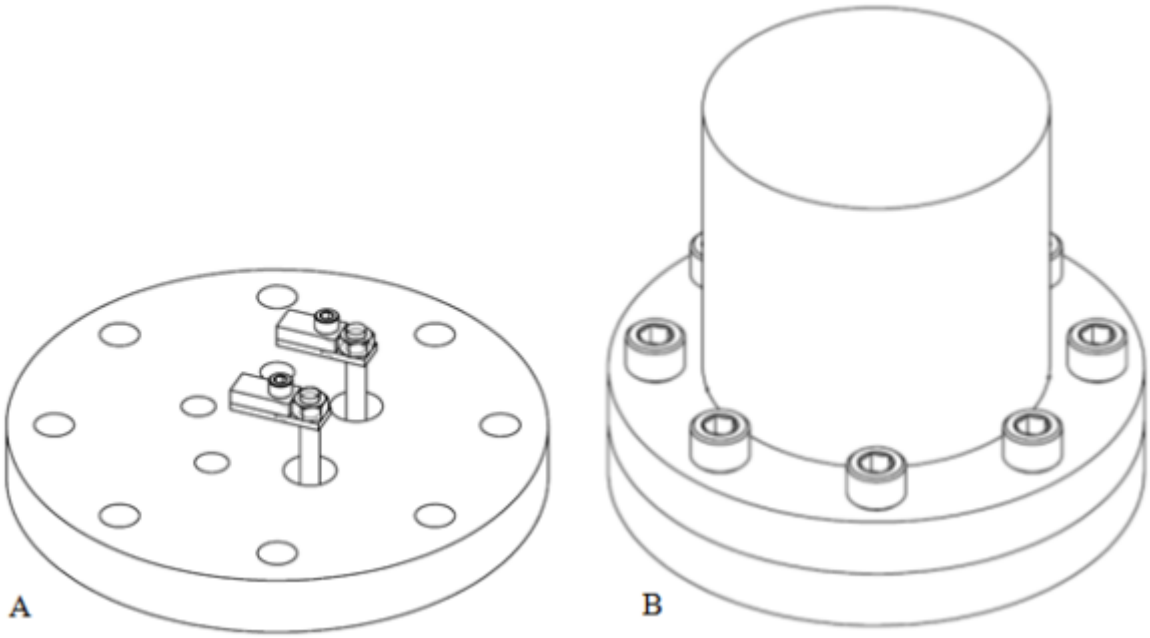

Figure 6: Isometric views of the pressure vessel (A) with copper studs and plates and (B) with socket bolts and top hat.

3.2.1.2 Fuel, Foil, and Wire-Mesh Assembly

3.2.1.2.1 Initial Test Campaign Assembly

Traditionally, the material that spans the electrodes of a wire-mesh apparatus is a fine, folded piece of wire-mesh as the name suggests (*7, 16, 19, 89, 90*). The apparatus described herein uses both a fine mesh and a foil that houses that mesh and a coal sample. A small piece of wire mesh, roughly 1 inch by 0.5 inches is folded into thirds and a coal sample of approximately 40 mg is folded in the mesh and again in thirds the other way creating a small 'fuel packet'. These fuel packets are then sandwiched between two layers of foil that span the copper plates of the grid support system. Figure 7 shows a photograph of a fuel packet both before heating (left) and after heating (right).

The fine mesh is constructed of a corrosion-resistant 304 stainless steel, 500 x 500 mesh (Tyler sizing) with a wire diameter of 0.0008 inches (20 microns) and an opening size of 0.0012 inches (30 microns), corresponding to 36% of the area. Figure 8 shows a scanning electron microscopy photograph of the mesh.

Figure 7: Photograph of a WMR fuel packet (left) before heating and (right) after heating.

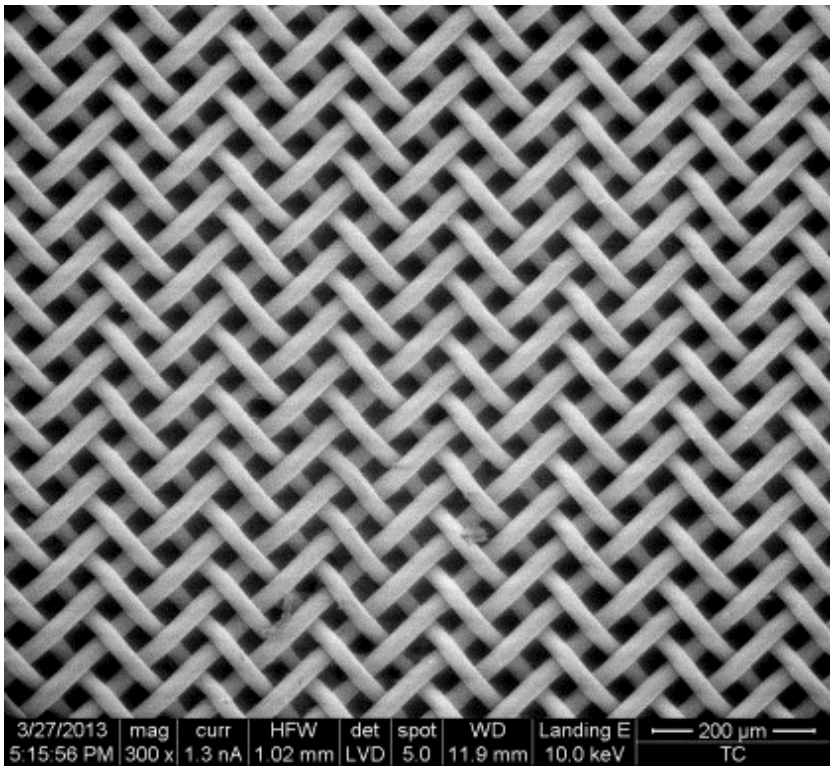

Figure 8: SEM photograph of the 500 Tyler mesh used in wire-mesh experiments.

The foil is made from 321 stainless steel 0.002 inches thick and is cut to a size of two inches by one inch for operation. A fine-gauge thermocouple is welded to the foil, which serves as a feedback control signal for the software to heat the sample. The thermocouple is 0.003 inches in diameter and is type-R (platinum and rhodium at 13%). This small diameter allows for a smaller time-constant capable of the high heating rates necessary for the operation of the reactor. A type-R thermocouple is used instead of the customary type-K thermocouples as with aforementioned studies in the event that the final temperature exceeds the published temperature limit of 1200 ℃ (*91*); the upper limit of a type-R thermocouple with a diameter of 0.003 inches is 1450 ℃. The operator welds the leads of the bare wire to the foil using a small spot welder. Figure 9 shows a photograph of the foil and thermocouple junction.

Figure 9: Photograph of the foil and thermocouple junction.

3.2.1.2.2 Atmospheric Pressure Test Campaign

Any additional testing performed at atmospheric pressure utilized the following mesh apparatus. For reasons given in Section 3.2.2.2, additional experiments did not use the foil and thermocouple assembly, but a previously established (*88*) assembly design of 500 by 500 Tyler mesh screen welded to the thermocouple. The fuel packet mesh is identical to the new mesh material.

3.2.1.3 Electronic Components

The electronic hardware consists of a National Instruments (NI) signal-conditioning box (model SC-2345) that houses the NI modules for feedback control of the reactor. Thermocouple (SCC-TC02) and digital output (SCC-DO01) modules read the temperature and output proportional control to the grid, respectively. A separate, custom-made phenolic board contains an AC/DC converter and large solid-state relay (SSR) responsible for power delivery to the grid (manufacturer and model, Power-IO CDD-1V300). The SSR operates at high current (up to 1000 amperes) and fast switching operation of 2000 Hz. The convertor transforms the 120 VAC supply to a 24 VDC signal to power the SSR. A Tripp-Lite (model PR-60) power supply provides the amperage necessary to heat the grid. Figure 10 shows the reactor workspace with electronic components, pressure vessel, and nitrogen cylinder used for pressurization. Figure 11 shows a photograph of the equipment.

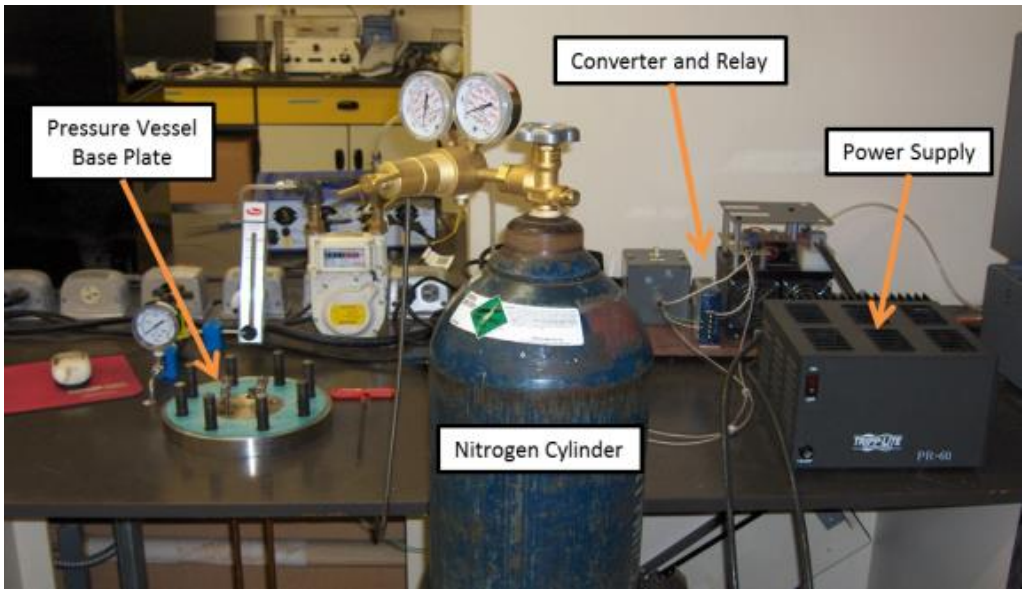

Figure 10: Wire-mesh heater workspace with electronic components, nitrogen cylinder, and the pressure vessel.

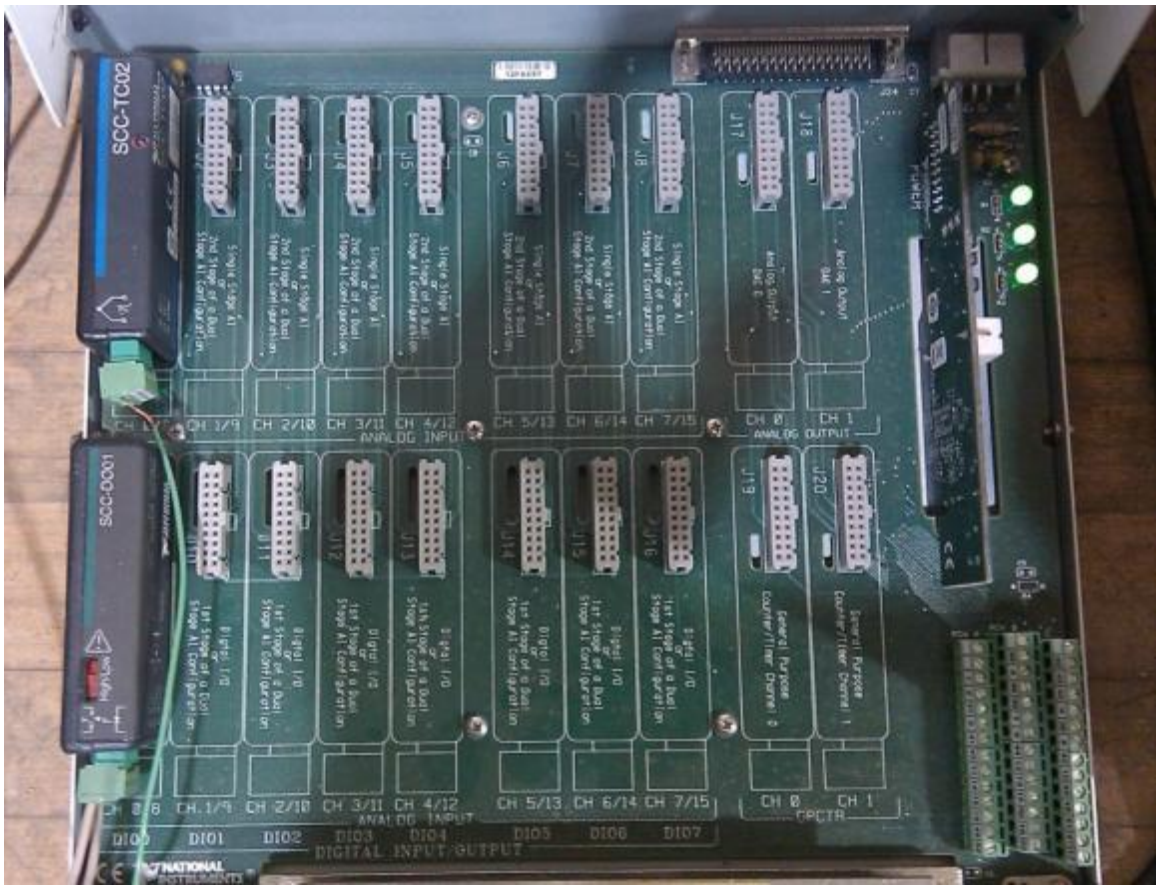

Figure 11: National Instruments signal conditioning box (SC-2345) with thermocouple and digital output modules.

3.2.1.4 Computer Interface and LabVIEW Software

National Instruments LabVIEW software release 8.6 manages the input parameters for the reactor. This software specifies the heating profile, temperatures, proportional, integral, and derivative (PID) gains, and power settings of the grid. Pulse-width modulation of the power signal allows for feedback control of the grid through the temperature measurements. Appendix A contains an excerpt of the published article describing the system in detail (*92*).

The operator specifies the settings for heating rate, temperature, power output, and PID gains in the LabVIEW Front Panel Display interface and is able to monitor the

progress of the run sequence. The temperature of the foil and mesh grid was verified using a color-changing lacquer, detailed in Appendix B.

3.2.2 Experimental Approach and Conditions

3.2.2.1 Initial Testing Conditions

The approach of the wire-mesh reactor campaign is to determine devolatilization parameters and influences of temperature, pressure, and hold time of the sample at the final temperatures. The heating rate is constant at 1000 ℃/s with final temperatures of 600, 800, and 1000 ℃. Experiment pressure ranges from one to 35 bar (0 to 500 psig). Table 6 shows the three experimental factors and settings for operating conditions.

A design of experiments methodology incorporated from the conditions shown in Table 6 results in 48 runs including duplicates. This methodology allows for the maximum utility of the data acquired by building a model to predict devolatilization behavior. Table 7 tabulates all run conditions shown in Table 6 including the presence of duplicates.

3.2.2.2 Atmospheric Pressure Testing Conditions

The factors for this testing matrix include temperature and hold time at the final temperature. Pressure is not a factor because hold time revealed to have a more significant influence on the yield of volatile components in previous testing. Table 8 presents the number of runs per test condition of this test campaign.

Table 6: Wire-mesh reactor experimental factors and conditions.

Factor	Low		Mid		High
Final Temperature (℃)	600		800		1000
Pressure (bar)	1	7	18	25	35
Hold Time (sec)	1		3		5

Table 7: Wire-mesh reactor design of experiments conditions.

Temperature (℃)	Pressure (bar)	Hold Time (sec)	Duplicates
600	1	1	
600	1	3	X
600	1	5	X
600	7	1	
600	18	1	X
600	18	3	
600	18	5	X
600	25	3	
600	25	5	
600	35	1	
600	35	3	
600	35	5	
800	1	1	
800	1	3	X
800	1	5	X
800	7	5	
800	18	1	X
800	18	3	X
800	18	5	
800	35	1	
800	35	3	X
800	35	5	
1000	1	1	X
1000	1	3	X
1000	1	5	
1000	7	1	
1000	7	3	
1000	18	1	
1000	18	3	X
1000	18	5	X
1000	25	1	
1000	25	5	
1000	35	1	
1000	35	3	
1000	35	5	

Table 8: Number of runs per condition of atmospheric pressure, wire-mesh reactor testing.

		Temperature (℃)		
		800	1000	1200
Hold Time (sec)	0	1	1	1
	3	1	5	1
	5	1	1	1

The previous data acquired with the wire-mesh reactor are compared to that of the atmospheric pressure tests in the next chapter. For this reason, the conditions were altered include temperatures of 1000 ℃ and 1200 ℃, while testing a new low temperature of 800 ℃ for the apparatus. The same rationale extends to hold time. Previous testing used three and five seconds, but a zero second hold time presents a new low end for the apparatus.

3.2.3 Experimental Procedure

Prior to the operation of the reactor, the operator must dry all fabricated fuel packets described in Section 3.2.1.2 and record the sample mass. In addition to the sample preparation, the operator also welds the fine thermocouple leads to the foil and characterizes the small assembly to obtain the PID parameters in LabVIEW. For system operation, the operator follows the following procedure.

1. The operator weighs and records the mass of the fuel packet and places it inside the fold of the foil. The operator then places the top of the pressure vessel on the base and tightens the bolts to a torque specification of 120 ft-lbs.
2. To purge the system of oxygen, the operator allows a minimum of 100 liters of nitrogen to run through the vessel. Then the operator closes the gate valve on the exhaust system allowing the vessel to pressurize to the desired pressure.

3. To apply current to the grid, the operator places the clamps from the power supply on one copper stud each and turns on the power supply. Within the LabVIEW Front Panel Display, the operator types in the desired file path to save the data, which takes the following form: Date-Temp-Pressure-Hold Time-Run Number (e.g. 130122-800-1-3-5.tdms). By clicking 'Start Profile' in Front Panel Display, the operator initiates the run.
4. Within 40 seconds of completing the run, the operator must save the data held in a temporary array in the program. Once the sequence stops, the operator removes the top of the pressure vessel after opening the exhaust valve and fully depressurizing the system. The operator then weighs the fuel packet and records the mass.
5. To review an individual run, the operator uses the LabVIEW subprogram DIADem to retrieve the run statistics including average temperature, standard deviation, and the range of temperatures seen during the sequence.

3.2.4 Data Analysis Methods

The wire-mesh data consist of char and volatiles yields. These figures of merit dictate a successful run and the software package JMP (version 9.0.2) analyzes these yields using a standard least squares approach. LabVIEW returns a .tdms file upon saving the data and the National Instruments program DIADem presents the data for inspection. Outlier analysis utilizes Chauvenet's criterion and aids in the development of error analysis. Built-in JMP models perform successful model building including potential fits of full factorial and response surface designs. Microsoft Excel analyzes all data not modeled by JMP including the fifth-order polynomial and rate calculation procedure.

3.3 Thermogravimetric Studies

This section outlines and discusses the thermogravimetric analyzer (TGA) and the experimental approach, including run conditions and experimental procedure. Data analysis methods are also discussed as they pertain to general TGA results and then compared to determine the best analysis methods and parameters.

3.3.1 Pressurized Thermogravimetric Analyzer Apparatus

The thermogravimetric analyzer (TGA) used for the test campaign described herein was a ThermoCahn Thermax model 500 capable of pressures up to 1500 psi at ambient temperature and 1000 psi at 1000 ℃ with a maximum heating rate of 25 ℃/min. The system consists of three main parts, a microbalance for continual weight measurement, the heated pressure vessel containing the sample, and a stand to support and align these components. Figure 12 shows a schematic of the system.

The base of the furnace vessel is an elevator lift that raises the vessel to house the sample that hangs from a balance extension wire. Once the vessel is raised, a collar is placed around the flange junction, securing the system for pressurized operation. Figure 13 shows an exploded view of the microbalance.

In Figure 13, the spacers in the housing occupy excess volume, reducing the amount of purge gas required. The weighing mechanism has a counter-balance on one side that requires adjustment before initial operation with an extension wire on the other side for the continual weighing of the sample. Figure 14 illustrates the extension wire and associated hardware.

The top hot-shaped balance is seen at the top of the figure with the extension wire traveling to the bottom with a hook for the attachment of a sample bucket. The baffle in

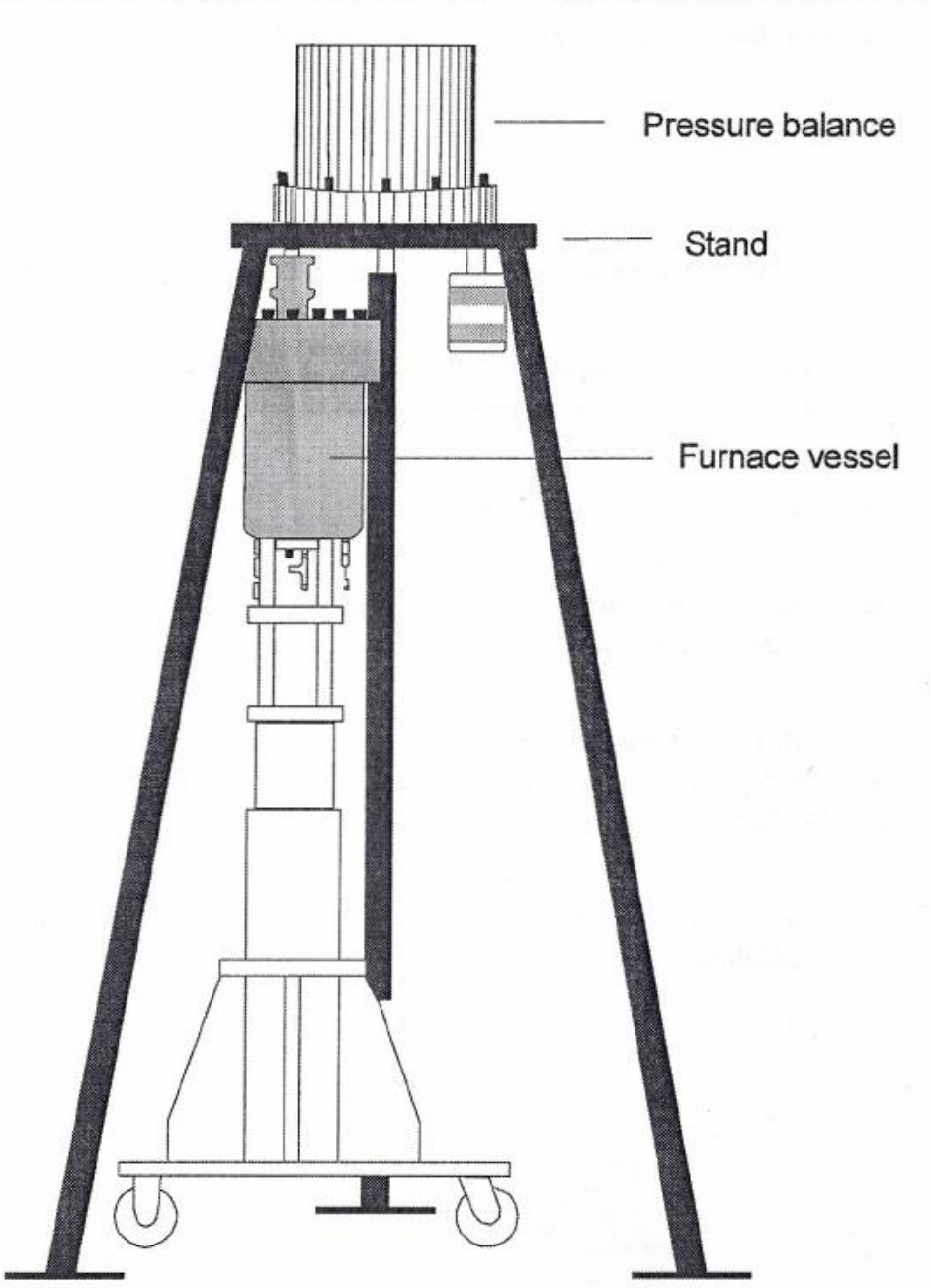

Figure 12: Schematic of the ThermoCahn Thermax 500 TGA apparatus. (*93*).

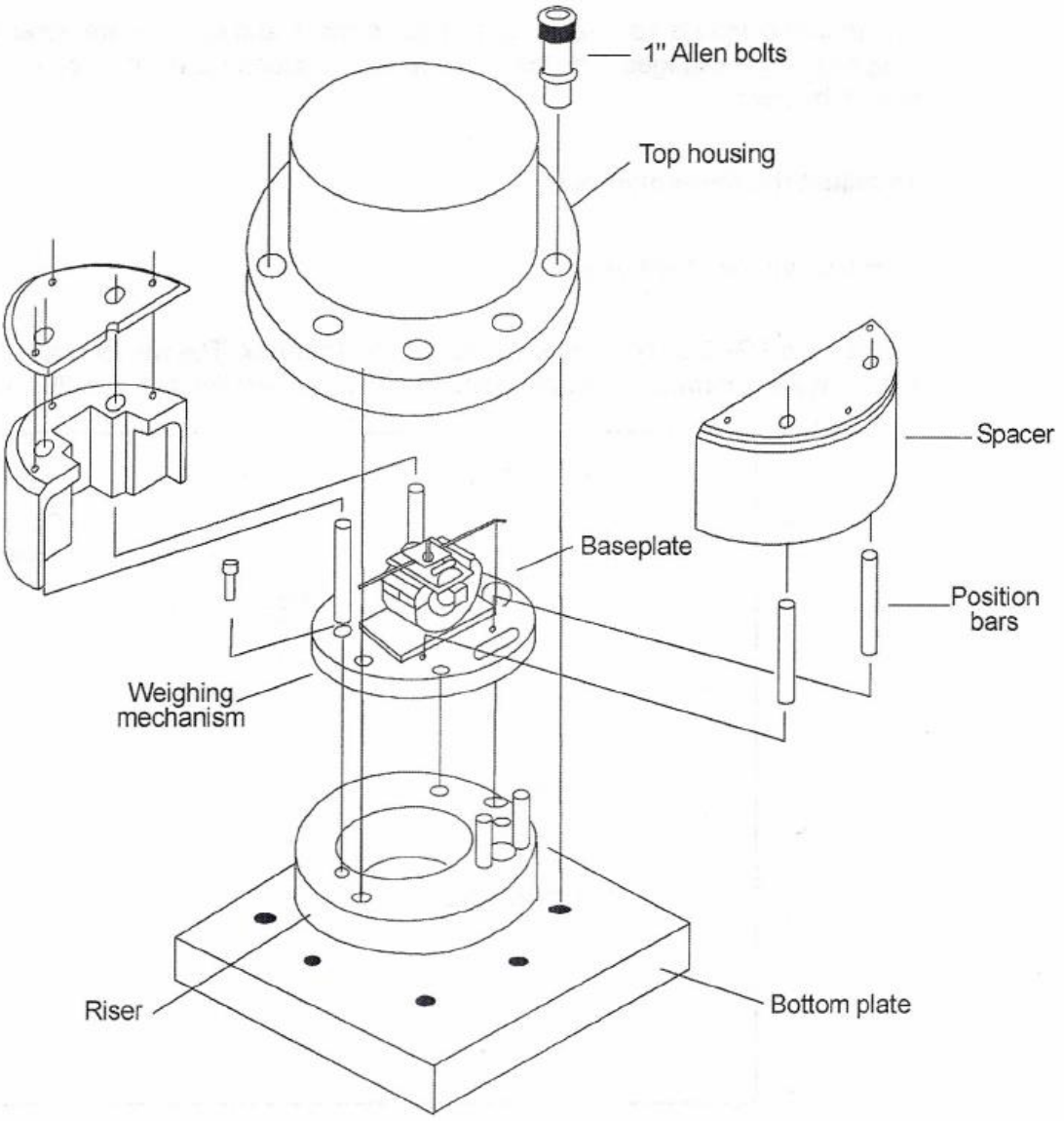

Figure 13: Exploded view of the pressurized microbalance. (*93*).

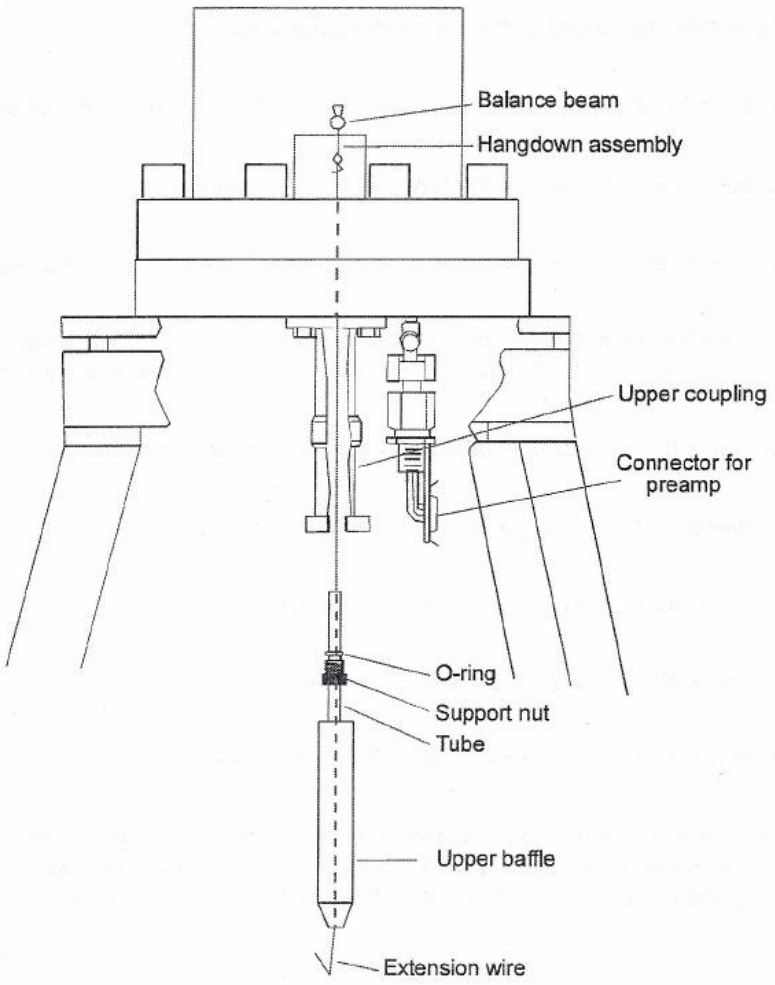

Figure 14: Schematic of the TGA extension wire and balance assembly. (*93*).

Figure 14 serves the same purpose as the spacers in the microbalance by reducing the volume required to purge. The upper coupling in the figure meets with the lower coupling on the vessel and the pressure coupling is attached for operation. Figure 15 displays a cut-away view of the furnace vessel along with the coupling and the end of the extension wire with sample bucket.

Upper and lower baffles are used to minimize volume and one thermocouple, seen at the bottom of the chamber, is used to control the furnace temperature. The total volume of the reaction chamber is 0.3 liters (*93*).

The TGA requires three gases for operation: reaction, purge, and furnace gases. These are controlled by mass flow controllers (Aalborg models DFC and GFC) and a back-pressure regulator housed in a ThermoCahn control box, which is the interface between the software and the TGA apparatus. Figure 16 diagrams these three flow paths in the reactor.

The reaction gas enters the bottom of the furnace chamber and flows upwards around the sample. A separate inert furnace gas flows outside the quartz reactor tube to keep the furnace chamber purged, both to avoid contamination of the furnace elements by reacting gases and to balance the pressure between the inside and outside of the quartz tube. The gases are combined downstream of the reactor and flow through the pressure control valve.

The sample vessel used was based on a previous design that held a sample as a thin cylindrical layer around a central post housed in a mesh. Figure 17 compares the previous sample vessel and the vessel used for all experiments described herein. Both sample vessels in Figure 17 are made of stainless steel and have a hole at the top to suspend from the extension wire from the balance, shown in Figure 14. The vessel on the left is the new

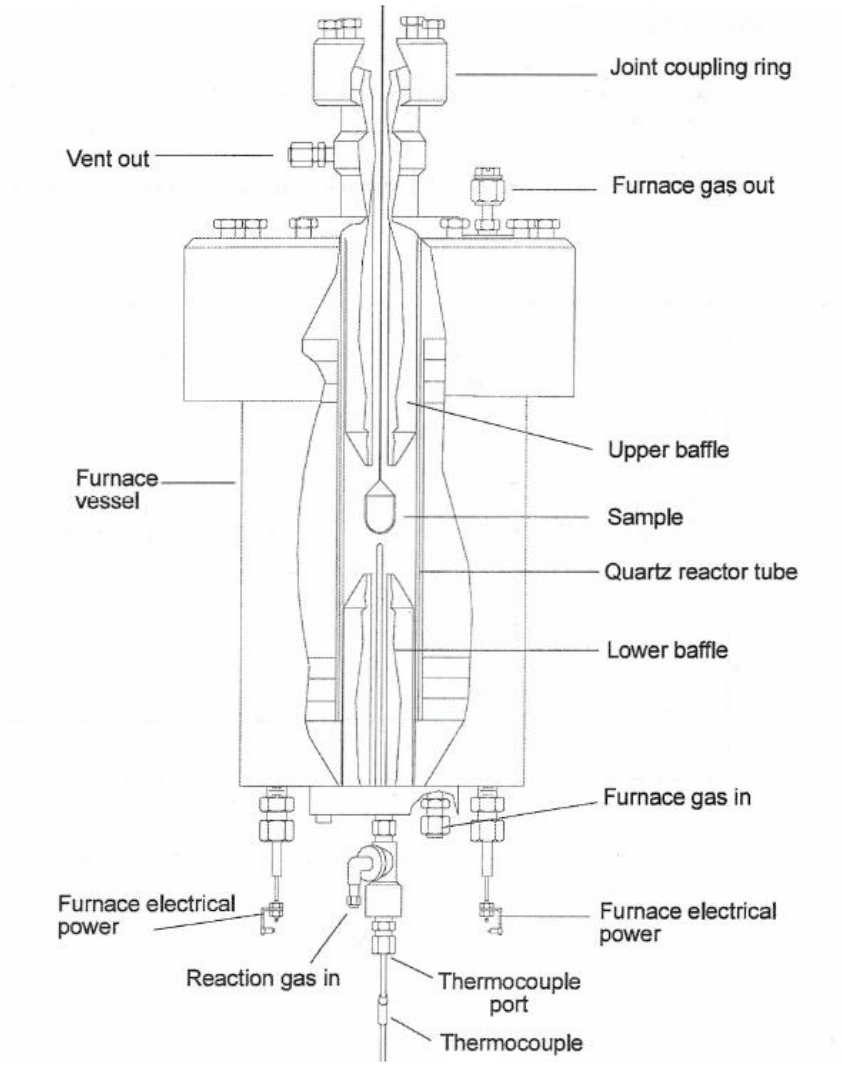

Figure 15: Cut-away view of the TGA furnace and pressure vessel. (*93*).

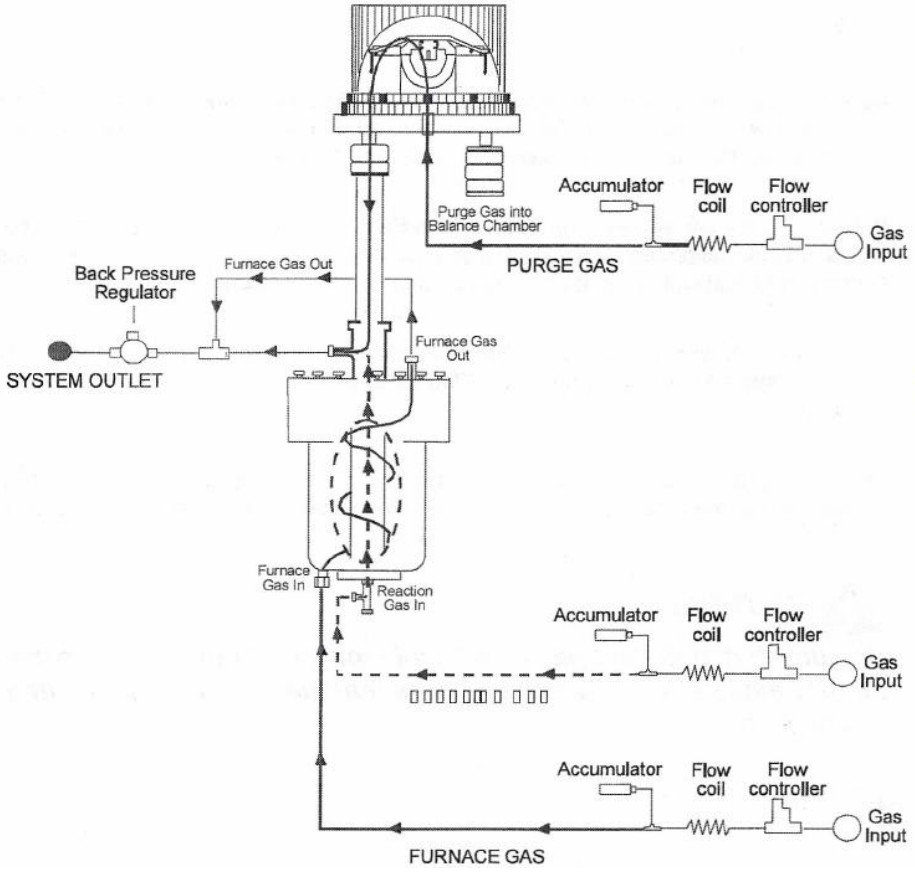

Figure 16: Gas flow diagram of the high pressure TGA. (*93*).

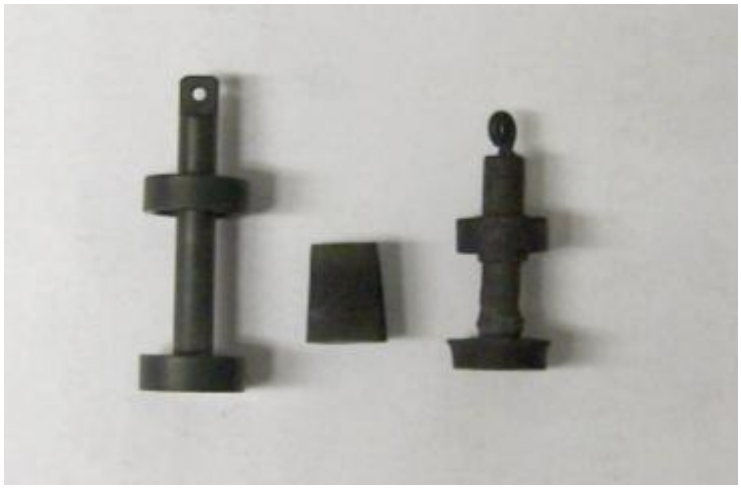

Figure 17: Thermogravimetric analyzer sample vessels.

one used for testing and the right vessel is the previous version, which shows signs of aging as ash and other particles have adhered to the post and excessive temperature and testing have degraded the metal. The mesh shown in the middle of the figure is made of 304 corrosion-resistant stainless steel and is 500 by 500 Tyler mesh screen.

3.3.2 Experimental Approach and Conditions

Similar to previous experiments conducted by the author, a design of experiments methodology was used to determine operating conditions. It was decided to perform experiments to determine both activation energy and the effects of pressure and carbon monoxide concentration on fuel gasification. Six tests were conducted in total to determine the activation energy. Temperatures of 900, 950, and 1000 °C were chosen with a CO concentration of two volume percent at a pressure of 245 psig (~18 bar). Carbon dioxide concentrations were consistently kept at 20 volume percent throughout the campaign with a balance of nitrogen. The remainder of the tests varied CO and pressure with the aim to quantify the influence of each on char reactivity and gasification behavior. Table 9 shows the full experimental condition matrix for the performed experiments.

At least one run of each condition shown in Table 9 was completed. Reasons for the lack of repeatability are equipment malfunctions and scheduling of the apparatus. While it was desired to obtain at least two data points of each condition, only 28 tests were run on the TGA; this number does not include runs that failed in the middle of operation. Of these 28, only 17 proved to yield quality data. These data are presented in the Results section of this report.

Table 9: Experimental conditions for TGA test campaign

Run Condition	Temperature, °C	Pressure, psig (bar)	CO vol %
1	900	245 (18)	2
2	950	245 (18)	2
3	1000	245 (18)	2
4	1000	0 (1)	2
5	1000	500 (35.5)	2
6	1000	0 (1)	4
7	1000	245 (18)	4
8	1000	500 (35.5)	4
9	1000	85 (7)	2
10	1000	85 (7)	4
11	1000	350 (25)	2
12	1000	350 (25)	4

3.3.3 Experimental Procedure

Each test followed the same overall procedure, described below.

1. The operator loads approximately 50 mg of sample into the sample vessel suspended from the microbalance extension wire. The operator raises the furnace into position and tightens the coupling ring around the joint between the microbalance and the furnace assembly.
2. Mass flow controllers feed nitrogen at a flow rate of 0.5 SLPM (standard liter/min, reference at 70°F) to the reactor and 3.0 SLPM of nitrogen to the furnace purge gas. The operator then closes the pressure control valve and the system begins to pressurize to the target pressure per run.
3. Once the reactor achieves the target pressure, the Thermax software increases the furnace temperature at 25°C/min to the desired run temperature. During this heating period, the fuel begins to devolatilize and lose weight.

4. Once the mass of the sample stabilizes, the operator switches the reacting gas from 0.5 SLPM of nitrogen to 3.0 SLPM of the reacting gas, comprised of a predetermined mixture of CO_2, CO, and N_2. After approximately 2 minutes, once the reacting gas reaches the sample, the mass of the sample begins to decrease mainly due to CO_2 gasification. The sample continues to react until either (1) the operator notices no continued mass loss, indicating a fully converted sample, or (2) the operator elects to shut down the run.
5. The operator switches the reaction gas back to nitrogen, depressurizes the system, and allows the furnace to cool. Once cool, the operator removes and weighs the sample on an external balance to determine the mass of the residue.

3.3.4 Data Analysis Methods

This section outlines methods of analyzing the TGA data by calculating the rate at 25% mass loss. Appendix C details two additional methods of rate analysis that were considered, integral and differential methods.

3.3.4.1 Mean R25 Method – MR25

This method is the most subjective of any considered because it requires the operator to look at individual data points and reject datum that does not suit a linear trend. Acquired data are normalized and a linear trend line drawn to obtain the slope of the mass loss between 20% and 30%, resulting in an average rate loss at 25%. Previously TGA rate analysis utilized this method, but the propagated error is sizable. Figure 18 shows the calculated slope at 25% mass loss of the original sample versus time. The short trend line represents the 20% to 30% mass loss data average.

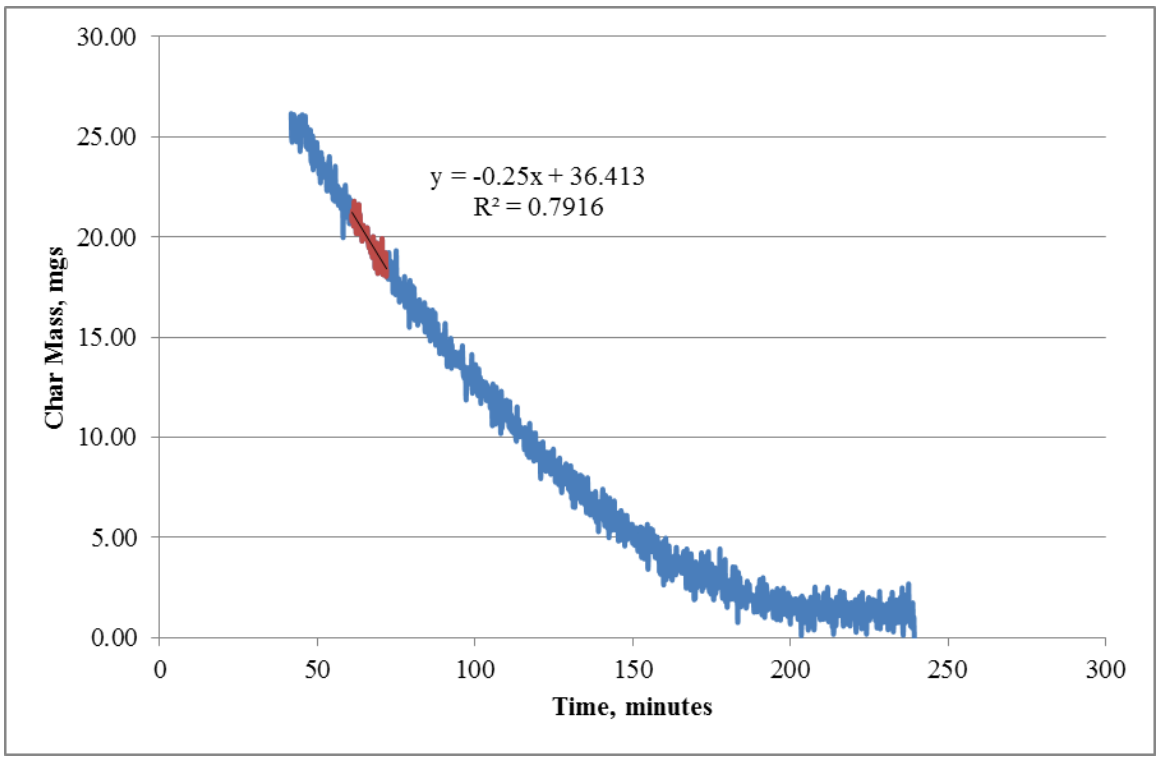

Figure 18: Char mass versus time for Sufco coal at 900 degress Celsius and 18 bar.

The slope of this line represents the R25 slope of char mass loss and Equation 2 represents the rate calculation, where GM is the gasifiable material, without ash.

$$\text{rate} = \left(\frac{-slope}{GM}\right) \qquad \text{Equation 2}$$

3.3.4.2 Polynomial R25 Method – PR25

This method combines the objective component of the integral and differential methods and the reliability of the mean R25 method. The recorded mass signal data are fit to a fifth-order polynomial and the derivative taken at 25% mass loss to obtain the slope. This modified fifth-order polynomial represents the fraction remaining and constructs a

normalized char remaining quantity. The same rate equation as in the MR25 method produces individual experimental rates.

3.3.4.3 R25 Comparison

This section compares the MR25 and PR25 methods. Figure 19 displays the acquired TGA rate data of the two rate methods, MR25 and PR25 with the 45° line for comparison. Figure 19 shows a strong goodness of fit and validates the polynomial rate method by comparing it to the mean rate method. Figure 20 shows the physical dependency of the two rate methods by plotting the natural logarithm of the rate versus absolute reciprocal temperature to obtain the activation energies from the slope.

The calculated activation energies for the MR25 and PR25 methods are 218 and 228 kJ/mol $\pm$24 kJ/mol, respectively. This difference of 10 kJ/mol, being less than 5% of the value, indicates that the polynomial rate does not only trend appropriately and show a good fit of the data, but a superior method to the MR25 because of the objectivity of the calculation, unlike the MR25 method. All subsequent rate analyses described herein utilize this method.

3.4 Entrained-Flow Gasifier

This section outlines and discusses the pressurized pilot-scale entrained-flow gasifier (EFG) and the experimental approach, including run conditions and experimental procedure. It also discusses data analysis methods pertinent to the EFG.

3.4.1 Pressurized Pilot-Scale Entrained-Flow Gasifier

The entrained-flow gasifier used for test campaigns described herein is housed at the University of Utah Industrial Combustion and Gasification Research Facility in Salt

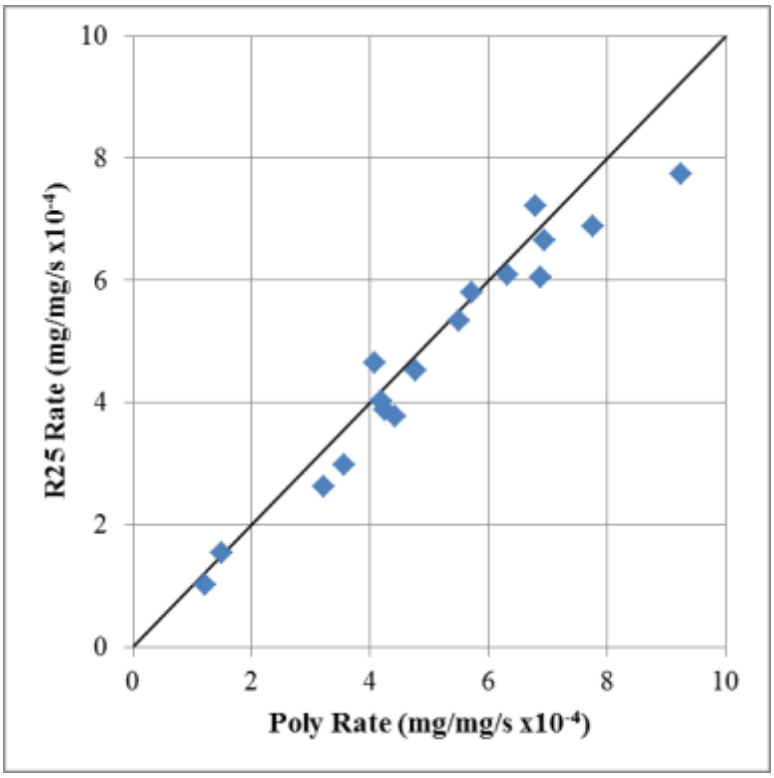

Figure 19: Rate comparison of MR25 and PR25, mg/mg/s x10^{-4} for conducted test campaign.

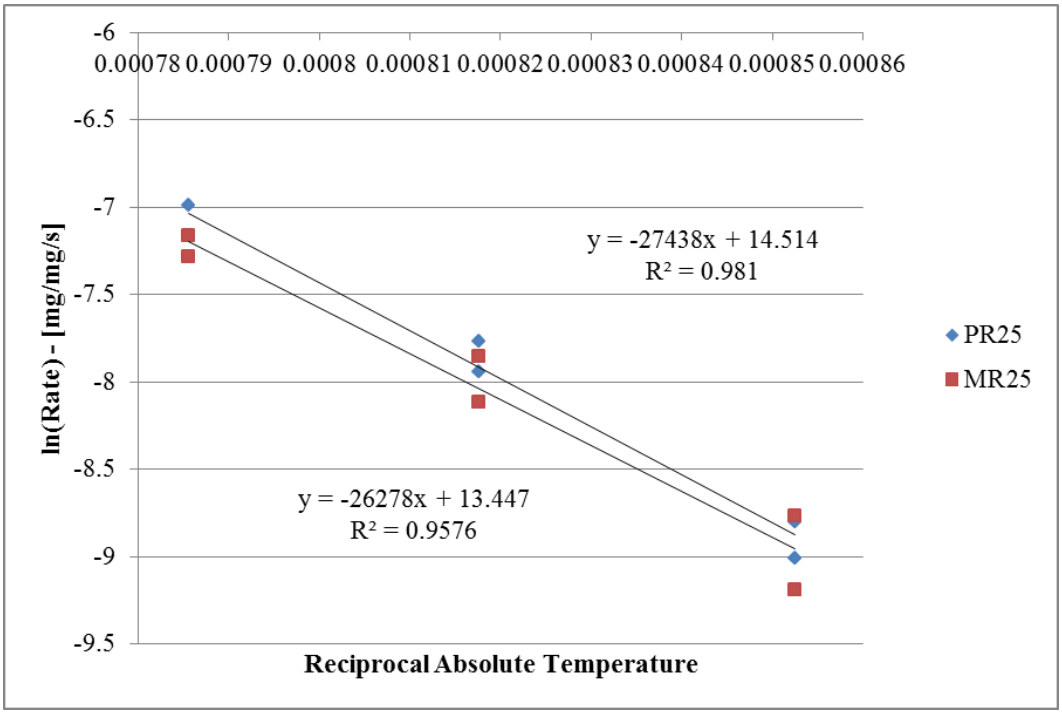

Figure 20: MR25 and PR25 rate comparison for ln(rate) versus inverse temperature.

Lake City, Utah. It is a Texaco-style gasifier standing 17.5 feet tall, including the reaction and quench zones, and is 2.5 feet in diameter. The reaction zone itself is 8 inches in diameter and 68 inches in length. Water-coal slurry is fed to the top of the reactor via a Moyno progressive cavity pump along with oxygen to atomize the fuel. The gasifier shell is rated to 2730 °F (1500 °C) at 450 psig (32 atm) and has a maximum heat input of 1 MMBtu/hr (300 kW). Feed flow rates are approximately five to 15 gallons per hour of coal slurry and 40 to 80 pounds per hour of oxygen. Figure 21 shows the gasifier (A) with the labeled sample port and (B) as a cross-section. The syngas that exits the gasifier is then routed to an atmospheric combustor, called the afterburner, which oxidizes the gases. The slag runs down the refractory walls of the gasifier and drops to the quench where it is retrieved after shutdown of the EFG.

3.4.2 High-Pressure Extractive Gas-Phase Sampling System

The basic design of the probe is a pneumatically controlled cylinder capable of precise reactor depth control via OPTO 22 hardware. The probe body travels through a pressure seal and enters the gasifier where it sits until sample procedures begin. The tip of the probe will remain near the interface of the hot and cold face refractory walls when not in use and will travel the length of the sample port to the desired radial location within the gasifier reaction zone.

3.4.2.1 Probe Extension and Assembly

The probe extension constitutes machined and welded parts of stainless steel. The cylindrical portion that traverses the gasifier is water-jacketed and made from three-quarter inch, one-half inch, and one-quarter inch stainless steel tubing. The one-quarter inch tube protrudes from the tip of the extension and has a one-eighth inch hole drilled on the under-

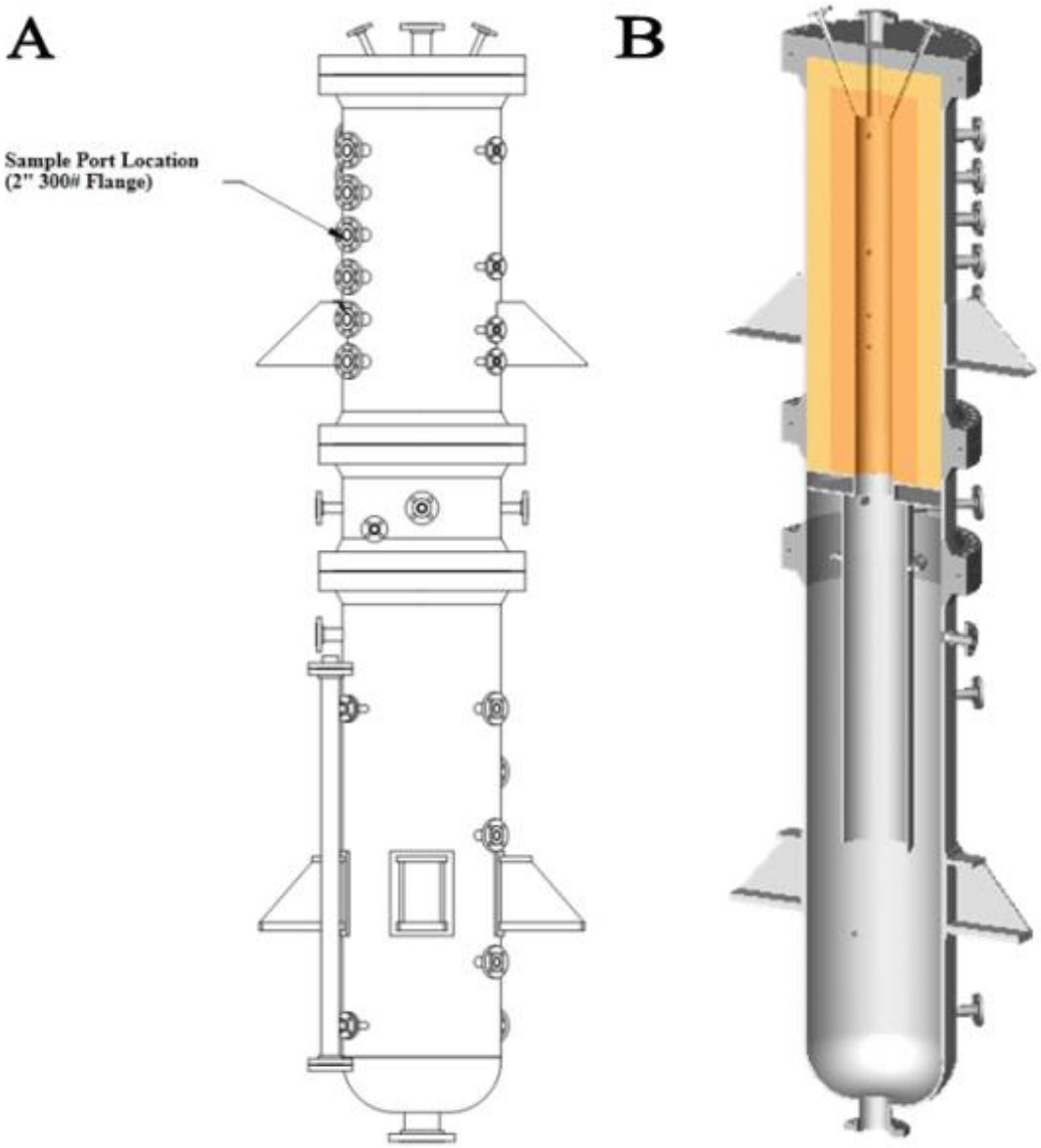

Figure 21: CAD rendering of the pilot-scale pressurized entrained-flow gasifier (A) designated sample ports and (B) cross-sectional view of the gasifier.

side of the protuberance for gas-phase extraction. The end of the ¼-inch tube is closed off in order to deter slag buildup. The small hole on the underside also serves as the purge for the sample system when sampling procedures are not being undertaken. Figure 22 and Figure 23 show the probe extension and probe tip, respectively.

The probe extension travels through a flange assembly called the seal housing and stabilizer. The seal housing consists of two pieces, one for the hot-face, or gasifier side, of the extension, and one for the cold-face of the extension. Each side has a machined stainless steel cooling trough welded into a two inch, 300-pound stainless steel slip-on flange. The hot-face seal housing has an additional recessed edge for the precise placement of the pressure seal. An adjustable guide resides at the nonreactor end of the seal housing to support the weight of the probe extension and offer rigidity to the apparatus. Appendix D details these seal housing components.

Figure 24 shows the whole flange assembly as an exploded view, including the stabilizer and cooling trough flange assembly.

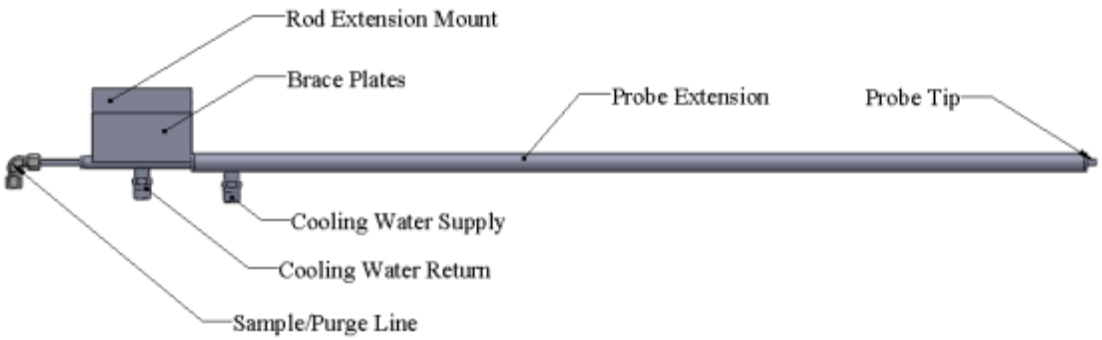

Figure 22: Probe extension and rod mount brace.

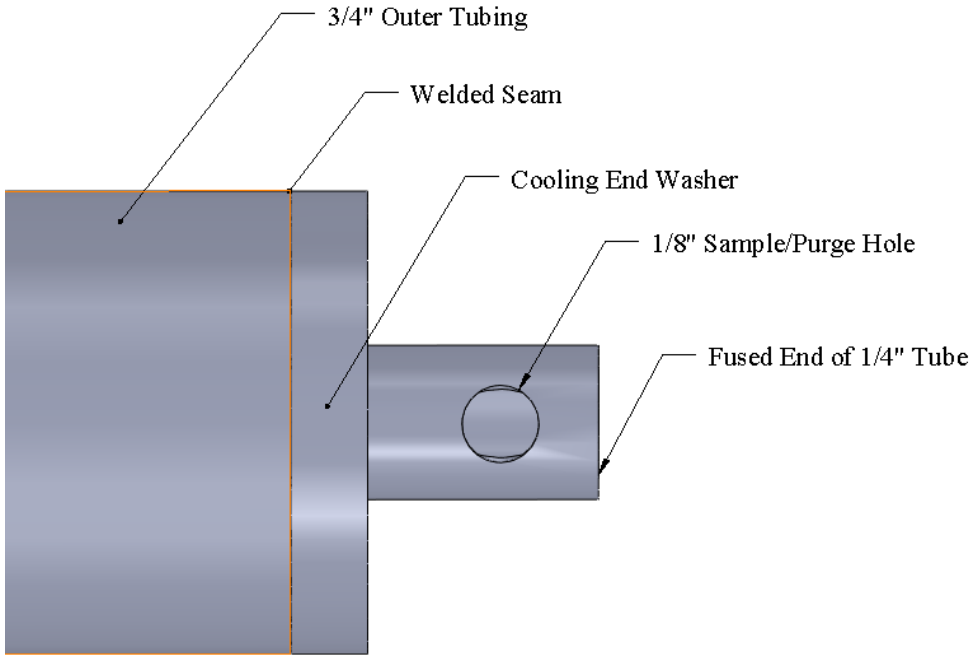

Figure 23: Close-up of the probe extension tip.

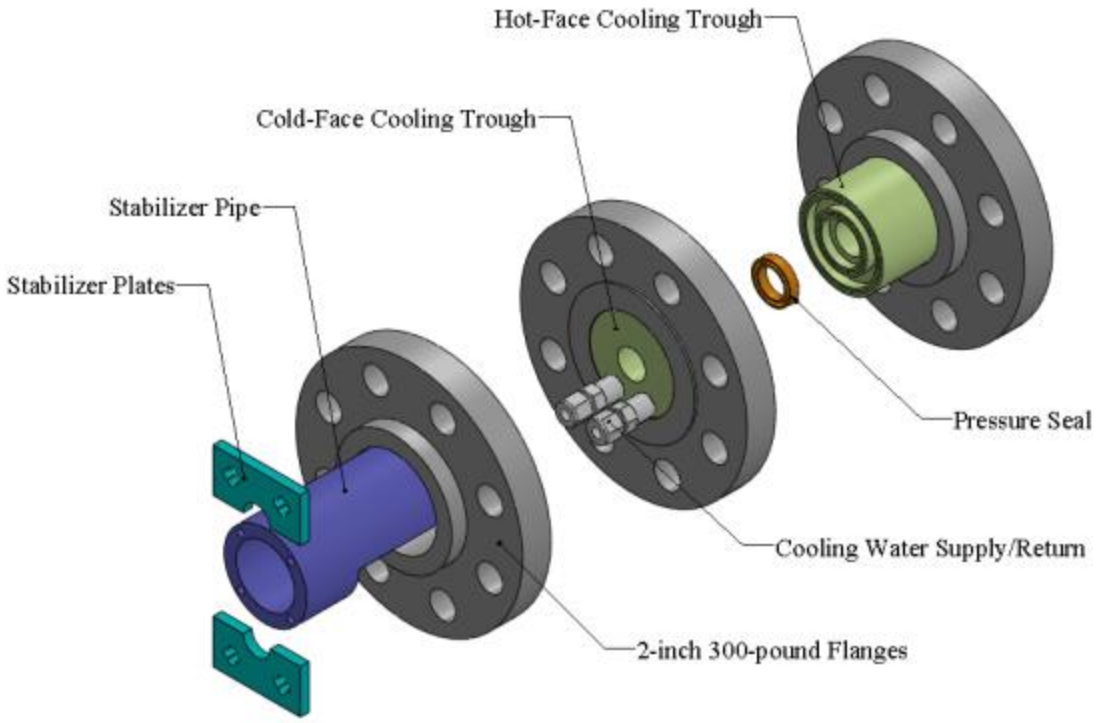

Figure 24: Exploded view of flange assembly and components. Stabilizer plates (aqua), stabilizer pipe (dark blue), cooling troughs (vomit), pressure seal (orange), and cooling water attachments.

This exploded view shows the major components of the seal housing and stabilizer with the exception of the silicon o-rings that sit between the two troughs. Figure 25 shows a photograph of the assembly attached to the gasifier with cooling lines for both the seal housing and the probe extension extending downward into the grating of the mezzanine. The cooling lines coming out of the grating connect to the same cooling system for the injector. Two lines extend from the mezzanine and supply cooling water, while the other two lines are return cooling water lines.

3.4.2.2 Probe Pneumatics and Control

The device that controls the depth and placement of the probe extension is a pneumatic piston, also called a position feedback cylinder (PFC). This piston has a stroke

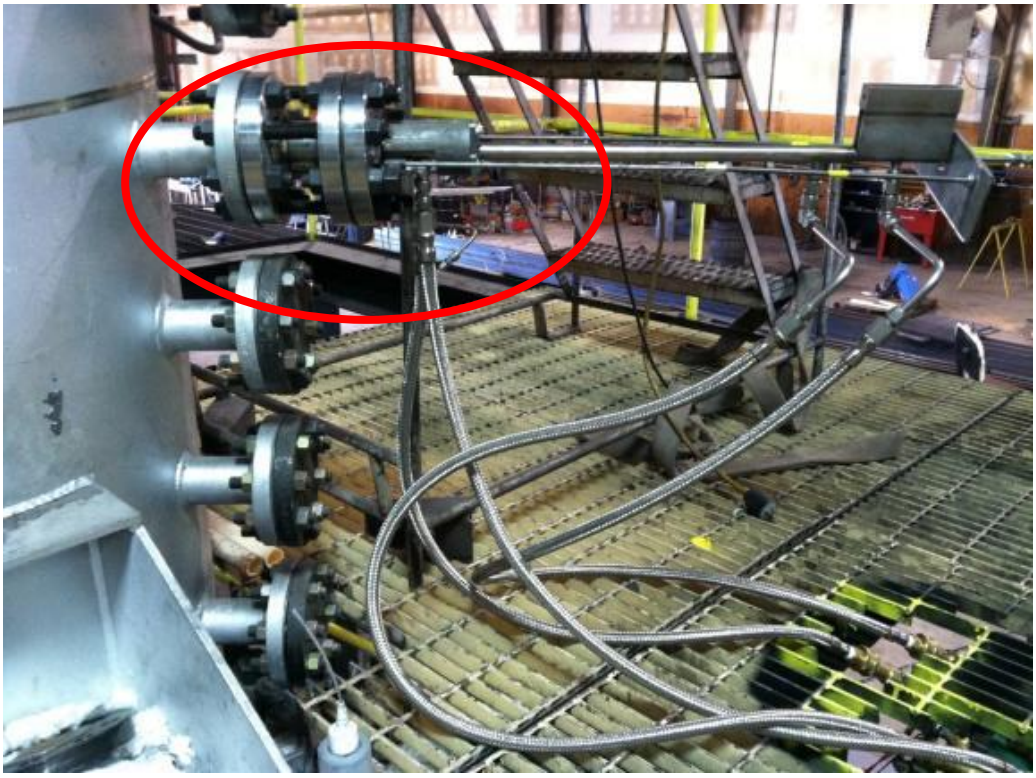

Figure 25: Probe assembly and cooling lines for the seal housing and probe extension. The flange assembly with stabilizer is circled in red.

length of 18 inches and has a bore size of three inches. Figure 26 shows a cross-sectional CAD drawing of the cylinder attached to the rear of the probe extension.

This piston was manufactured by Bimba Manufacturing; model number PFC-7018-L-Y. The internal mechanism of the piston is a magnet that runs in the middle of the rod down its length and is able to transmit the current location. The rod position of the PFC is controlled by the position control system (PCS), which is a small control box that houses two solenoid valves, one for the push direction and one for the pull direction. The PCS also contains a circuitry that transmits the current position and setpoint between the PFC and the distributive control system OPTO 22, discussed in the next section.

Figure 27 shows the full assembly of the probe, including flange assembly, probe extension, and PFC/PCS systems. Here, all of the major parts of the system are visible except for the computer and OPTO control system, which are located on the main level of the gasifier and not the mezzanine. Moving from left to right, the major components are flange assembly and cooling lines, stabilizer, probe extension and cooling lines, ball joint guide, threaded rod extensions and U-brace, pneumatic cylinder, support stand, and pneumatic control box. Appendix E details these components.

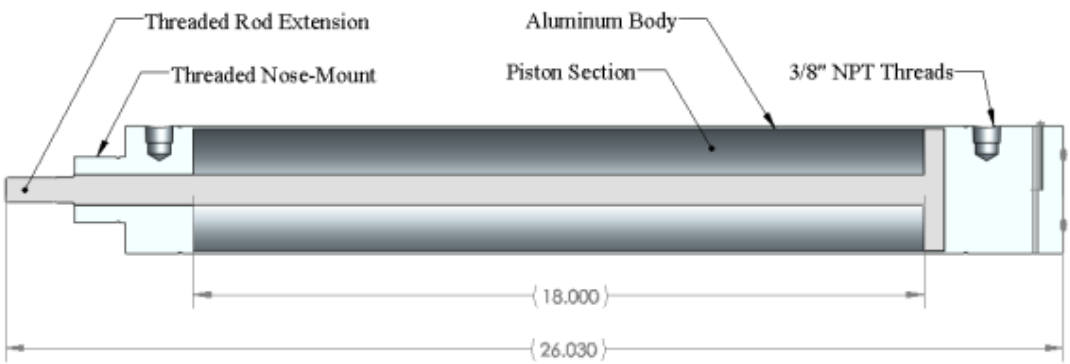

Figure 26: Cross-section of the pneumatic feedback cylinder.

Figure 27: Photograph of the entire probe assembly including (from left to right) flange assembly and cooling lines, stabilizer, probe extension and cooling lines, ball joint guide, threaded rod extensions and U-brace, pneumatic cylinder, support stand, and pneumatic control box.

3.4.2.3 Additional Equipment

A small cart beneath the mezzanine controls the probe, which contains a computer, a control box for the distributive control system OPTO 22, and various parts and instrumentation. Figure 28 shows a photograph of the cart. The cart is close to the sampling locations in order to decrease the total sample time and allow more samples to be taken in a more efficient manner. During sampling, gases travel through the probe assembly and into 0.25 inch tubing and a water-knockout system before elutriated particles are removed by a 15-micron filter. Five-liter tedlar bags capture the gases after traveling through a series of solenoids and a critical orifice then analyzed by gas chromatography. Figure 29 displays a close-up of the solenoid manifold in Figure 28. Here, all three solenoids can be seen along with the critical orifice placement. Two pressure gauges are at the outlets of the three-way solenoid to ensure flow is supplied to the afterburner during the purge of excess nitrogen and previous sample gases form the system. The range on the

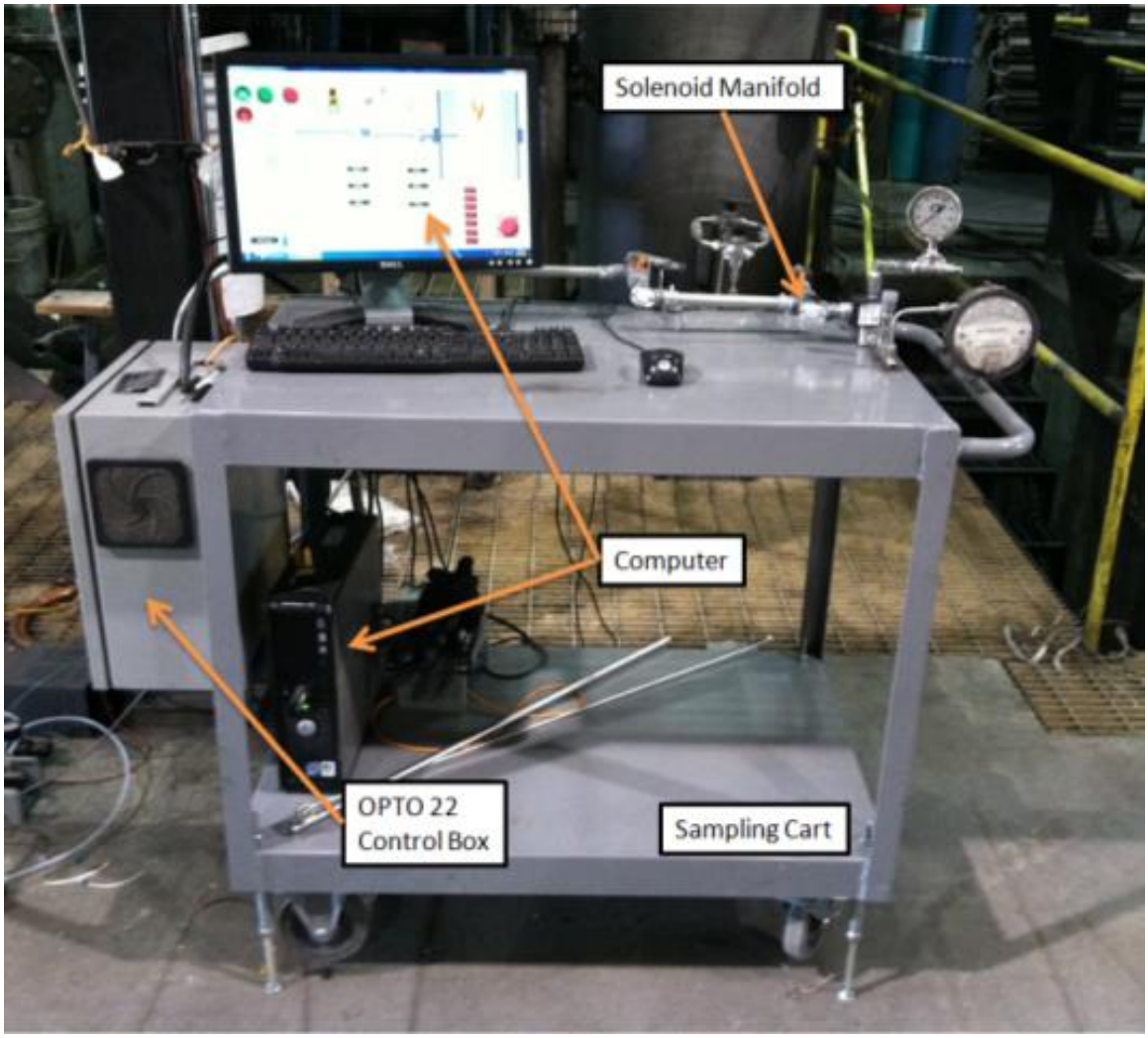

Figure 28: Computer and OPTO 22 control cart.

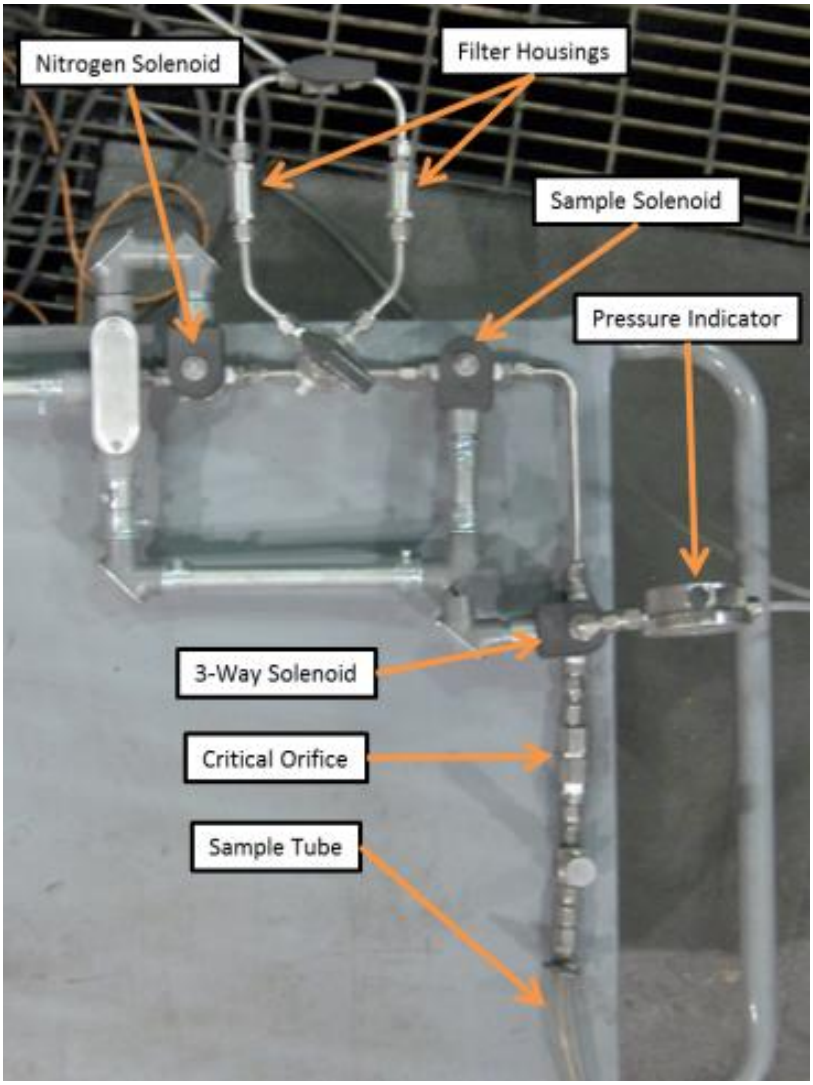

Figure 29: Solenoid manifold close-up.

pressure gauge of the sample outlet of the three-way solenoid is from 0 to 10 inches of water. This will ensure the manual filling of the tedlar bag is performed at a nonhigh pressure and in the event of excess filling, the operator can take the bag from the sampling port on the solenoid manifold and not cause the bag to burst. A needle valve is also installed to target a 10 to 20 second sample time. Figure 30 illustrates a piping and instrumentation diagram of the sampling system.

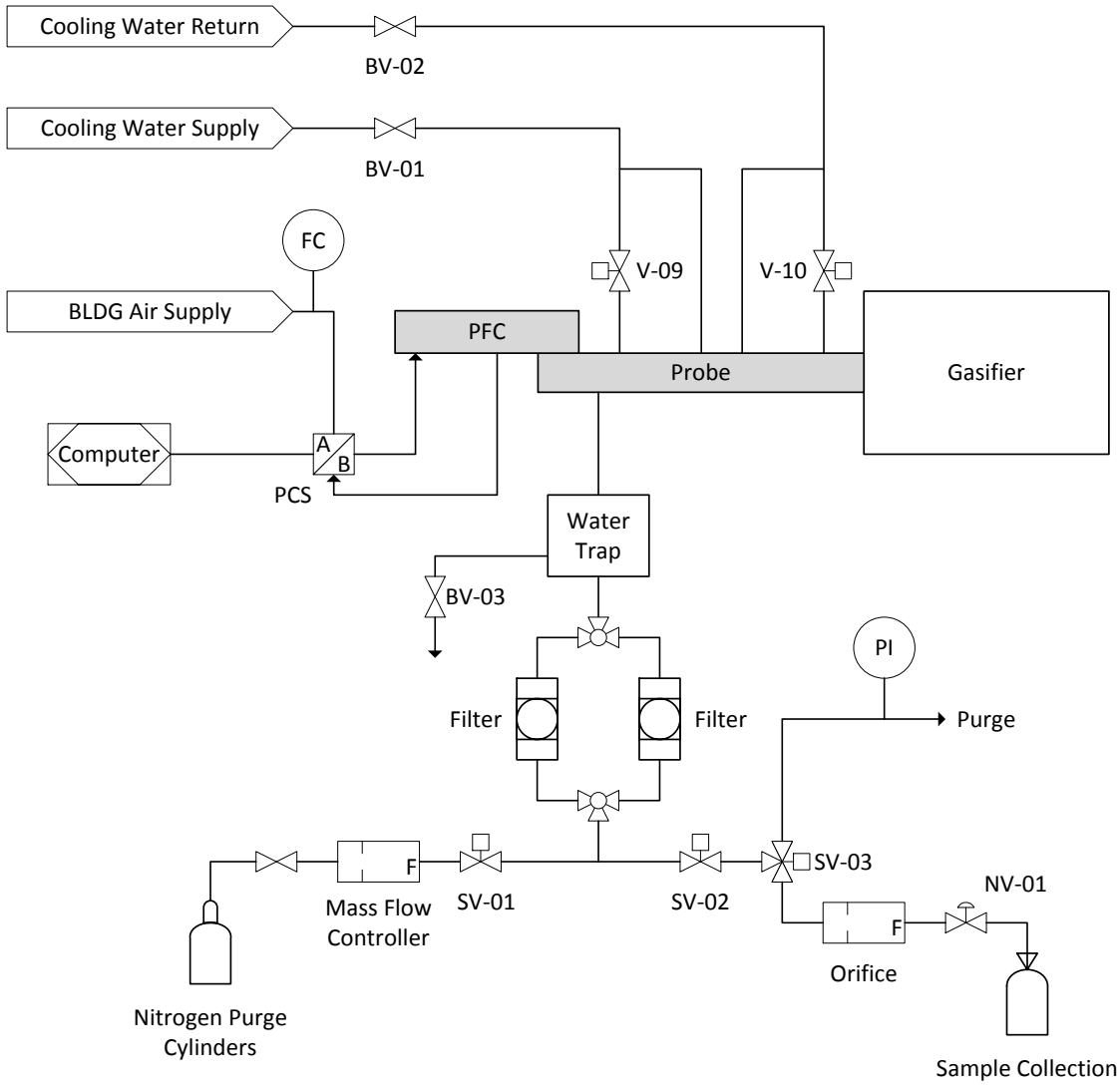

Figure 30: Piping and instrumentation diagram of the sampling system. BV indicates ball valve, SV indicates solenoid valve, and NV indicates needle valve. FC indicates flow control device and PI represents pressure indicator.

From Figure 30, it can be seen that the operation of the sampling system is dependent upon the building (BLDG) air supply and cooling tower. The nitrogen purge, seen at the bottom of the figure, is attached to the same nitrogen purge used for the flame detectors and has a supply pressure of approximately 400 psig, not including line losses. Purge flow rates of nitrogen are controlled by a mass flow controller (Bronkhorst, model F-202AI-M20) before being routed to the sampling system described above.

3.4.2.4 Sampling System Computer Interface and OPTO 22 Components

OPTO 22 Control is the program that transfers all the code and software settings to the hardware and the brain/controller inside the control box. Here, charts are composed or written for every step the program takes to ensure safe operation. Appendix F details the logic diagram, or chart, that controls all instrumentation for the probe and its systems as well as summarizes the OPTO hardware.

The probe and control system were characterized at atmospheric pressure in preparation for pressurized operation. A correlation of the probe setpoint and the actual probe location was established. Figure 31 shows probe displacement versus time for the probe setpoint and the probe position as well as the absolute difference between the two. The reference point is the zero value of the cylinder; the rod extension fully retracted.

From Figure 31, a base value of the difference between the probe setpoint and its actual location is approximately 0.25 inches. This value can be as high as 0.31 inches when extended to 18 inches. In terms of operation, about a one-quarter inch is added to the setpoint value to sample at that point. An example is sampling at 12 inches into the reactor from the fully retracted position of the cylinder. If the target were 12 inches (actual), then the setpoint would be 12.25 inches.

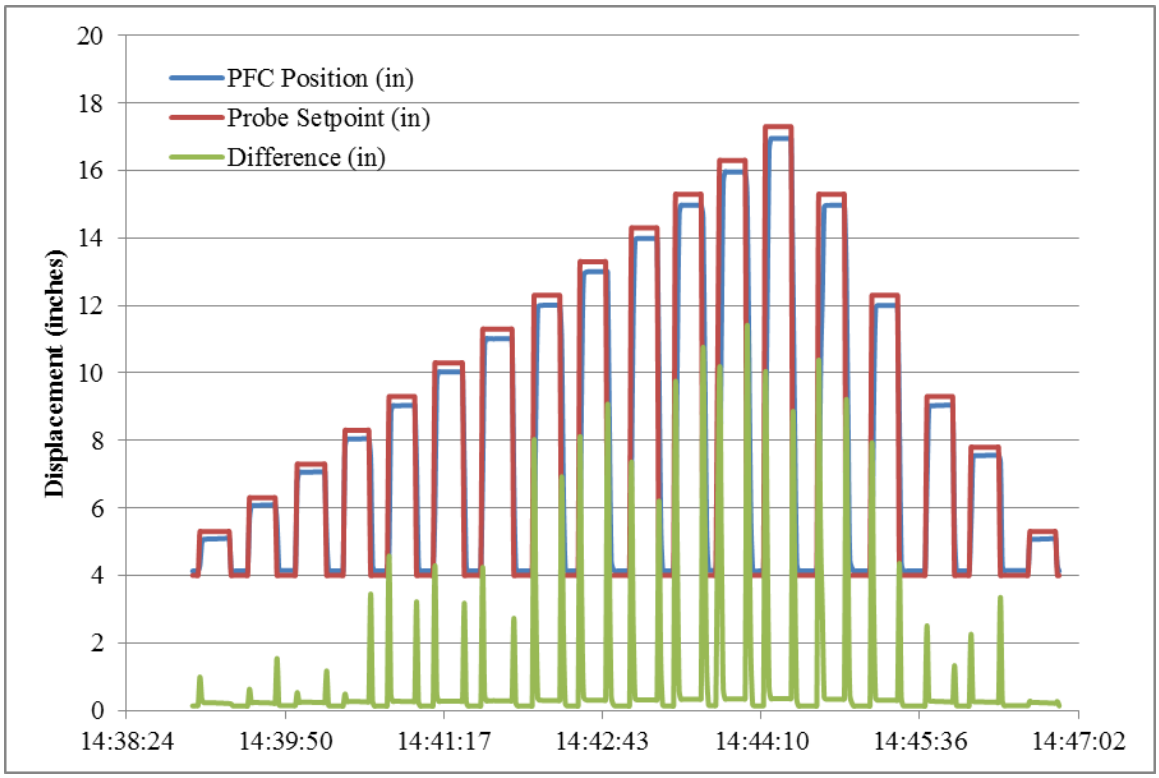

Figure 31: Displacement versus time of the sample probe; OPTO readouts.

As a reassurance to the operator of the probe, the probe was extended into the gasifier, past the centerline and held there for a short amount of time in order to view the probe from the injector port atop the gasifier. Figure 32 shows the top view of the reactor and down the length of the reaction zone with (A) no probe and (B) with the probe extended. These photographs were taken after heating the gasifier by natural gas combustion, but before the coal slurry injector was installed for operation. The bright, near white, color is the radiation emitted from slag near the bottom of the reaction zone.

3.4.3 Experimental Approach and Conditions

Confidence was high that sampling hot, pressurized gases was achievable as long as the system was not too complicated and the likelihood of gasifier depressurization via

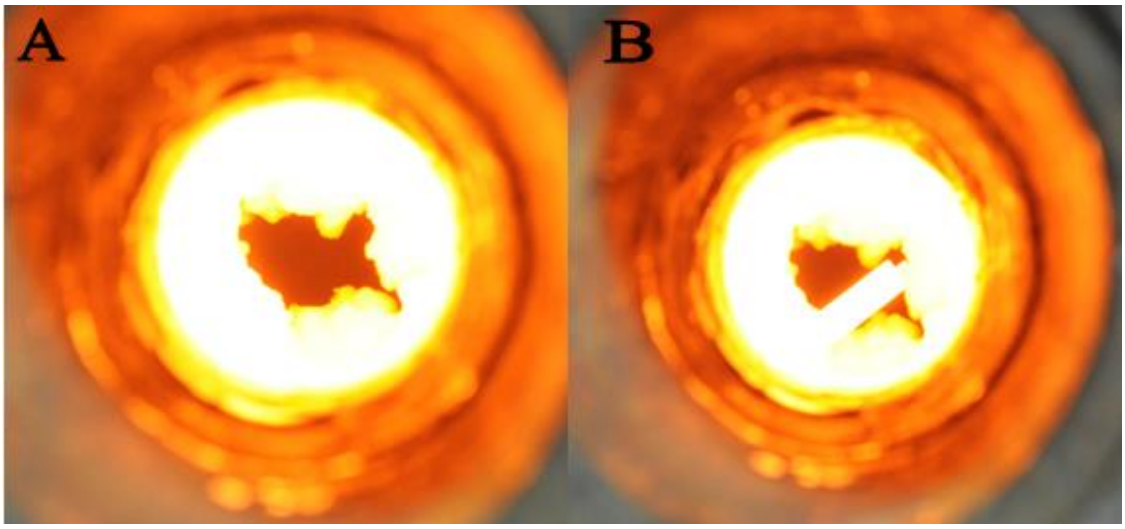

Figure 32: EFG reaction zone (A) Top view without probe (B) Top view with probe extended to centerline sample point.

the sampling system was low. The sampling system was designed for temporary operation and not to be attached to the reactor for long periods of time and/or while the EFG was idling on natural gas to maintain high temperatures.

Based on operator experience, coal slurry and oxygen feed rates were adjusted to achieve one of three target temperatures. At location three of the gasifier, the probe extracts three samples, one at the reaction zone wall (W), one at the centerline of the reaction zone (C), and one between the wall and centerline (H); duplicates taken at the leisure of the probe and EFG operators enhance data analysis methods. These sample points correspond to setpoints zero (W), four (C), and two inches (H), respectively. For the campaign described herein, the slurry solids loading is 56.5%. Table 10 summarizes all EFG target conditions and major operating conditions.

It is important to note that the dry coal, slurry, and oxygen feed rates were not chosen before operation and the values in Table 10 were taken from the log files of the EFG control computer and averaged over the total sampling time. The main reason for this

Table 10: EFG target conditions and major operating parameters.

Target Temperature (°F)	2500	2650	2800
Thermal Input (MBTU/hr)	741	697	622
Wall (W) Sample	X	X	X
Halfway (H) Sample	X	X	X
Centerline (C) Sample	X	X	X
Slurry Feed (gal/hr)	11.49	10.80	9.64
Dry Coal Feed (lb/hr)	62.29	58.56	52.26
Oxygen Feed (lb/hr)	64.91	63.99	65.10
Slurry Specific Gravity	1.15		
Slurry Solids Percent	56.47%		
Gasifier Pressure (psig)	150		
EFG Sample Port	3		
Fuel Name	Sufco		

is the hysteresis of the EFG. Experience has proven that it is easier and safer to monitor feedback from the gasifier and then increase or decrease feed flow rates and increase operating pressure. These feedback variables include syngas oxygen concentration, response of the control valves above the afterburner, thermocouple response, and others.

A pressure of 200 psig was initially targeted for operation, but was decreased to 150 psig due to problems with the probe seal. A minor misalignment during the setup of the probe caused syngas to leak from the pressure seal flange housing, but during pressurization of the EFG, the operator checked the seal for leaks approximately every 50 psi increase. The engineers and operators determined that 150 psig was a safe operating pressure for the purpose of gas-phase extraction and to continue the run.

3.4.4 Experimental Procedure

The sampling system procedure depends upon safe and steady state operation of the EFG and is subject to the discretion of the EFG operator. Sampling begins once the

operator has taken proper safety precautions and reasons that the gasifier has reached steady state. Prior to the sampling procedure, however, the operator must install the probe. These installation and sampling procedures are outlined below.

Installation Procedure:

1. Ensure the OPTO 22 charts are running and logging all activity. Attach cooling water lines and open flow to the probe extension; ball valves and solenoids must be open. With the natural gas heating of the EFG stopped and the reactor under balanced pressure, the operator removes the sampling port flange and the refractory/insulation plug. The operator then bolts the hot-face flange to the gasifier and centers the stabilizer and cold-face flanges around the probe extension. The operator then attaches the remainder of the flange assembly to the hot-face flange and immediately begins running cooling water to the seal housing. This must be done quickly to preserve seal integrity, as the shell of the gasifier is in excess of 350 °F.
2. The operator then attaches the pneumatic cylinder to the threaded rod and U-brace assembly via the large threads at the front of the PFC. The operator then tightens the aluminum nut at the nose-end of the PFC and threads the extension rod into the mount at the rear of the probe. A fair degree of slack should be present in the system to allow proper alignment. The operator places the small tripod stand under the rear of the PFC and attaches the cable at the rear to the PCS in addition to connecting the three-eighths inch Viton lines extending from the valve side of the PCS to the PFC.

3. Operator ensures cooling water is running and all connections are necessarily tight; this includes flange bolts, wires and cables, and compression fittings. The initial location of the probe is input in OPTO Runtime and the air supply to the PCS valves is opened.

Sampling Procedure:

4. The operator begins sampling once the gasifier reaches a steady state. The desired distance is specified in Runtime under 'Probe Sample Location' and the desired times for the sample line purge and sample time are specified as well. The deadband of the probe location should not be less than 0.5 inches, but low enough to indicate if the probe is not moving; it is 1.0 inch for all tests described here. The operator specifies 'EFG Pressure', "Sample Port Location', 'Fuel Type', and 'Fuel Solids %' within Runtime.
5. When all parameters are set, a 5-liter tedlar sample bag is placed at the outlet of the sample tube and the septum is opened. 'Sample Start/Stop' is pressed to initiate sampling. Once the sequence is complete, the septum valve is quickly closed on the bag and place to the side for analysis. The system then reinitializes and is ready for the next sample.

3.4.5 Data Analysis Methods

A Varian micro-gas chromatograph, model 4900, analyzes all gas samples with Chrome software made available by Agilent Technologies. Once calibrated, the GC measures the mole percent of the key syngas species, CO, H_2, CO_2, CH_4, and H_2S in addition to higher molecular weight hydrocarbons. Microsoft Excel prepares all data and summarizes all calculations for use in JMP Pro (version 9.0.2). This program utilizes built-

in models as well as user-defined parameters for analysis, including but not limited to full factorial and response surface designs. Correlations and gasification metrics include prediction analysis of major gas components as a function of temperature as well as heating value.

CHAPTER 4

EXPERIMENTAL RESULTS AND DISCUSSION

4.1 Wire–Mesh Product Yields

This section presents the collected data from the tests described earlier in addition to previous data collected from the wire-mesh reactor. Shown in this section is how the pressure affects the yields to a lower degree than temperature and hold time so an additional campaign was carried out at atmospheric pressure.

4.1.1 Atmospheric Data

The product yields of the atmospheric tests show strong correlations for temperature and hold time with a heating rate of 1000 ℃/s. Tremel, et al. (*5*) present comparable results where for a bituminous coal, the volatiles yield is close to the proximate volatile matter on a dry, ash-free basis (daf). Figure 33 and Figure 34 show the volatiles yield weight percent (daf) versus final temperature of the wire-mesh. The proximate volatile matter for the Sufco coal used is 45.0%. Figure 34 shows only the 3 and 5 second hold time cases to make the error bars visible. Indicated vertical error is the standard error at a 95% confidence level.

In Figure 33 and Figure 34, the horizontal error is the standard deviation from the average soak temperature of each run. The values were calculated using the National Instruments software program DIADem. The plotted temperature value for the zero second data is only the maximum temperature recorded.

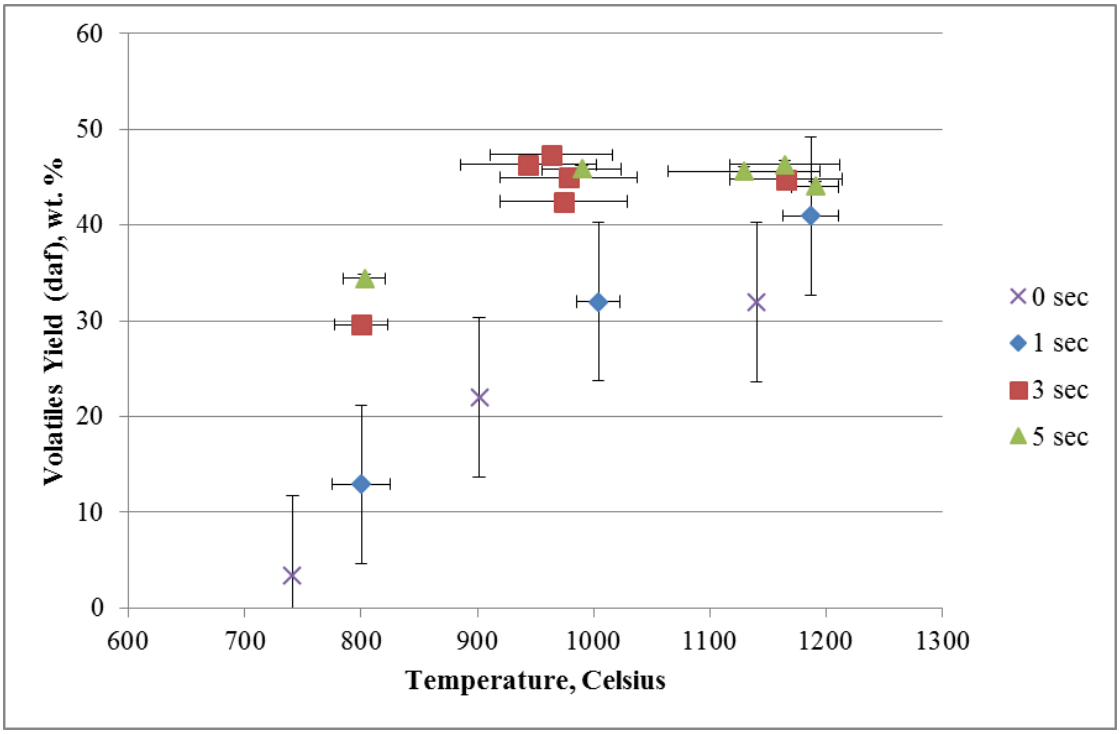

Figure 33: Volatile yields, wt.% (daf) versus final temperature for hold times of 0 sec (×)1 sec (◆), 3 sec (■), and 5 sec (▲).

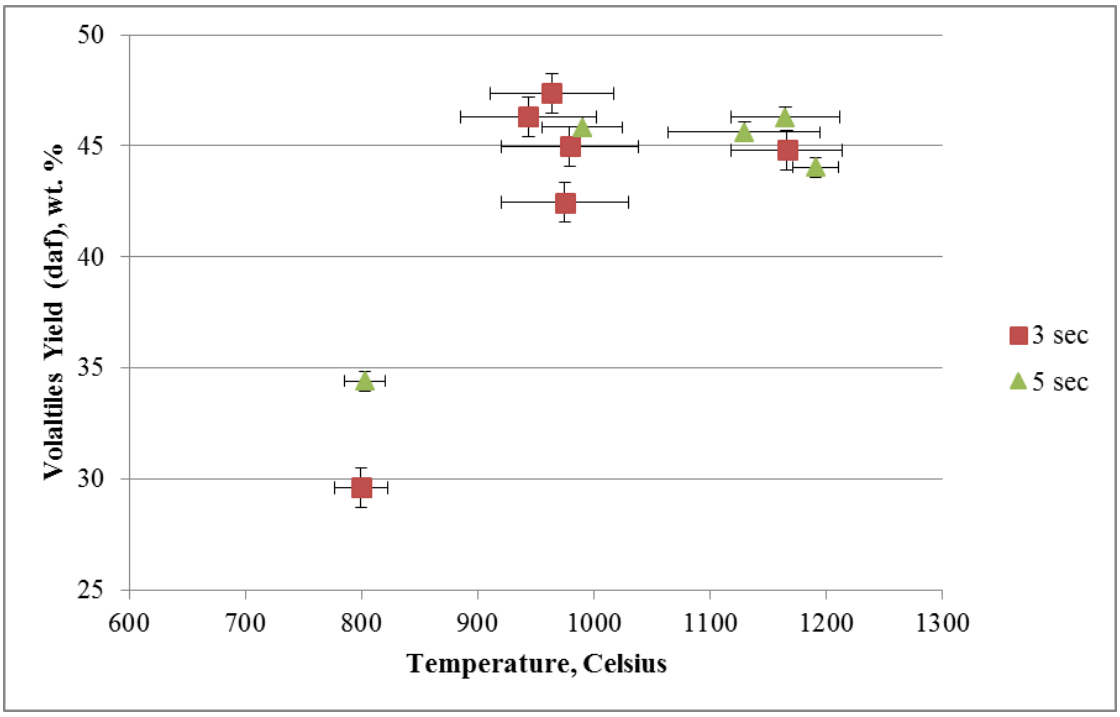

Figure 34: Volatile yields, wt.% (daf) versus final temperature for hold times of 3 sec (■), and 5 sec (▲).

The initial data were also divided by the individual hold times of each run to determine weight loss per time for a submodel of an additive reaction time model. While this equation can only be directly applied to the parameters tested, modifications are made in section 5.1.1 to correct for pressure and other factors. Figure 35 shows the volatiles yield per hold time versus temperature for cases of 1, 3, and 5 second hold time, while Figure 36 only shows data for 3 and 5 second hold times to appreciate the error associated with the yields. Temperature error is the standard deviation about the average.

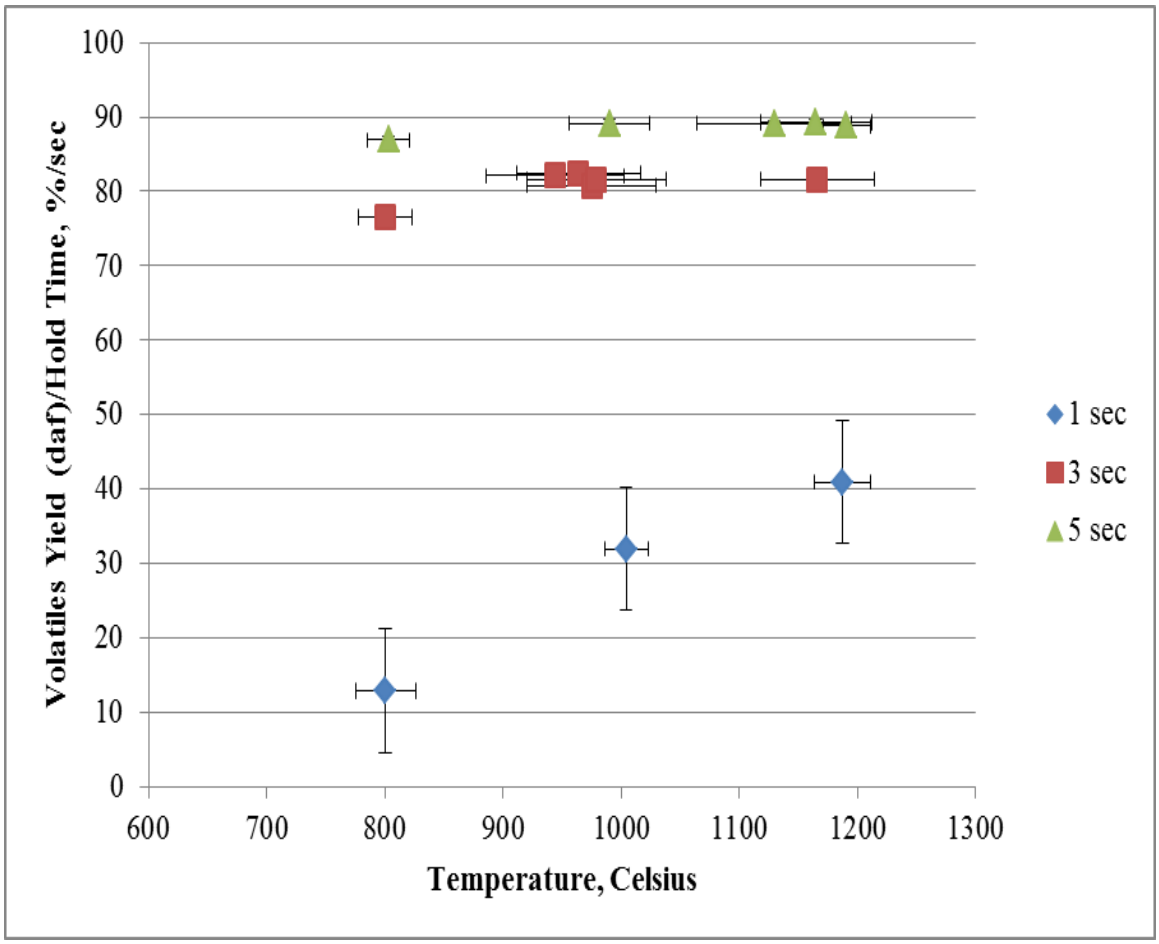

Figure 35: Volatile yields per hold time, wt.%/s (daf) versus final temperature for hold times of 1 sec (◆), 3 sec (■), and 5 sec (▲).

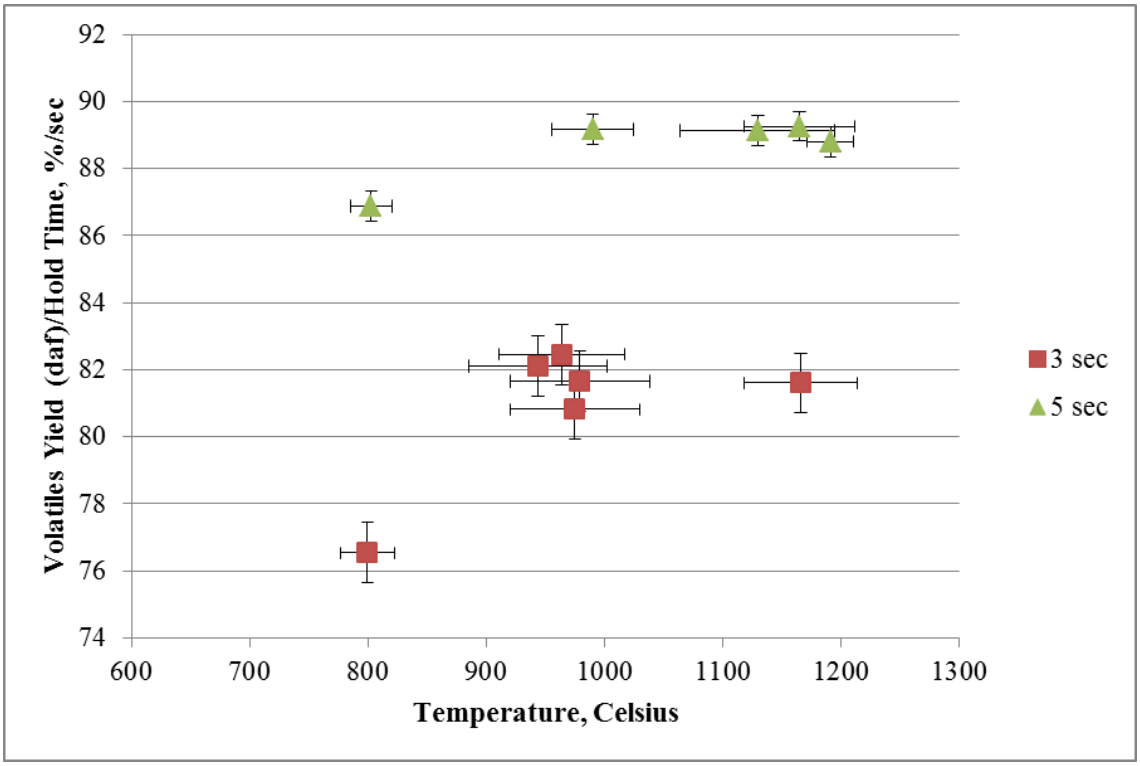

Figure 36: Volatile yields per hold time, wt.%/s (daf) versus final temperature for hold times of 3 sec (■), and 5 sec (▲).

The error associated with the higher temperature runs as in Figure 33 and Figure 34 is much smaller than that of 0 and 1 second hold times. This could indicate that the carbon structure is broken down enough and the tars are subjected to high enough temperatures that all available lighter weight volatiles are emitted. Equation 3 and Equation 4 describe the volatiles yield and volatiles yield per time. Table 11 presents the values of the coefficients A, B, C, D, E, m, and n.

$$VY = A + BT + CH + D(T - m)^2 + E(H - n)^2 \quad \text{Equation 3}$$

$$VY/t = A + BT + CH + D(T - m)^2 + E(H - n)^2 \quad \text{Equation 4}$$

Table 11: Summary of coefficients for Equation 3 and Equation 4.

Eq.	A	B	C	D	E	m	n
3	-7.433	$4.356 \cdot 10^{-2}$	3.228	$-2.140 \cdot 10^{-4}$	-1.127	$9.929 \cdot 10^{2}$	2.706
4	$2.366 \cdot 10^{1}$	$2.539 \cdot 10^{-2}$	$1.136 \cdot 10^{1}$	$-8.322 \cdot 10^{-5}$	-5.668	$-1.007 \cdot 10^{3}$	-3.286

The values of m and n are effectively the averages of tested temperature and hold time, respectively. Figure 37 and Figure 38 show the experimental volatiles yields and volatiles yields per time plotted against the calculated yields using Equation 3 and Equation 4. A 45° line is plotted for comparison. Both Figure 37 and Figure 38 show standard error of the values in a 95% confidence level. The coefficients of determination of Figure 37 and Figure 38 are 0.943 and 0.972, respectively.

Hold time is seen to affect the volatiles yield with increasing trends as seen in Figure 39. Here, the yields are plotted versus hold time for the variable temperature runs with standard error at a 95% confidence level. As hold time increases, the yields increase as well, ultimately reaching a maximum for 1000 ℃ and 1200 ℃ at approximately 45 weight percent. This coincides with the dry proximate value of the volatile matter.

A similar study presents data as in Figure 39 (*23*) where two competing reactions take place to accommodate for high volatile and low volatile yields. Although Kobayashi et al. (*23*) operated a laminar flow furnace and proposed these competing reactions, a wire-mesh reactor, operated as a batch system, has similar results. Within the batch and flow systems, the high volatile reaction is assumed to occur rapidly when compared to the residue reaction. The devolatilization of the residue will occur at a slower rate and have a lower volatiles yield than its precursor. Kobayashi continues to explain that the faster reaction will undergo decomposition reactions and have a higher activation energy than the slower, condensation reactions that lead to char formation. Adopting this reaction

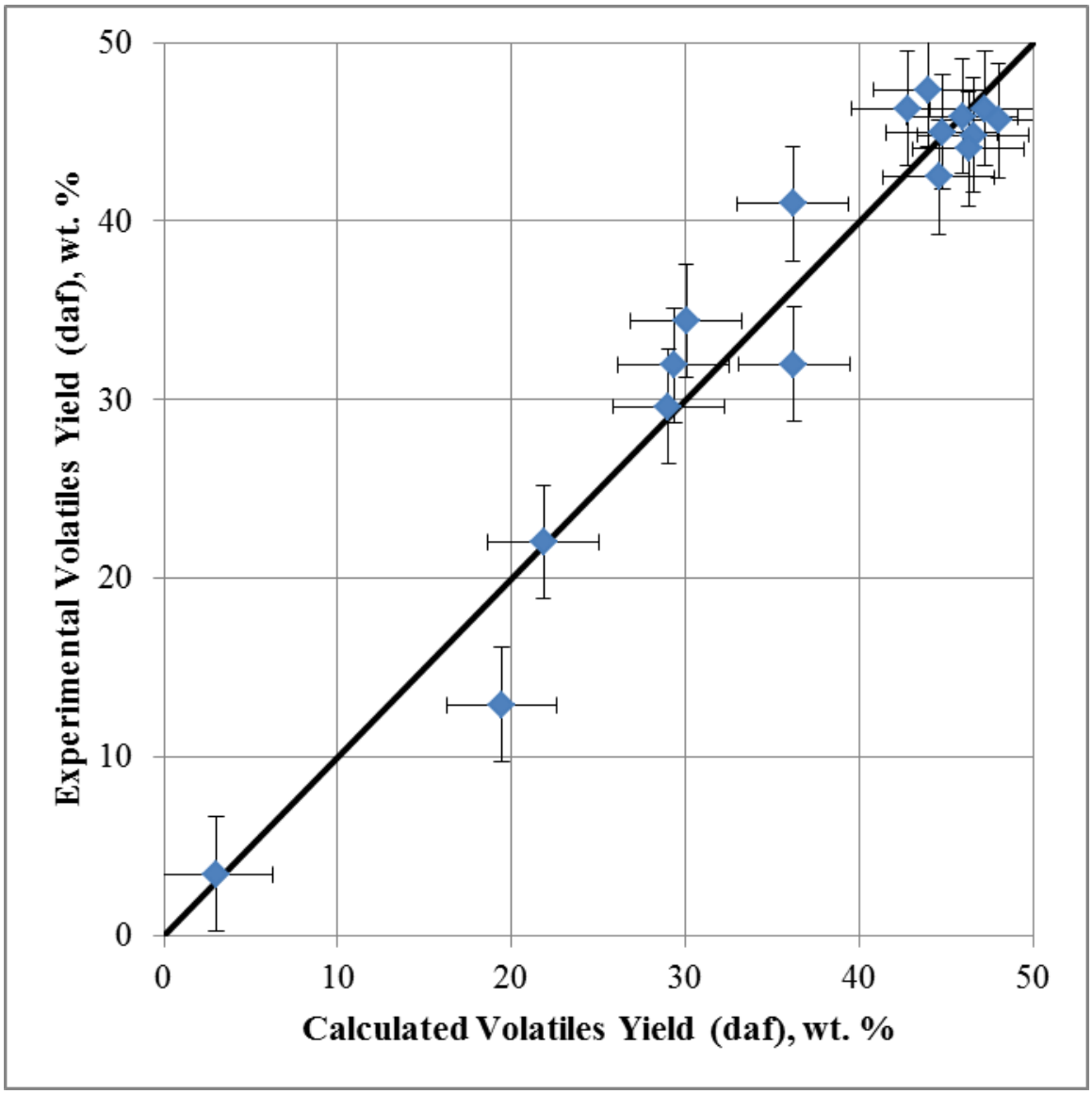

Figure 37: Experimental versus calculated volatiles yields (daf) of Sufco coal.

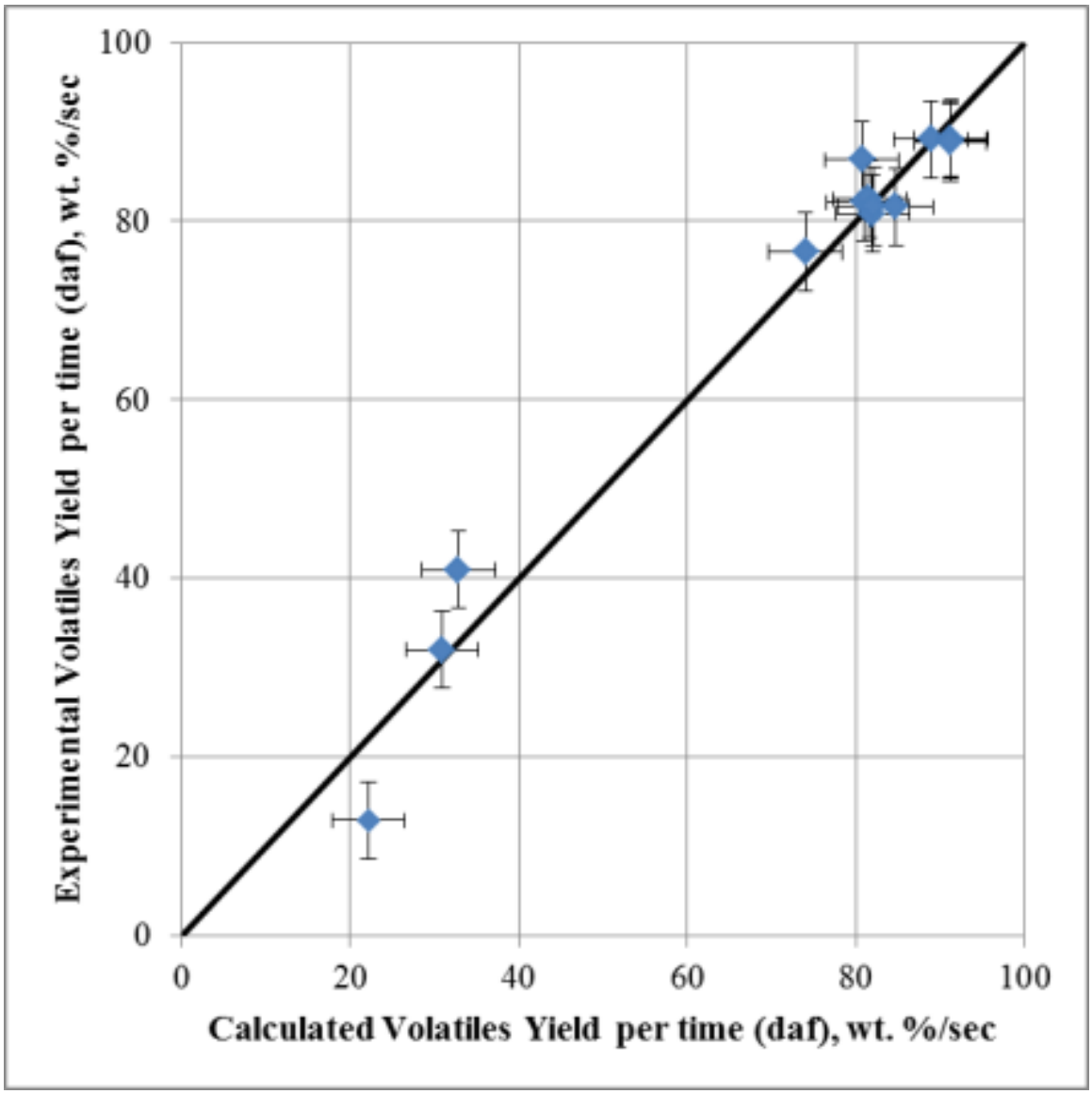

Figure 38: Experimental versus calculated volatiles yields (daf) per hold time of Sufco coal.

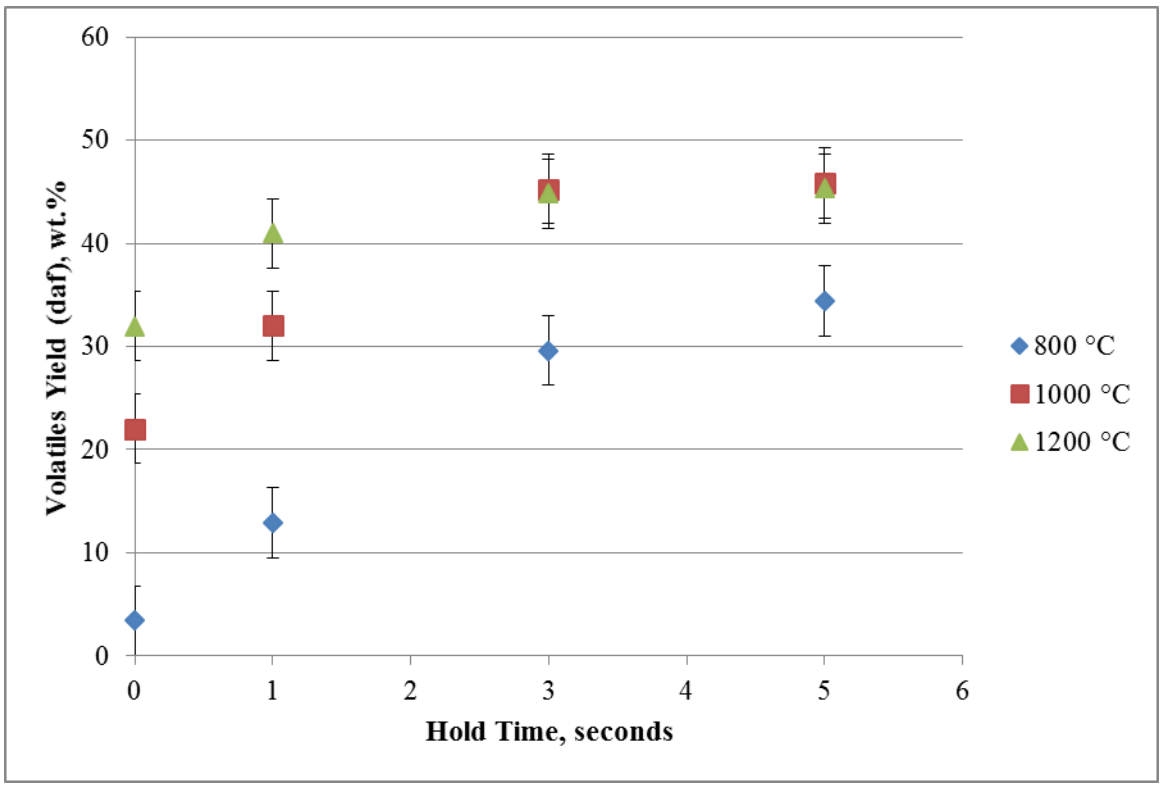

Figure 39: Volatiles yield, wt% daf, versus hold time of sample for tested final temperatures.

mechanism and assuming that successive reactions yield less volatiles and higher residue levels, the activation energies of hold time-specific runs are calculated.

Using Equation 5 as a definition for the rate, the activation energy per hold time was calculated with the aid of Arrhenius plots for the temperatures of 800, 1000, and 1200 ℃ at each hold time. Figure 40 shows the activation energy of volatile decomposition versus hold time.

$$rate = \frac{Char\ Yield}{Hold\ Time} = \left[\frac{mg}{mg \cdot s}\right] \qquad \text{Equation 5}$$

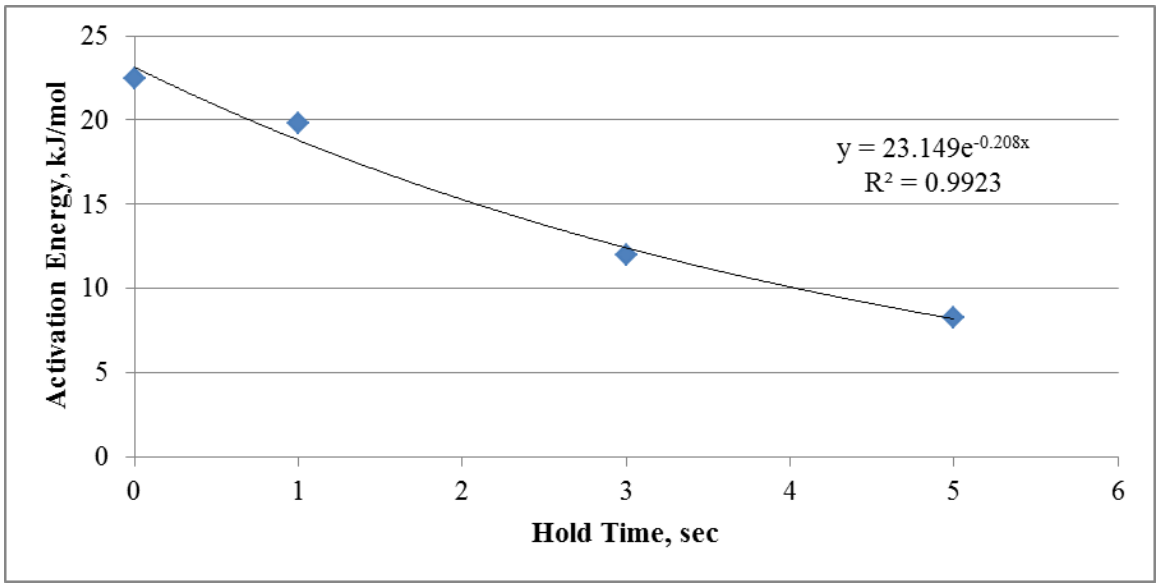

Figure 40: Activation energy of volatile decomposition versus hold time.

The activation energy per hold time of Figure 40 is not absolute and is effectively an average of the two competing processes described by Kobayashi et al. The values qualitatively show that as hold time increases, residue and char reactions become increasingly important and dominate the overall reaction via condensation and cross-linking reactions. For the case of 0 second hold time, residue reactions contribute minimally to the volatiles productions, but for the 5 second case, the opposite is true and residue reactions contribute greatly to the volatiles yield.

4.1.2 Previous Wire-Mesh Reactor Data

A similar analysis was performed using data obtained earlier in Wagner (*88*) and is used to support the atmospheric pressure test campaign. The previous data were collected from an Eastern U.S. bituminous coal with a proximate volatile matter of 44.2% (daf). The test campaign varied temperature and hold time, but also pressure, which will be used in a

similar submodel as described in the previous section. Table 12 presents all run conditions and char and volatiles yields from the previous campaign.

The mean final temperature of Table 12 was also determined using the software program DIADem from National Instruments. Analyzing the volatiles yields in the same manner as the previous wire-mesh reactor data yields Equation 6 and Equation 7.

$$VY = A + BT + CP + DH + E(T-q)(P-r) + F(T-q)(H-s) + G(P-r)(H-s) + I(T-q)(P-r)(H-s) \quad \text{Equation 6}$$

$$VY/t = A + BT + CP + DH + E(T-q)(P-r) + F(T-q)(H-s) + G(P-r)(H-s) + I(T-q)(P-r)(H-s) \quad \text{Equation 7}$$

These two equations are in the same format as the two from the atmospheric pressure data analysis, but with the added effect of pressure. Here, q, r, and s are equal to 1100, 28.8, and 3, the averages of the tested temperatures, pressure, and hold times, respectively. Table 13 shows the values of the coefficients A through I; H is not a coefficient and represents hold time. Although nine constants are fit to 11 data points in Equation 6 and Equation 7, a factor could easily be neglected if it is established to have a minor effect on the volatiles yield. For this reason, the previous campaign was only operated at one pressure since hold time and temperature were found to have larger effects.

Figure 41 and Figure 42 show the experimental volatiles yields and volatiles yields per time plotted against the calculated yields using Equation 6 and Equation 7. A 45° line is plotted for comparison. Both Figure 41 and Figure 42 show standard error of the values in a 95% confidence level. The coefficients of determination of Figure 41 and Figure 42 are 0.966 and 0.943, respectively.

Table 12: Previous test campaign run conditions and char and volatiels yields (daf).

Target Final Temp, ℃	Mean Final Temperature, ℃	Pressure, bar	Hold Time, sec	Char Yield (daf), wt.%	Volatiles Yield (daf), wt.%
1100	1015	21.4	3	64.68	35.32
1000	905	62.2	1	68.22	31.78
1200	1203	62.2	5	65.99	34.01
1200	1165	1.0	1	55.36	44.64
1000	1039	1.0	1	81.15	18.85
1100	977	21.4	3	67.76	32.24
1000	985	62.2	5	61.09	38.91
1200	1235	1.0	5	52.63	47.37
1000	937	1.0	5	54.11	45.89
1200	1198	62.2	1	69.92	30.08
1100	1134	21.4	3	68.30	31.70

Table 13: Summary of coefficients for Equation 6 and Equation 7.

Eq.	A	B	C	D	E	F	G	I
1	-2.86	$2.97 \cdot 10^{-2}$	$-7.74 \cdot 10^{-2}$	2.66	$-1.38 \cdot 10^{-3}$	$-1.84 \cdot 10^{-2}$	$-3.8 \cdot 10^{-2}$	$4.31 \cdot 10^{-4}$
2	-1.20	$3.25 \cdot 10^{-2}$	$2.80 \cdot 10^{-3}$	-5.74	$-1.18 \cdot 10^{-3}$	$-1.70 \cdot 10^{-2}$	$-5.0 \cdot 10^{-3}$	$5.35 \cdot 10^{-4}$

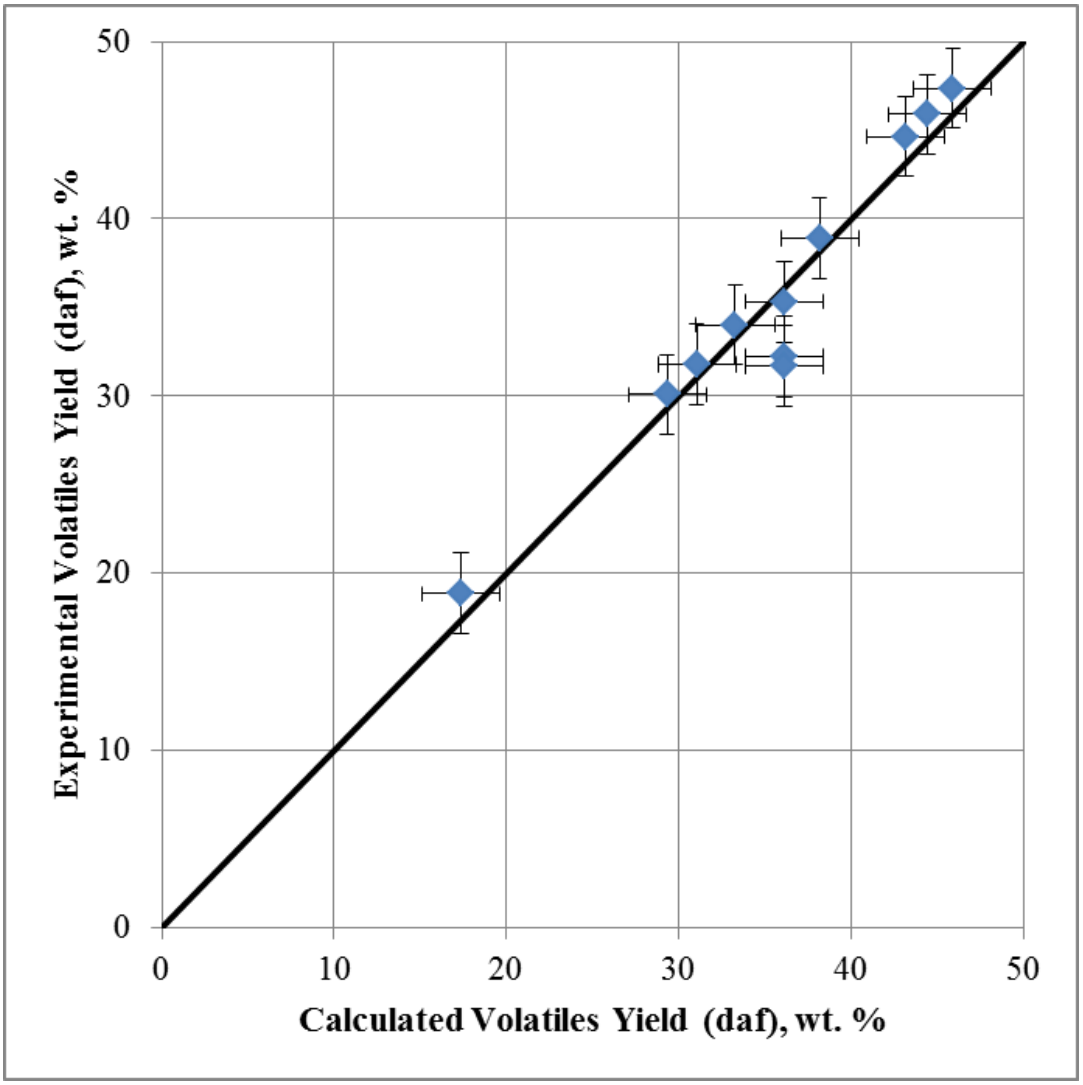

Figure 41: Experimental versus calculated volatiles yields (daf) of Eastern U.S. bituminous coal.

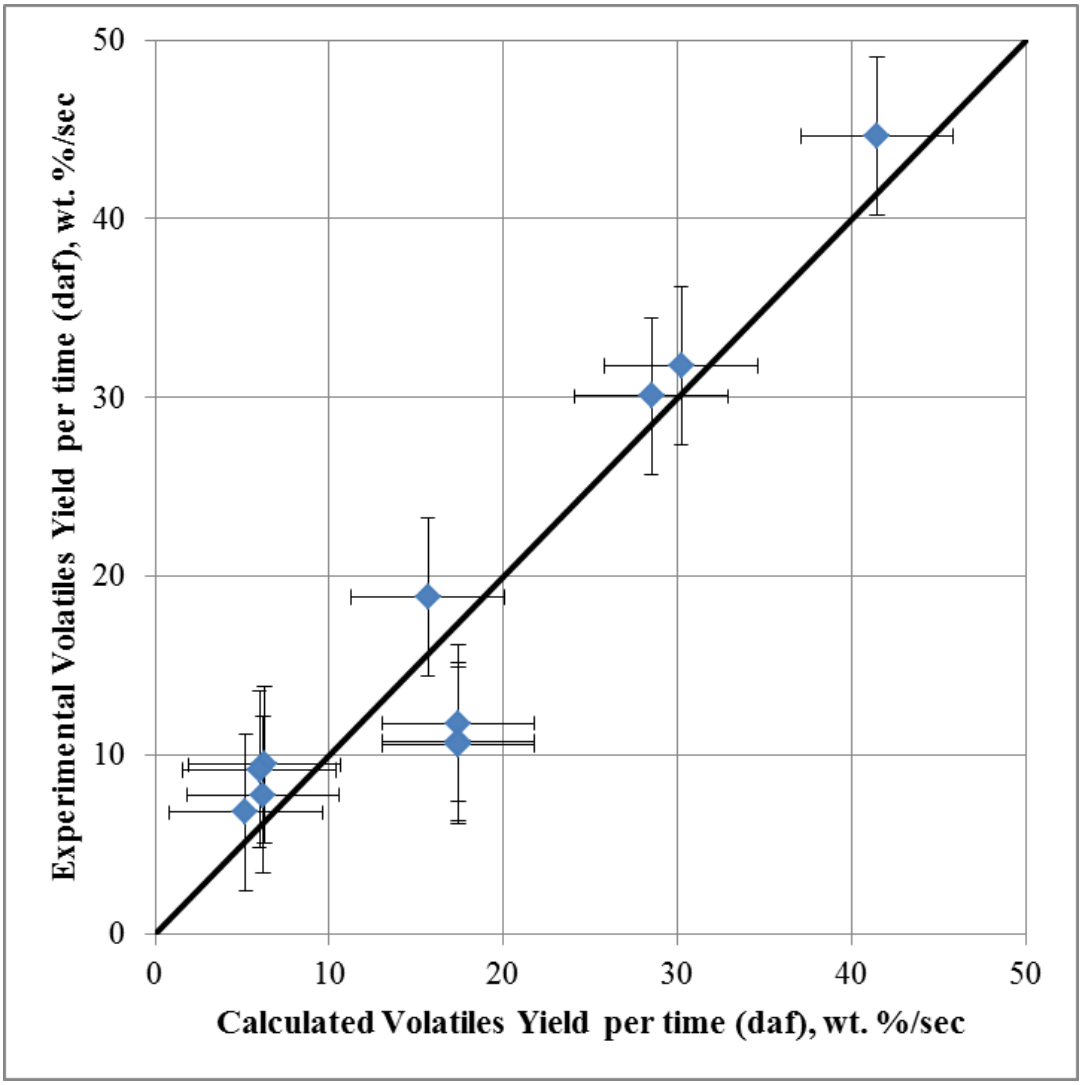

Figure 42: Experimental versus calculated volatiles yields (daf) per hold time of Eastern U.S. bituminous coal.

4.1.3 Initial Wire-Mesh Product Yields

A significant difference between the previous test campaigns is the fuel packet methodology. While results comparable to proximate volatile matter yields were expected, this was not the outcome. Resulting yields ranged from approximately 1% to 10% over the range of pressures, temperatures, and hold time. Of the 53 experiments run, 11 were deemed outliers based on Chauvenet's criterion and removed. The remaining 42 runs weaken the objective of a design of experiments procedure and invalidate any quantitative results from this procedure.

While quantitative results cannot be obtained from the experiments performed, qualitative indications can be made when compared to prior operation. Figure 43 shows the volatile yields as a function of temperature, pressure, and hold time for the 42 tests. Pressures of 7 and 25 bar have minimal results and qualitative conclusions cannot be made. If pressure is removed from the plot, however, distinct trends arise of temperature and hold time as in Figure 44. As temperature increases from 600 ℃ to 1000 ℃, the volatile yields increase and reach a maximum at 1000 ℃ and a 5 second hold time. These results agree with literature in that with increasing temperature and hold time, volatile yields increase. No direct conclusions can be drawn for pressure, as the yields are quantitatively low and within the standard deviations of the all operating pressures.

Due to a lack of quantitative results using the fuel packet method as opposed to the previous mesh assembly, it is advised that the fuel packets should not be used for wire-mesh reactor operation. Additional mass transfer resistances are assumed present, causing heavier volatile species and tars to become trapped within the mesh packet and unable to escape the surrounding foil.

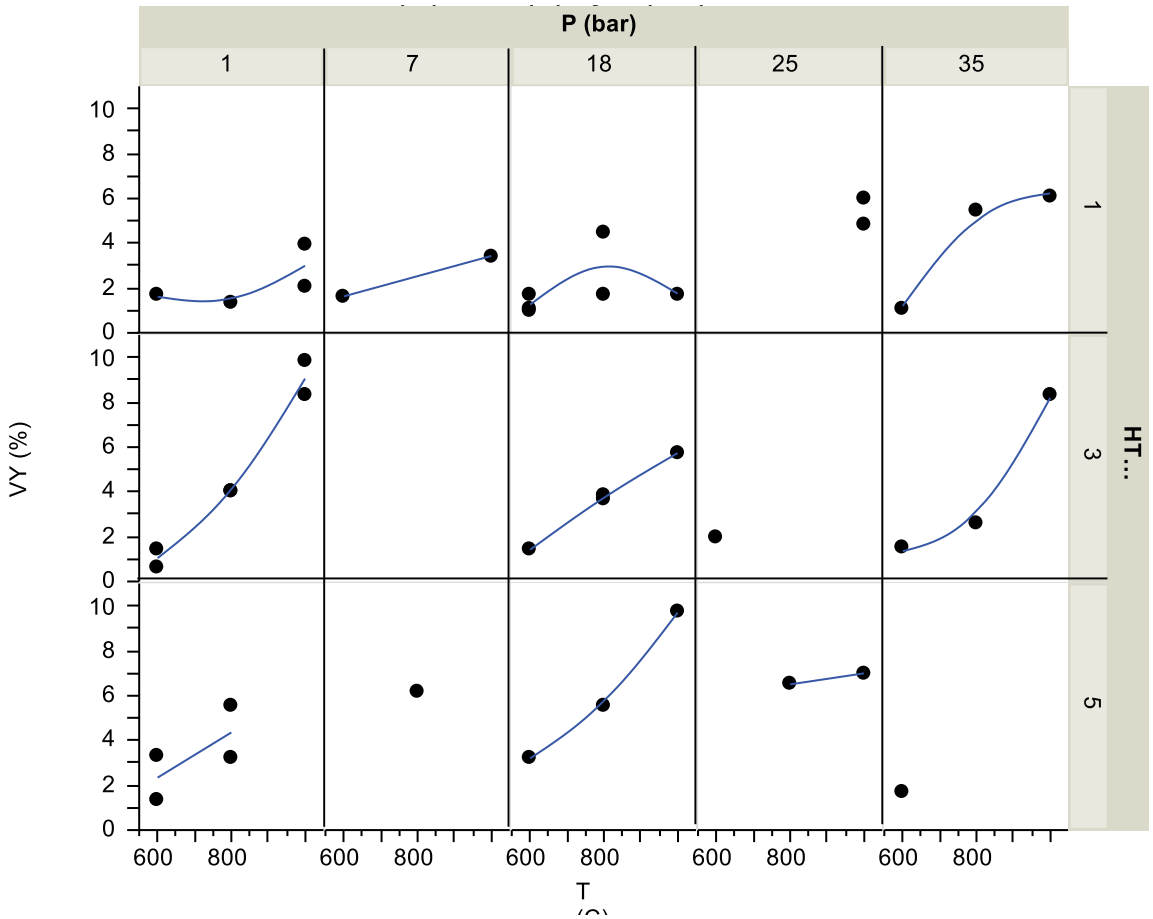

Figure 43: Wire-mesh reactor volatile yields (VY, %) versus temperature (°F), pressure (bar), and hold time(sec).

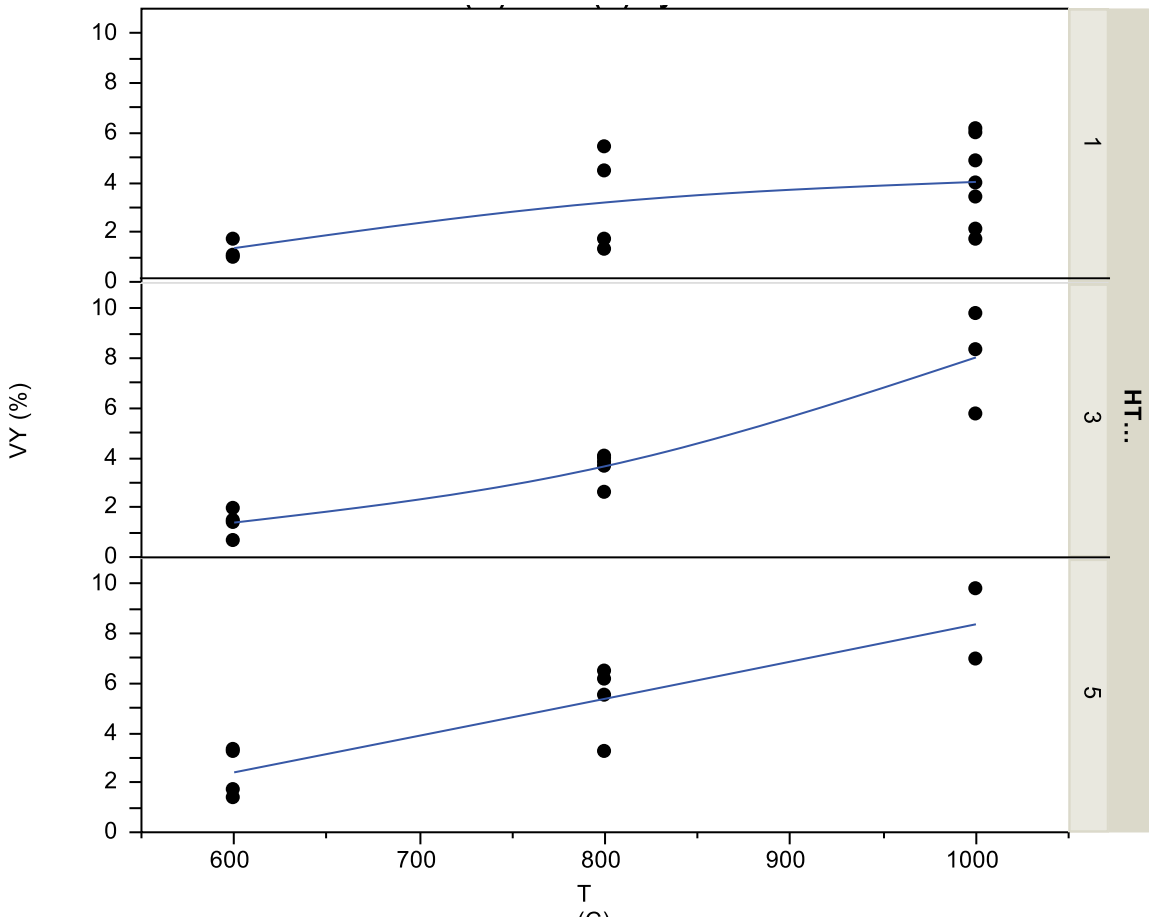

Figure 44: Wire-mesh reactor volatile yields (VY, %) versus temperature (°F), and hold time(sec).

4.1.4 Comparison of Wire-Mesh Data

The maximum volatiles yield seen in section 4.1.1 and section 4.1.2 is also approximately the value of the proximate volatile matter for each fuel. Any significant deviation of the data presented for the Eastern U.S. bituminous coal, however, could be attributed to the fact that the coal was not dried before operation of the wire-mesh reactor and the volatiles yield shown was corrected for moisture after the run. Anthony et al. (*70*) draws the same conclusion for Montana lignite and the proximate volatile matter value for similar temperatures and hold times of 5 to 20 seconds. An inert atmosphere of helium

was used along with an average particle size of 70 microns at atmospheric pressure. Figure 34 exemplifies this fact for Sufco bituminous coal.

Previous data of Eastern bituminous coal are used to determine how pressure affects volatiles yield. Figure 45 shows a variability chart of the volatiles yields of Table 12. The group means presented on the chart are the means of hold time and pressure for the respective groups and the lines connecting the points show trends within the tested parameter. Figure 45 shows that as pressure increases, the average volatiles yield decreases within a specified hold time. This indicates that the increase in pressure increases diffusion limitations within the particle. Bulk diffusion is neglected because once the volatiles species are emitted from the particle, it is assumed that they do not travel in the reverse direction. This is evident of pore diffusion being dominant at higher pressures. As hold time increases, however, the average volatiles yield increases as well. This is because the particles are held at the temperatures for a longer period of time and the volatiles are more readily emitted. The influence of pressure can be significant as shown in Figure 45, but hold time can be just as important as seen in Figure 46 for the atmospheric pressure Sufco data.

The four purple lines in Figure 46 show the average volatiles yields for the hold times tested and increase with increasing hold time. This variability chart shows the volatiles yield approaches the proximate volatile matter value of 45.0% (daf) previously discussed.

The conclusions that can be drawn from the variability charts are in agreement with previously stated trends that volatile yields increase with increasing final temperature, increasing hold times, and at lower pressures. Initial data presented in Figure 44 aid in

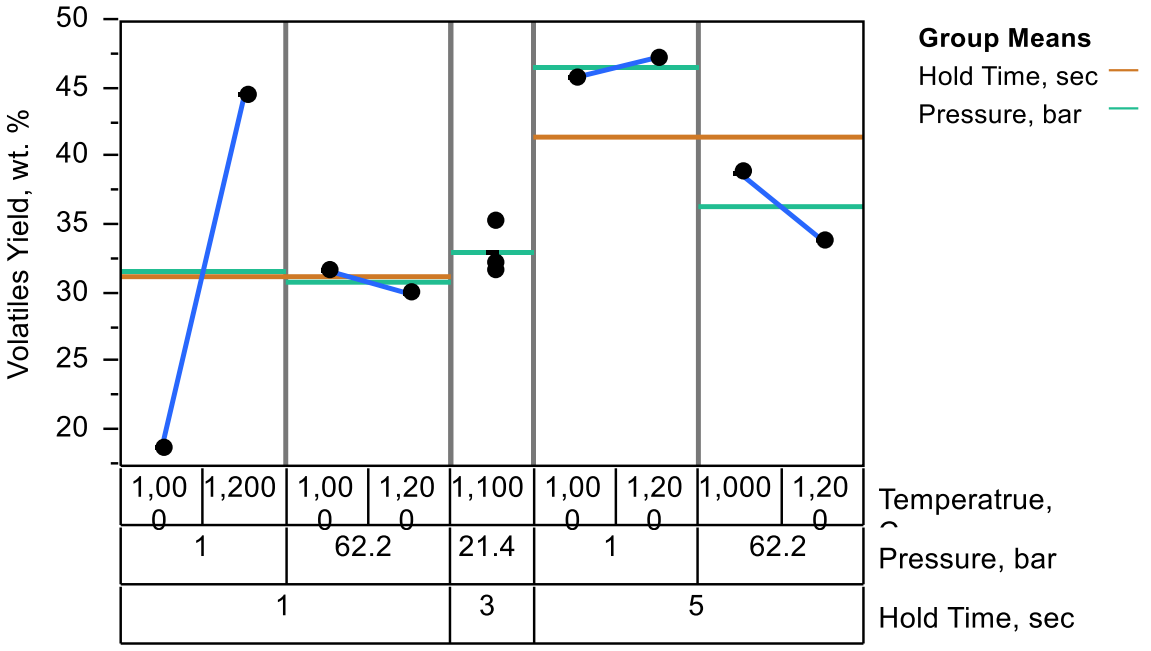

Figure 45: Variability chart of Eastern bituminous coal volatiles yields (daf).

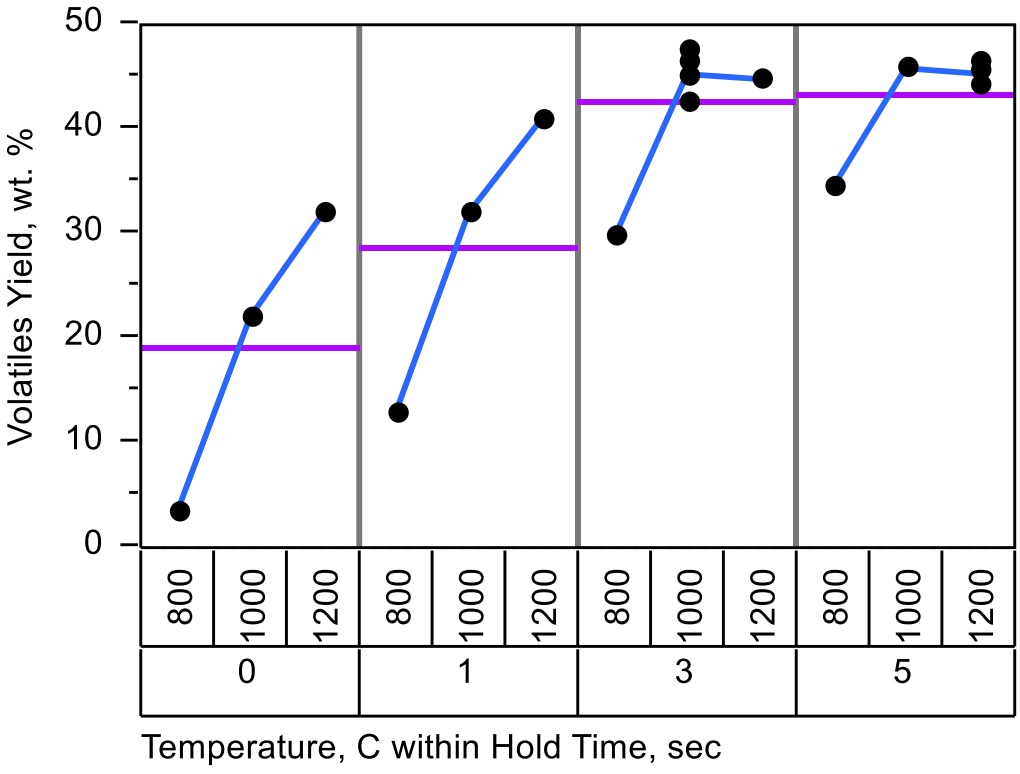

Figure 46: Variability chart for Sufco coal volatiles yields at 1 bar versus temperature and hold time.

these conclusions with their limited reliability, but this also validates the qualitative results of the atmospheric pressure data and previous data from Wagner (*88*) at lower temperatures of 600 ℃ and 800 ℃.

4.2 Thermogravimetric Rates

4.2.1 Atmospheric Pressure Data

Initial thermogravimetric analysis was performed at atmospheric pressure to determine the maximum derivative weight and the presence of primary and secondary pyrolysis. Figure 47 shows the weight loss and temperature curves as a function of time. Taking the derivative of the weight loss function in Figure 47 and dividing by the mass at time t, the rate of mass loss versus temperature can yield the maximum derivative weight. Equation 8 shows the rate equation.

$$rate = \frac{dm}{dt}\frac{1}{m_t} \qquad \text{Equation 8}$$

By plotting Equation 8 versus temperature, as in Figure 48, the maximum derivative weight is determined to be $5.10 \cdot 10^{-5}$ mg/mg/s at a temperature of 455 ℃. Figure 48 also shows the water loss and primary and secondary pyrolysis. The first peak at approximately 100 ℃ is water loss following by primary devolatilization. After this stage, secondary pyrolysis liberates the more compact volatiles inside the particles as well as higher molecular weight species and tars. The secondary pyrolysis peaks at a temperature of approximately 715 ℃, after which char gasification is assumed to dominate reaction pathways and the rate decreases almost monotonically.

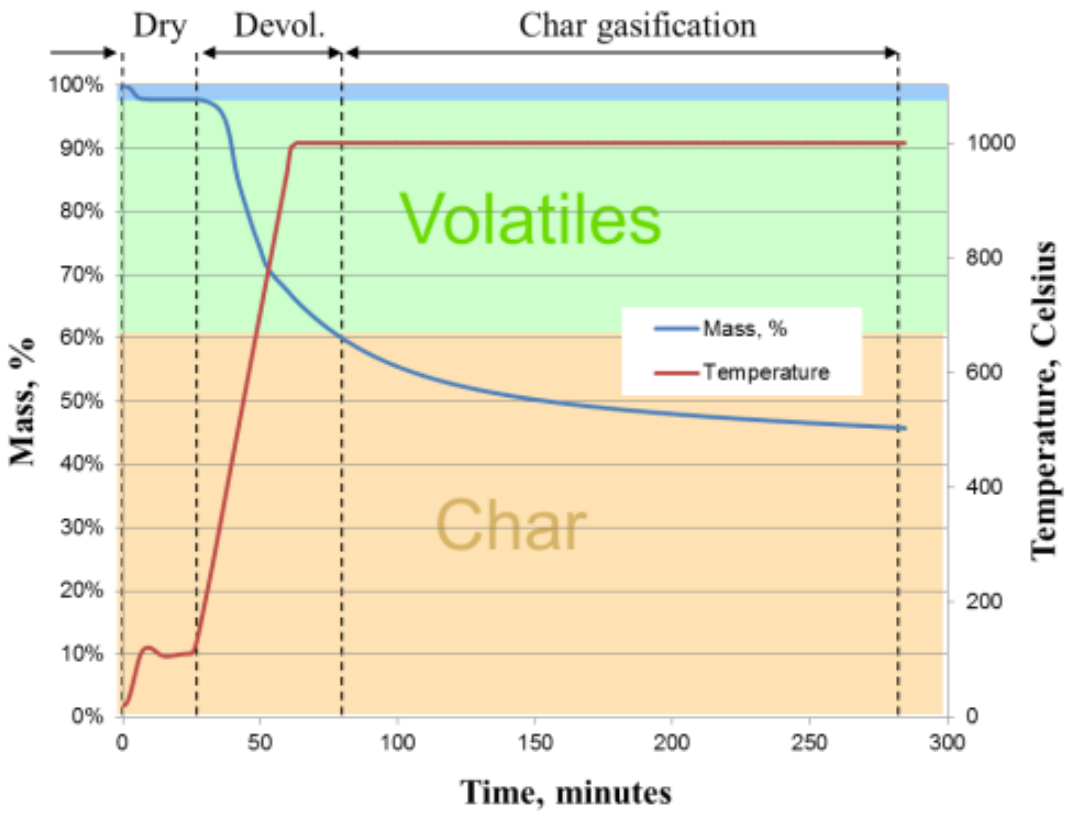

Figure 47: Atmospheric TGA run in nitrogen.

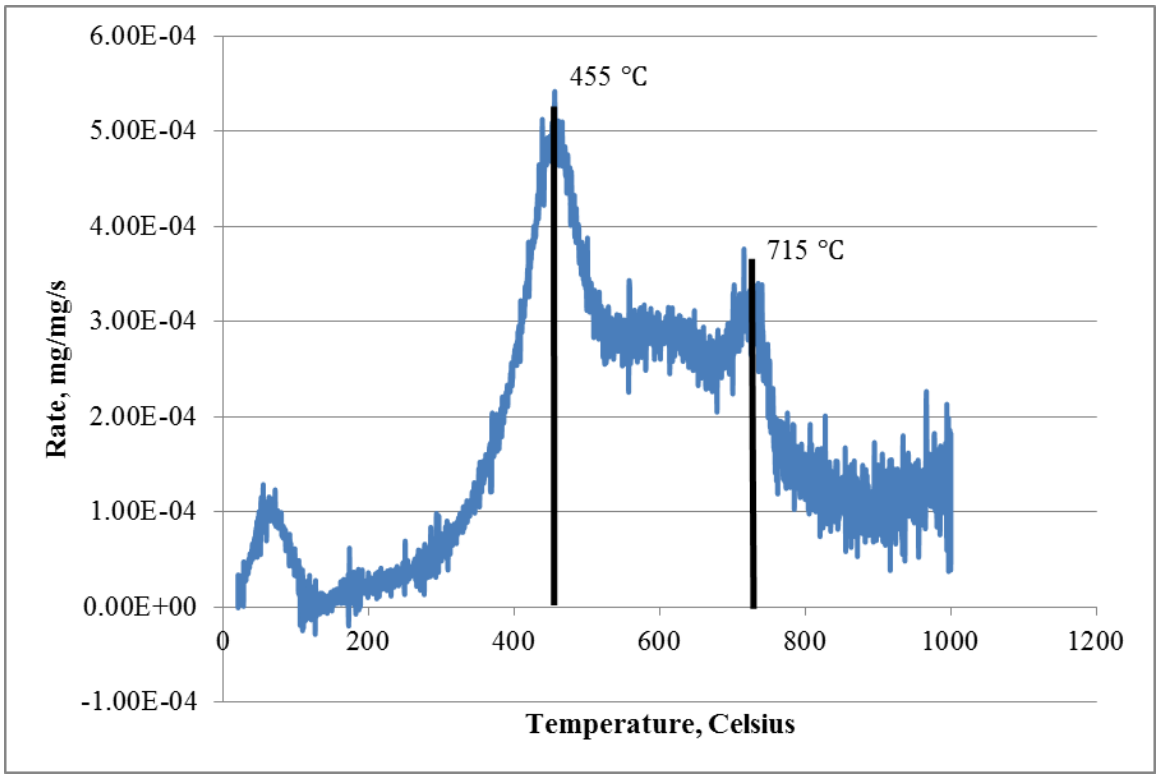

Figure 48: Rate versus temperature for atmospheric pressure TGA operation in nitrogen.

4.2.2 Pressurized Thermogravimetric Data

Concerning the pressurized thermogravimetric analyses, two tests were discarded based on Chauvenet's criterion for error analysis, yielding 17 experiments. Table 14 shows the run conditions and calculated rates using the polynomial rate method described in the previous chapter. Here, the slope is determined using Equation 9, where GM is the available gasifiable material.

$$rate = \frac{dm}{dt}\frac{1}{GM} \qquad \text{Equation 9}$$

Table 14: All TGA run conditions and calculated rates.

Temperature (℃)	Pressure (bar)	CO (%)	PR25 (mg/mg/s x10^4)
900	17.7	2	1.50
950	17.7	2	3.55
1000	17.7	2	7.76
900	17.7	2	1.22
950	17.7	2	4.24
1000	17.7	2	9.24
1000	17.7	4	6.95
1000	1.0	2	6.87
1000	1.0	4	4.78
1000	1.0	4	5.49
1000	1.0	2	6.31
1000	35.0	2	3.22
1000	35.0	4	4.42
1000	6.8	2	6.79
1000	6.8	4	5.71
1000	24.8	2	4.19
1000	24.8	4	4.08

The variable temperature runs of Table 14 are used to calculate the activation energy of the fuel by creating an Arrhenius plot. This plot is shown in Figure 49 with the linear trend line and expression with error at a 95% confidence level.

Figure 49 indicates the slope of the linear function is -27438, and multiplying by 0.008314 kJ/mol·K yields an activation energy of 228 $\pm$ 24 kJ/mol. A pressure-dependent rate equation is assumed and is shown as Equation 10.

$$rate = P_{CO} \cdot P_{CO_2} \cdot k \cdot f(P,T) \qquad \text{Equation 10}$$

Here, k is the rate constant, T is absolute temperature, and P is the partial pressure for CO and CO_2. The function, $f(P,T)$, represents a complex expression for the rate as a function of partial pressures and temperatures. The rate equation is divided by the pressure

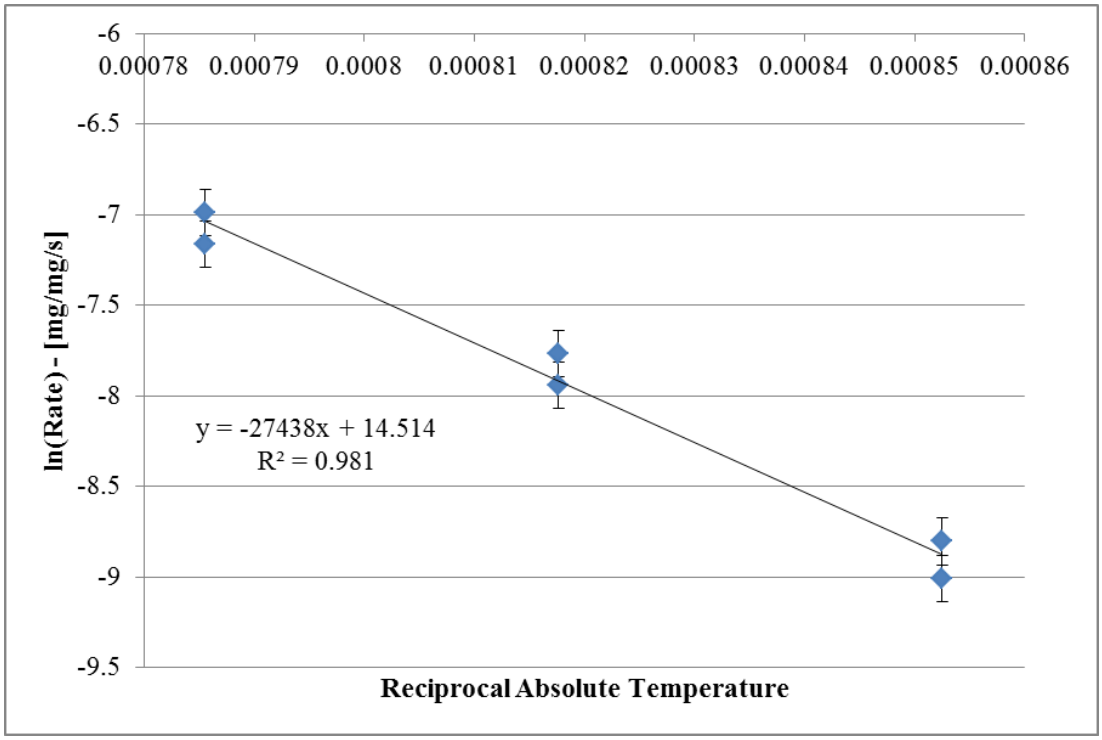

Figure 49: Arrhenius plot for Sufco fuel at 245 psig. The calculated activation energy is 228 $\pm$ 24 kJ/mol.

terms for CO and CO_2 and the natural logarithm is taken of both sides. Figure 50 shows the natural logarithm of the PR25 rate divided by the pressure terms versus total pressure. Error is calculated at a 95% confidence level.

A strong correlation is realized when fitted to a logarithmic trend for the rate expressions of Figure 50 for both 2% and 4% CO in the gasifying environment. This suggests the right-hand side of Equation 10 is a complex expression of temperature and partial pressures. Figure 50 shows, however, that with an increase in CO partial pressure, there is a decrease in the rate, demonstrating the inhibitive nature of carbon monoxide.

The discussion of temperature effects is furthered in Figure 51, where instantaneous rates are plotted versus char conversion for the runs conducted to obtain activation energy.

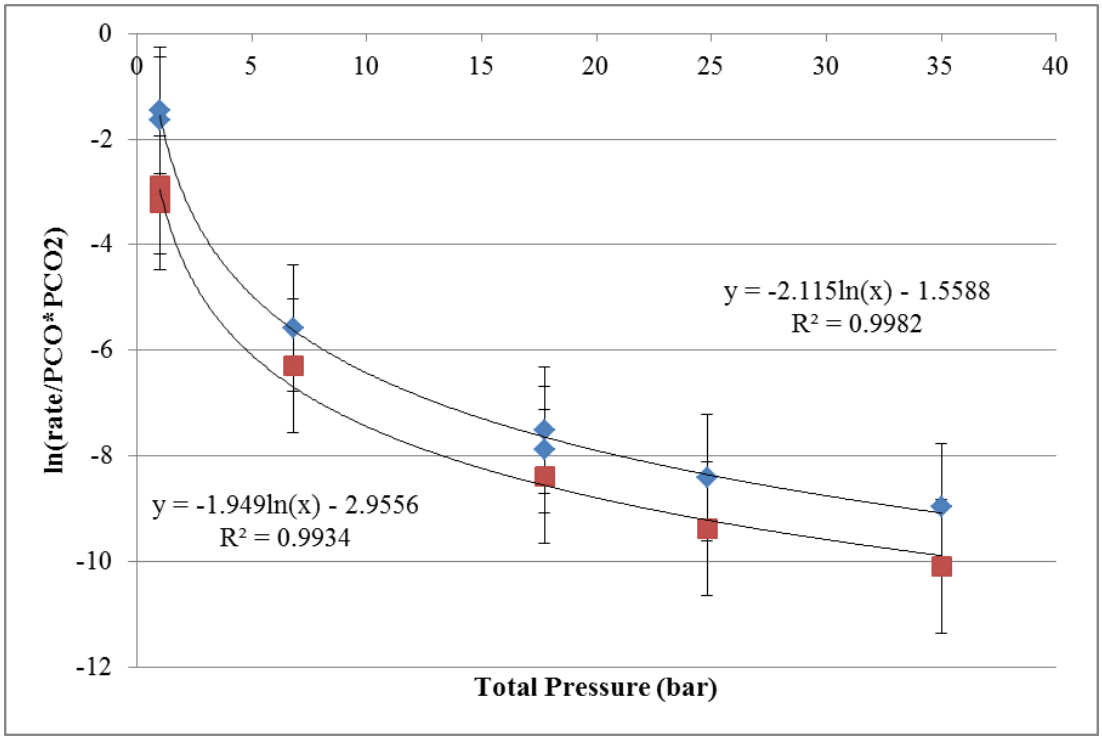

Figure 50: Logarithmic trends for rate versus total pressure for 2% CO (◆), and 4% CO (■) gas environments.

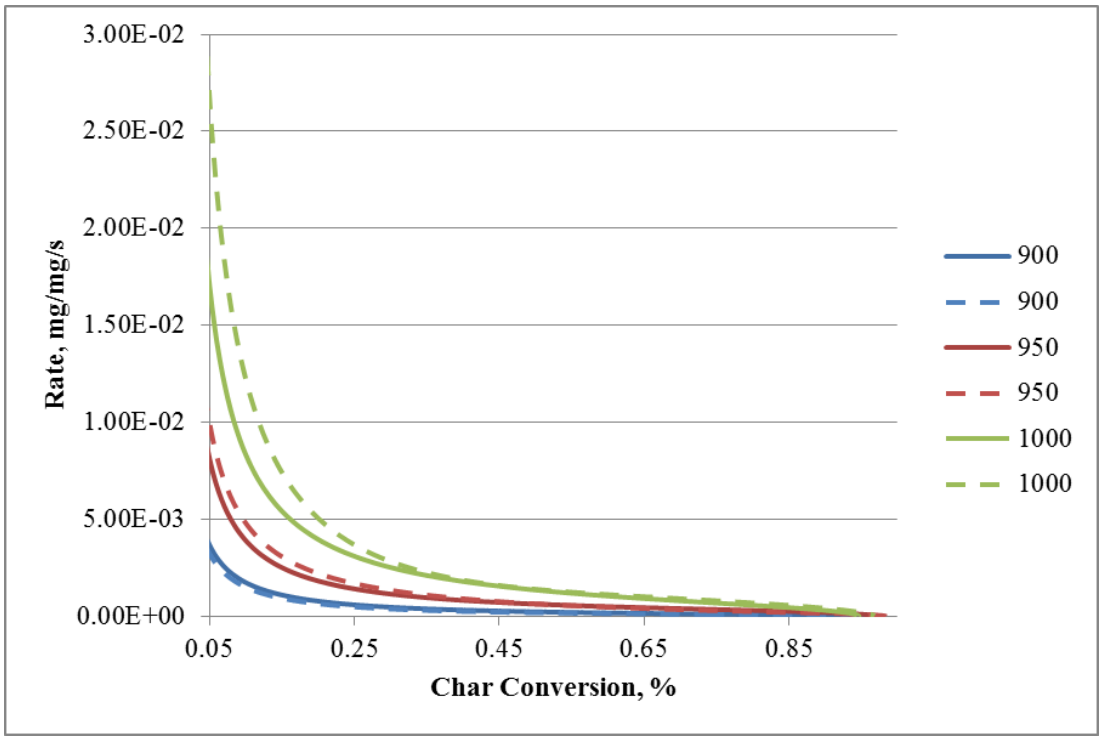

Figure 51: Influence of temperature on instantaneous rate versus char conversion at 2% CO and 18 bar.

There is no difference between the dotted and solid lines; they are repeats of the same temperature, pressure, and CO combination.

Figure 51 shows a clear dependency on temperature. At lower conversion, the rate decreases rapidly and levels out at higher conversion. The dotted line at 1000 ℃ in Figure 51 shows increased variability at the higher temperature and could be present from operator error.

While the derivation of the reaction order plot is temperature driven, Figure 51 shows temperature dependence of the instantaneous rate, it is important to understand how the pressure of the system influences that rate as well. Figure 50 shows this as a function of total pressure for variable temperature, and Figure 52 and Figure 53 show pressure dependence based on the partial pressure, or mole fraction, of carbon monoxide. For the plots in Figure 52, as pressure increases, the rate decreases, indicated by the general slope of the line. Pressures of 24.8 bar and 35.0 bar exemplify this trend better than other pressures, which are clustered together. Figure 53 complicates these trends by spreading the plots out over the time coordinate for the same pressures. A pressure of 35.0 bar is still the slowest reacting, followed by 24.8 bar, but the lower pressure runs also begin to slow down. The deductions of Figure 52 and Figure 53 are reinforced by linking them to Figure 54 and Figure 55 for two and four mole percent CO, respectively.

Figure 54 and Figure 55 share the same difficulties as Figure 52 and Figure 53 when discussing the case of higher CO partial pressure. As the partial pressure of CO is increased, the clustering effect disappears and the rates spread more uniformly. No significant inferences can be made for the case of higher carbon monoxide when comparing Figure 54 and Figure 55 with the exception of the 35 bar case that consistently has lower

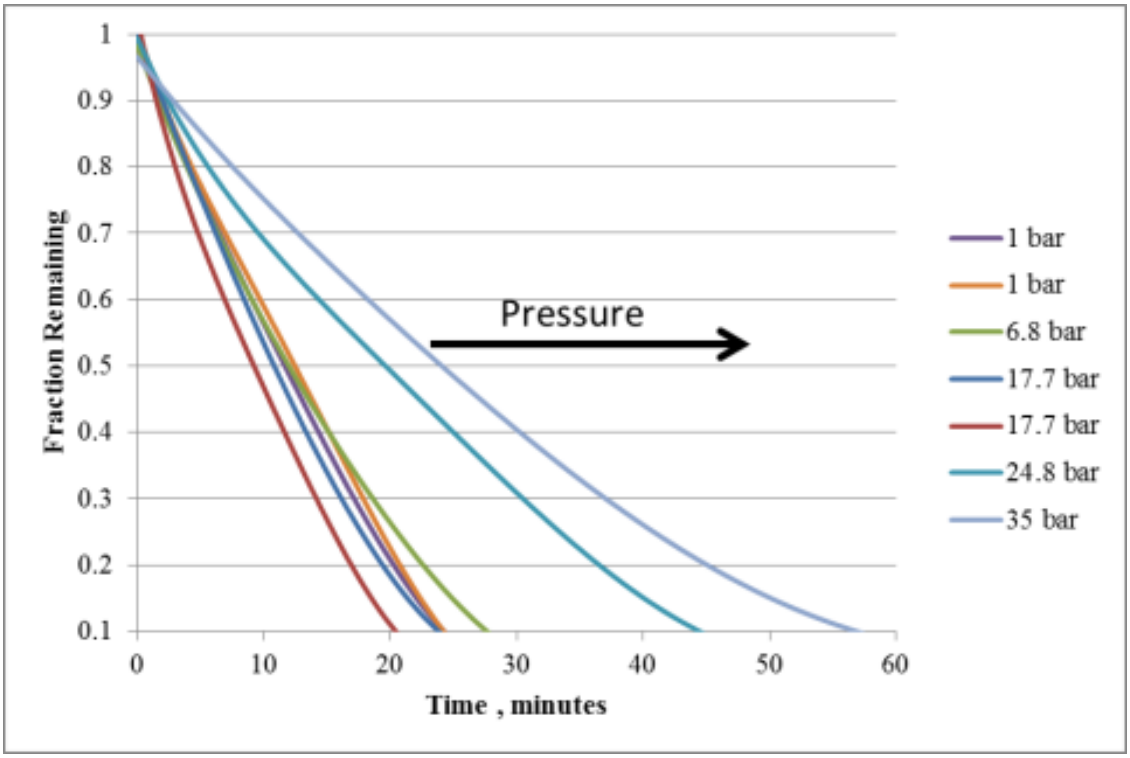

Figure 52: Pressure dependency on fraction remaining versus reaction time in 2% CO.

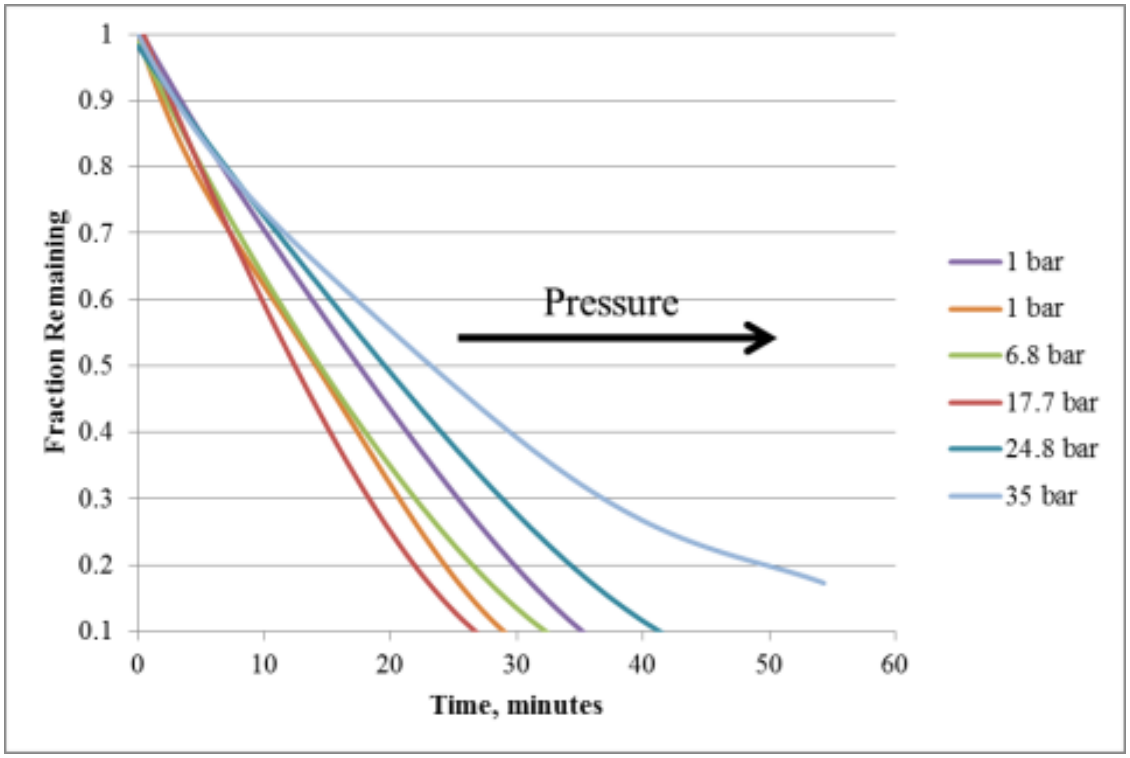

Figure 53: Pressure dependency on fraction remaining versus reaction time in 4% CO.

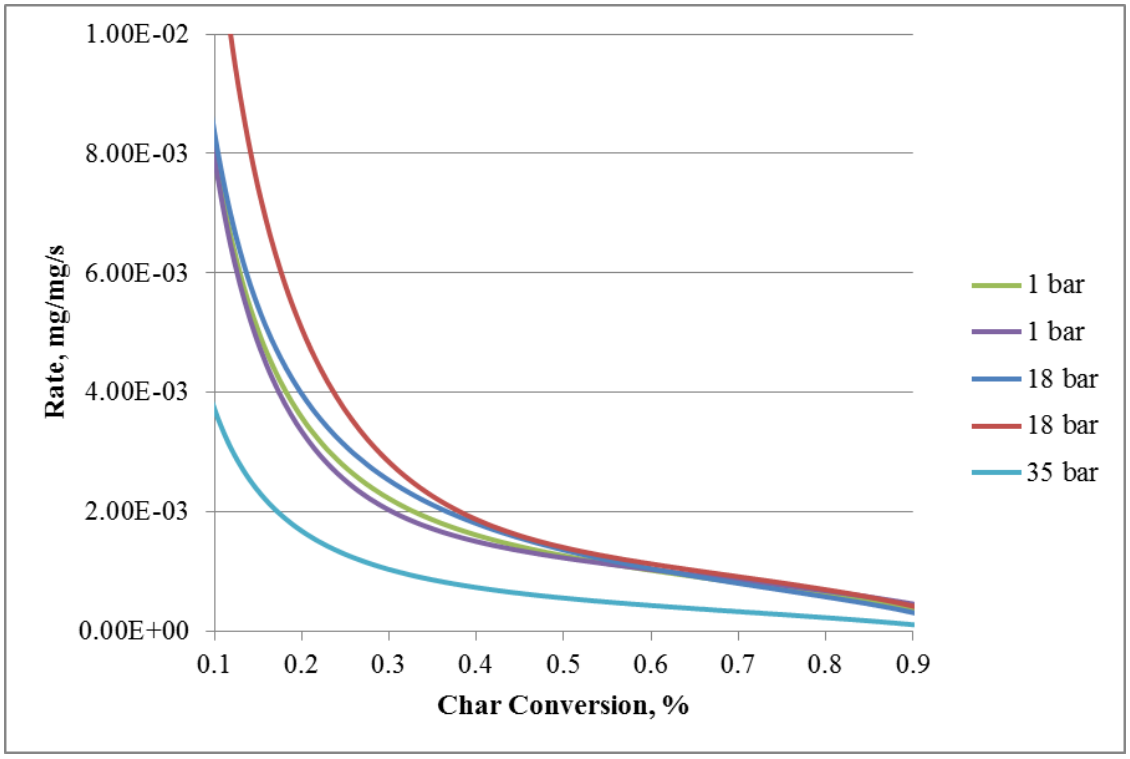

Figure 54: Influence of pressure on instantaneous rate versus char conversion at 2% CO.

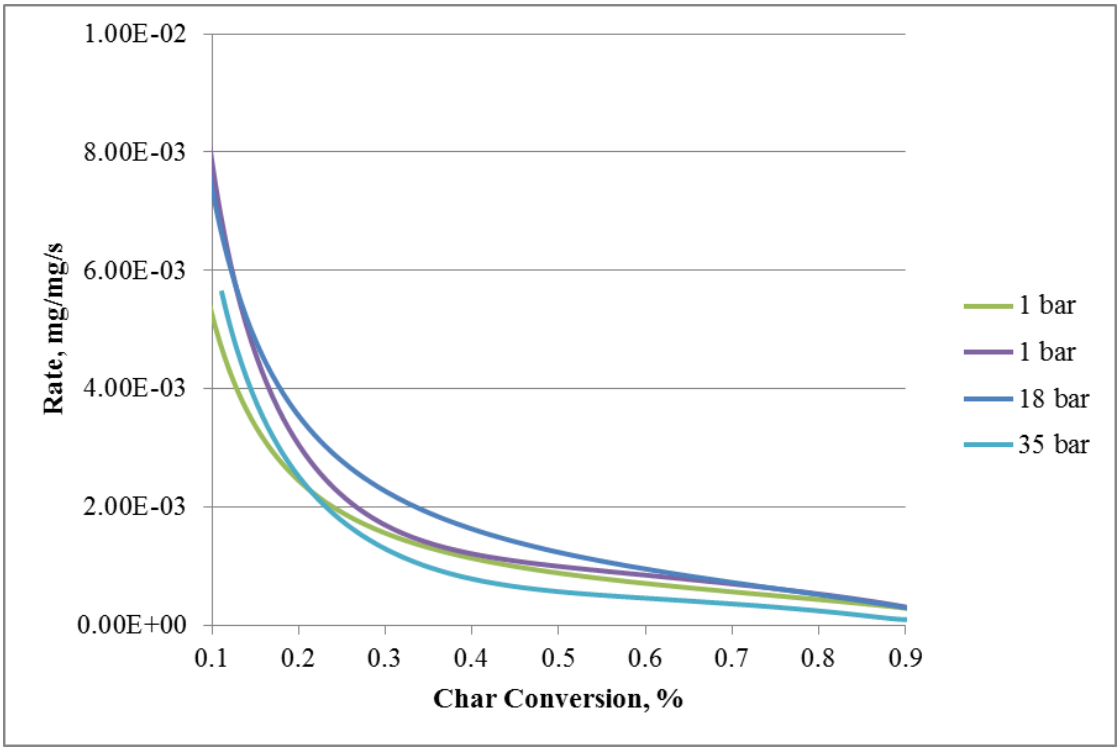

Figure 55: Influence of pressure on instantaneous rate versus char conversion at 4% CO.

instantaneous rates for char conversion above 25%. Because CO and CO_2 are the only reactive gases introduced in the reactor and the volume of the gases is larger than any volatiles species that evolve from the sample, the Boudouard reaction, given in Reaction 3, can explain the pressure dependency of CO and CO_2.

$$C + CO_2 \rightarrow 2CO$$ Reaction 3

Since the Boudouard reaction is endothermic, requiring 173 kJ/mol, higher temperatures will drive the reaction to produce more carbon monoxide by converting fuel-bound carbon as well breaking the carbon-oxygen bonds of carbon dioxide. This phenomenon is evident in Figure 56.

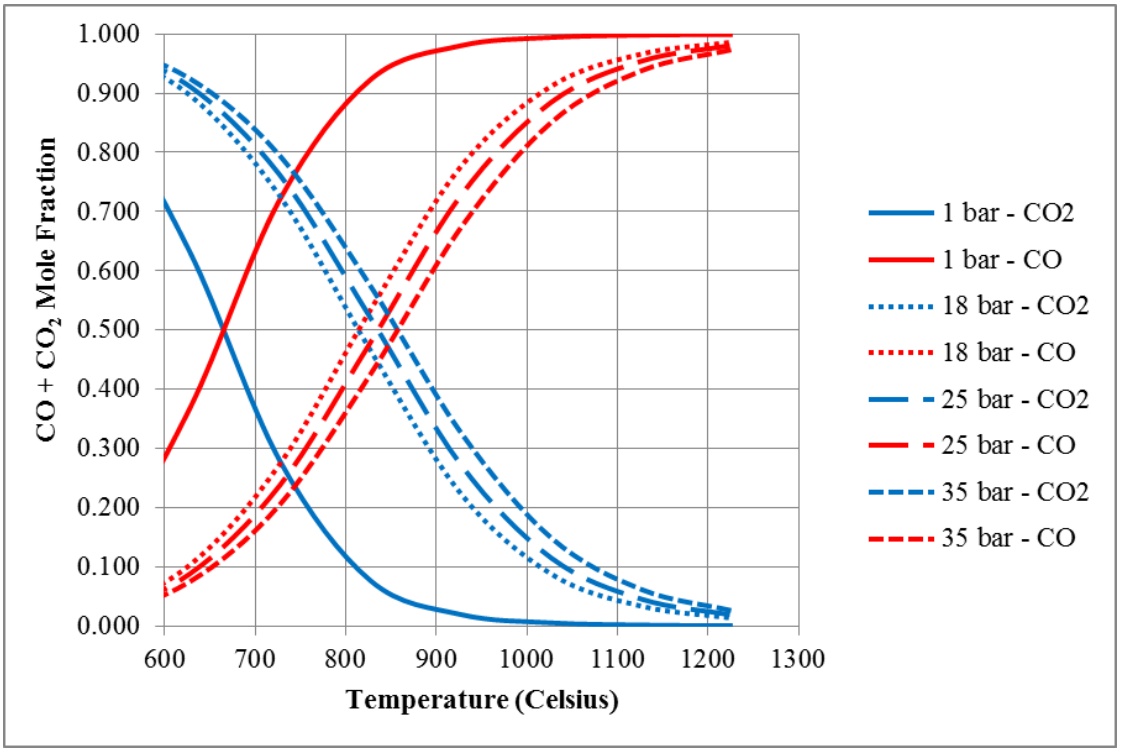

Figure 56: CO and CO_2 equilibrium versus temperature (℃) for variable pressure (bar).

Here, carbon monoxide and carbon dioxide are plotted versus temperature to appreciate the influence that pressure has on Reaction 3. Figure 56 shows that equilibrium shifts CO and CO_2 mole percent farther apart as temperature rises, and above 1200 ℃ the reaction produces more than 95% carbon monoxide. The deviation in mole percent at 1000 ℃ is only ~10%, which could explain the clumped nature of the rates.

4.3 Entrained-Flow Extractive Gas Sampling

4.3.1 Gas-phase Results

Nineteen samples were taken in total during operation of the gasifier; duplicates at each of nine locations and temperatures and one triplicate. Figure 57 shows the reactor temperature taken at thermocouple 2 with the sample target temperatures in blue and actual sample temperatures in green. The actual temperature was obtained from matching timestamp records from the main control and the probe computers.

Figure 58 shows the average dry gas yields of carbon monoxide, hydrogen, and carbon dioxide for the respective sample locations and temperatures. The variability seen at 2650 ℉ is explained by the inconsistent temperatures shown in Figure 57. Problems with oxygen and slurry feed rates caused erratic behavior at the middle temperature setpoint. The error shown in Figure 58 is at a 95% confidence level.

While Figure 58 shows distinct trends, the significance of radial sample location is not as apparent. Figure 59 shows the major gas species with varying target temperature and sample location. The dimensionless diameter corresponds to the location at which the sample was taken in the gasifier and indicates how far the probe extended in the reaction zone (e.g. 0.0 corresponds to the wall and 0.5 corresponds to the centerline).

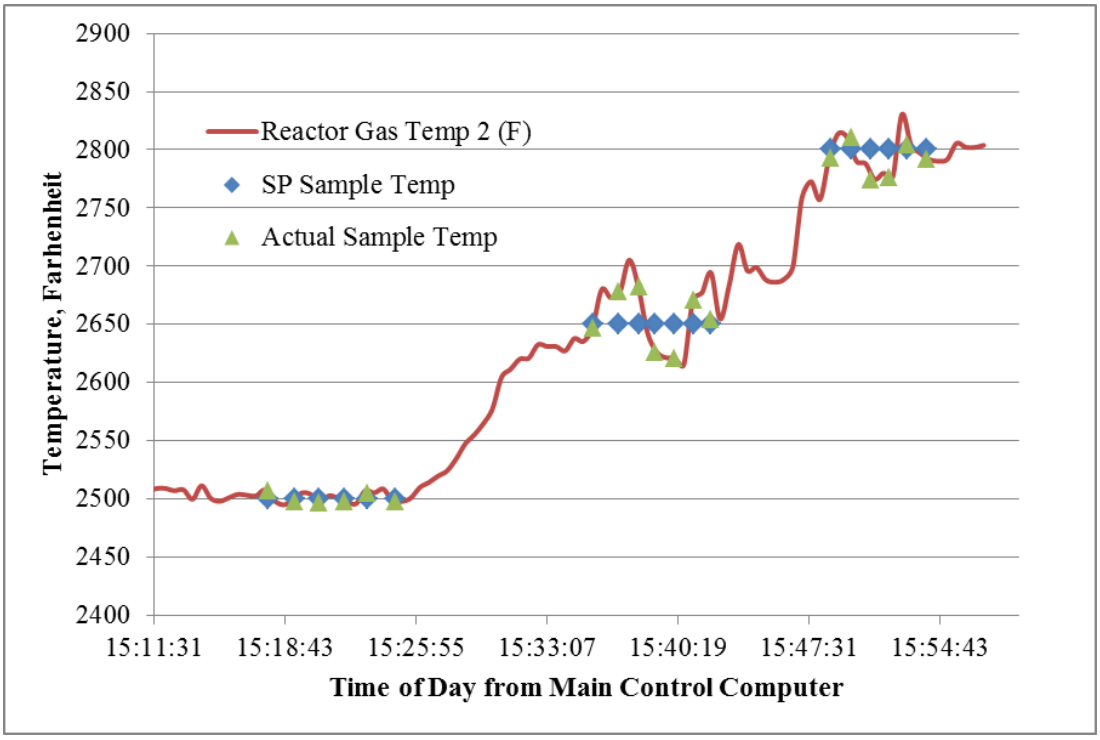

Figure 57: Reactor and sample temperatures for actual and targeted values.

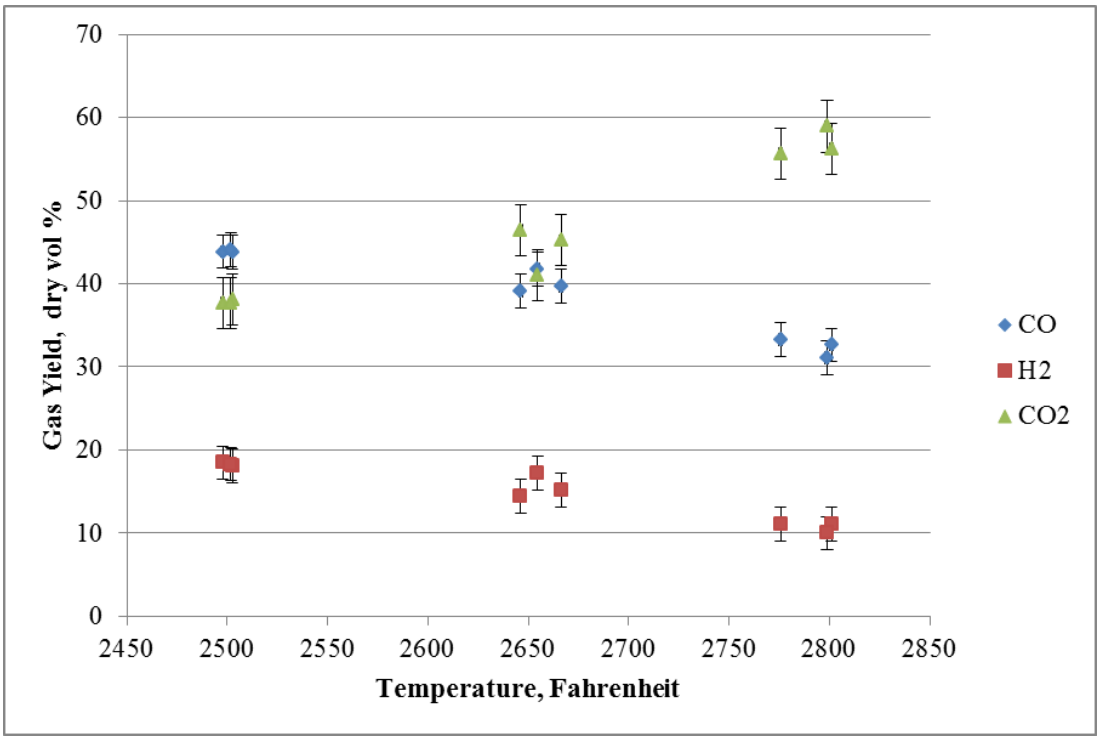

Figure 58: Average gas yields for carbon monoxide (◆), hydrogen (■), and carbon dioxide (▲), dry volume percent at respective sample locations.

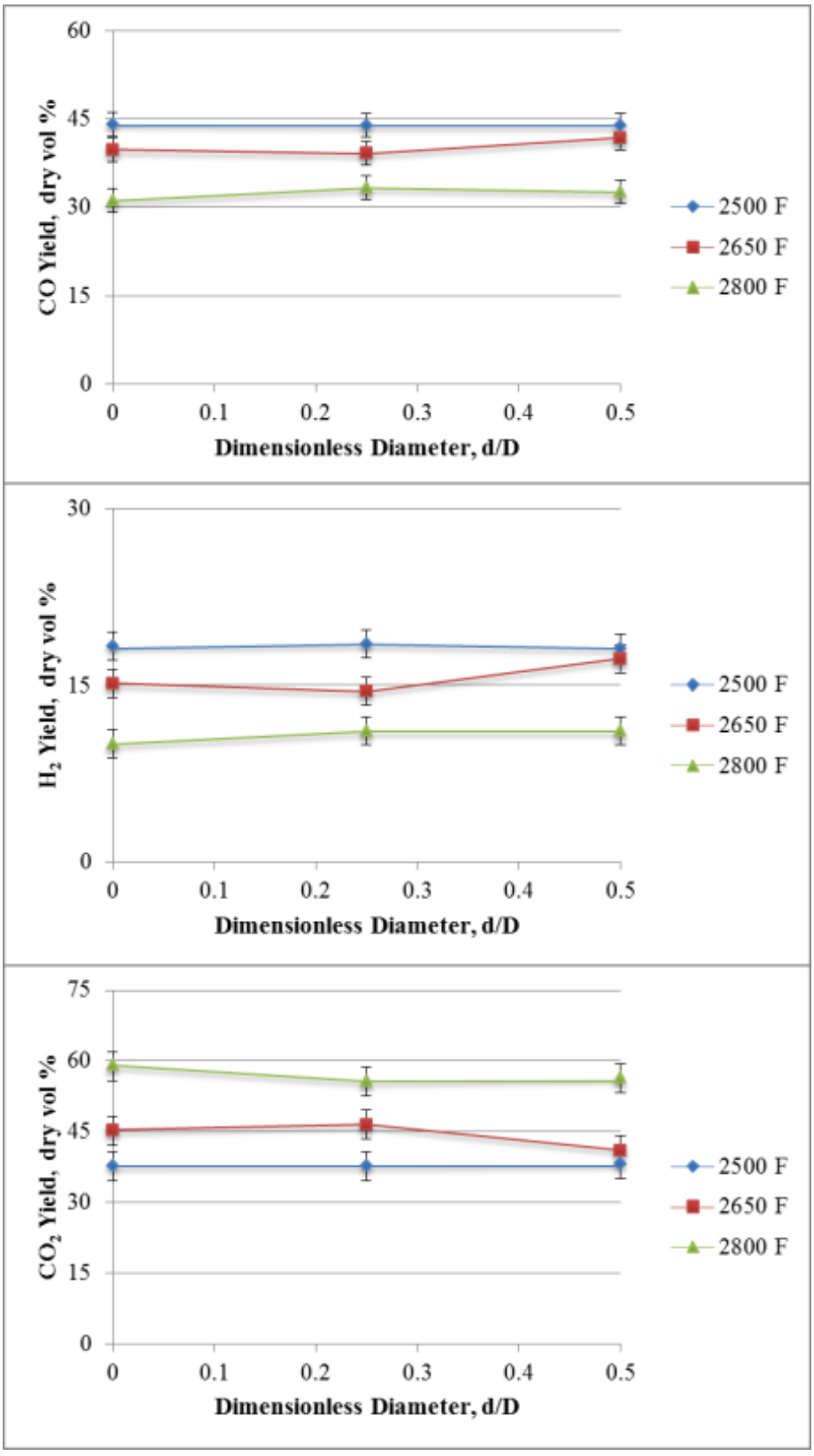

Figure 59: Radial gas compositions as a function of temperature, dry volume percent. Temperature trends are indicated as 2500 °F (◆), 2650 °F (■), and 2800 °F (▲).

The error represented in Figure 59 is the standard error calculated from the original 19 samples at 95% confidence. The clear trends that emerge from Figure 58 are that as temperature increases, both carbon monoxide and hydrogen yield decrease, while carbon dioxide increases. The lower temperature samples show less of a deviation than the higher temperatures, most likely attributed to a more steady state operation of the gasifier in the beginning of the campaign. This is not the case, however, with the varying radial sample location as seen Figure 59. Two of the most significant deviations in radial location are the yields for carbon dioxide at 2800 °F and the yields of all three gases at the middle temperature of 2650 °F. This suggests that as temperature increases, to an undefined threshold, the carbon monoxide and carbon dioxide yields deviate. Figure 60 supports this evidence by plotting the CO/CO_2 molar ratio versus actual gasifier temperature, and not target temperature.

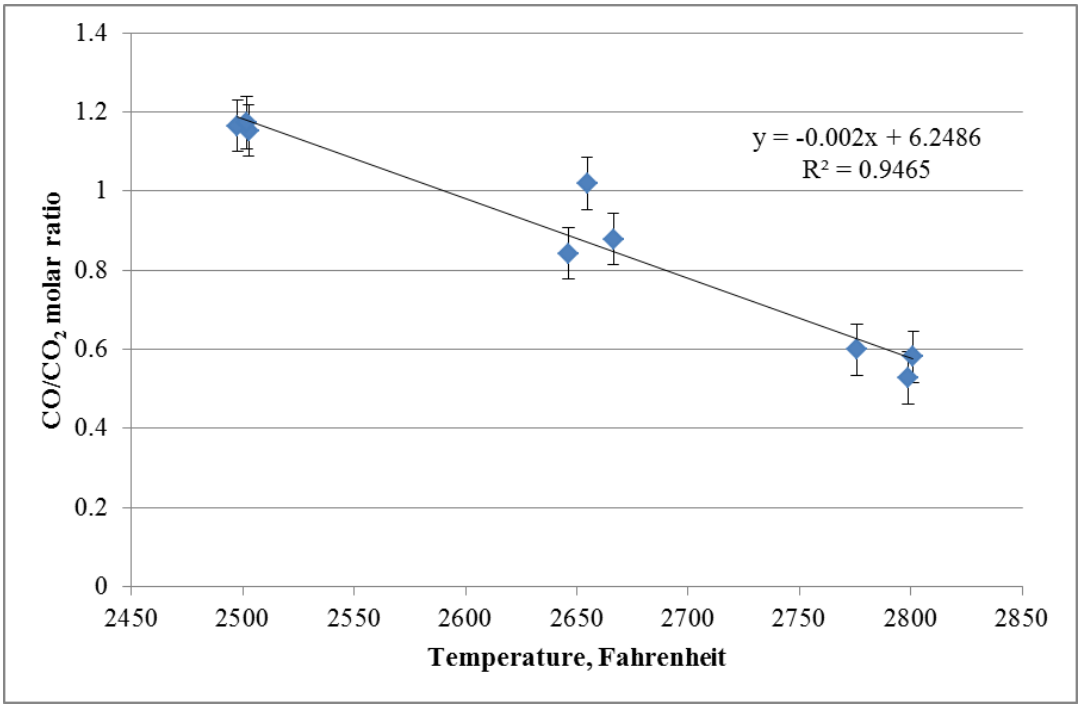

Figure 60: CO/CO2 molar ratio versus temperature, dry basis.

This decrease in CO/CO2 ratio also appears in dry-feed systems that alter the steam feed rate. Azuhata (*32*) showed that with an increase in oxygen flow rate, the CO/CO2 ratio decreased in a pilot-scale dry-feed entrained-flow gasifier at Brigham Young University. As the temperature is raised in the University of Utah's entrained-flow gasifier, the slurry flow rate decreases, introducing less water and coal to the system and increasing the oxygen to carbon feed ratio.

The heating value of the intermediate syngas from the gasifier and syngas outlet differ. Centerline gas composition and gasifier outlet higher heating values (HHV) are shown in Table 15 and calculated via thermodynamic heats of formation. As the target temperature increases, the heating value decreases. This is likely from the higher production of carbon dioxide and less production of hydrogen and carbon monoxide as determined from Figure 58 and Figure 60 in addition to higher oxygen flow rates that increase the amount of carbon dioxide produced and decreasing the heating value.

Using JMP, a data analysis software, quadratic equations for major gas species were determined as a function of temperature. Radial sample location proved to show no significant correlation to syngas yield. The general form is seen as Equation 11.

$$Yield\ [\%] = AT^2 + BT + C \qquad \text{Equation 11}$$

Here, T is temperature in degrees Fahrenheit and A, B, and C are coefficients. Table 16 shows the values for CO, H_2 and CO_2. These three equations are compared to the experimental findings in Figure 61 where the two are plotted against one another.

Figure 61 indicates the quadratic fits agree well with the experimental findings and can aid in prediction of the syngas composition within the gasifier.

Table 15: Higher heating values (Btu/SCF) of intermediate and outlet syngas compositions.

Target Temperature (°F)	**2500**	**2650**	**2800**
Centerline HHV (Btu/SCF)	196	187	138
Syngas Out HHV (Btu/SCF)	208	195	179

Table 16 Species coefficients for Equation 11.

Gas Specie	**CO**	**H_2**	**CO_2**
A	-1.00E-04	-5.04E-05	1.50E-04
B	-3.95E-02	-2.58E-02	6.54E-02
C	144.91	84.01	-128.92

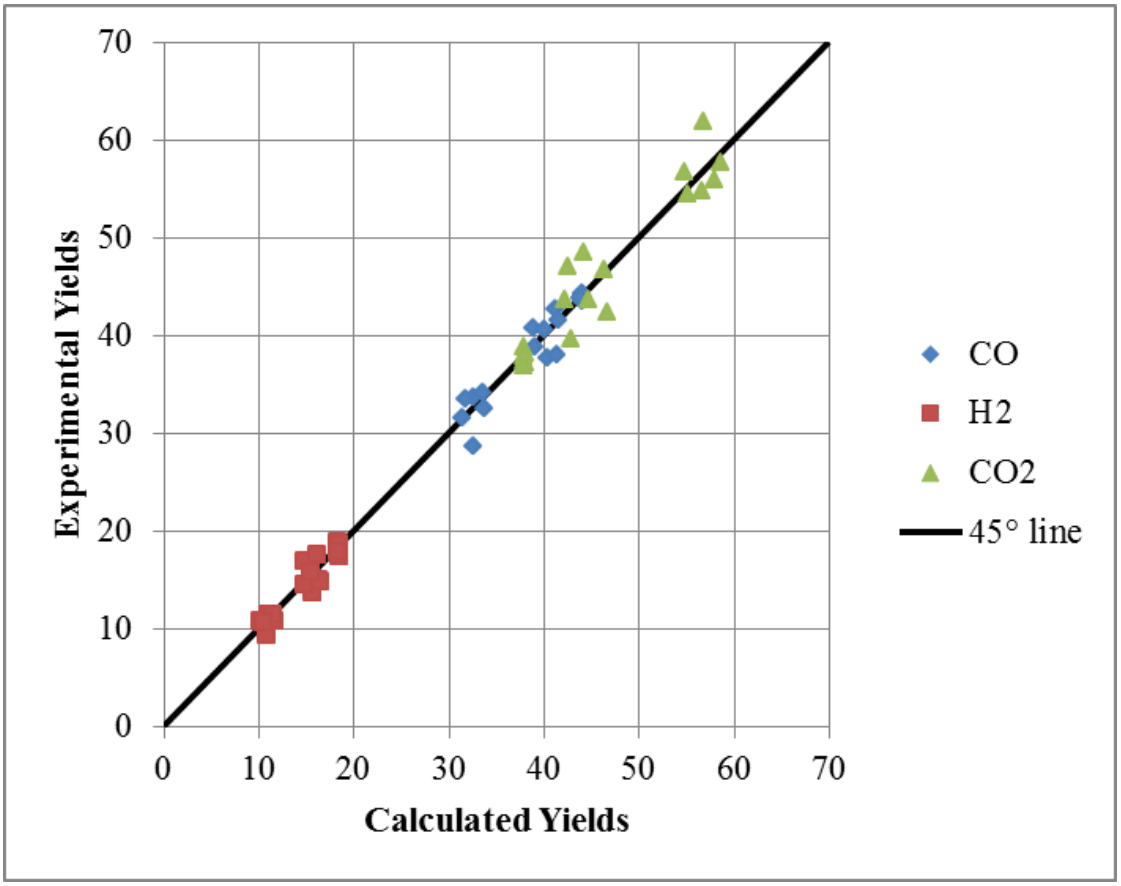

Figure 61: Experimental versus calculated yields for carbon monoxide (◆), hydrogen (■), and carbon dioxide (▲), dry volume percent.

Even simple modeling and trends like ones above can be helpful on industrial scales. In some systems, knowing how to measure conversion, even qualitatively, can be useful and utilized to increase overall efficiencies. The significance of the water-gas shift reaction becomes more important on large-scale systems where plus or minus 1% of carbon monoxide or hydrogen correlates to thousands of dollars at the end of the process and can alter downstream compositions. In the quench region of the EFG, sprays fan out across the reactor and seize the high temperature reactions at the end of the reaction zone. This assumes the composition does not change significantly, if at all, before the composition is measured by gas chromatography once the flows enter the quench. Analyzing the effluent syngas in the same manner as the probe samples above reveals significant changes in the compositions of carbon monoxide, hydrogen, and carbon dioxide. Figure 62 shows the centerline reaction zone gas concentrations, labeled as "Pre-Quench" and the product syngas concentrations, labeled "Post-Quench" for the three temperatures tested. Blue, red, and green bars indicate 2500 °F, 2600 °F, and 2800 °F, respectively.

Using nitrogen in the gas stream as a tracer, the qualitative and quantitative gas concentrations of CO, H_2, and CO_2 become easier to decipher. It is important to note that these are on a dry basis and do not directly consider the water added in the quench region, which become significant when stating that all gas concentrations increase when going through the quench sprays of the gasifier. The only exception is carbon dioxide at 2800 °F. The hydrogen concentration at all three temperatures more than doubles, indicating a strong connection to the water-gas shift reaction where water is added and drives the production of hydrogen. At 2800 °F, the hydrogen concentration triples and carbon dioxide decreases, but the carbon monoxide concentration does not increase as much as the other

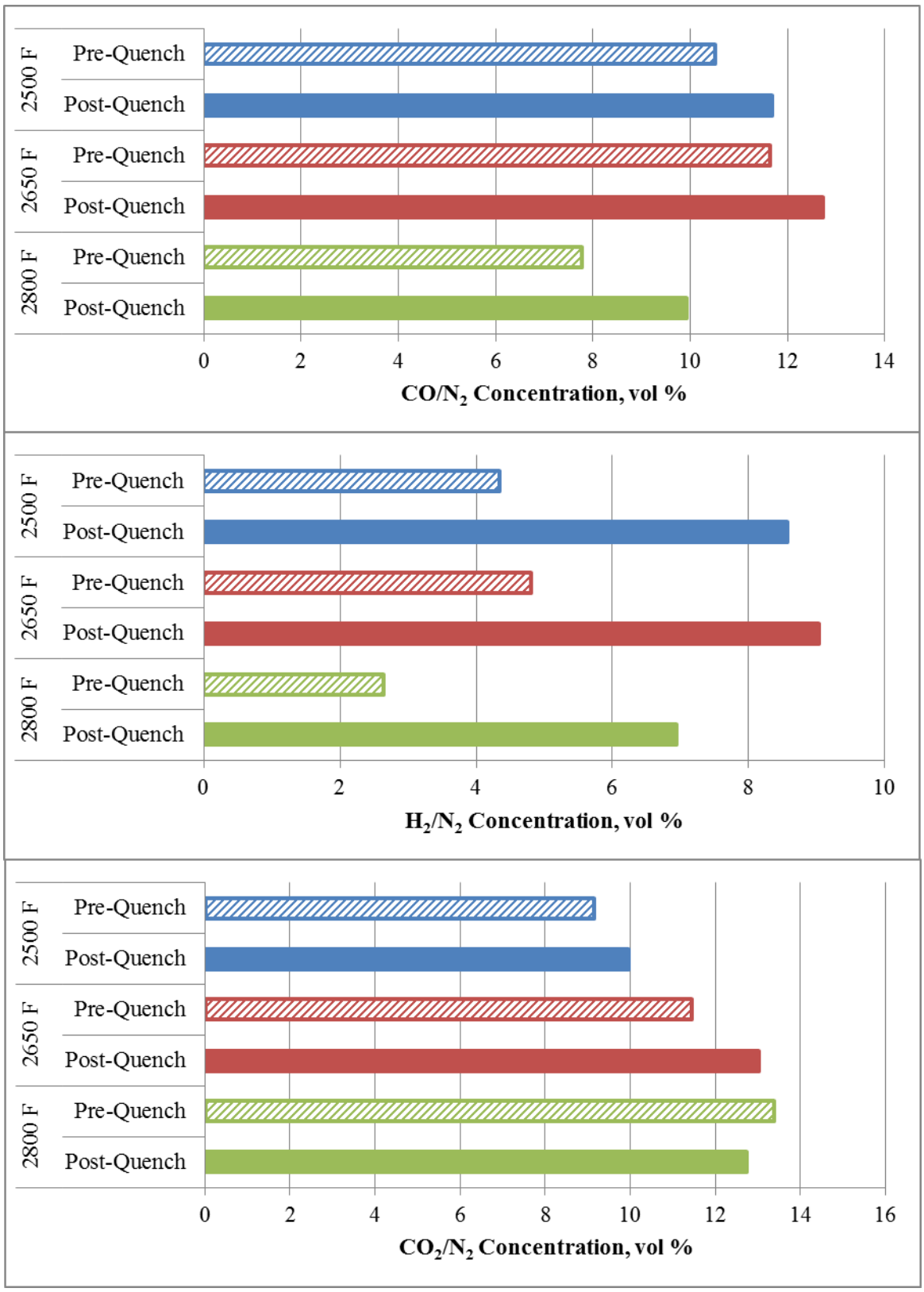

Figure 62: Comparison of pre- and post-quench syngas compositions with a nitrogen tracer.

two temperatures. This is another indication of the importance of the water-gas shift reaction where more moles of hydrogen are produced at the expense of CO_2 being converted to CO on a small scale.

4.3.2 Sampling System Performance

It is important to describe the performance of the system to not only aid in the significance of the work accomplished, but also because this system is the first to successfully sample a slurry-fed, entrained-flow gasifier. The design motivation was to make a sample system as simple as possible and with the fewest moving components as possible. Ultimately, the only moving part was the pneumatic cylinder to sample the different radial locations. The pressure seal performance was greater than expected and the only problems associated with the seal were the mounting and alignment procedure when attaching the flange assembly and probe extension to the gasifier sample port. Any misalignment would result in a leaking seal when the probe was extended into the gasifier. If the probe alignment was only off by fractions of a millimeter, the seal would warp from different forces being applied to the front of the housing than the backside. For this reason, any future iteration of the sampling system should use a dual seal with a nitrogen purge around the seals in the event of a failure.

Alternate materials should also be investigated for probe extension. In a retracted position within the refractory wall of the gasifier, the extension would consistently be subjected to a corrosive atmosphere in excess of 2500 °F (1370 °C). When in an extended position at the wall or at the centerline of the reaction zone, the probe extension would be exposed to similar atmospheres, but in excess of 4000 °F (2200 °C). A ceramic tipped probe extension would be ideal unless slag builds up across the port, causing the cylinder

to continue to push and break at the probe tip at a metal/ceramic junction. The metal tubing would still be necessary to guide the extension through the pressure seals and not cause the flange assembly to leak.

Even though the probe extension is water cooled, thermal deformation of the probe extension can still occur as seen in Figure 63. Here, the flame view of the extension is shown with a significant amount of deposit and sintering. The pressure seal can be seen at the right-hand side. The darkened metal surface has been warped due to the high gasifier temperatures and has been caused by longer sampling times at each of the three setpoints. Figure 64 shows a close-up view of the underside of the probe tip where the 1/8-inch hole has been eroded and melted away.

Previous operation of the probe in the gasifier was minimized for shakedown purposes and to verify the different systems worked. When sampling the gasifier for the results described herein, the sample time was extended for a five-liter tedlar bag sample, whereas previously the sample bags were only three liters. This time difference accounts for the burned probe extension.

Figure 63: Top view of probe extension after gasifier sampling.

Figure 64: Close up view of probe extension tip underside.

The volume of gas sampled from the gasifier is of concern when sizing the critical orifice and tubing line size in the sampling train. For a ¼-inch tube and critical orifice size of 16, the calculated radius of sampling from the probe in the gasifier is 2.6 inches. This value assumes a 5 second residence time in the reaction zone. The value of the radius accounts for the constant gas compositions across the reactor at all three targeted temperatures. Additional work is required to minimize the sample volume of the gasifier and to acquire data at specific radial locations. This task is accomplished using a combination of increasing coolant rate of the probe extension to reduce temperature, decrease the size of the critical orifice to choke the flow rate and increase mass flow rate, and decrease the size of the hole at the probe extension tip. One or a combination of these factors will necessitate the fabrication of a new probe tip using material with a higher melting point because the sample time will increase as well to achieve a large enough gas volume for gas chromatography analysis.

The dilemmas with the probe extension were the only major problems that provided resistance to acquiring additional data. The software had no glitches and performed exactly

as planned, and the pneumatic cylinder functioned better than the operator expected. Future modifications are necessary, however, for the successful and consistent operation of the sampling system. If particles are to be captured using a similar probe system, downstream modifications are necessary including solvent baths to capture tars by using the reactor to atmosphere pressure differential as a driving force. Particles were inadvertently captured while collecting the gas-phase data and images of these particles are presented in the next section.

4.3.3 Particle Capturing

During sample system operation, particles adhered to the water-cooled surface of the probe. These particles were collected over the course of the entire run; they do not pertain to individual run conditions and sample locations. Five samples were collected in total and scanning electron microscopy (SEM) was performed on some of the samples. External analyses (including ultimate and proximate analyses) could not be performed due to a lack of quantity of char sample. The five samples collected were from the tip of the probe extension, from 0 to 2 inches back from the probe tip, 2 to 4 inches back from the probe tip, 4 inches back from the tip to the flange face, and the flange face itself. Some of the more indicative photographs of char gasification are presented here.

Figure 65, Figure 66, and Figure 67 show SEM photographs of three different probe extension positions, between 0 and 2 inches from the probe tip, between 2 and 4 inches from the probe tip, and of the flange face, respectively. Although all three show particles with what appear to be holes caused by volatile and tar evolution, they are not representative of the position from which they were taken.

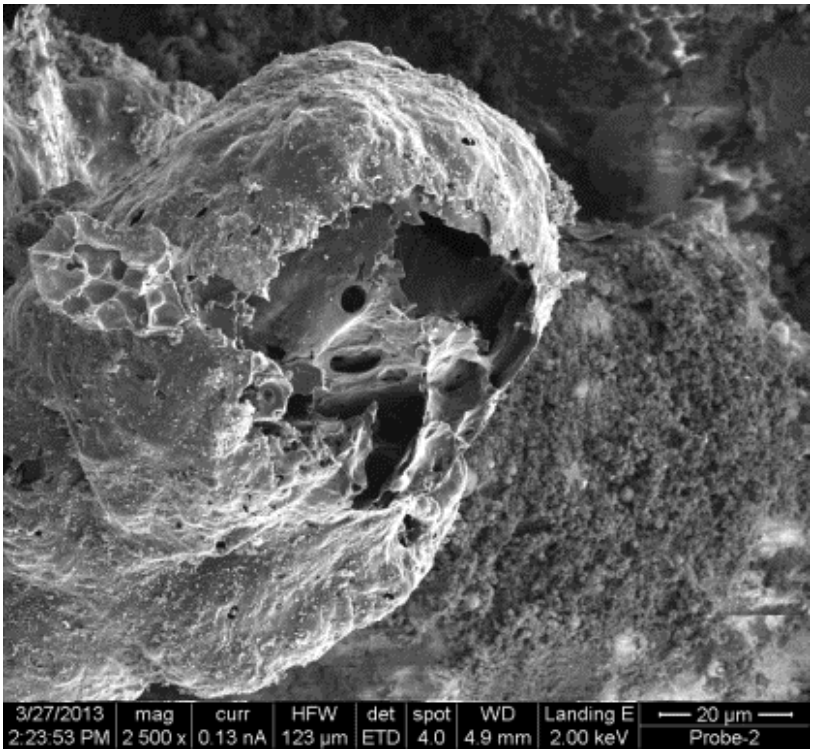

Figure 65: SEM photograph of a particle agglomeration between 0 and 2 inches from the probe tip.

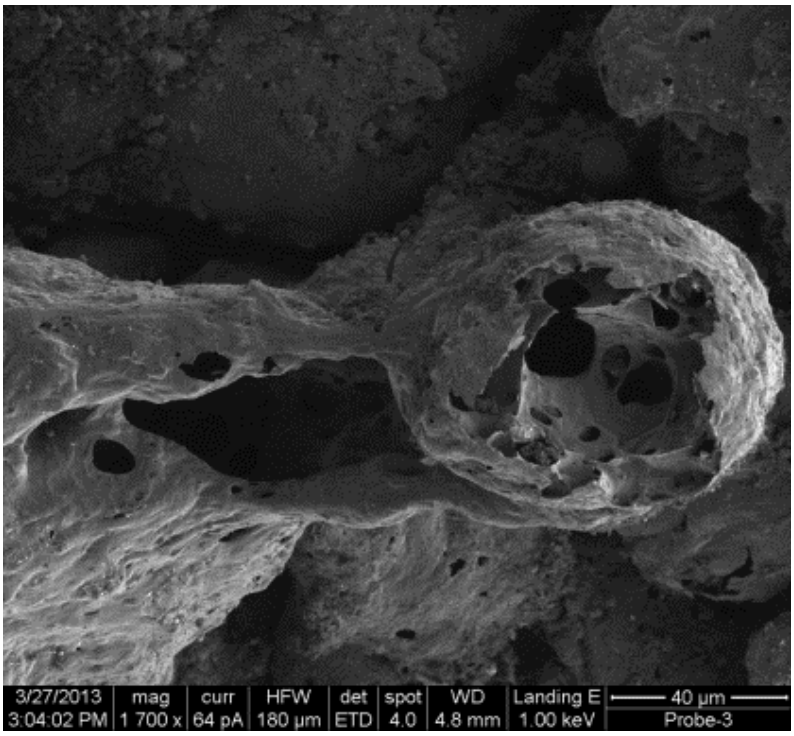

Figure 66: SEM photograph of a particle between 2 and 4 inches from the probe tip.

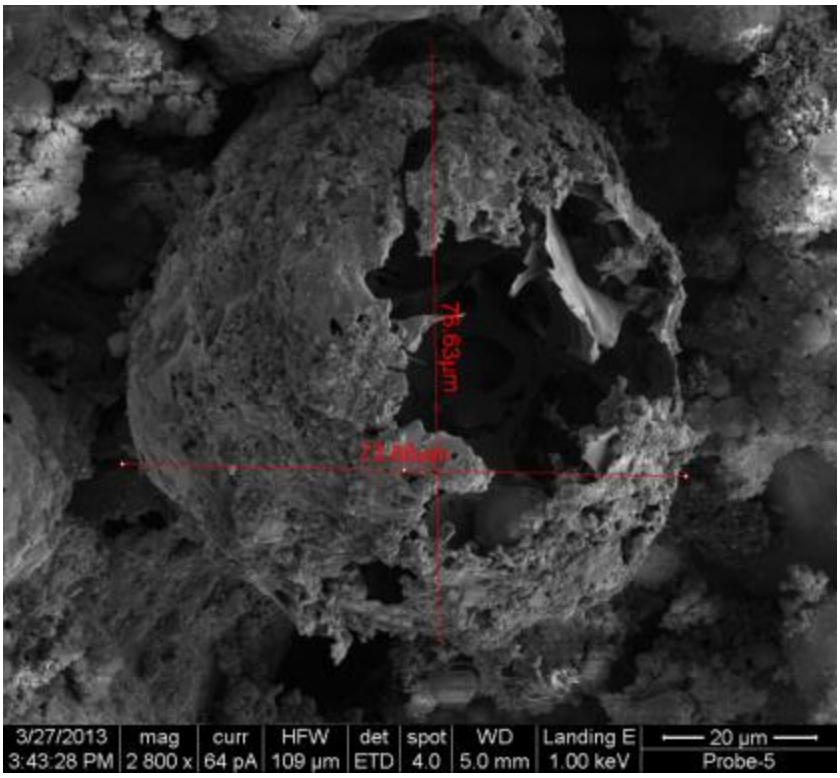

Figure 67: SEM photograph of a near spherical particle from the probe assembly flange face.

While the previous three figures show particles that have partially devolatilized, Figure 68 shows the other type of particle commonly seen. The spherical particles are likely high in ash and have been subjected to temperatures above the ash fusion point for prolonged periods. Another possibility is the droplets from which the particles came from the injector saw a greater degree of devolatilization while in the reaction zone of the gasifier before adhering to the probe extension surface. These spherical particles were found in all samples investigated by SEM as well as the TGA experiments.

Energy Dispersive Spectroscopy (EDS) was performed on the TGA ash particles, revealing a significant amount of silicon and aluminum oxides. The particle on which EDS was performed and the results are shown in Figure 69 and Table 17, respectively.

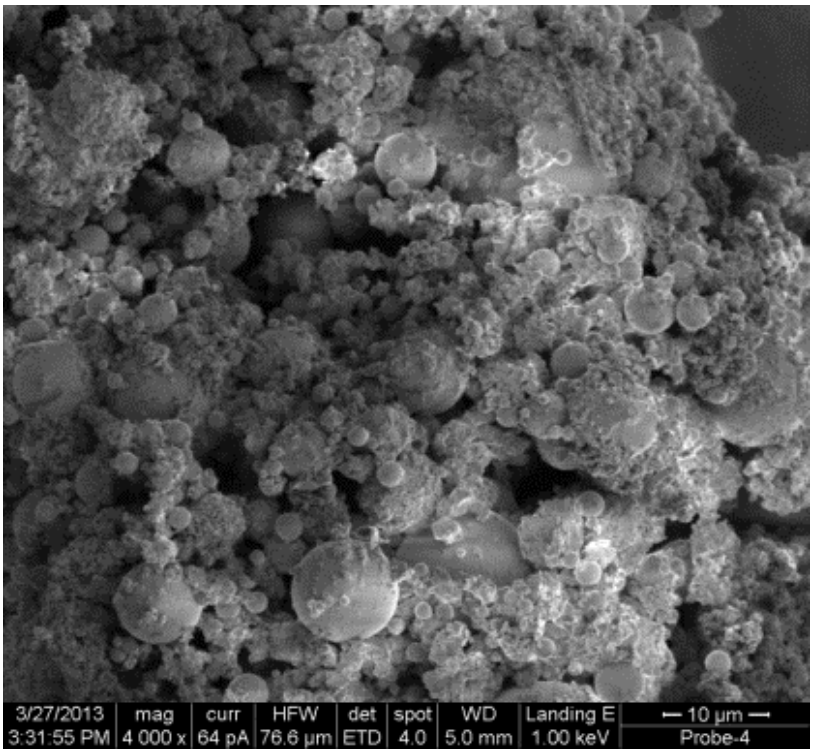

Figure 68: SEM photograph of spherical particles between 4 inches back from the probe tip and the flange face.

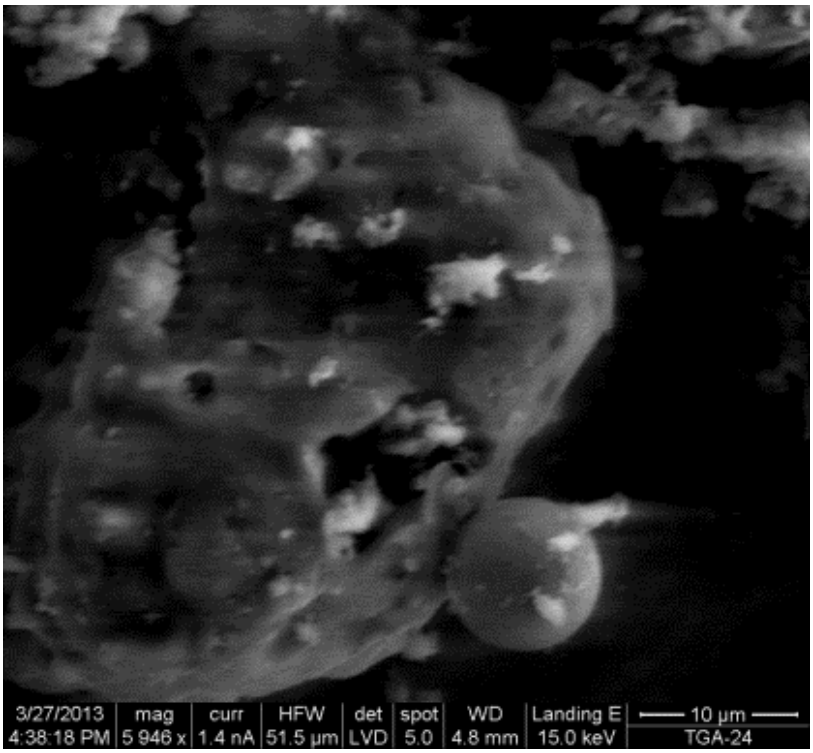

Figure 69: TGA-produced spherical particle on which EDS was performed.

Table 17: EDS results for TGA-produced particle.

Specie	**Weight %**	**Mole %**
Na_2O	8.33	9.22
MgO	1.04	1.77
Al_2O_3	30.38	20.44
SiO_2	52.95	60.45
K_2O	1.62	1.18
CaO	5.68	6.94
Total	100	100

Additional work is required to determine the influence of temperature on the pressurized entrained-flow gasification of particles. A supplemental probe extension is necessary to actively capture such particles and preserve them for analysis.

CHAPTER 5

MODELING RESULTS AND DISCUSSION

To bring the experiments together, a previously created Aspen simulation was used to compare the results in addition to an additive reaction time model developed from the correlations and results of the previous section and a one-dimensional model of the gasifier as a function of residence time and axial length.

5.1 Aspen Simulation

5.1.1 Simulation Description

A model for the entrained-flow gasification of coal was developed by AspenTech using Aspen Plus. The model version is v7.3.2, revised in 2012. The Texaco-style model is steady-state and accounts for coal pyrolysis, volatile combustion, and char gasification. To simplify the model, no pressure drop is considered, the gas and solid phases are assumed to be well mixed, the coal particles are assumed to be spherical and have uniform size, in addition to an unreacted-core, shrinking model. The hydrodynamics of the system can also be used to calculate a residence time of the solids.

Major gas species are considered, including carbon monoxide, carbon dioxide, hydrogen, oxygen, water (as steam), nitrogen, hydrogen sulfide, methane, and benzene to approximate tar evolution. In the solid phase, carbon is assumed as graphite and sulfur is considered. The basis of the model stems from the work of Wen and Chaung (*94*) in which coal-water slurry is gasified and the entrainment of the solids and gas-phase is considered.

The key inputs of the Aspen model are ultimate, proximate, and sulfur analyses. The submodels and processes that are carried out in the model are coal pyrolysis, volatile combustion, and char gasification.

The coal pyrolysis submodel considers the general devolatilization reaction where coal is thermally broken down to yield char, tar (as benzene), inert species (e.g. nitrogen), and volatile gases (CO, CO_2, H_2, H_2O, CH_4, and H_2S). The submodel is actually semi-empirical and based on pyrolysis data collected from Suuberg (*95*) and Wen and Chaung (*94*). The data from Suuberg were acquired from atmospheric pressure data of a wire-mesh reactor test campaign. Suuberg's data are categorized as one of three types, tars that condense at room temperature, product gases that are vapor at room temperature, and char. Suuberg's atmospheric results are scaled to operating pressure from Wen and Chaung's equation to correct for total volatiles yield, seen in Equation 12.

$$V_2 = V_1 \cdot (1 - a \cdot lnP_t) \qquad \text{Equation 12}$$

Here, V_2 is the total volatiles yield at the gasifier pressure, P_t (atm), and V_1 is the total volatiles yield at atmospheric pressure. The coefficient a is determined to be 0.066 for bituminous coal (*94*). The heating rate used in Suuberg's work was 1000 ℃/s, which was the same rate used for the wire-mesh experiments for the work described in the previous sections.

The volatile combustion submodel considers reactions and reaction kinetics on a more theoretical basis than the coal pyrolysis, but assumes Reaction 4 through Reaction 7 go to completion.

$$C_6H_6 + 7.5O_2 \rightarrow 6CO_2 + 3H_2O$$ Reaction 4

$$H_2 + 0.5O_2 \rightarrow H_2O$$ Reaction 5

$$CO + 0.5O_2 \rightarrow CO_2$$ Reaction 6

$$CH_4 + 2O_2 \rightarrow CO_2 + 2H_2O$$ Reaction 7

By assuming the above reactions go to completion, the product syngas should have no oxygen present. The four reactions also provide the system with a substantial amount of energy to allow the endothermic reactions to take place in the gasification of char.

In the char gasification submodel, the heat and products from volatile combustion and the char from the coal pyrolysis, as well as the other species, aid in forward and reversible pathways seen in Reaction 8 through Reaction 14.

$$C + \frac{1}{\varphi}O_2 \rightarrow 2\left(1 - \frac{1}{\varphi}\right)CO + \left(\frac{2}{\varphi} - 1\right)CO_2$$ Reaction 8

$$C + H_2O \rightarrow CO + H_2$$ Reaction 9

$$C + CO_2 \rightarrow 2CO$$ Reaction 10

$$C + 2H_2 \rightarrow CH_4$$ Reaction 11

$$S + H_2 \rightarrow H_2S$$ Reaction 12

$$CH_4 + H_2O \leftrightarrow CO + 3H_2$$ Reaction 13

$$CO + H_2O \leftrightarrow CO_2 + H_2$$ Reaction 14

The coefficient of Reaction 8, φ, is a function of the coal particle diameter, which can be found in Appendix G for varying coal particle size in addition to kinetic parameters

for Reaction 8 through Reaction 14. The reaction kinetics considers the effects of ash layer diffusion, gas film diffusion, and chemical reactions, resulting in the rate expression seen in Equation 13.

$$R_{C-i} = \frac{1}{\frac{1}{k_{diff}} + \frac{1}{k_s Y^2} + \frac{1}{k_{dash}}\left(\frac{1}{Y} - 1\right)} (P_i - P_i^*) \qquad \text{Equation 13}$$

Here, R_{C-i} is the reaction rate [grams carbon/(cm^2 particle surface area)·s], $(P_i - P_i^*)$ is the partial pressure of component i considering the reverse reaction, and $Y = r_c/r_p$ where r_c and r_p are radii of the unreacted core and particle with ash layer, respectively. The constants k_{diff}, k_s, and k_{dash} are for gas film diffusion [g/cm^2·atm·s], surface reaction [g/cm^2·atm·s], and the ash film diffusion [g/cm^2·atm·s], respectively. A model accompanying the AspenTech document (*96*) describes the process in detail for determining the partial pressures of component i and contains a more in-depth discussion of the rate equation.

The simulation procedure and flow sheet is assembled using the submodels described above and shown in Figure 70. The coal pyrolysis submodel is carried out in yield-based reactors and corrected for the pressure in a real gasifier. Volatiles combustion is carried out in a stoichiometric reactor model that allows the gases, ash, and char to be separated based on phase and destination. The char gasification step is carried out in a plug flow reactor model with the syngas being the only outlet since the ash is assumed inert and is transported through the processes. Other blocks in Figure 70 include mixers and separators to achieve the desired reaction pathways. A detailed description of the hydrodynamics and the residence time is given in the manual (*96*), but in short, is calculated

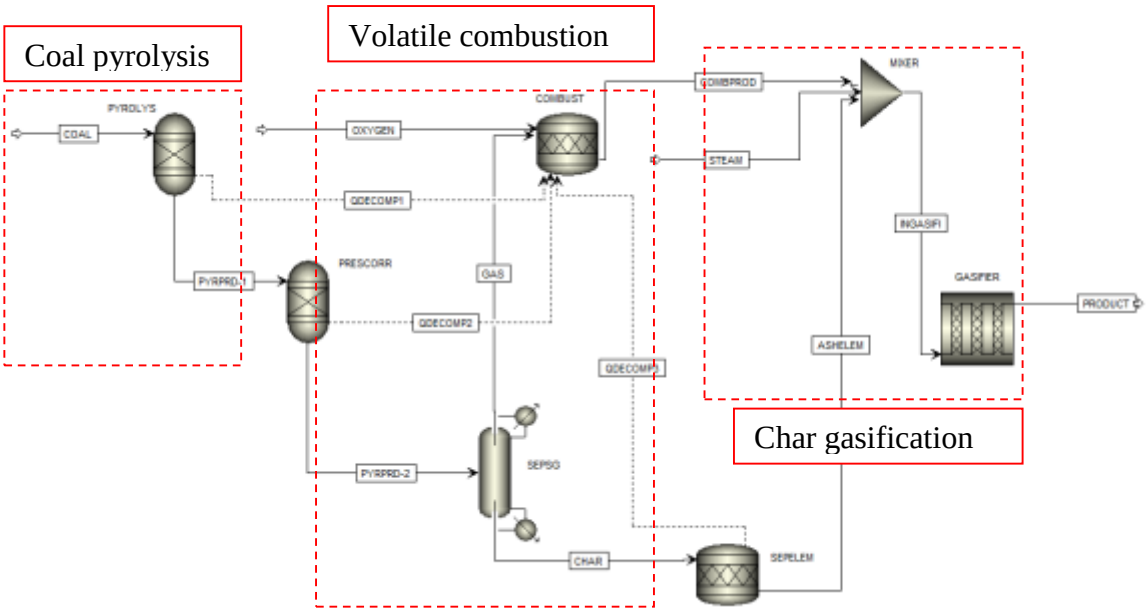

Figure 70: Aspen flowsheet of the Texaco-style gasification model.

using Equation 14. Here, t is time in seconds, V is the volumetric flow rate of gas, and V_R is the reactor volume.

$$t = \int_0^{V_R} \frac{1}{V} dV_R \qquad \text{Equation 14}$$

5.1.2 Simulation Results

The model described in the previous section was modified with respect to the operating conditions of the University of Utah's entrained-flow gasifier (EFG) from which data are presented herein. The geometry of the plug flow reactor in the Figure 70 flowsheet was changed to an 8 inch diameter and a 60 inch length to match the EFG. The pressures of individual blocks were set to 11 bar (150 psig) and the proximate and ultimate analyses for Sufco coal replaced the previous bituminous data, but the product yields of Suuberg (*95*) were preserved. The dry gas-phase composition of the syngas at a location 18 inches

down the reaction zone is shown in Figure 71 for both the ASPEN simulation and the centerline EFG data presented in previous sections.

The large discrepancy of the gas compositions of Figure 71 could be caused by a number of factors, including incomplete (or intermediate) conversion of the fuel in the EFG or incomplete gas-phase kinetic data in the simulation. The simulation was also found to reach a steady state relatively quickly and indicated that equilibrium occurred at 40% of the reactor length. Figure 72 shows the gas composition versus reactor length for the lowest temperature of 1370 ℃ (2500 °F). Here, the reactor comes to steady state quickly and the difference between the effluent syngas composition and any point after 2 feet is small compared to the EFG composition differences.

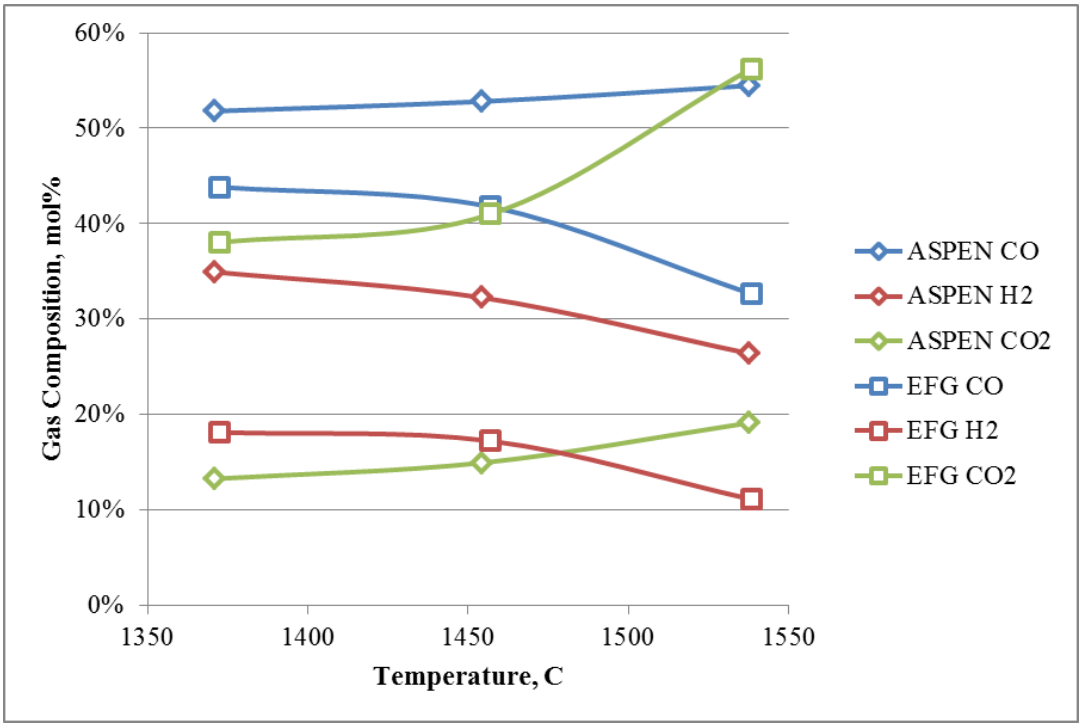

Figure 71: ASPEN simulated and EFG gas compositions versus temperature 18 inches downstream of the injector.

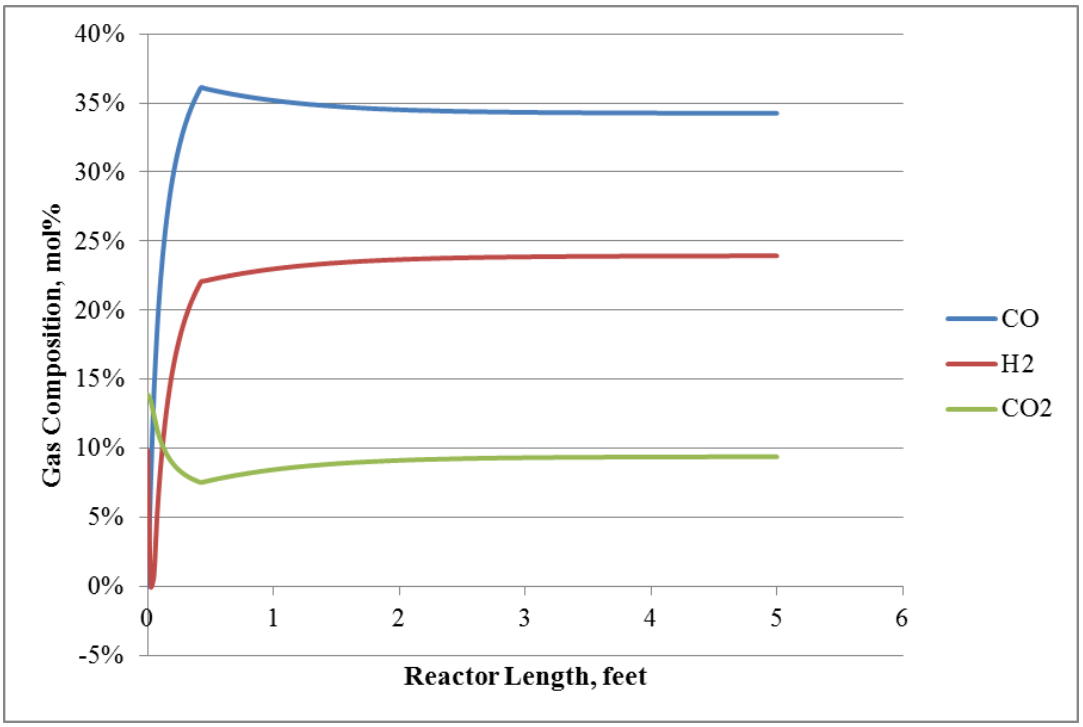

Figure 72: Gas composition versus reactor length for the ASPEN simulation at 1370 ℃ (2500 °F).

5.2 Additive Reaction Time Model

5.2.1 Model Description

A basic model was constructed to predict the influence of drying, devolatilization, and char gasification of a single particle on the entire gasification process. Microsoft Excel was used in the event that the developed model was concise and user-friendly in order to be used quickly at the University of Utah's Industrial Combustion and Gasification Research Facility. The model is based on the law of additive reaction times (*97*), which compares the times for a specified conversion to take place in only chemically controlled, diffusion, or external mass transfer regimes. Figure 73 shows the law of additive reaction times.

$$\begin{bmatrix} Time \\ required \\ to\ attain\ a \\ certain \\ conversion \end{bmatrix} = \begin{bmatrix} Time\ required \\ to\ attain\ the \\ same\ conversion \\ with\ chemical \\ reaction\ control \end{bmatrix} + \begin{bmatrix} Time\ required \\ to\ attain\ the \\ same\ conversion \\ under\ intrapellet \\ diffusion\ control \end{bmatrix} + \begin{bmatrix} Time\ required \\ to\ attain\ the \\ same\ conversion \\ under\ external \\ mass\ transfer \\ control \end{bmatrix}$$

Figure 73: Law of additive reaction times

This law was extended to drying and devolatilization for coal gasification by incorporating Equation 7 for devolatilization and the lumped capacitance method for the drying stage (*98*). Since the lumped capacitance method of transient conduction recognizes that the rate of heat loss from a particles surface is equal to the rate of change of internal energy, the assumption that a coal particle is spatially uniform with respect to temperature is necessary. After conducting an energy balance and separating variables from Fourier's Law and Newton's Law of Cooling, the drying time is solved for using Equation 15. Here, density, ρ, is multiplied by the droplet volume, V, and fluid specific heat, c. This product is divided by the convective heat transfer coefficient, h, and droplet surface area, A_s. The quotient is multiplied by the natural logarithm of the ratio of temperature differences of the initial particle temperature and surface temperature to that of the surroundings, θ_i and θ, respectively.

$$t = \frac{\rho V c}{h A_s} ln \frac{\theta_i}{\theta} \qquad \text{Equation 15}$$

This time is added to the total time for gasification in addition to the time necessary for devolatilization before calculating the char gasification steps. The general global reaction for char gasification is seen in Reaction 15.

$$A_{(g)} + bB_{(s)} \rightarrow cC_{(g)} + dD_{(s)}$$ Reaction 15

Here, the solid char, B, reacts with either carbon dioxide or steam as specified in the model and produces volatile species, C, and ash, D. The general form of the char gasification equations is shown in Equation 16. The general forms of the $g_{F_g}(X)$ and $P_{F_p}(X)$ terms are given in Equation 17 and Equation 18, respectively for a given conversion, X. In both of these equations, the shape factor, F_p, is assumed three for spherical grains and pellets. With this specification, Equation 18 becomes Equation 19.

$$t^* = g_{F_g}(X) + \hat{\sigma}^2 \left[P_{F_p}(X) + \frac{4X}{Sh} \right]$$ Equation 16

$$g_{F_g}(X) = 1 - (1 - X)^{1/F_p}$$ Equation 17

$$P_{F_p}(X) = 1 - \frac{F_p(1 - X)^{2/F_p} - 2(1 - X)}{F_p - 2}$$ Equation 18

$$P_{F_p}(X) = 1 - 3(1 - X)^{2/3} + 2(1 - X)$$ Equation 19

In Equation 16, $\hat{\sigma}$ is the generalized gas-solid reaction modulus and is defined in Equation 20. Sh is the Sherwood number, defined by Equation 21, and Equation 22 is responsible for translating the dimensionless time of Equation 16 to tangible time that can be approximated as the residence time necessary to achieve a specified conversion, X.

$$\hat{\sigma}^2 = \frac{\alpha_B k C_{A_0}^{n-1} F_p}{2D_e}\left(\frac{A_g}{F_g V_g}\right)\left(\frac{V_p}{A_p}\right)^2 \qquad \text{Equation 20}$$

$$Sh = \frac{k_m d_p}{D_e} \qquad \text{Equation 21}$$

$$t^* = \frac{b k C_{A_0}^n}{\rho_m}\left(\frac{A_g}{F_g V_g}\right) t \qquad \text{Equation 22}$$

As is customary in modeling, some parameters are difficult to approximate or are simply not known, as was the case for the Sherwood number. After a correlation was found for the effective diffusivity (*99*) and assuming a turbulent environment around the particle, the Schmidt number (Sc) was assumed unity. This assumption allowed the kinematic viscosity to equal the value of the effective diffusivity as defined by the Schmidt number and provide data for a Reynolds number calculation. With an initial particle velocity of approximately 10 m/s (*100*) and assuming forced convection around the spherical particles, the Sherwood number is defined in Equation 23 (*101*). From this correlation, the mass transfer coefficient of Equation 21 is found.

$$Sh = 2 + 0.60 Re^{1/2} Sc^{1/3} \qquad \text{Equation 23}$$

The solution procedure of the model begins with a specified slurry solids percent of 55% by weight. From this value, it is assumed that all water of the slurry droplet surrounds the coal particle uniformly and evaporates uniformly. Each slurry droplet is 45% water by weight and an effective volume of water is calculated that is necessarily evaporated to complete drying (e.g. for a coal particle of 74 microns, the slurry droplet

diameter is 93 microns). Assuming the slurry is pumped at 38 ℃ (100 ℉) to the gasifier and the temperature at which all water is driven off is the saturation temperature, Equation 15 is used to calculate the drying time. For a pressure of 11 bar (150 psig), the saturation temperature of water is 185 ℃ (365 ℉) and all moisture is converted to steam. Radiative heat transfer is neglected for the drying stage and all subsequent steps.

The devolatilization submodel uses Equation 7 to calculate the required time for all proximate volatile matter to evolve from the dry particle. The composition of these volatiles was taken from the ASPEN simulation (*96*) procedure and Suuberg's data (*95*) to better estimate a final syngas composition. During this stage, it is also assumed that all oxygen undergoes combustion with methane. This reaction consumes all oxygen and leaves small levels of methane, while producing water vapor and carbon dioxide. After all volatile species have been driven from the particle, the remaining char is essentially the fixed carbon percentage of the proximate analysis and ash is assumed inert for all stages. For the gasifier operating conditions of oxygen and slurry flowrates, temperature, slurry solids concentration, and slurry specific gravity, the submodel outputs are an intermediate syngas composition and time for devolatilization.

For the char gasification submodel, GASIFY, Equation 16 through Equation 22 are used to specify the general physical problem, but in a nondimensional form as Equation 16 suggests. It is important to understand that only the Boudouard (Reaction 10) and steam gasification (Reaction 9) reactions are considered in the model described herein, and are treated as separate, noncompeting reactions. The reason for this is to measure the influence of the individual reactions and calculate a theoretical minimum and maximum time for char

gasification within an entrained-flow gasifier based on the rapid steam gasification kinetics and the slower CO_2 gasification rate.

The assumptions discussed above and specific methods are summarized in Figure 74 per submodel, DRY (drying), DEVOL (devolatilization), and GASIFY (char gasification). After the three submodels of Figure 74 are complete, the mass percentages were used as inputs for a Gibbs energy minimization calculator from the Colorado State University website, titled Chemical Equilibrium Calculation (*102*). From the output of the chemical equilibrium calculator and the model itself, a syngas composition was determined as well as a total required residence time for complete conversion of carbon.

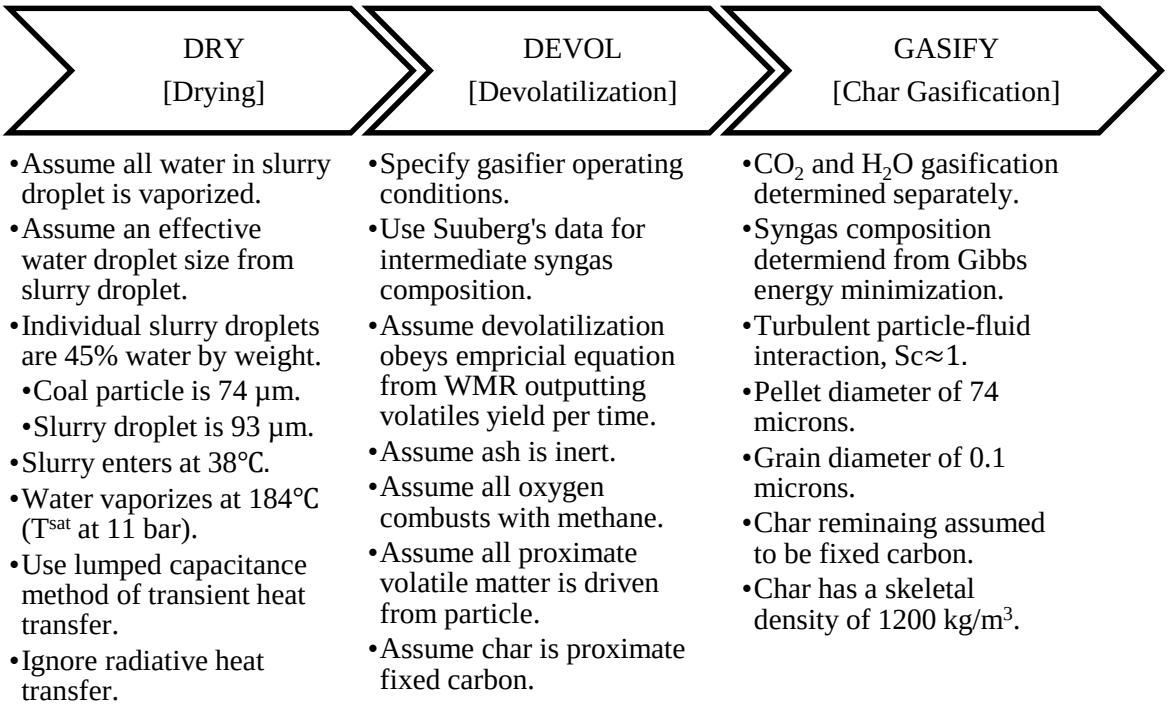

Figure 74: Summary of model assumptions and methods.

5.2.2 Model Implementation and Results

The model developed herein is for the direct use on the University of Utah's entrained-flow gasifier, but with minimal alterations, can be applied to any entrained-flow gasifier. At the discretion of the operator of the gasifier, this model is used as a guide and validation tool to predict conversion and reasonable syngas compositions.

The model was run at a pressure of 11 bar (150 psig) and temperatures of 1371 ℃ (2500 ℉), 1454 ℃ (2650 ℉), and 1538 ℃ (2800 ℉). These conditions were chosen in order to compare the results to the ASPEN simulation and experimental data presented previously. Table 18 and Table 19 show the individual reaction times for the various stages and the total time for gasification to take place for 100% conversion of carbon.

From Table 18 and Table 19, steam gasification is seen to take place at a faster rate and accounts for as little as 2 to 3% of the total residence time required. Carbon dioxide gasification requires up to 65% of the residence time and as little as 39%, but still occurs at a slower rate than any case of steam gasification. Based on the model results, it is expected that the residence time the gasifier be between 1.7 seconds and 5.5 seconds for the comfortable operating window of 1371 ℃ to 1538 ℃ (2500 ℉ to 2800 ℉). The model also assumes that stages of drying and devolatilization are independent of gas composition except for what is driven off at the end of each stage and how much is initially present.

Figure 75 and Figure 76 show the gas phase compositions for dry and wet syngas, respectively, for the two cases of CO2/steam (case 1) and pure steam gasification (case 2). The combination of CO2/steam was required to gasify completely the remaining char. Only ~40% of the char was converted utilizing Boudouard kinetics, and remainder converted by steam gasification. While carbon monoxide mole percentages of Figure 75

Table 18: CO_2 and steam gasification reaction times.

Temperature (℃)	1371	1454	1538
Drying Time (sec)	1.213	1.154	1.101
Devolatilization Time (sec)	0.739	0.625	0.541
Chemical Reaction Control (sec)	3.461	1.977	1.002
Intrapellet Diffusion Control (sec)	0.006	0.005	0.004
External Mass Transfer Control (sec)	0.038	0.035	0.029
Steam Gasification Time (sec)	0.051	0.032	0.021
Total Time (sec)	**5.507**	**3.828**	**2.698**
Drying Time %	22%	30%	41%
Devol Time %	13%	16%	20%
Char Gas. Time %	65%	54%	39%

Table 19: Steam gasification reaction times.

Temperature (℃)	1371	1454	1538
Drying Time (sec)	1.213	1.154	1.101
Devolatilization Time (sec)	0.739	0.625	0.541
Chemical Reaction Control (sec)	0.052	0.030	0.018
Intrapellet Diffusion Control (sec)	0.004	0.004	0.004
External Mass Transfer Control (sec)	0.005	0.004	0.004
Total Time (sec)	**2.013**	**1.817**	**1.668**
Drying Time %	60%	63%	66%
Devol Time %	37%	34%	32%
Char Gas. Time %	3%	2%	2%

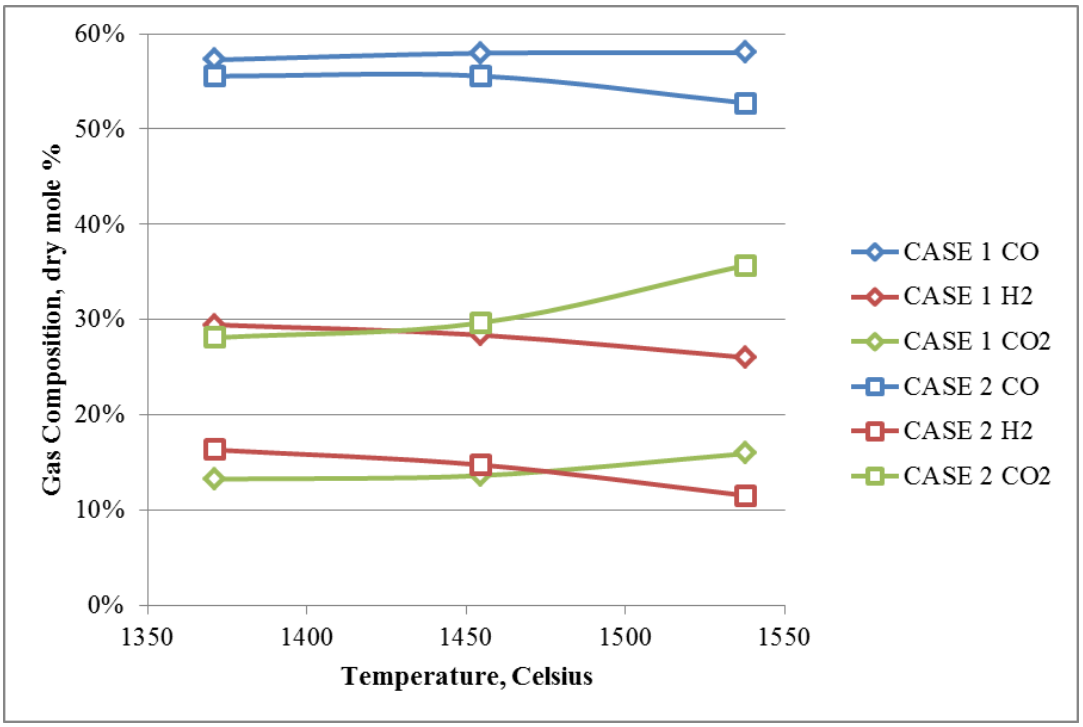

Figure 75: Model results for CO_2 and steam gasification syngas compositions versus temperature, dry mole %.

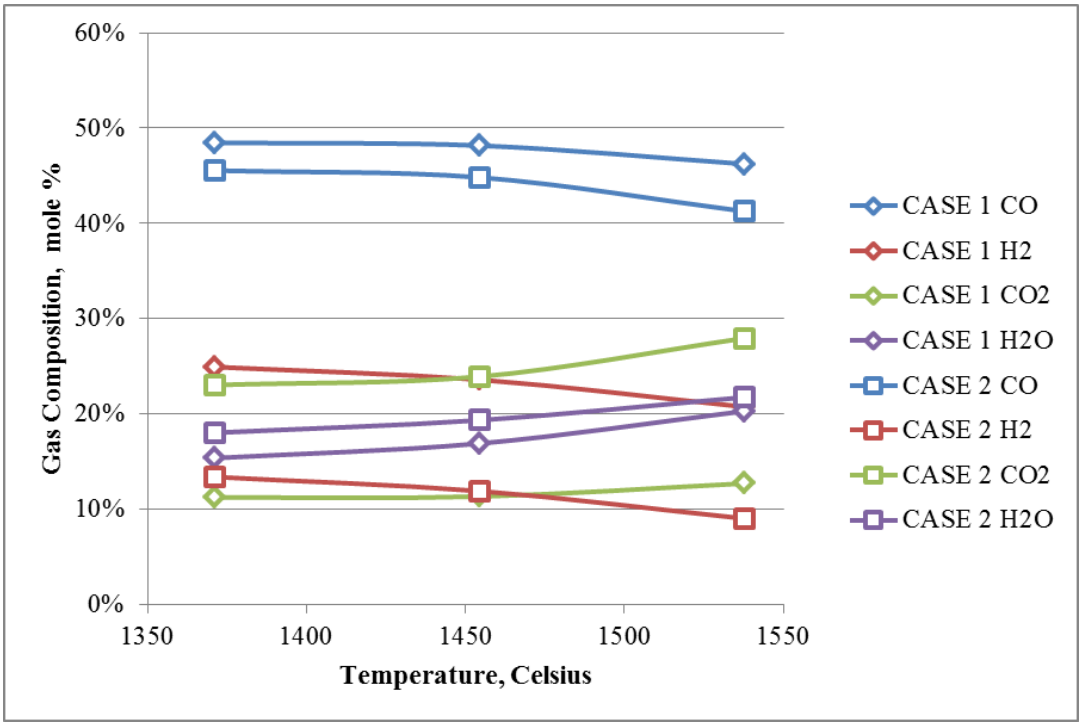

Figure 76: Model results for CO_2 and steam gasification syngas compositions versus temperature, mole %.

only deviate by 2 to 5% for the two cases, hydrogen and carbon dioxide appear to be switched, but still trend as expected. As with the previous EFG data, hydrogen decreases with increasing temperature and carbon dioxide increases. The large deviations in hydrogen and carbon dioxide could be associated with the difference in steam concentration as seen in Figure 76. Since steam is denser than hydrogen, smaller fluctuations of steam produced could influence hydrogen production and in turn, carbon dioxide yield. The next section compares the pilot-scale gasifier data, the ASPEN simulation and these model results.

5.2.3 Gasifier Data, Model, and ASPEN Simulation Comparison

The gasifier data presented in this section are only of the effluent syngas and not the data acquired from the extractive sampling system. All effluent syngas compositions are compared within this section to indicate the limitations or predictive behavior of each.

In an effort to correlate the model and simulation results to the EFG compositions, all results are presented on a dry basis as the gas-chromatograph gasifier results are on a dry basis. The dry mole percentages of carbon monoxide, hydrogen, and carbon dioxide are shown in Figure 77. The model and simulation results are shown to correlate the best and disagree with the EFG results. One key difference between the EFG data and the model and simulation results is that the EFG did not achieve 100% conversion as the computer-generated results indicate. This would account for the significant differences in the syngas compositions. While the EFG data deviate significantly from the predicted values, these values are closer to literature dry gas compositions. Higman and van der Burgt (*1*) summarize syngas compositions with 55% CO, 39% H_2, and 6% CO_2, which is reasonable when comparing the computer-generated results. Additionally, Williams (*103*)

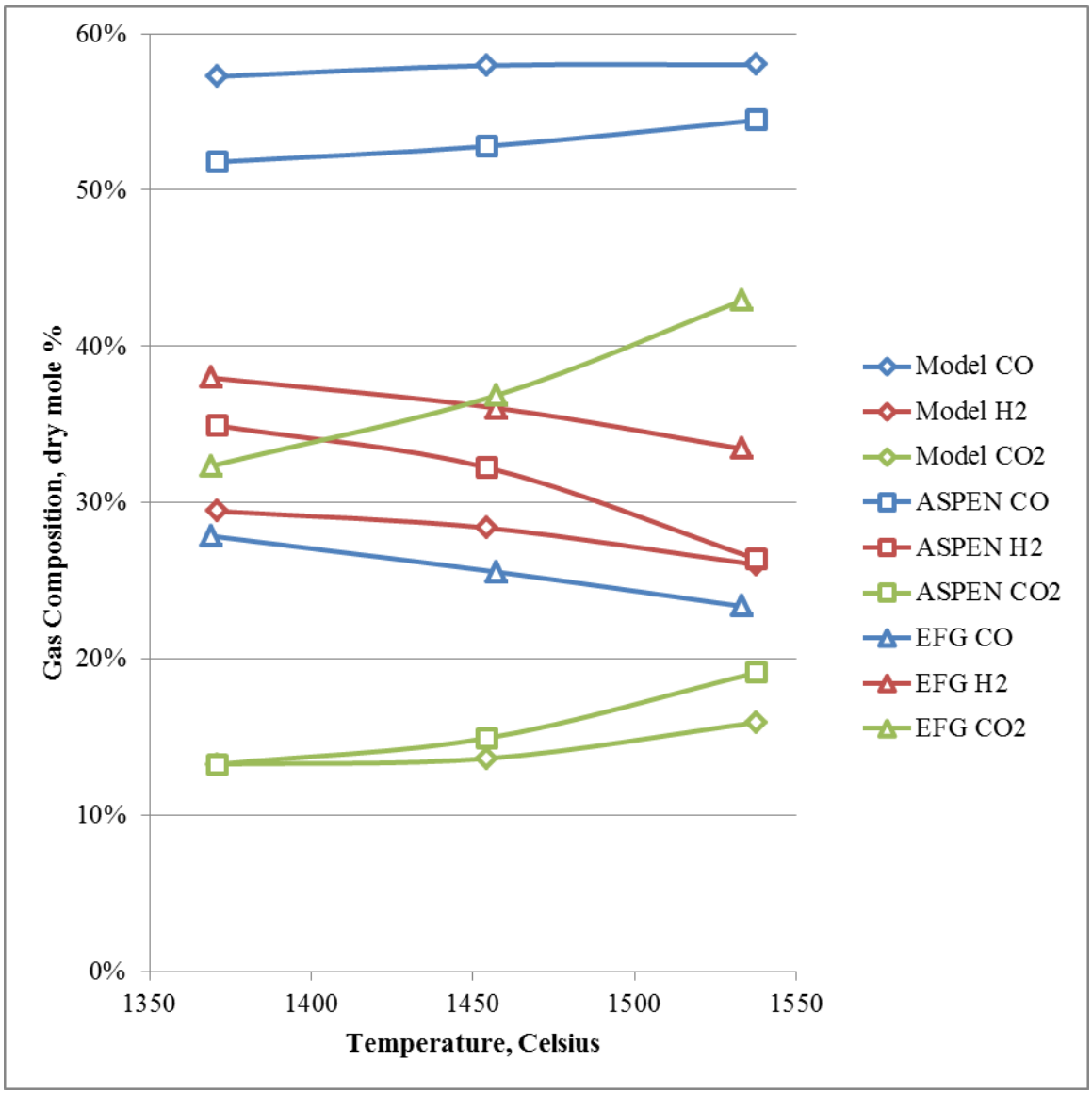

Figure 77: Model, ASPEN, and EFG dry gas-phase compositions versus temperature of product syngas.

describes typical syngas compositions of 49% CO, 34% H_2, and 10% CO_2 for industrial type gasifiers. With real gasifier values like these, the predictability of the model and the ASPEN simulation are reasonable, but due to the complexity and fewer assumptions, the simulation is likely more robust than the model. In addition, the model was only developed for bituminous coal.

Residence time is another indication of coal conversion assuming good atomization of the fuel and adequate heat and mass transfer into and out of the particles. The residence time of the EFG is not currently known, but the residence time of the ASPEN simulated gasifier and the developed model are shown in Table 20.

In Table 20, the residence time is constant for the ASPEN simulation when compared to the model results for carbon dioxide and steam gasification. An important distinction must be made between the simulation and model results, however, in that the simulation actually has residence time as an output, but the model calculates the time required for 100% carbon conversion. In this sense, the model results can be viewed as maximum allowable residence times to ensure complete gasification of a fuel. For the case of combined CO_2 and steam gasification, the only corresponding ASPEN simulation value that allows for compete conversion is the highest temperature at 1538 ℃. For the steam gasification case, all conversion times are less than the residence time calculated by ASPEN. Since steam gasification rates are much faster than CO_2 gasification rates, the practical residence time is most likely closer to the ASPEN results and the case of hydrogasification for complete conversion to occur in the EFG.

Table 20: Residence times for model and simulation at variable temperature.

Temperature (℃)	1371	1454	1538
ASPEN residence time (sec)	3.70	3.64	3.58
Model CO_2/steam time (sec)	5.51	3.83	2.70
Model hydrogasification time (sec)	2.01	1.82	1.67

5.3 One-Dimensional Model

5.3.1 Introduction

A one-dimensional (1-D) model has been developed using Microsoft Excel for entrained-flow gasification and uses the practical inputs that entrained-flow gasifier operation requires. These are oxygen flow [lbs/hr], slurry flow rate [gal/hr], slurry specific gravity [-], slurry solids content [%], pressure [psig], and temperature [°F]. This methodology of the model process is depicted in Figure 78. Here, the gasifier is assumed to operate as a plug-flow reactor of constant volumes, dV. Once the inputs have been specified, the model calculates the product syngas composition, coal conversion, and reaction zone residence time. These are also calculated as a function of zone length.

Figure 79 shows the flow diagram for inputs, processes, and what each node, or control volume, considers. The gasifier inlet node only considers the introduction of oxygen to the system and allows mixing of coal slurry in the first node. Devolatilization begins in the first node as well and the product gases are forced to equilibrium via the water-gas shift reaction (WGSE). Each subsequent nodes inputs are the outputs from the previous one. For nodes n_{i+1} to n_{g-1}, only devolatilization is considered. This is based on the assumption that a significant amount of volatiles is being evolved and heterogeneous char gasification reactions do not occur at an appreciable rate. Once devolatilization reaches a user-specified percentage (e.g. 80%), heterogeneous reactions begin, denoted in

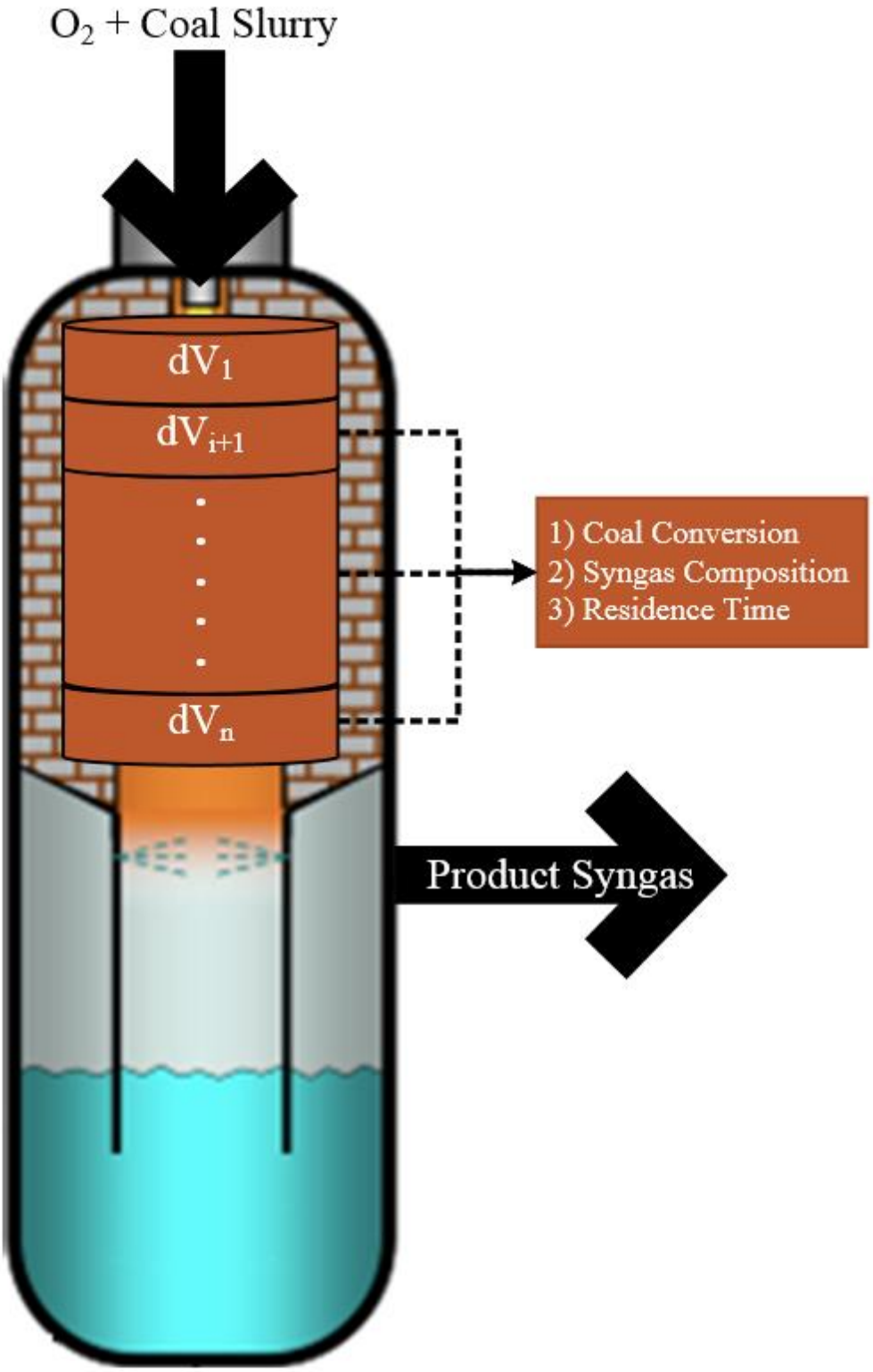

Figure 78: Gasifier representation of control volume method with overall inputs and outputs.

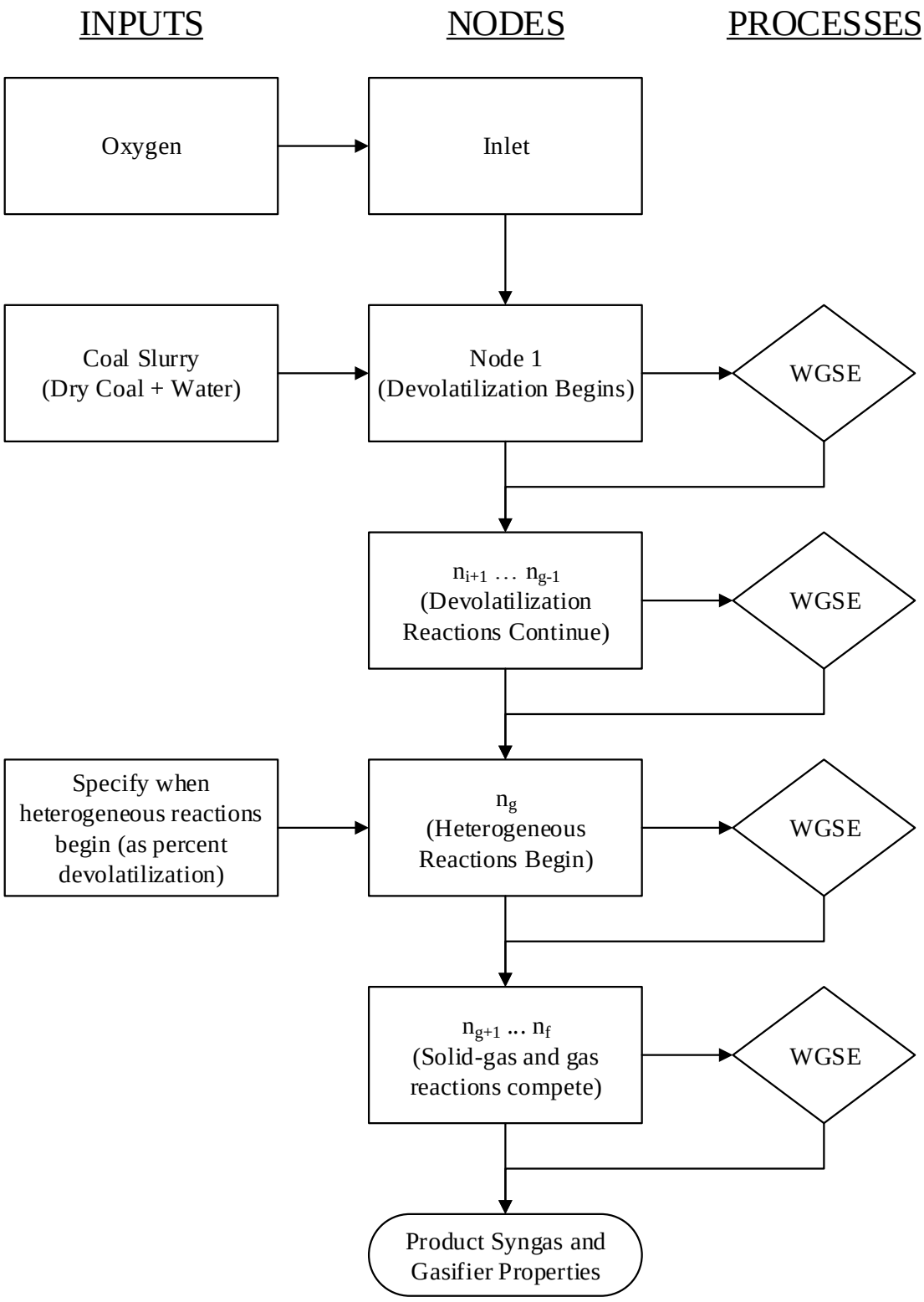

Figure 79: Model flow diagram for inputs, nodes, and processes.

node n_g. From this point forward, both char gasification and gas-phase reactions occur and add to the net generation of gases. Each node is forced to equilibrium via water-gas shift, including the final node, n_f, which produces the final syngas composition in terms of gas species O_2, H_2O, CO_2, CO, H_2, and CH_4. Each node is represented as a constant control volume that yields a syngas composition as well as residence time and coal conversion.

The key assumptions of the model are that the system is isothermal and isobaric and that drying, devolatilization, and char gasification occur in distinct stages with minor overlap of the three. Mass balances of carbon, hydrogen, and oxygen satisfy the conservation of mass, while coal-bound sulfur and nitrogen are neglected. A thermal treatment of the gasifier is not conducted in the current model and only mass conservation is required, not energy conservation. Ash is assumed inert and the current model does not consider any slag or ash properties. Individual process are listed below with pertinent assumptions that pertain to the process followed by a discussion of the results.

Other inputs that are model specific and not part of any practical consideration are at what devolatilization percentage char gasification begins, the reference gasification rate determined by thermogravimetric analysis, and the devolatilization coefficient, A, used for devolatilization rates as a function of residence time.

5.3.2 Drying

The current model does not include particle characteristic parameters that can show the influence of particle size and distribution. The slurry that is introduced to the model is assumed to behave like the slurry during operation of the entrained-flow gasifier. This means the particle size distribution of the particle-laden slurry is 70% minus 200 mesh (i.e. 70% of the particles pass through a 200 Tyler mesh screen, 74 micron). The moisture

content of the slurry is measured during EFG operation and the input to the model slurry solids percent is this value (e.g. 56.5%). No direct assumptions are made as to what the coal-water complex looks like, but all water is assumed to evaporate within the first node of the model based on radiative heat transfer to the particle. Using the lumped capacitance method of transient heat transfer, as with the previous time-dependent model, the heat transfer coefficient is modified to only consider radiation, as the high temperatures and higher heating rates will have more of an influence on drying than convection and conduction combined. This modified radiative heat transfer coefficient is Equation 24.

$$h_{rad} = \sigma\varepsilon\left(T_w^2 + T_p^2\right)\left(T_w + T_p\right) \quad \text{Equation 24}$$

Here, σ is the Stefan-Boltzmann constant, ε is the emissivity of the coal particle (assumed 0.95), T_w is the gasifier wall temperature, and T_p is the particle temperature. Additionally, since all water is assumed to evaporate in the first node, the slurry droplet size has no impact on drying because it is assumed that all water is on the surface of the particle. This also indicates that the specific heat of the particle is not taken into consideration and due to rapid heating of the particle, which is on the order of 10^5 to 10^6 ℃/s, the particle attains a uniform temperature instantaneously.

5.3.3 Devolatilization

The devolatilization coefficient, A, is determined by fitting Equation 25 to the wire-mesh reactor data, where t is time in seconds and VY is volatiles yield.

$$VY\ [\%] = 1 - e^{A \cdot t} \quad \text{Equation 25}$$

The value of the devolatilization coefficient, A, of Equation 25 is assumed to be a constant of 1.248 based on volatiles yields of wire-mesh reactor experiments. The wire-mesh volatiles yields (as percent of full devolatilization) were plotted as a function of residence time in the apparatus and exponential curves were produced to find the coefficient, A. Figure 80 shows these curves with exponential fit equations per experimental temperature and Figure 81 shows the coefficient value versus temperature. The "Average" point in Figure 81 is the average of the 1000 ℃ and 1200 ℃ values. The average was taken because both temperatures show full volatiles conversion at residence times above three seconds. The coefficient is assumed 1.248 for temperatures above 1000 ℃ and is shown to converge at higher temperatures. The devolatilization coefficient parameter is not extended to temperatures less than 1000 ℃ because these temperatures are not practical for entrained-flow gasification and could not be sustained within the gasifier.

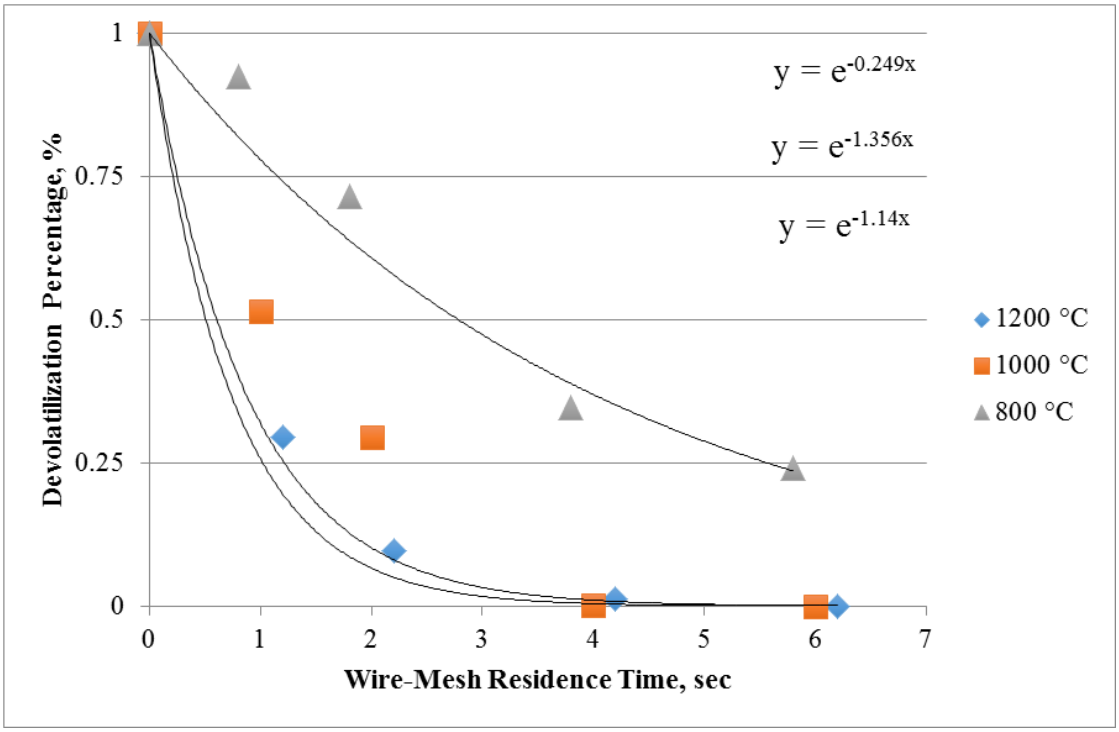

Figure 80: Devolatilization curves versus wire-mesh reactor residence time.

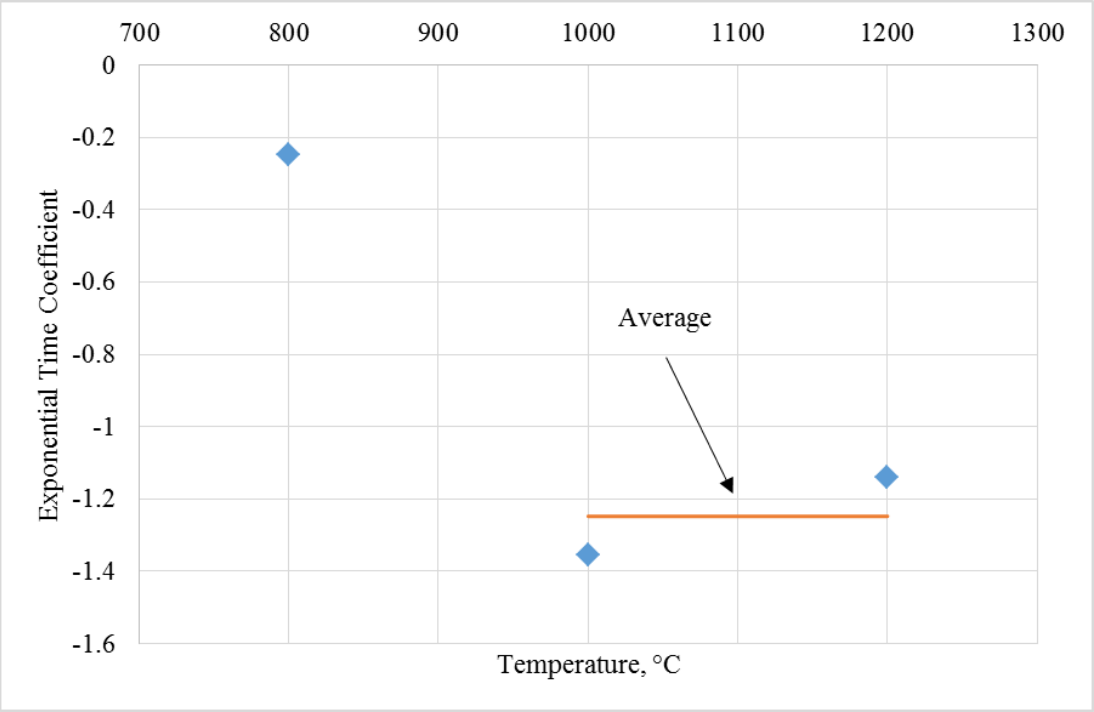

Figure 81: Exponential coefficient values versus temperature for wire-mesh reactor experiments.

As discussed in the previous section, it is assumed that the particles attain gasifier temperature instantaneously once the water has been evaporated from the particle and that the particles have a uniform temperature distribution. This was determined again by using the lumped capacitance method as in the additive reaction time model. The time to heat a warm, dry particle to a hot, almost devolatilizing particle is about 0.006 seconds, which is only 8% of the residence time of the first node when devolatilization begins. This time value is so low that it is assumed instantaneous for all subsequent calculations.

The mechanism for devolatilization is based on the measured gas quantities during devolatilization of Sufco coal from a United States Department of Energy final report in 1992 (*104*). The authors heated various coals and measured the quantities of hydrocarbons, H_2, CO, and CO_2 that evolved and at what temperatures the highest quantities were seen.

It is important to note that these devolatilization rates were determined form slow heating experiments and not rapid heating rates as seen in a gasifier. Using this data, relative rates of devolatilization were determined for atomic hydrogen, oxygen, and carbon, which would generate one of four gases, CO_2, H_2, CO, or CH_4. At the exit of each node, the water gas shift reaction would be forced to equilibrium to determine the intermediate gas compositions at that point. It is assumed that one fourth of the oxygen atoms released will create carbon dioxide and three fourths will create carbon monoxide. Equal atomic quantities of carbon are utilized for the generation of CO and CO_2 and the remainder generates CH_4. Four hydrogen atoms are then used for each carbon atom in methane and the remainder generate H_2. Volumetric flow rates of each gas are then determined form the molar flow rates calculated from this process.

The methane that is generated from the process described above does not undergo methane steam reforming, which will inflate the instantaneous and final values of the gas. Also, since methane is not a component of the water-gas shift reaction, its concentration does not appreciably along the gasifier length. The only point where the concentration of methane significantly changes is the point where it combusts with oxygen to produce carbon dioxide and water. Since these products are in the shift reaction, they are allowed to influence the equilibrium composition. Because methane is the only gas that combusts with oxygen, once the oxygen is utilized, methane production is essentially constant because by this time, devolatilization of the coal has reached upwards of 75%.

5.3.4 Char Gasification

In order to approximate the rate of char gasification, data were used from the thermogravimetric experiments. A TGA determined rate of $6.5 \cdot 10^{-4}$ mg/mg/s is used as a

reference rate for the char gasification. Assuming the reaction is first order, the Arrhenius expression for an adjustment of rate with temperature is utilized to determine the rate of char gasification at the higher gasifier temperature. Equation 26 shows the Arrhenius expression.

$$rate_{gas} = rate_{ref} e^{\frac{E_a}{R}\left(\frac{1}{T_{ref}} - \frac{1}{T_{gas}}\right)} \quad \text{Equation 26}$$

Here, the gasification rate is equal to the reference rate multiplied by the exponential term of the activation energy, E_a, divided by the universal gas constant, R, multiplied by the inverse temperature difference of reference temperature, T_{ref}, and the gasification temperature, T_{gas}. The modeled gasification rate is also multiplied by 1.33 to account for the reference rate being determined at 25% conversion in the TGA and is multiplied by seven to account for the relative rates of steam gasification and carbon dioxide gasification. It is assumed steam gasification occurs seven times faster than CO_2 gasification. Then by multiplying this expression by the coal, assumed to be only carbon, leaving the previous node, the rate of gasification within node, V_i, is determined. With char gasification added to the model, overall coal conversion that only considers carbon in the current model, is calculated by dividing the carbon in the gas phase to the carbon remaining in the particle/char.

5.3.5 Model Outputs

The current version of the model contains numerous intermediate calculations to achieve a final syngas composition, residence time, and coal conversion, but any of these intermediate calculations can be utilized as necessary. Volumetric flow rates of all gas

species are calculated at each node for devolatilization and char gasification as well as molar flow rates of atomic hydrogen, oxygen, and carbon for equilibrium calculations. Instantaneous rates of char gasification and devolatilization are also available at each node in addition to residence time. The Microsoft Excel user-interface allows many parameters to be calculated as a function of reactor length, residence time, or gasification rate at the behest of the user.

5.3.6 Model Results

The results for lower temperature modeling agree less with experimental values as seen in Figure 82, where CO_2, CO, and H_2 concentrations are plotted against temperature for the sample port location. The analysis of the model and experimental results for the extractive gas-phase sampling are continued in Figure 83 and Figure 84. Figure 83 shows the absolute difference of the model and sample (EFG) data points of Figure 82, while Figure 84 shows the ratio of the component concentrations seen in Figure 82. It is evident from both Figure 83 and Figure 84 that higher temperatures yield more accurate modeling results when compared to experimental values. From Figure 84, the model-to-experimental ratios of CO and CO2 are seen to switch, with CO2 being over predicted at 2650 °F and CO being slightly over predicted at 2800 °F.

The degree of devolatilization at lower temperatures has a significant influence on the intermediate syngas compositions as best seen in Figure 82. Here, the level of CO_2 is above 90 vol.% at 2500 °F and decreases to about 60% at 2650 °F. The lower temperature alters the gas composition because oxygen is still present in the system at an appreciable amount and higher temperatures allow rapid combustion in the beginning of the gasifier. From a practical standpoint, the flame can be thought as extending over a greater portion

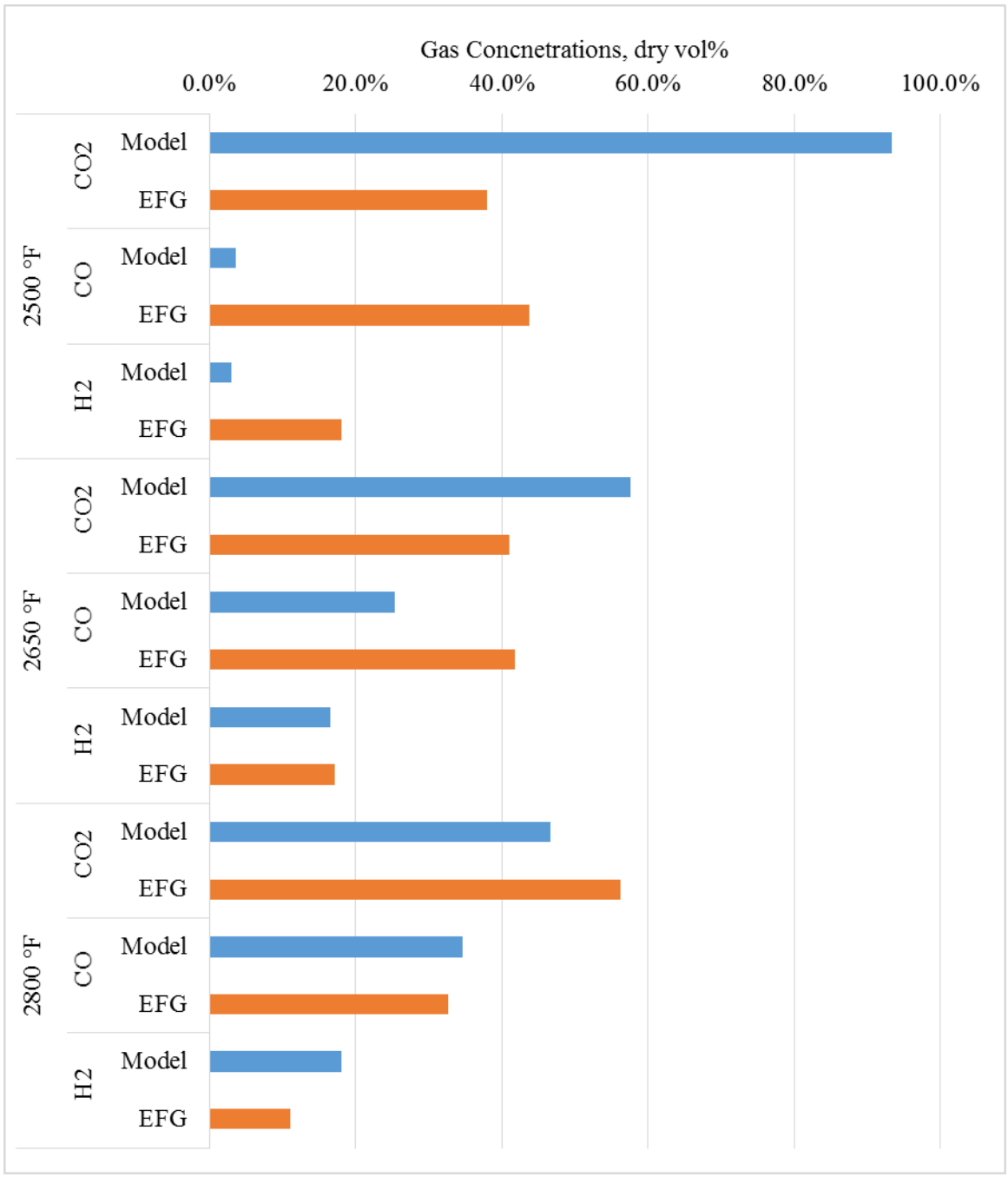

Figure 82: Model and experimental gas concentrations for varying temperature at sample port three location.

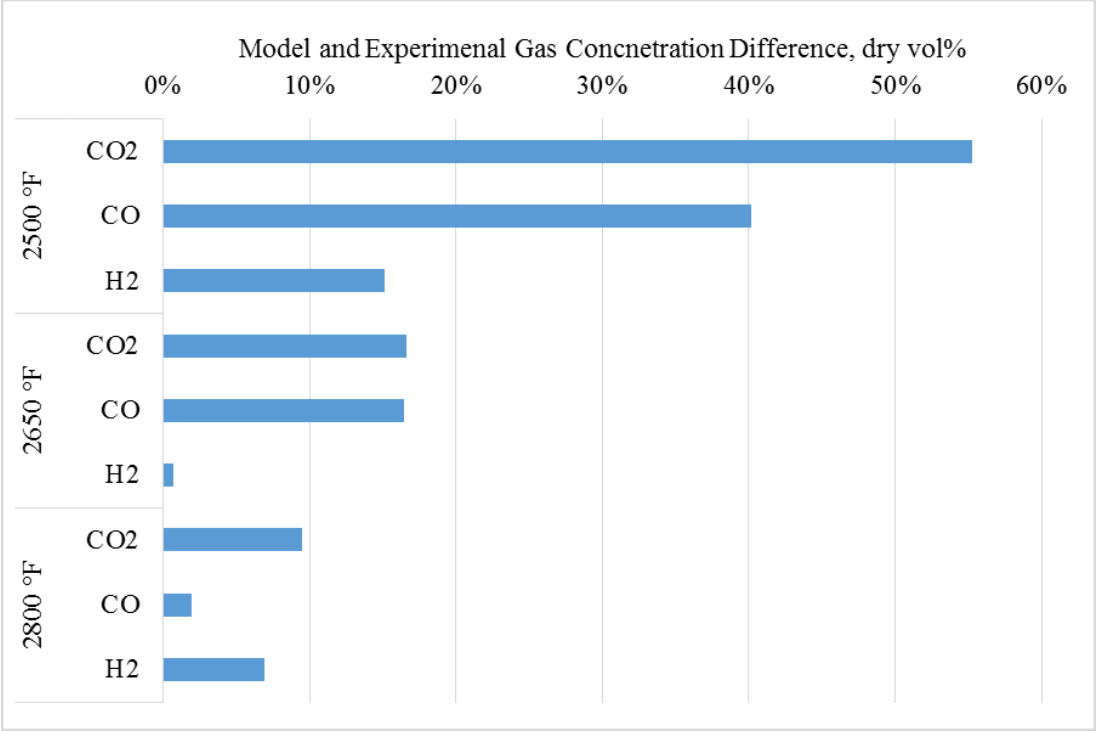

Figure 83: Difference between model and experimental concentrations for major gas species with varying temperature.

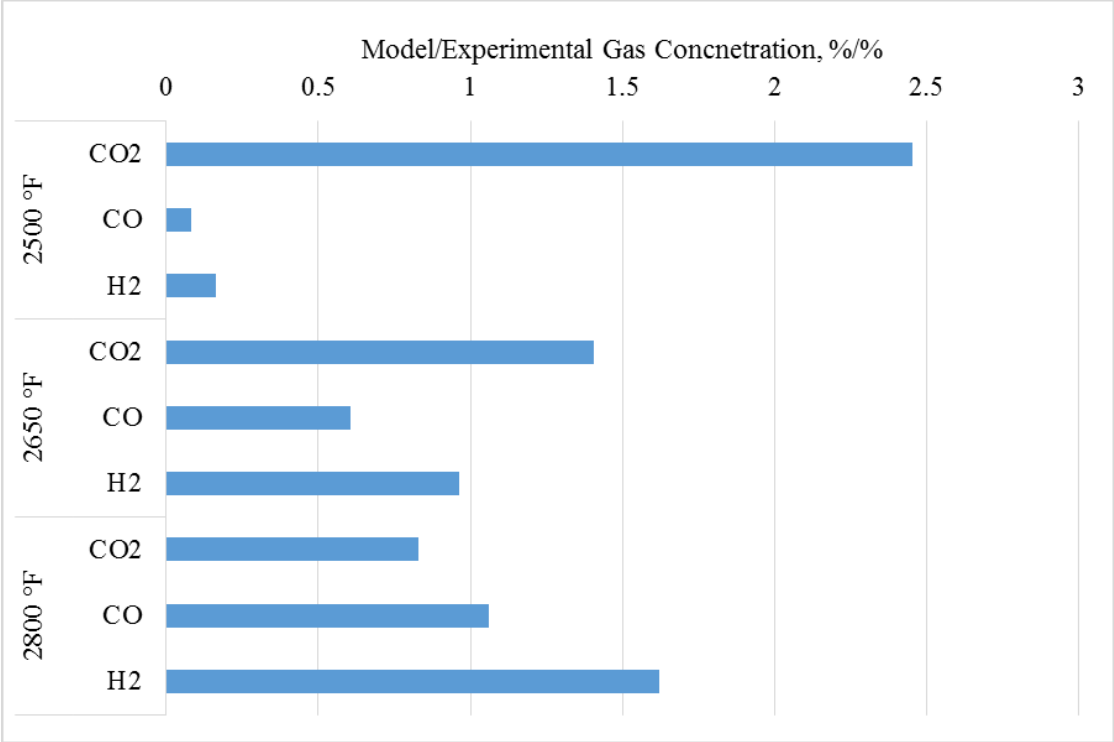

Figure 84: Ratio of model to experimental gas concentrations, dry [vol%/vol%].

of the gasifier at lower temperatures and causing intermediate syngas compositions to read artificially high. This is similar to a probe sampling within the flame as opposed to immediately after the flame or farther down the reaction zone.

Looking at the gas-phase and conversion profiles along reactor length, it is apparent that higher temperatures allow equilibrium to take place at a shorter distance and in less time, as is expected. This behavior is seen in Figure 85 for 2500 °F and Figure 86 for 2800 °F. These are on a dry basis in order to correlate the findings to the experimental extractive, gas-phase data of sample port three. The inputs of the model to produce Figure 85 and Figure 86 were the extractive sample operating conditions per target temperature. Comparing the conversions of Figure 85 and Figure 86, it is also apparent that higher

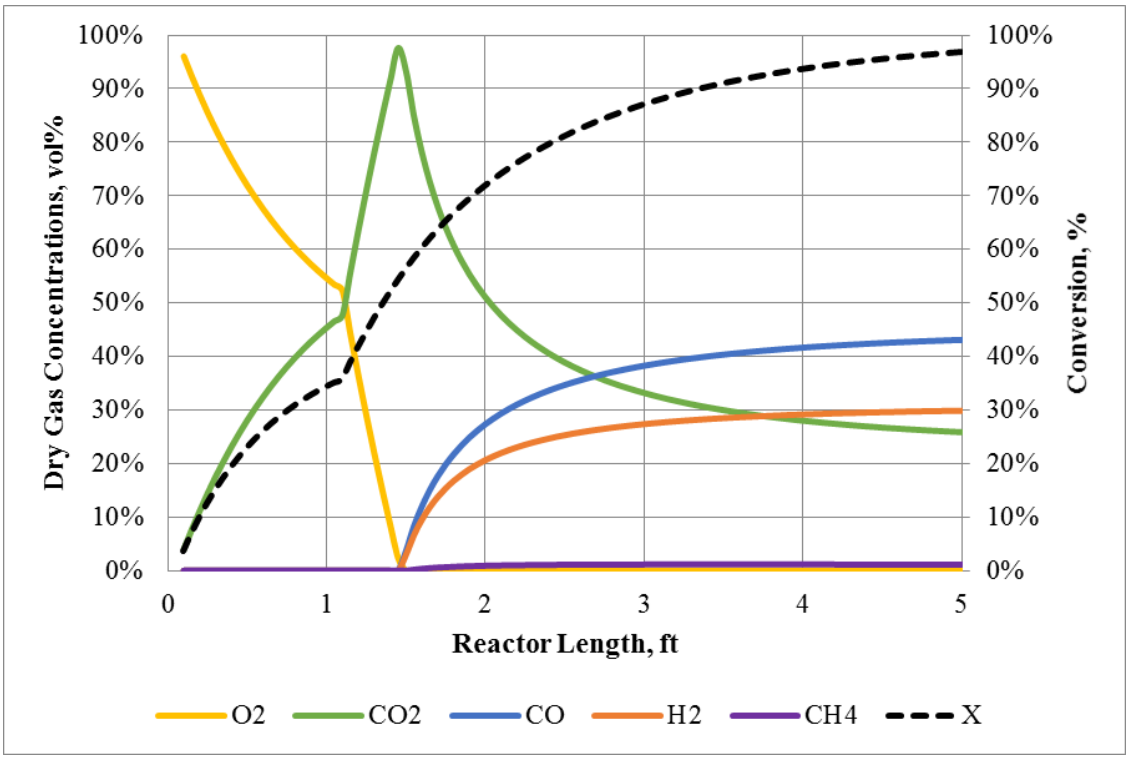

Figure 85: Gas species and conversion profiles for a gasifier temperature of 2500 °F.

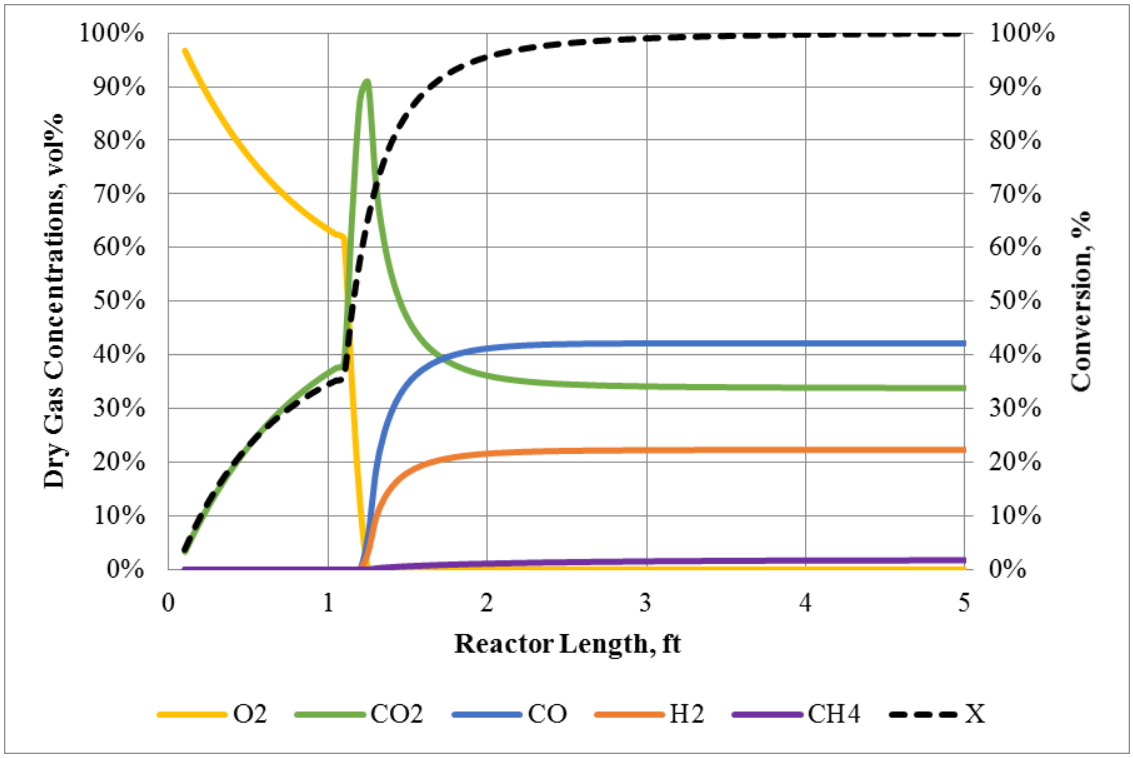

Figure 86: Gas species and conversion profiles for a gasifier temperature of 2800 °F.

temperatures yield higher conversions, as expected. The conditions at 2500 °F allow for 97% conversion, while those at 2800 °F allow for 100% conversion, indicating the required length for conversion is less than the reactor length. The results show that the model is suitable for gasifier syngas and conversion behavior at temperatures above 2600 °F. It should be noted that with a decrease in temperature, the accuracy of the model decreases.

The manner in which the EFG is operated is simple; a temperature and pressure are targeted by adjusting flow rates of oxygen and coal-water slurry. For example, if the target temperature is 2800 °F, the inlet flows are adjusted to maintain the temperature, or another way to say it is the O/C feed ratio is changed. On a mole-to-mole basis, this O/C ratio is similar to a traditional stoichiometric ratio in combustion systems. Keeping the oxygen flow consistent in order to maintain proper atomization exiting the slurry injector and to

sustain system pressure, the slurry flow rate is changed, thereby changing the O/C ratio. Figure 87 shows the effect of O/C ratio on syngas composition at 2800 °F. Higher O/C ratios are seen to favor CO_2 and H_2O production, while decreasing CO and H_2 because of the water-gas shift behavior that drives the reaction to the right.

The complicated part of explaining the physics behind Figure 87 is that the temperature is forced to be 2800 °F, but adjusting the O/C ratio changes the temperature by feeding more or less oxygen relative to coal-water slurry with one input held constant. For this reason, it is recommended that energy balances be added to the model in order to predict a temperature profile that is dependent on the oxygen and slurry feeds. Figure 87 does show that with an increasing pseudo-temperature (i.e. O/C ratio), the syngas components trend as expected with increasing carbon dioxide and steam, and decreasing

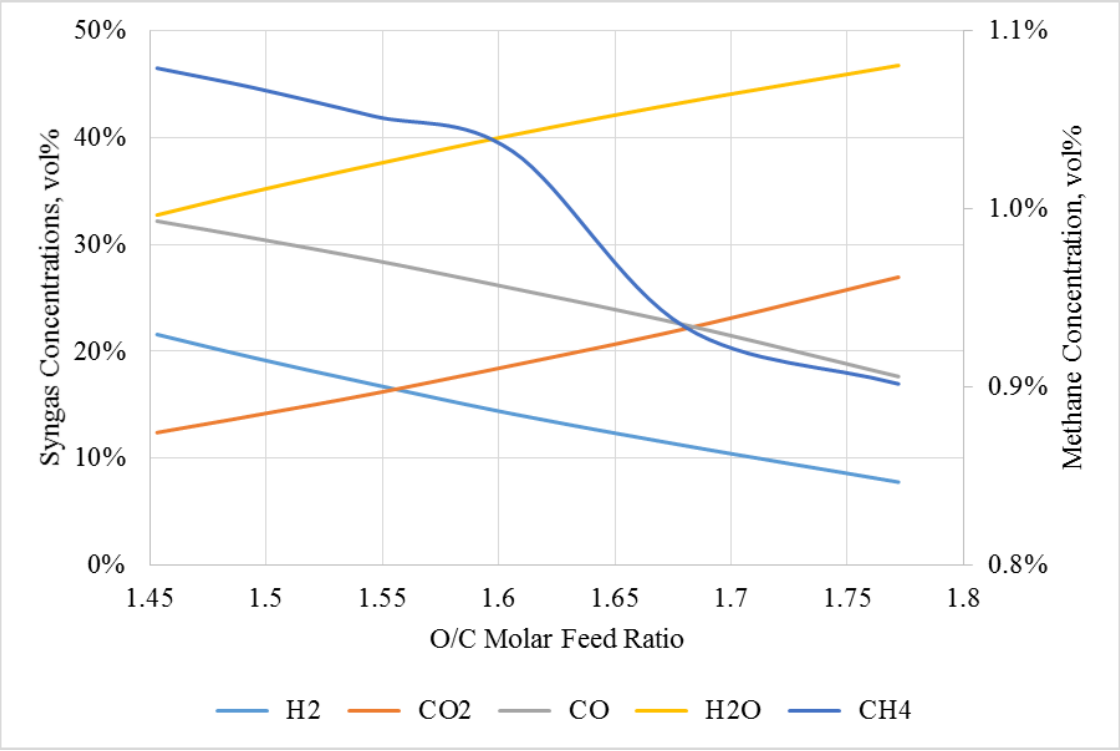

Figure 87: Product syngas composition versus O/C feed ratios for a constant temperature of 2800 °F.

carbon monoxide and hydrogen. Methane also trends as expected, decreasing with an increase of O/C ratio. This decrease is also seen in industrial gasifiers that are unable to have thermocouples near the reaction zone due to excessive erosion and heat. By monitoring the methane concentration in the syngas, a temperature can be extrapolated and the gasifier be optimized for the fuel being gasified.

Figure 88 shows the model extended to pulverized coal combustion with a specified temperature of 2800 °F and an O/C feed ratio of 2.269. Once the O/C ratio exceeds 2.0, the reactor firing regime switches from gasification to combustion. Here, with a higher value of O/C, the product gas composition has excess oxygen, and high steam and carbon dioxide concentrations with concentrations of zero for CO, H_2, and CH_4. This result shows how the model could be extended to combustion with corrected parameters for devolatilization and char gasification, now combustion, as the rates will change with the change in operating regime.

For practical purposes (e.g. when operating the EFG), the model is of highest utility when flow rates are known for slurry and oxygen. The shortcomings of a model arise when seemingly reasonable values on paper are attempted during operation. This could raise the temperature of the gasifier to nonsafe levels or lower the temperature profile along the gasifier length enough to cool slag and prevent the viscous material from falling into the quench. The short answer to why values cannot simply be placed in a model is that there are more factors in real systems than can be considered in a model. For this reason alone, it is advised that the 1-D model be used as a reference and prediction tool once the operator of the entrained-flow gasifier becomes familiar with the real system and aware of the shortcomings of the model.

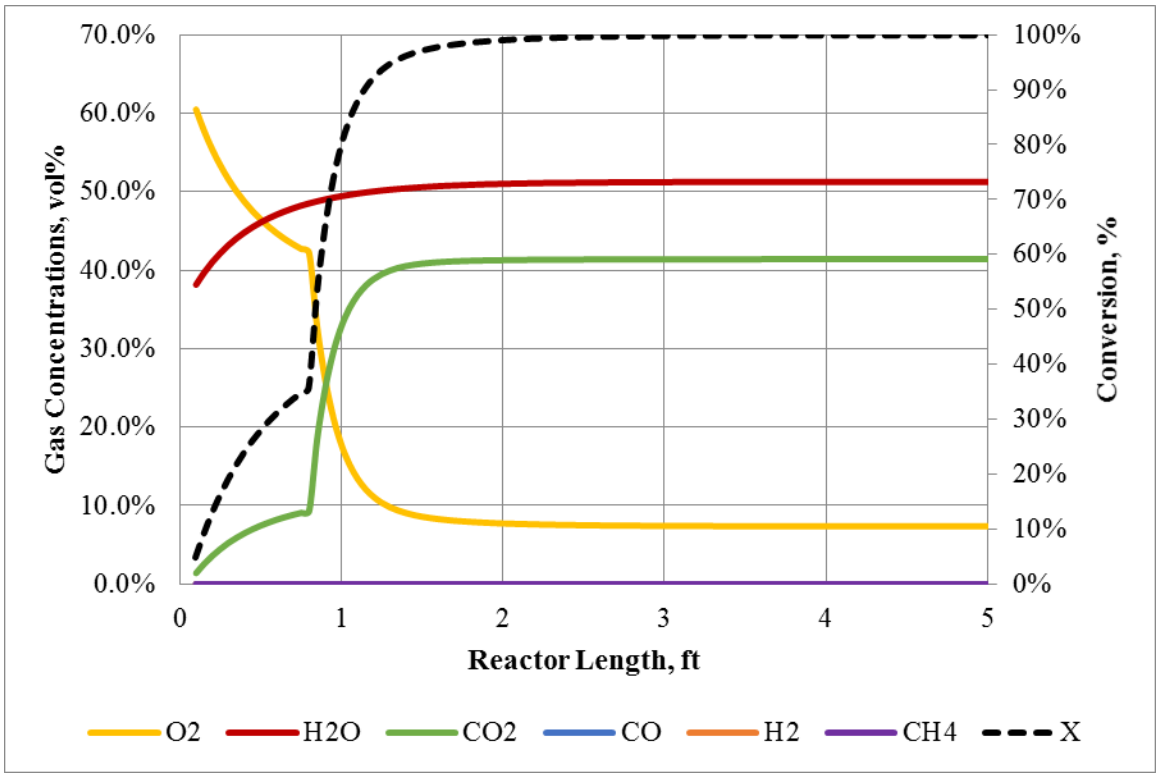

Figure 88: Syngas and coal conversion profiles over gasifier length for combustion case of O/C feed ratio 2.269.

CHAPTER 6

CONCLUSIONS AND RECOMMENDATIONS FOR FUTURE WORK

The application of bench-scale experimentation has been shown to correlate well with pilot-scale entrained-flow coal gasification studies through the use a developed model. This model predicts syngas compositions and residence times as well as conversion behavior as a function of reactor volume, while assuming plug-flow along a one-dimensional coordinate. The model was able to predict to within 20% of syngas concentrations from what was measured with the fabricated extractive gas-phase sampling system at temperatures above 2600 °F. The system successfully sampled gas compositions from a pilot-scale, entrained-flow gasifier at 150 psig and temperatures up to 2800 °F. The gas compositions were analyzed by gas chromatography and major trends in gas composition, temperature, and heating value were concluded. As temperature increases from 2500 °F to 2800 °F, carbon monoxide and hydrogen yields decrease as carbon dioxide increases. This results in a decline of CO/CO_2 molar ratio as temperature increases. No discernible changes were determined for gas-phase compositions from variable radial sample locations ranging from the wall to the centerline of the reaction zone. Comparing the reaction zone and product syngas compositions show that heating values decrease as temperature increases for all radial samples as well as the product syngas.

Additional laboratory-scale results shows that carbon monoxide inhibits char gasification and is exacerbated when coupled with high pressures. Gasification rates of the bituminous coal also proved higher at low pressures for equivalent carbon conversion at high pressure. Activation energy was calculated to be 228 $\pm$ 24 kJ/mol and regression analysis shows the gasification rates are logarithmically dependent on pressure.

Wire-mesh studies proved to be useful when modeling devolatilization. The new method of heating fuel packets to reduce time and expenses exhibited additional mass transfer resistances. This level of resistance was not seen in previous experiments. Results do agree with literature, however, in that higher temperatures and/or longer hold times allow for greater volatile yields. The greatest yields were seen at the highest temperature and longest holding time of the samples.

Utilizing an extensive Aspen Plus simulation, reaction kinetics and reactor dynamics can be determined. Altering the existing simulation for the purposes of the University of Utah's entrained-flow gasifier can offer predictions of syngas compositions, temperature distributions, and residence time. By comparison, the developed models, both the additive reaction time model and the 1-D model, can offer a discrete volume account of the processes taking place in the reaction zone of the gasifier. By simplifying the processes of gasification and making appropriate assumptions, a user-friendly Microsoft Excel-based model was developed.

Future work with wire-mesh studies should not include a fuel packet methodology and should contain a wider range of temperatures. These higher temperatures will require mesh materials with higher melting points to satisfy realistic gasifier environments. In addition to temperature, higher pressures should be tested, especially if modifications can

be made to the high-pressure thermogravimetric analyzer to make correlations. Since the vessel of the WMR has been pressure tested to 1000 psig, which is more realistic of industrial-scale values, this supplemental work would be a valuable asset. A sampling procedure of the wire-mesh apparatus with the addition of gas analysis for the evolved species is also recommended, perhaps using tedlar bags to acquire a batch sample. Concerning the pilot-scale gasifier, further work is required to link the gas-phase results to the char collected from the quench zone. An additional probe extension must be fabricated to continue sampling and extend the work described herein. It is recommended to add a dual seal to the flange assembly in the event that the first seal is breached by hot, pressurized syngas. With this modification and another sampling system attached to the gasifier, data that are more useful can be acquired for simulation validation of pressurized, entrained-flow gasification.

Future non-CFD modeling work will include adding energy balances to the 1-D model and perhaps including a value for back mixing of the flows, effectively creating a 1-D turbulent model. This back mixing is more evident of the flow types seen in entrained-flow gasifiers. The inclusion of energy balances will allow temperature to be variable along the reactor length and allow for more realistic flow patterns and temperature distributions. Concerning the devolatilization behavior of the 1-D model, it would be beneficial for future studies to include rapid heating of coal and measure the rates and quantities of the volatiles evolved. This would allow the model to represent the reactions and devolatilization within the gasifier to a higher level of accuracy. Overall, more data points from TGA and wire-mesh studies will broaden the capabilities of the 1-D model and allow for better prediction of future testing.

APPENDIX A

WIRE-MESH REACTOR CONTROL ALGORITHM

The following is an excerpt from an article in which the control algorithm and electronics were described in detail for the wire-mesh reactor. Reprinted with permission from David Ray Wagner and Kevin J. Whitty, Review of Scientific Instruments, 83, 115116 (2012).

III. Heater Temperature Control

The heating phase of an experiment in the wire-mesh apparatus may, for example, involve heating at 3000 K/s to 1273 K, thereby completing in about 330 milliseconds. Because devolatilization behavior is sensitive to heating rate, it is important to maintain a linear temperature profile during this phase. As the sample devolatilizes, it undergoes endothermic decomposition reactions that release gas that passes through the grid, so dynamically controlling the rising temperature of the grid can be challenging. AC-based systems, which operate line frequency (50-60 Hz), operate by "chopping" the sine wave during a given cycle. The theoretical maximum number of control cycles that can be achieved is thus 50 to 60 per second. For an experiment with a temperature rise of 1000 K at 3000 K/s this offers just 17-20 feedback cycles with roughly 55 degrees of temperature rise between cycles. This makes accurate control of this dynamic system, particularly PI or PID control, very challenging. The system described here overcomes that by using DC

power and a very fast solid state relay (SSR, rated to 2000 Hz), combined with a National Instruments LabVIEW-controlled pulse-width modulation (PWM) scheme, for power control. For the experiment described above, the SSR-based system at 2000 Hz would offer approximately 670 temperature control cycles. With direct current a consistent signal can be delivered with grid temperatures being taken before the circuit is switched to the "on" position. The temperature of the grid is measured during the "off" position in order to remove any interference from other electronic signals. This is superior to AC-based systems, which attempt to measure temperature when the power voltage sine wave equals 0 volts, and which in some cases must average two temperature measurements to compensate for noise associated with a phase-angle shift [1]. Even if there is residual electronic noise on the grid, the National Instruments thermocouple module (SCC-TC02) is protected against voltage interference up to 14 volts. Also, by using direct current the presence of wave-chopping or segmentation required by AC-based systems is removed. The overall result is a smoother, more consistent, and more tightly controlled heating profile that is independent of system pressure, gas atmosphere or, fuel characteristics.

The PWM frequency is calculated within LabVIEW by dividing the counter frequency (or loop rate of the LabVIEW data acquisition chip, which operates at a higher frequency than the SSR) by a constant simply called the divider, which sets the sampling frequency. The divider allows the two major loops of the LabVIEW programming to synchronize the temperature measurement and duty cycle, or power being supplied to the grid. The PID settings are calculated for each iteration and sent to the digital output loop via the duty cycle. Figure 89 demonstrates the use of PWM frequencies and duty cycle

[1] Gibbins, J. R., R. A. V. King, R. J. Wood, and R. Kandiyoti. Review of Scientific Instruments 60, no. 6 (1989): 1129-39.

with power delivered. The LabVIEW programming is best represented by Figure 90, a flowchart of all major programming decisions and processes.

After beginning the program, the temperature is read and a setpoint is calculated based on the value of the reading. The required power output is also calculated and applied via PI or PID settings, in conjunction with desired pulse-width modulation settings. Upon completion of this loop, the temperature is read and based on the operator's criteria, will continue heating, soaking at the final temperature, or end the program. If the temperature is at the calculated setpoint, the final temperature, and has soaked for the desired hold time, the program will end and power is cut to the system.

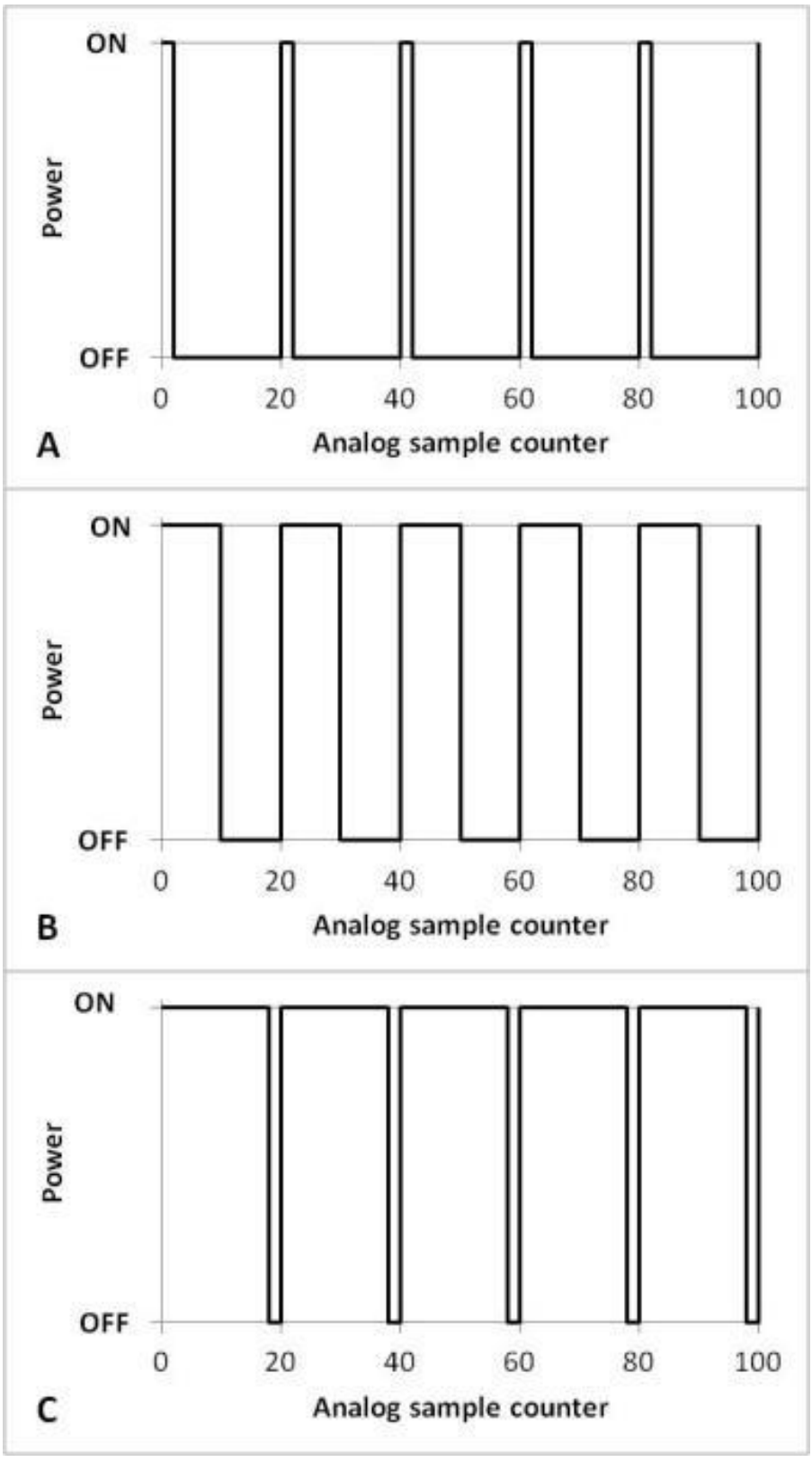

Figure 89: Simulated power versus PWM sample frequency for (A) 10% duty cycle (B) 50% and (C) 90%.

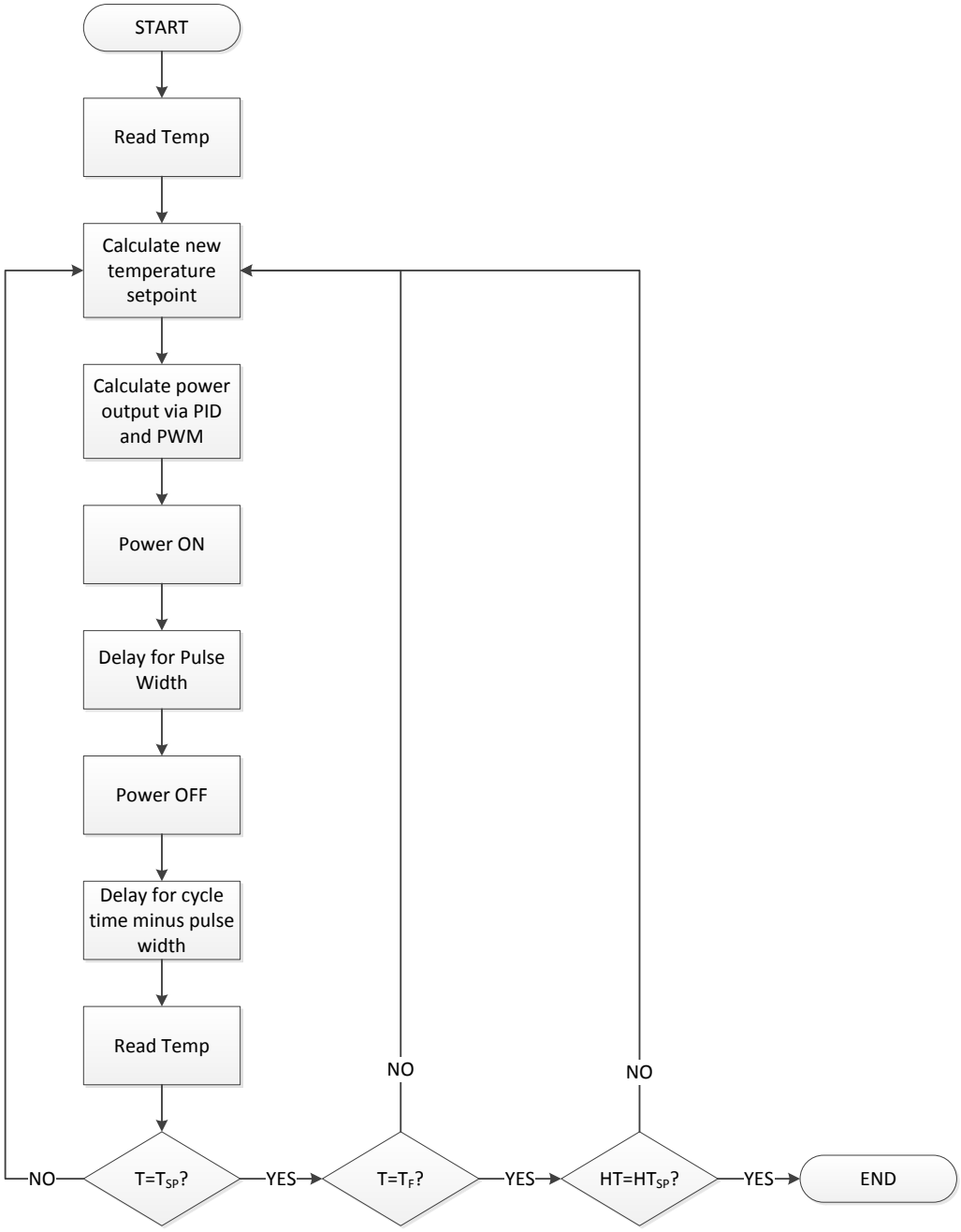

Figure 90: LabVIEW programming flowchart. Subscripts "SP" and "F" denote setpoint and final values, respectively. HT denotes hold time.

APPENDIX B

TEMPERATURE VALIDATION FOR WIRE-MESH REACTOR

To validate the heating rate specified by LabVIEW, two lacquers were purchased from Omega Engineering that change color at specified temperatures, model OMEGALAQ (*88*). The two lacquers purchased were for 427 ℃ (800 ℉) and 816 ℃ (1500 ℉). Figure 91 shows the lacquer directly applied to the mesh prior to heating and Figure 92 shows the mesh after it has been heated to 450 ℃. This validation was performed at the relatively low temperature of 450 ℃ and at the higher temperature of ~800 ℃ to show the path to be linear and not dependent on the PID values and upper limit specified within LabVIEW.

Figure 91: OMEGALAQ-1500 temperature indicating lacquer before heat application.

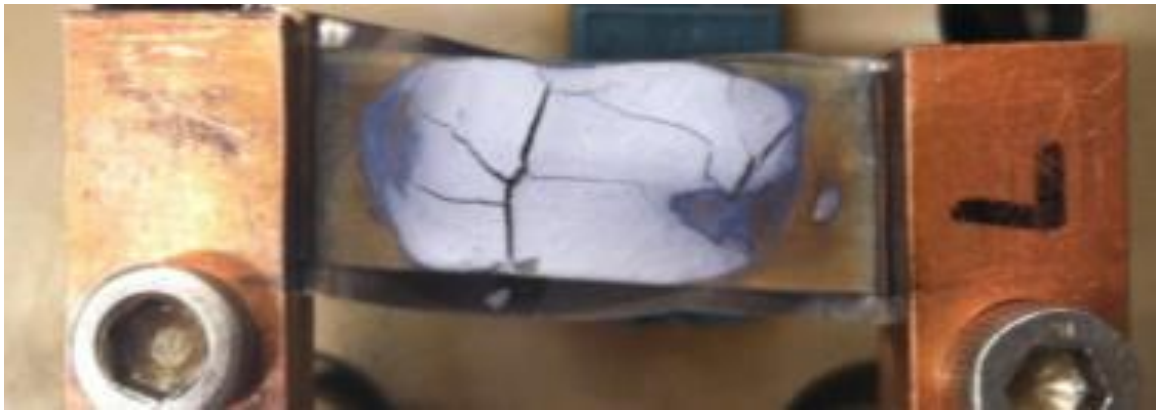

Figure 92: OMEGALAQ-1500 temperature indicating lacquer after heat application.

APPENDIX C

ADDITIONAL TGA RATE EXPRESSIONS

C.1 Differential Method

P.J. Haines outlines this method in Principles of Thermal Analysis and Calorimetry (*105*). The differential method tends to amplify any noisy signal and make kinetic parameters difficult to calculate. For this reason and since the HPTGA creates a noisy mass signal, the recorded mass is fit to a fifth-order polynomial. This makes the data much easier to manipulate, but also assumes the data perfectly fit the polynomial function. The coefficient of determination validates this assumption, commonly referred to as the "R^2-value". Figure 93 shows the polynomial fit of the HPTGA data for the same test as Figure 18 at 900 degrees Celsius and 18 bar.

This polynomial fit is necessary based on the acquired datasets and is not used by Haines. The polynomial fit is substituted into the kinetic expressions of Haines and recalculated as α - the fraction reacted. Haines diagrams the differential method by plotting the original data of fraction reacted (α) versus time and then differentiating this function. The derivative is plotted versus a given function $f(\alpha)$, satisfying the differential equation, Equation 27.

$$\frac{d\alpha}{dt} = kf(\alpha) \qquad \text{Equation 27}$$

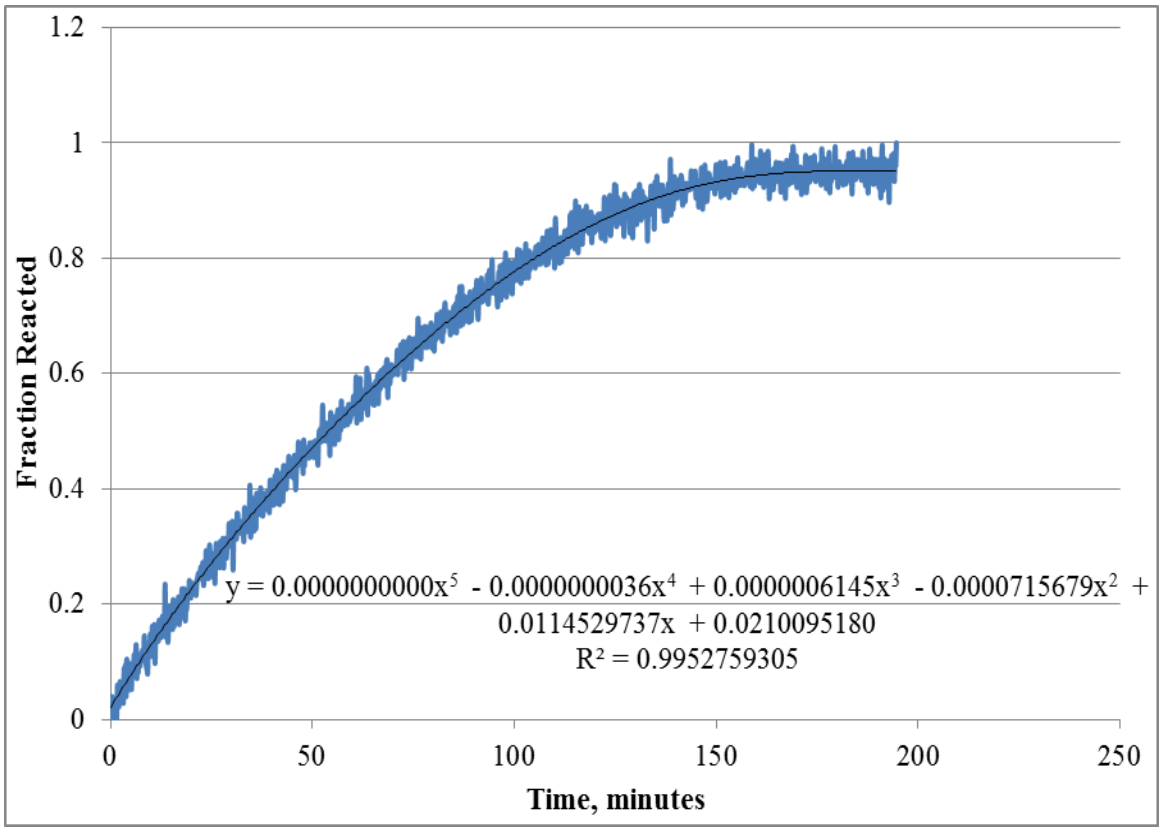

Figure 93: Polynomial fit of the HPTGA mass signal for Sufco coal at 900 degrees Celsius and 18 bar.

A table in the text lists possible expressions for $f(\alpha)$. These functions vary from diffusion-controlled reactions, sigmoidal α-time curves, orders of reaction, geometric models, and power laws; there are 17 equations in total in both differential and integral form. Preliminary data analysis led to plotting and comparing these expressions against each other for linearity. Table 21 summarizes the four equations that have the best linear fit equations for the rate constant, k. When plotting $d\alpha/dt$ versus a given function and fitting a linear trend line, the slope will yield the value of k in the Arrhenius equation, Equation 35.

Table 21: Equations used for solid-state reactions from Haines (*105*).

Eq.	Integral Form, $g(\alpha)$	Differential Form, $f(\alpha)$	Name
Equation 28	$kt = -ln(1-\alpha)$	$\frac{d\alpha}{dt} = k(1-\alpha)$	First Order
Equation 29	$kt = 2\left[1-(1-\alpha)^{1/2}\right]$	$\frac{d\alpha}{dt} = k(1-\alpha)^{1/2}$	Interface (contracting area)
Equation 30	$kt = 3\left[1-(1-\alpha)^{1/3}\right]$	$\frac{d\alpha}{dt} = k(1-\alpha)^{2/3}$	Interface (contracting volume)
Equation 31	$kt = \frac{3}{2}\left[1-(1-\alpha)^{2/3}\right]$	$\frac{d\alpha}{dt} = k(1-\alpha)^{1/3}$	Interface

$$k = A \cdot exp\left(\frac{-E_a}{RT}\right) \qquad \text{Equation 32}$$

C.2 Integral Method

The integral method follows the same rational as the differential method including the fifth-order polynomial fit to smooth data. Integration of the differential equation, Equation 27, takes the form $g(\alpha)$.

$$\frac{d\alpha}{dt} = kf(\alpha) \qquad \text{Equation 33}$$

$$\int \frac{d\alpha}{f(\alpha)} = \int k dt \qquad \text{Equation 34}$$

$$g(\alpha) = kt \qquad \text{Equation 35}$$

Here, $g(\alpha)$ is a modified alpha function represented in Table 21. The fifth-order polynomial is substituted into the kinetic expressions of Haines and recalculated as α - the

fraction reacted. Figure 94 shows the integral expressions of Table 21 for Sufco coal at 900 degrees Celsius and 18 bar, the same run as in Figure 18 and Figure 93.

As in the differential method, the slope of the linear fit corresponds to the rate constant, k. Although preliminary data show a good fit of the integral and differential methods, subsequent data analysis will not utilize the methods because the rates lack goodness of fit when compared to other established methods. In addition, the calculated activation energies are ~180 and ~240 kJ/mol for the differential and integral methods, respectively. This difference exhibits the range of anticipated rates and variable rate expressions.

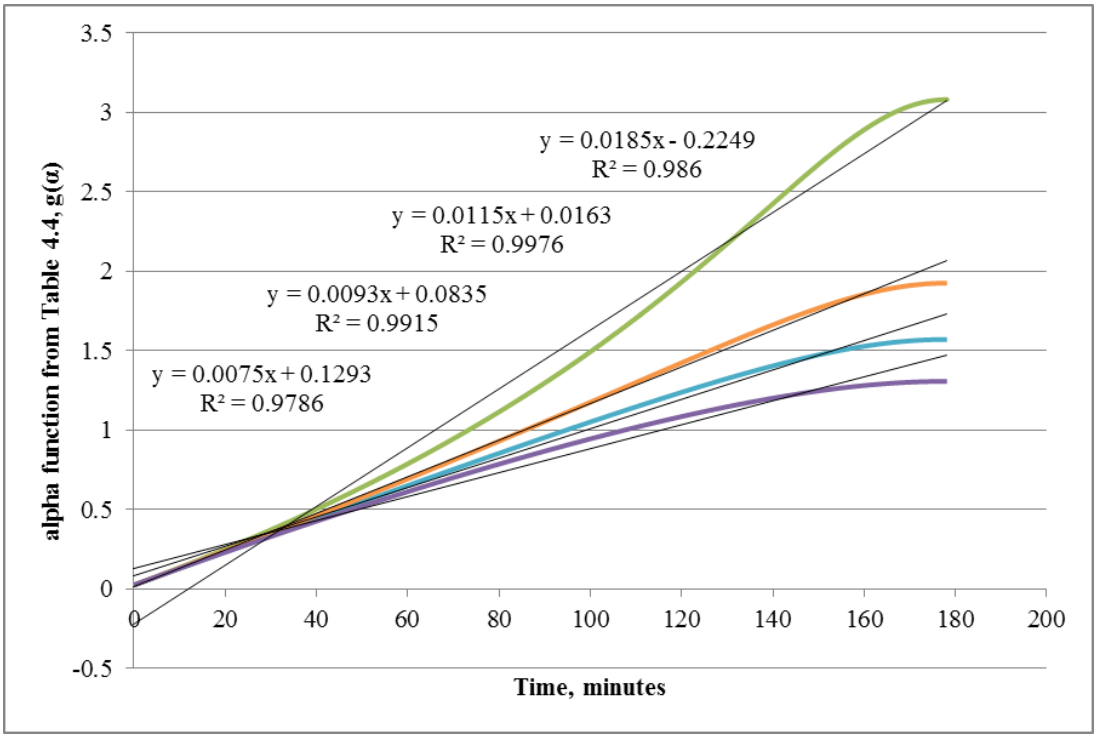

Figure 94: Alpha function, g(α), versus time for equations from Table 4.4 for 900 Celsius and 18 bar. The equations from Table 21 correspond to the following colors: Equation 28 (green), Equation 29 (orange), Equation 30 (blue), and Equation 31 (purple).

APPENDIX D

SAMPLING SYSTEM FLANGE ASSEMBLY

Figure 95 and Figure 96 detail the cold-face and hot-face seal housing troughs, respectively. Also shown in Figure 95 are the holes for cooling water supply and return. The cooling trough was machined as a long crescent shape in order to promote continual flow, leaving a small divider between the return and supply holes. These holes are ¼-inch in diameter and have socket-weld ¼-inch Swagelok fittings on the reverse side for cooling water line attachment. Figure 97 contains a detailed schematic of the hot-face seal housing with dimensions.

O-rings are seated on the outside and inside of the cooling water trough to prevent leaking. They are made of silicon and are 1/16-inch in width. The inner and outer O-ring sizes are 026 and 034, respectively. The pressure seal is manufactured by American High Pressure Seals and made of Teflon. It has a U-shape with a spring energizer that allows the seal to flex and press against the rod, providing a seal up to 5000 psi. The Teflon is rated to 500 °F and is cooled on the outside and inside by the cooling trough and probe extension, respectively, to maintain a low and operationally safe temperature. Figure 98 shows a drawing of the pressure seal and housing requirements as per the manufacturer.

Attached to the opposite face of the cold-face cooling flange is a small assembly called the stabilizer. As the name suggests, this keeps the probe extension stable as it

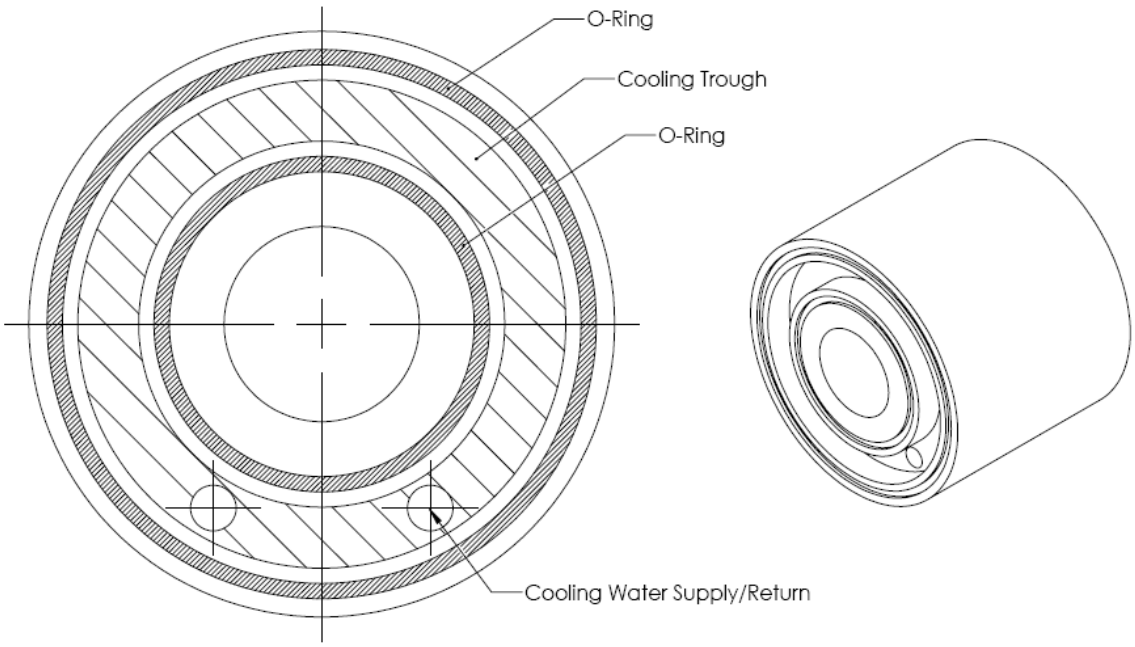

Figure 95: Schematic of cold-face pressure seal housing trough (left) and isometric view (right).

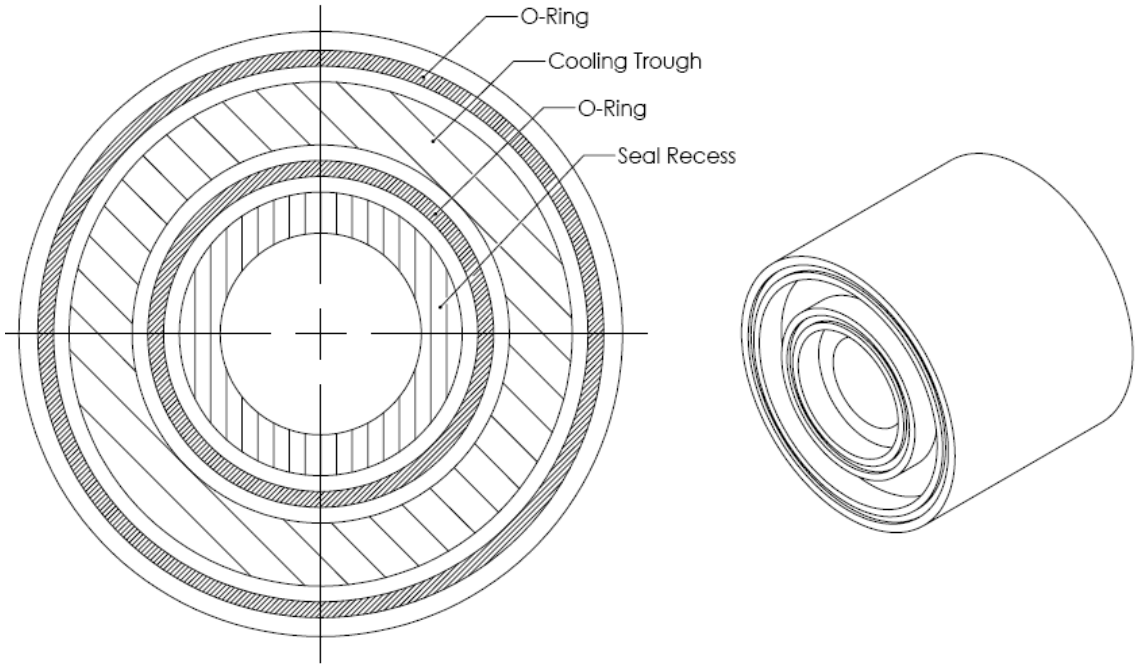

Figure 96: Schematic of hot-face pressure seal housing trough (left) and isometric view (right).

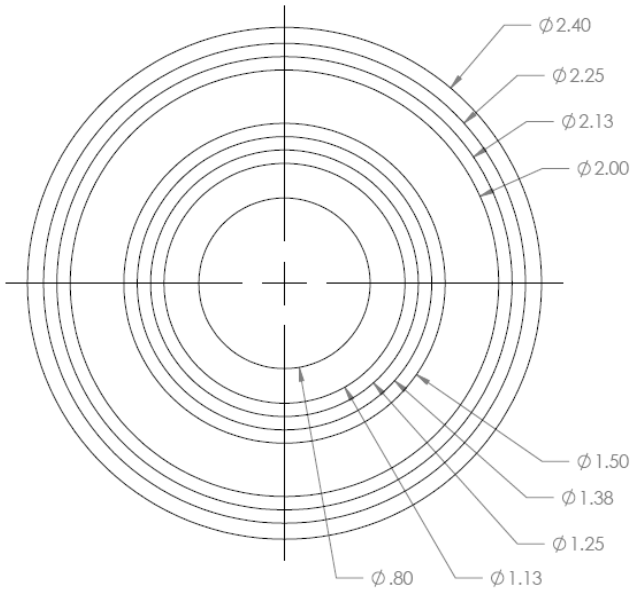

Figure 97: Detailed schematic of the hot-face seal housing. All dimensions are in inches.

travels farther into the gasifier. The body is constructed of a 5 inch piece of 2 inch SCH 160 stainless steel pipe welded to a 2 inch 300-pound slip on flange. On the back of the pipe are four threaded holes for precise placement of the extension. Figure 99 and Figure 100 show a back view and side view of the stabilizer, respectively.

The larger schedule of pipe allows thicker bolts to hold the stabilizer plates on the back of the assembly via size #10-32 bolts. A section on the front of the stabilizer pipe was removed in order to accommodate the cooling lines to and from the seal housing. The probe stabilizer offers greater support for the probe extension because the stabilizer plates are 7 inches behind the seal housing, making the assembly more rigid. The stabilizer plate is 3/16" thick stainless steel plate. Figure 101 shows a single plate in more detail; all units are in inches. A single stabilizer plate is fixed under the probe extension and another sits atop to prevent the extension from moving an excessive amount. The tolerance of the

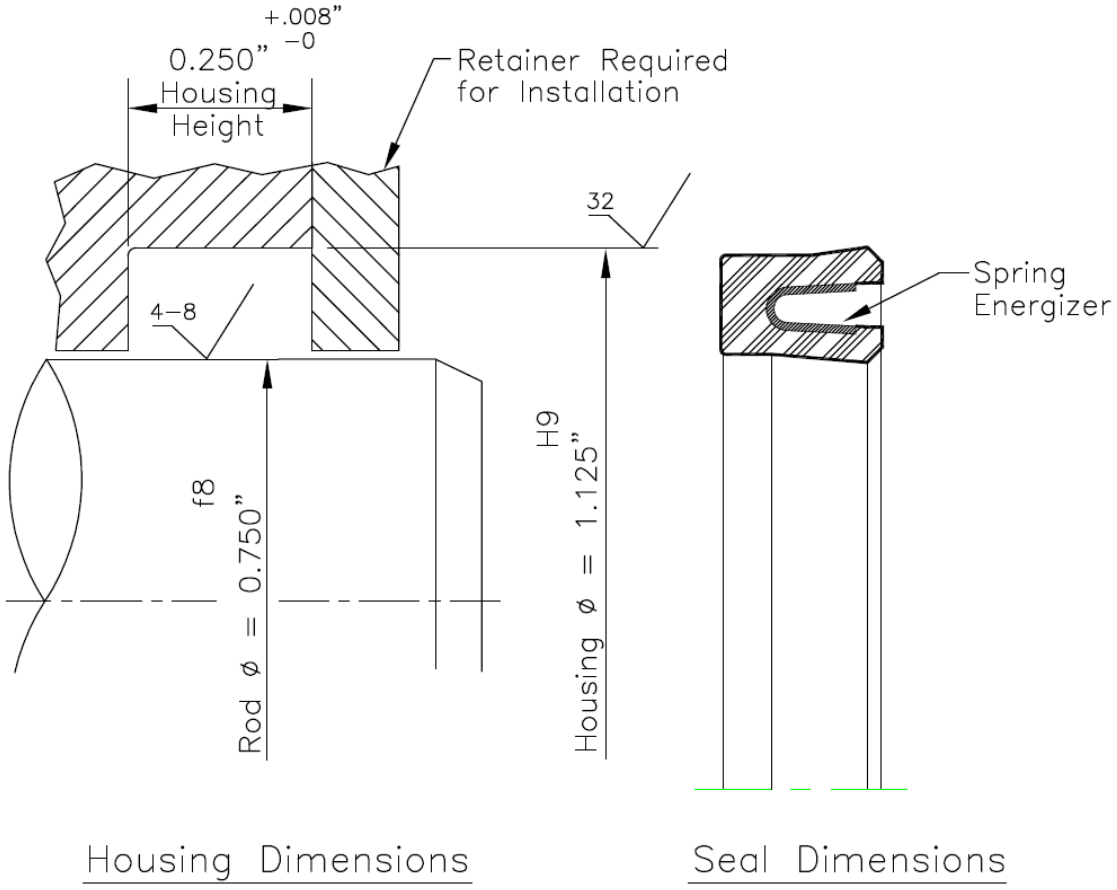

Figure 98: Manufacturer drawing of the seal and required housing specification (*106*).

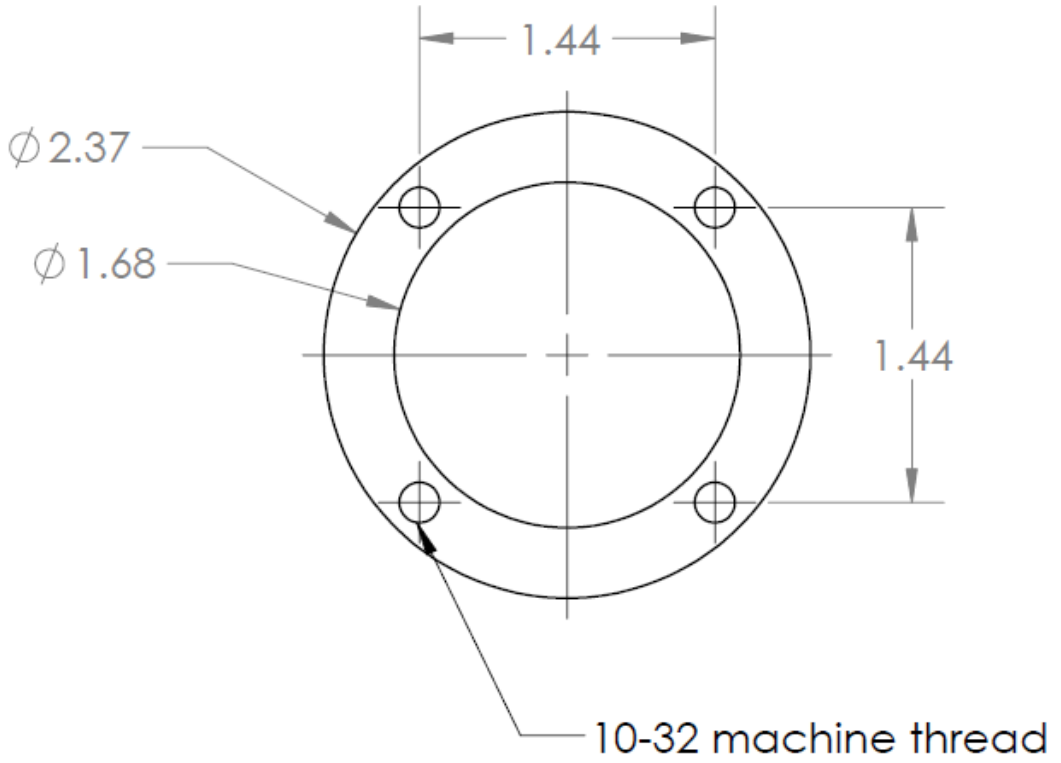

Figure 99: Back view of the probe stabilizer. All dimensions are in inches.

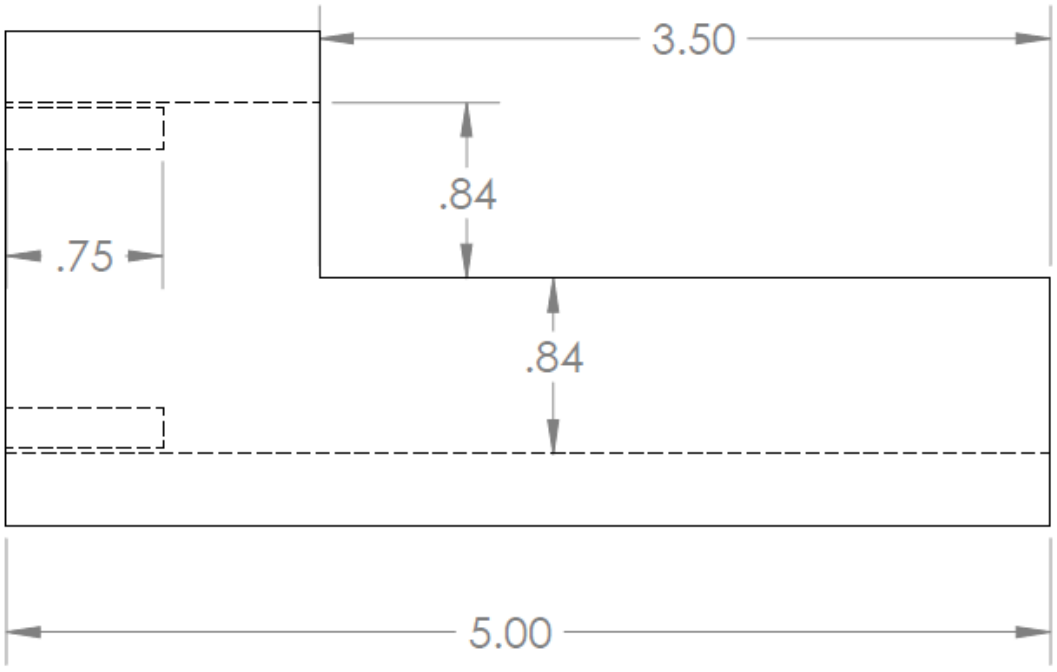

Figure 100: Side view of the probe stabilizer. All dimensions are in inches.

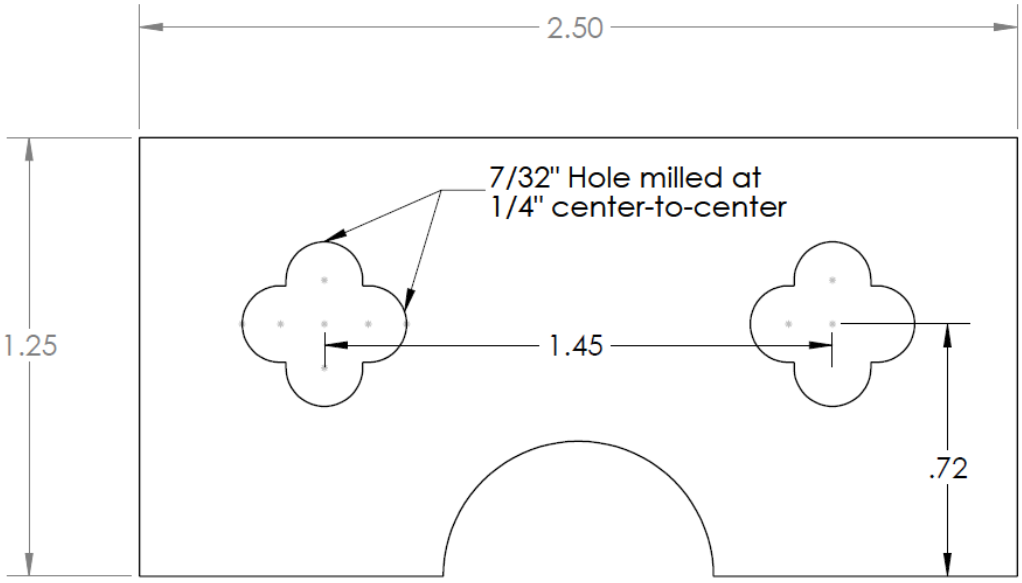

Figure 101: Stabilizer plate half.

hole made by the plates is only 1/100 of an inch. The four-point pattern milled out on either side of the plate allows for the probe to be centered about the seal housing every time the whole assembly is placed on the gasifier and to prevent leaks from around the probe extension in the housing itself.

APPENDIX E

SAMPLING SYSTEM PNEUMATICS

Figure 102 displays a schematic of the PFC and PCS with necessary pneumatic and electronic connections.

The PCS, labeled ‘control system’ in Figure 102, has three inputs, the control main, which is the OPTO 22 control system, the PFC cable, which interfaces with the PFC for feedback control via the control main, and a 24 VDC power supply. This power supply is dedicated and produces low current to reduce interference from other equipment.

The PFC attaches to the gasifier via a ball joint and rod extension mount welded to the probe extension. The ball joint is threaded into this mount and custom threads join the rod extension of the PFC on the opposing send of the joint. Figure 103 displays a CAD drawing of the ball joint.

This ball joint allows the mounting of the PFC to be within a certain tolerance when aligning the probe system. It keeps the probe from becoming rigid and decreases the likelihood of a complete pressure seal failure. In addition to this supporting piece of the probe assembly is a bracket that allows for rigid attachment of the flange assembly and the PFC. The brace itself is made of ¼-inch thick, 304 stainless steel. The plate supports the front of the cylinder by using the large nose-end threads and aluminum nut. All-thread is attached to the back end of the flange assembly bolts using all-thread couplings and run to

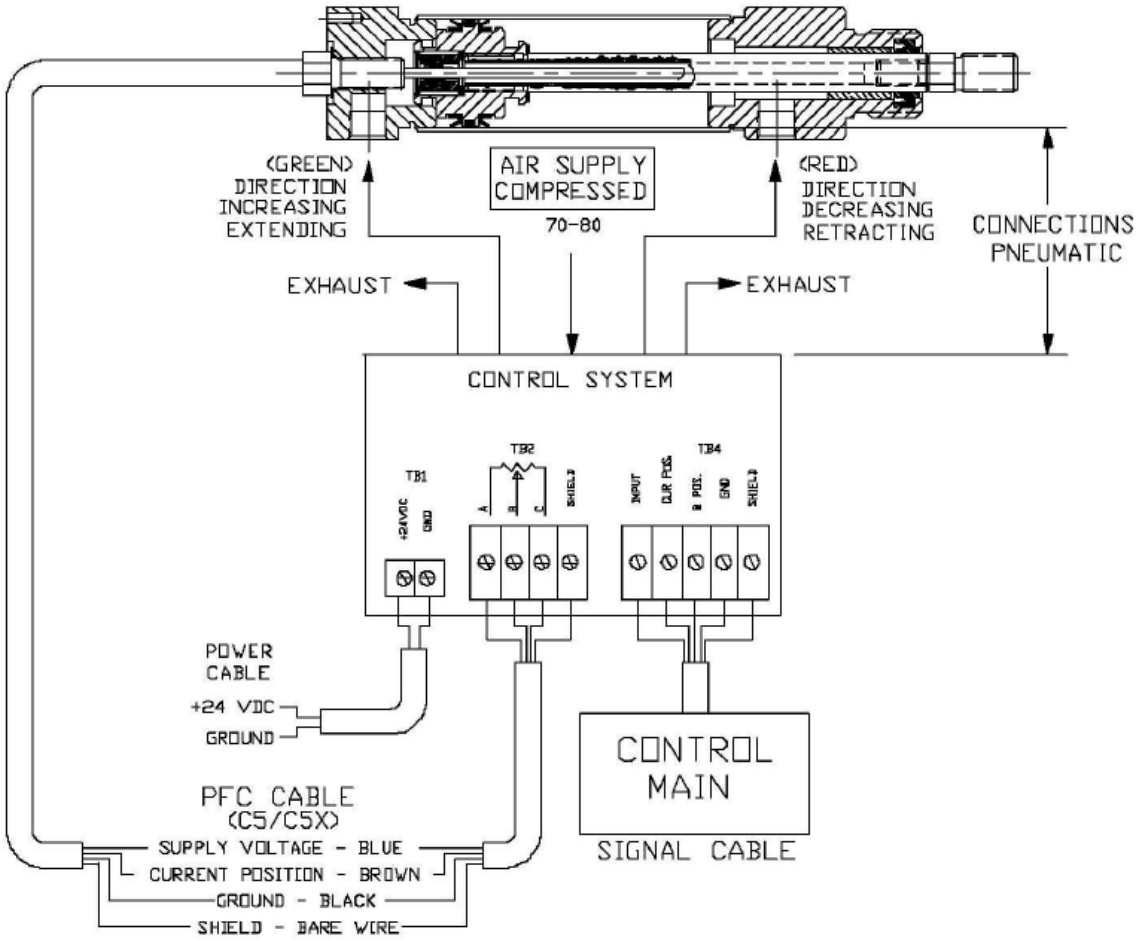

Figure 102: Schematic of the PFC and PCS with electronic and pneumatic connections (*107*).

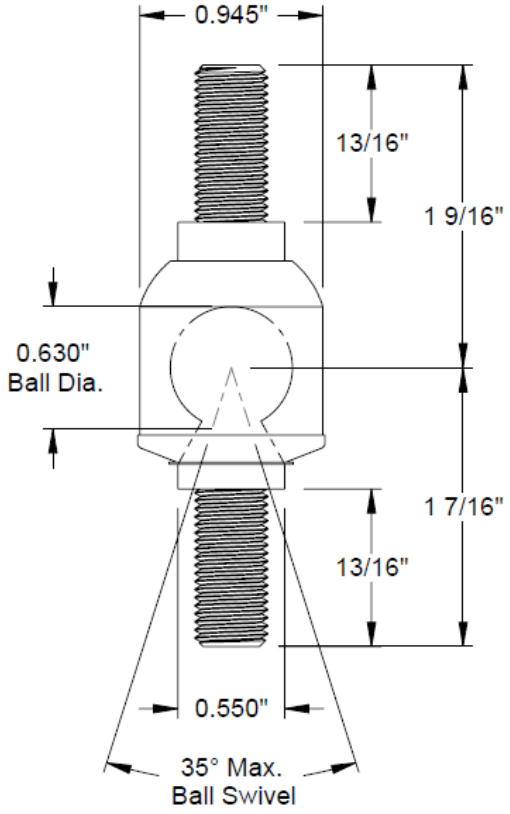

Figure 103: CAD rendering of the ball joint between the PFC extension and the probe extension rod mount (*108*).

the stainless steel plate. The all-thread and couplings are 5/8”-11. Figure 104 shows a photograph of the brace plate. Figure 105 shows the U-brace incorporated with the rest of the probe assembly in addition to the all-thread and ball joint, while Figure 106 shows the gasifier side of the all-thread supports for the U-brace.

Figure 104: Brace plate (U-brace) for probe cylinder support.

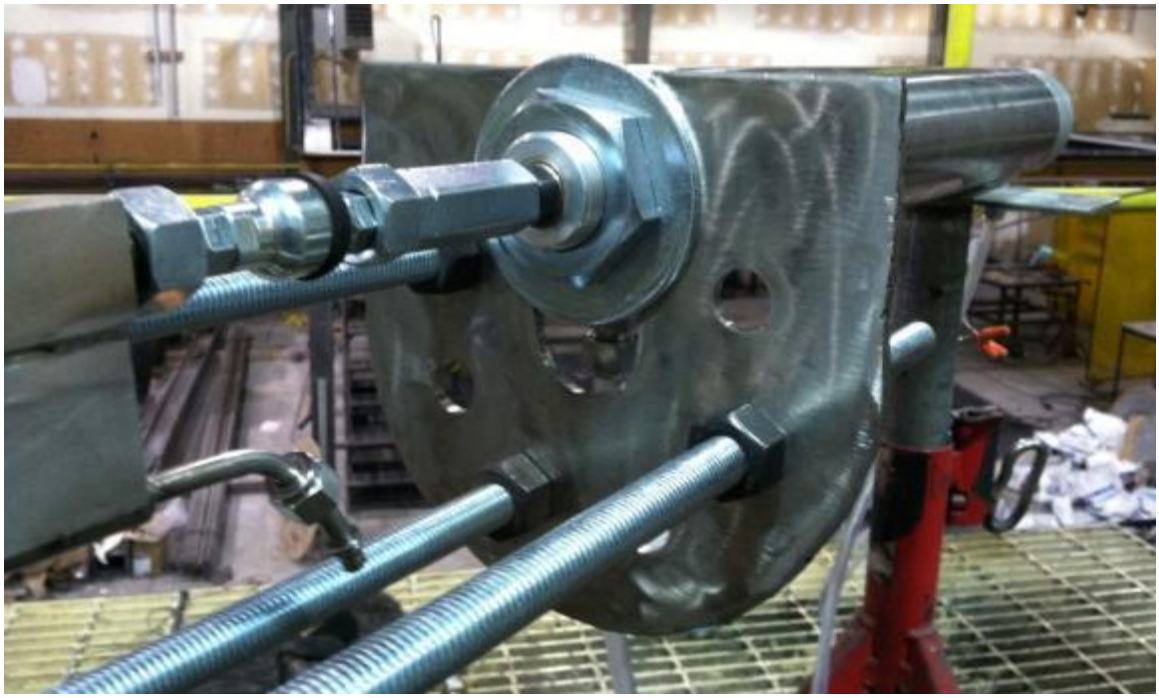

Figure 105: Pneumatic cylinder nose and U-brace with threaded rod extensions for stability.

Figure 106: Probe flange assembly with stabilizer and threaded rod extensions for pneumatic cylinder and U-brace.

APPENDIX F

SAMPLING SYSTEM OPTO CONTROL

The sample sequence is orchestrated by OPTO 22 software and hardware. Figure 107 shows the OPTO 22 control box previously seen in Figure 28. The control box measures 20 inches by 16 inches and is 8 inches deep; the box also has a clear viewing window to ensure instrumentation is working properly. In Figure 107, the right-hand side contains power distribution blocks including the 120 VAC power supply coming in from the top of the box and two OPTO 22 power supplies, one at 24 VDC, the other at 5 VDC. A fan is on the right-hand side of the box to keep equipment from overheating. On the left-hand side of Figure 107 are the individual OPTO modules and the brain/controller. From the top down, the equipment are brain/controller (OPTO model R1), input for probe location (OPTO module AIV-4), output for probe setpoint (module AOV-5, solenoid manifold outputs as seen in Figure 29 (module OAC5), and the cooling water solenoid outputs (module OAC5MA).

The circular path of Figure 108 is broken down into either action blocks (blue) or decision blocks (green). When the chart opens and the operator starts using OPTO Display Runtime, the nitrogen solenoid opens and the probe system begins purging with nitrogen. This also allows a constant flow past the tip of the probe in hopes to minimize the amount of slag and particle buildup. On another chart, called ‘Traffic Light’, is a checklist that the

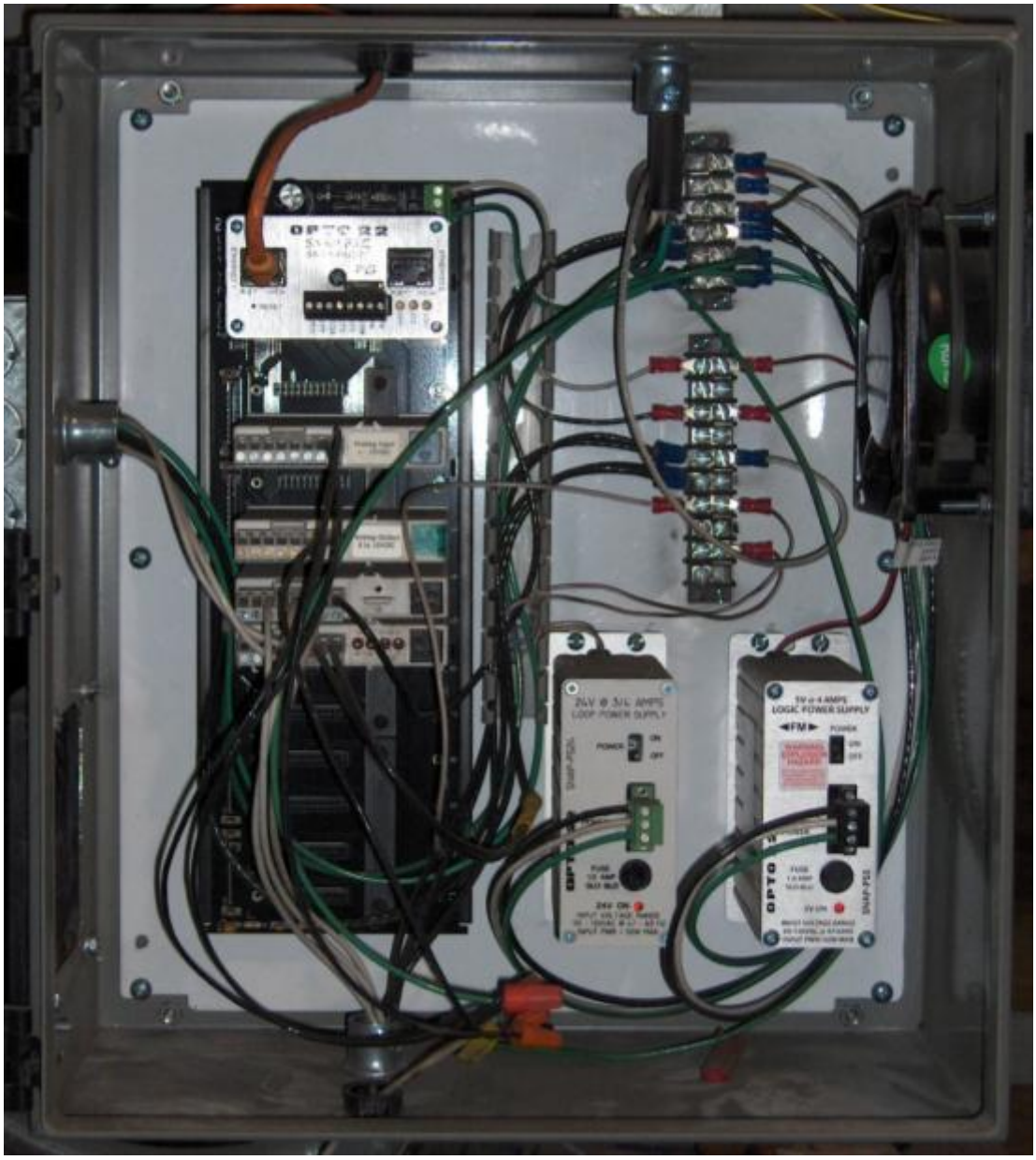

Figure 107: OPTO 22 control box.

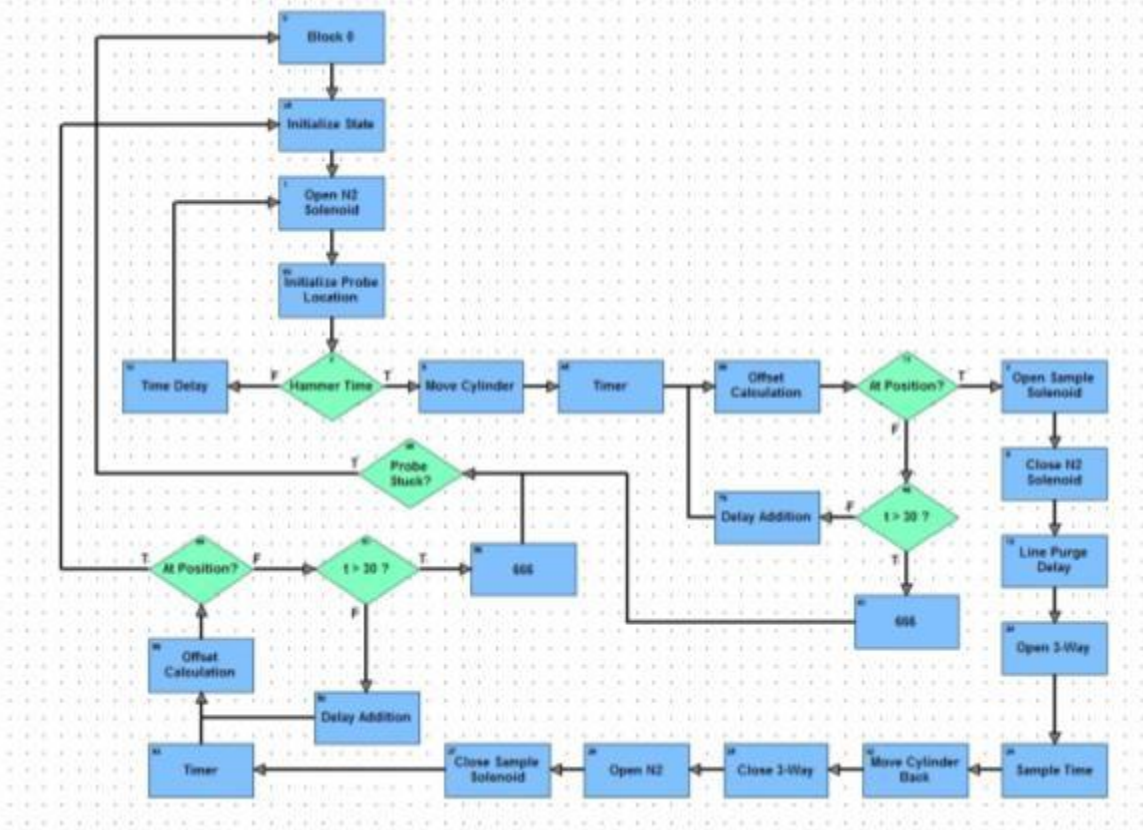

Figure 108: Screenshot of the OPTO 22 Control chart, ‘Probe’.

program runs through, making sure cooling water is on, the system is logging all pertinent values, and the nitrogen solenoid remains open until otherwise ordered; this is the first small loop in Figure 108. Figure 109 shows the ‘Traffic Light’ chart.

After meeting these conditions, the operator begins the sample sequence by clicking ‘Sample Start/Stop’ in OPTO Runtime to initiate ‘Hammer Time’ in the control strategy seen in Figure 108. While nitrogen continues to flow through the line, the pneumatic cylinder pushes the probe extension into the entrained-flow gasifier reaction zone. Once the extension has started moving, a timer begins to count. If this timer reaches 30 seconds before the probe reaches its setpoint, an alarm is triggered via block ‘666’ and a notice

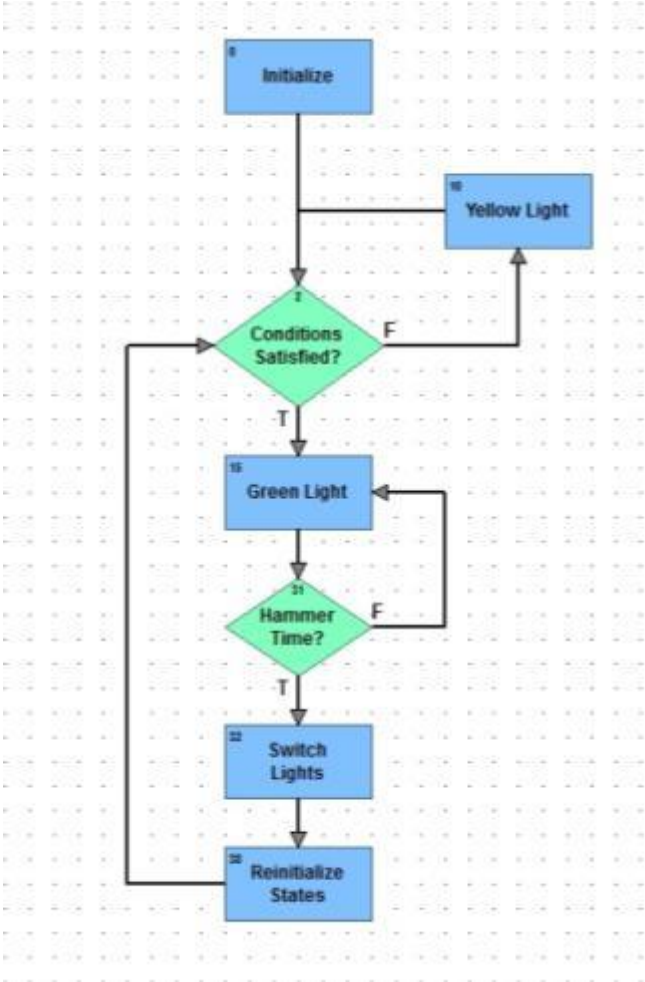

Figure 109: 'Traffic Light' chart in OPTO 22 Control.

flashes on the computer screen. In the event of the probe operating successfully and reaching its setpoint within 30 seconds, the sample solenoid will open and the nitrogen solenoid will close. This will cause the flow direction in the sample to switch and sample, or syngas, will begin to flow. The sample solenoid will remain open for approximately 20 seconds allowing the line to purge of nitrogen before the three-way solenoid is opened to the sample container. Both the sample solenoid and three-way solenoid will remain open for 10 to 20 seconds or until the sample is complete; this time will not exceed 30 seconds in order to minimize the time the probe is subjected to the reaction zone of the gasifier.

Once the sample is taken, the probe will begin to move back to a safe distance inside the refractory wall and both the sample solenoid and three-way solenoid will close as the nitrogen solenoid opens again. There will never be a stagnant gas volume in the probe lines nor will the lines be allowed to pressurize. Again, a small loop in the code will ensure the probe is back to a safe setpoint, or initial location. If the probe becomes stuck upon reentry of the refractory, an alarm will trigger and flash on the screen, activated by block '666' seen in Figure 108. The operator will then decide to shut cooling water to the probe, but never to the seal housing. In the event that the probe stops moving and the cooling water to the probe extension is shut, a failsafe initiates and the gas solenoids switch to purge the system with nitrogen. If the water were to stop flowing to the seal housing, the Teflon seal would breach and the reactor could depressurize and issue syngas into the lab. There is no solenoid in line with the seal housing; water is always flowing to the housing. Once the sample sequence is complete, the system will reinitialize itself and the next sample is ready to be taken at the discretion of the operator.

The program OPTO Display Runtime is the user interface for OPTO Control. Runtime allows the user to construct a custom panel of instrumentation and feedback information and enables the recording of variables and figures. Figure 110 shows a custom panel for the above sample sequence from the operating computer.

Figure 110 shows a diagram of the probe system and entrained-flow gasifier along with switch states and user-interface buttons. The six black-outlined rectangles near the center of the image are the current position of the position feedback cylinder (PFC Position), the sample time and purge delay for the sample line that are set by the user, along with the initial probe location that the user specifies to be somewhere in the refractory wall,

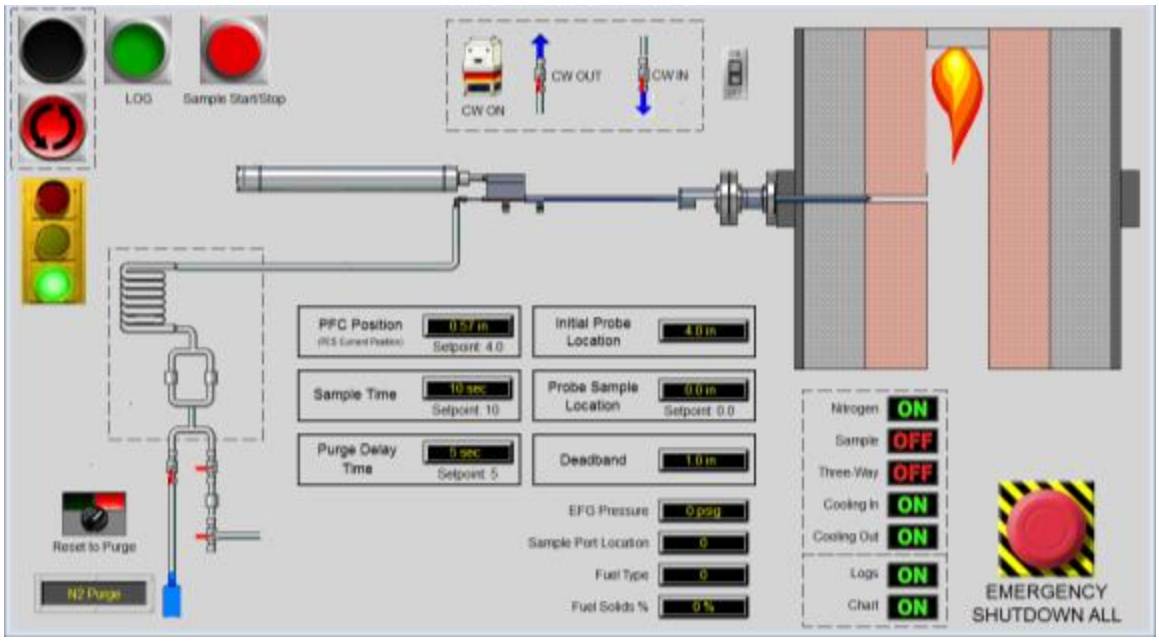

Figure 110: Screenshot of OPTO 22 Display Runtime program user interface.

and the location at which the sample is to be taken (Probe Sample Location). The sixth box, Deadband, is a user-defined variable that signifies how far the actual probe location can be from the setpoint, in inches. This value is ultimately responsible for when the alarm triggers and signifies that the probe is not moving. Most of the current values in Figure 110 are not representative of the real values to be used during sampling.

At the top left-hand side of the image are buttons for starting and stopping the chart, seen in Figure 108, accompanied by a start/stop button for sample collection that begins the extended sequence seen in Figure 108, and the log button that records all values and states of variables. The traffic light at the left-hand side is a simple way to determine if everything is satisfactory to begin sampling; green signifies that sampling may begin. The dashed box at top-center holds the solenoids and cooling water start options for the system and can be seen at the bottom either as an ON or OFF state along with the other three solenoids, the charts, and the log status. The large red button at the lower right-hand corner

turns off the cooling water to the probe extension itself, but not the seal housing as well as switches the gas solenoids to purge the system with nitrogen. The four black readouts near the bottom of Figure 110 show user inputs for the EFG pressure, sample port location, fuel type, and the solids percent of the slurry.

APPENDIX G

KINETIC PARAMETERS FOR ASPEN MODELING

Table 22: Expressions for coal particle size.

d_p (cm)	φ	
<0.005	$\frac{2Z+2}{Z+2}$	$Z = \frac{[CO]}{[CO_2]} = 2500\, e^{-\frac{6249}{T}}$
0.005-0.1	$\frac{(2Z+2)-\frac{Z(d_p-0.005)}{0.095}}{Z+2}$	
>0.1	1.0	

Table 23: Parameters for kinetics of reactions 8 through 12.

R	k_{diff}	k_s	$(P_i - P_i^*)$	
8	$\frac{0.292\phi\left(\frac{4.26}{T}\right)\left(\frac{T}{1800}\right)^{1.75}}{P_t d_p}$	$8710e^{-\frac{17967}{T}}$	P_{O_2}	
9	$\frac{10\times10^{-4}\left(\frac{T}{2000}\right)^{0.75}}{P_t d_p}$	$247e^{-\frac{21060}{T}}$	$P_{H_2O}-\frac{P_{H_2}P_{CO}}{K_{eq}}$	$K_{eq} = e^{17.644-\frac{30260}{1.8T}}$
10	$\frac{7.45\times10^{-4}\left(\frac{T}{2000}\right)^{0.75}}{P_t d_p}$	$247e^{-\frac{21060}{T}}$	P_{CO_2}	
11	$\frac{1.33\times10^{-3}\left(\frac{T}{2000}\right)^{0.75}}{P_t d_p}$	$0.12e^{-\frac{17921}{T}}$	$P_{H_2}-\sqrt{\frac{P_{CH_4}}{K_{eq}}}$	$K_{eq} = \frac{0.175}{34173}e^{\frac{18400}{1.8T}}$
12	$\frac{1.33\times10^{-3}\left(\frac{T}{2000}\right)^{0.75}}{P_t d_p}$	$0.12e^{-\frac{17921}{T}}$	$P_{H_2}-\frac{P_{H_2S}}{K_{eq}}$	$K_{eq} = e^{-5.0657+\frac{18557.7225}{T}}$

Table 24: Kinetics of additional reactions 5 through 7, 13, and 14.

R	Reaction Rate		Units
5	$8.83\times10^{5}e^{-\frac{9.976\times10^{4}}{8.315T}}C_{H_2}C_{O_2}$		mol/m^3 s
6	$30.9e^{-\frac{9.976\times10^{4}}{8.315T}}C_{CO}C_{O_2}$		mol/m^3 s
7	$3.552\times10^{11}e^{-\frac{9.304\times10^{5}}{8.315T}}C_{CH_4}C_{O_2}$		mol/m^3 s
13	$312e^{\frac{30000}{1.987T}}\left(C_{CH_4}-\frac{C_{CO}\cdot C_{H_2}^{3}}{K_{eq}\cdot C_{H_2O}}\right)$	$K_{eq}=e^{33.1371-\frac{25014.0499}{T}}$	mol/m^3 s
14	$F_w\times2.77\times10^{5}\left(x_{CO}-x_{CO}^{*}\right)\cdot e^{-\frac{27760}{1.987T}}\cdot P_t^{0.5-\frac{P_t}{250}}\cdot e^{-8.91+\frac{5553}{T}}$	$x_{CO}=\frac{P_{CO}}{P_t}$ $x_{CO}^{*}=\frac{1}{P_t}\cdot\frac{P_{CO_2}P_{H_2}}{K_{eq}P_{H_2O}}$ $K_{eq}=e^{-3.6893+\frac{7234}{1.8T}}$	mol/s·gram of ash

REFERENCES

(1) Higman, C.; Van der Burgt, M. *Gasification*; Gulf Professional Publishing, 2003.

(2) Merrick, D. *Coal combustion and conversion technology*; 1984.

(3) Liu, T.; Fang, Y. An experimental investigation into the gasification reactivity of chars prepared at high temperatures. *Fuel* **2008**, *87*, 460–466.

(4) Smoot, L. Controlling mechanisms in gasification of pulverized coal. *Fuel* **1987**.

(5) Tremel, A.; Haselsteiner, T.; Kunze, C.; Spliethoff, H. Experimental investigation of high temperature and high pressure coal gasification. *Applied Energy* **2012**, *92*, 279–285.

(6) Gasification Behavior of Australian coal at High Temperature and Pressure.

(7) Suuberg, E. M. Product Compositions and Formation Kinetics in Rapid Pyrolysis of Pulverized Coal - Implications for Combustion.

(8) Hindmarsh, C. J.; Thomas, K. M.; Wang, W. X.; Cai, H. Y.; Güell, A. J.; Dugwell, D. R.; Kandiyoti, R. A comparison of the pyrolysis of coal in wire-mesh and entrained-flow reactors. *Fuel* **1995**, *74*, 1185–1190.

(9) Chen, L.; Zeng, C.; Guo, X.; Mao, Y.; Zhang, Y.; Zhang, X.; Li, W.; Long, Y.; Zhu, H.; Eiteneer, B.; Zamansky, V. Gas evolution kinetics of two coal samples during rapid pyrolysis. *Fuel Processing Technology* **2010**, *91*, 848–852.

(10) Peralta, D.; Paterson, N.; Dugwell, D.; Kandiyoti, R. Pyrolysis and CO2 gasification of Chinese coals in a high-pressure wire-mesh reactor under conditions relevant to entrained-flow gasification. *Energy and Fuels* **2005**, *19*, 532–537.

(11) Anthony, D. B.; Howard, J. B.; Hottel, H. C.; Meissner, H. P. Rapid devolatilization and hydrogasification of bituminous coal. *Fuel* **1976**, *55*, 121–8.

(12) Chen, H.; Yang, H.; Ju, F.; Wang, J.; Zhang, S. The influence of pressure and temperature on coal pyrolysis/gasification. In; John Wiley and Sons Ltd: State Key Laboratory of Coal Combustion, Huazhong University of Science and Technology, Wuhan, 430074, China, 2007; Vol. 2, pp. 203–212.

(13) Tamhankar, S. S. .; Sears, J. T. .; Wen, C. Y. Coal pyrolysis at high temperatures and pressures.

(14) Niksa, S.; Russel, W. B.; Saville, D. A. Time-resolved weight loss kinetics for the rapid devolatilization of a bituminous coal. In *Symposium, International, on Combustion*; 1982; pp. 1151–1157.

(15) Niksa, S.; Russel, W. B.; Saville, D. A. Captive sample reactor for kinetic studies of coal pyrolysis and hydropyrolysis on short time scales. *Fuel* **1982**, *61*, 1207–1212.

(16) Gibbins, J. R. .; King, R. A. V. Variable heating-rate wire-mesh pyrolysis apparatus. *Review of Scientific Instruments* **1989**, *60*.

(17) Tremel, A.; Haselsteiner, T.; Nakonz, M.; Spliethoff, H. Coal and char properties in high temperature entrained-flow gasification. *Energy* **2012**.

(18) Manton, N.; Cor, J.; Mul, G.; Eckstrom, D.; Malhotra, R.; Niksa, S. Impact of pressure variations on coal devolatilization products. 2. Detailed product distributions from 1.0 MPa. *Energy & Fuels* **2004**, *18*, 520–530.

(19) Sathe, C. .; Hayashi, J. I. .; Li, C. Z. Release of volatiles from the pyrolysis of a Victorian lignite at elevated pressures. *Fuel* **2002**, *81*, 1171–8.

(20) Guell, A. J.; Kandiyoti, R. Development of a Gas-Sweep Facility for the Direct Capture of Pyrolysis Tars in a Variable Heating Rate High-Pressure Wire-Mesh Heater. *Energy & Fuels* **1993**, *7*, 943–952.

(21) E.M. Suuberg, W.A. Peters, J. B. H.; Suuberg, E. M. . E. M.; Peters, W. A. .; Howard, J. B. J. B.; Peters A., W. A Comparison of the Rapid Pyrolysis of a Lignite and a Bituminous Coal. In *Thermal Hydrocarbon Chemistry*; 1979; Vol. 17, pp. 239–257.

(22) Zeng, D. .; Fletcher, T. H. Effects of pressure on coal pyrolysis and char morphology. *Energy & Fuels* **2005**, *19*, 1828–1838.

(23) H. Kobayashi, J.B. Howard, A. F. S. Coal devolatilization at high temperatures. *Symposium (International) on Combustion* **1977**, *16*, 411–425.

(24) Serio, M. A.; Solomon, P. R.; Heninger, S. G. Coal pyrolysis in a high pressure entrained-flow reactor. *Preprints of Papers - American Chemical Society, Division of Fuel Chemistry* **1986**, *31*, 210–221.

(25) Roberts, D. G.; Ilyushechkin, A. Y.; Harris, D. J.; Tremel, A. Linking laboratory data with pilot scale entrained-flow coal gasification performance. Part 1: Laboratory characterisation. *Fuel Processing Technology* **2012**, *94*, 26–33.

(26) Zeng, D. .; Clark, M. Swelling properties and intrinsic reactivities of coal chars produced at elevated pressures and high heating rates. *Proceedings of the Combustion INstitute* **2005**, *30*.

(27) Shurtz, R. C.; Hogge, J. W.; Fowers, K. C.; Sorensen, G. S.; Fletcher, T. H. Coal Swelling Model for Pressurized High Particle Heating Rate Pyrolysis Applications. *Energy & Fuels* **2012**, *26*, 3612–3627.

(28) Nichols, K.; Hedman, P.; Smoot, L. Fate of coal-sulphur in a laboratory-scale coal gasifier. *Fuel* **1989**.

(29) Azuhata, S.; Hedman, P.; Smoot, L. Effects of flame type and pressure on entrained coal gasification. *Fuel* **1986**.

(30) Cope, R.; Smoot, L. Effects of pressure and coal rank on carbon conversion in an entrained-coal gasifier. *Fuel* **1989**.

(31) Sathe, C.; Pang, Y.; Li, C.-Z. Effects of Heating Rate and Ion-Exchangeable Cations on the Pyrolysis Yields from a Victorian Brown Coal. *Energy and Fuels* **1999**, *13*.

(32) Azuhata, S.; Hedman, P.; Smoot, L. D. Carbon conversion in an atmospheric-pressure entrained coal gasifier. *Fuel* **1986**, *65*, 212–217.

(33) Johnson, J. L. *Kinetics of Coal Gasification*; John Wiley and Sons Inc., 1979.

(34) Senneca, O.; Salatino, P.; Masi, S. Microstuctural changes and loss of gasification reactivity of char upon heat treatment. *Fuel* **1998**, *77*.

(35) Liu, T.; Fang, Y.; Wang, Y. An experimental investigation in to the gasifiaction reactivity of chars prepared at high temperatures. *Fuel* **2008**, *87*, 460–466.

(36) Matsuoka, K.; Akiho, H.; Xu, W.; Gupta, R.; Wall, T. F.; Tomita, A. The physical character of coal char formed during rapid pyrolysis at high pressure. *Fuel* **2005**, *84*, 63–69.

(37) Liu, H.; Kaneko, M.; Luo, C.; Kato, S.; Kojima, T. Effect of Pyrolysis time on the gasifications reactivity of char. *Fuel* **2004**, *83*, 1055–1061.

(38) Brown, B.; Smoot, L. Effect of coal type on entrained gasification. *Fuel* **1986**.

(39) Skinner, F.; Smoot, L. Mixing and Gasification of Coal in an Entrained-flow Gasifier. *Paper No. 80-WA/HT-30, ASME Winter Annual* **1980**.

(40) Prlce, T. D.; Smoot, L. D.; Hedman, P. Measurement of Nitrogen and Sulfur Pollutants in an Entrained-Coal Gasifier. *Society* **1983**, 110–116.

(41) Gasification, C.; Shadle, L. Coal Gasification. *Kirk-Othmer Encyclopedia 6*.

(42) Schilling, H. D.; Bonn, B.; Krauss, U. *Coal Gasification: Existing processes and new developments*; 1979.

(43) Experimental Methods. *Ullmann's Encyclopedia of Industrial Chemistry* **1998**.

(44) Soelberg, N. R.; Smoot, L. D.; Hedman, P. O. Entrained-flow gasification of coal 1. Evaluation of mixing and reaction processes. *Fuel* **1985**, *64*, 776–781.

(45) B. W. Brown, L. D. Smoot, P. J. Smith, P. O. H. Measurement and prediction of entrained-flow gasification processes. *AIChE* **1988**, *34*, 465–446.

(46) Smith, P. J. Theoretical Modeling of coal and gas fired turbulent combusiton and gasification processes, Brigham Young University, 1981.

(47) Smoot, L. D.; Pratt, D. T. *Pulverized Coal Combustion and Gasificaiton*; Plenum Press: New York, NY, 1979.

(48) Smoot, L. D.; Smith, P. J. *Coal Combustion and Gasification*; Springer, 1985.

(49) Liu, G.-S.; Rezaei, H. R.; Lucas, J. A.; Harris, D. J.; Wall, T. F. Modelling of a pressurised entrained-flow coal gasifier - the effect of reaction kinetics and char structure. *Fuel* **2000**, *79*, 1767–1779.

(50) Lopez, E. M.; Garza, V.; Acevedo, J. Modelling and Simulation of Coal and Petcoke Gasification in a Co-current Flow Reactor. In *16th European Symposium on Computer Aided Process Engineering and 9th International Symposium on Process Systems Engineering*; 2006; pp. 577–582.

(51) Tremel, A.; Spliethoff, H. Gasification kinetics during entrained-flow gasification – Part I. Devolatilisation and char deactivation. *Fuel* **2013**, *103*, 663–671.

(52) Goyal, A. Mathematical Modeling of Entrained-Flow Coal Gasification Reactors, Illinois nstitute of Technology, 1980.

(53) Vamvuka, D.; Woodburn, E. T.; Senior, P. R. Modeling of an entrained-flow coal gasifier. *Fuel* **1995**, *74*, 1452–1450.

(54) Rasband, M. No Title.

(55) Govind, R.; Shah, J. Modeling and Simulation of an Entrained-flow Coal Gasifier. *AIChE Journal* **1984**, *30*, 79–92.

(56) Wu, Y.; Smith, P. J.; Zhang, J.; Thornock, J. N.; Yue, G. Effects of Turbulent Mixing and Controlling Mechanisms in an Entrained-flow Coal Gasifier. *Energy & Fuels* **2010**, *24*, 1170–1175.

(57) Kumar, M.; Ghoniem, A. F. Multiphysics Simulations of Entrained-flow Gasification. Part II: Constructing and Validating the Overall Model. *Energy & Fuels* **2012**, *26*, 464–479.

(58) Wang, B.; Li, X.; Xu, S.; Paterson, N.; Dugwell, D. R.; Kandiyoti, R. Performance of Chinese coals under conditions simulating entrained-flow gasification. *Energy and Fuels* **2005**, *19*, 2006–2013.

(59) Wu, Y.; Zhang, J.; Smith, P. J.; Zhang, H.; Reid, C.; Lv, J.; Yue, G. Three-dimensional simulation for an entrained-flow coal slurry gasifier. *Energy and Fuels* **2010**, *24*, 1156–1163.

(60) Watanabe, H.; Otaka, M. Numerical simulation of coal gasification in entrained-flow coal gasifier. *Fuel* **2006**, *85*, 1935–1943.

(61) Monaghan, R. F. D.; Ghoniem, A. F. A dynamic reduced order model for simulating entrained-flow gasifiers: Part I: Model development and description. *Fuel 91*, 61–80.

(62) Monaghan, R. F. D.; Ghoniem, A. F. A dynamic reduced order model for simulating entrained-flow gasifiers. Part II: Model validation and sensitivity analysis.

(63) Solomon, P. R.; Serio, M. A.; Suuberg, E. M. Coal Pyrolysis - Experiments, Kinetic Rates, and Mechanisms. *Progress in Energy and Combustion Science* **1992**, *18*, 133–220.

(64) Wall, T. F.; Liu, G.-S.; Wu, H.-W.; Roberts, D. G.; Benfell, K. E.; Gupta, S.; Lucas, J. A.; Harris, D. J. The effects of pressure on coal reactions during pulverised coal combustion and gasification. *Progress in Energy and Combustion Science* **2002**, *28*, 405–433.

(65) Mathews, J. P.; Chaffee, A. L. The molecular representations of coal – A review. *Fuel* **2011**.

(66) Liu, G.-S.; Niksa, S. Coal conversion submodels for design applications at elevated pressures. Part II. Char gasification. *Progress in Energy and Combustion Science* **2004**, *30*, 679–717.

(67) Sommariva, S.; Maffei, T.; Migliavacca, G.; Faravelli, T.; Ranzi, E. A predictive multi-step kinetic model of coal devolatilization. *Fuel* **2010**, *89*, 318–328.

(68) Sadhukhan, A. K.; Gupta, P.; Saha, R. K. Modelling of combustion characteristics of high ash coal char particles at high pressure: Shrinking reactive core model. *Fuel* **2010**, *89*, 162–169.

(69) Barranco, R.; Rojas, A.; Barraza, J.; Lester, E. A new char combustion kinetic model 1. Formulation. *Fuel* **2009**, *88*, 2335–2339.

(70) Anthony, D. B.; Howard, J. B.; Hottel, H. C.; Meissner, H. P. Rapid Devolatilization of Pulverized Coal. *Symposium (International) on Combustion* **1975**, *15*.

(71) Unger, P. E.; Suuberg, E. M. Modeling the devolatilization behavior of a softening bituminous coal. In *18th Symposium (International) on Combustion*; 1981; pp. 1203–1211.

(72) Rojas, A.; Barraza, J.; Barranco, R.; Lester, E. A new char combustion kinetic model – Part 2: Empirical validation. *Fuel* **2012**.

(73) San Shwe HLA; HARRIS, D. J.; ROBERTS, D. G. CFD Modeling for an Entrained-flow Gasification Reactor Using Measured "Intrinsic" Kinetic Data. In *Fifth International Conference on CFD in the Process Industries*; 2006; pp. 1–7.

(74) Shurtz, R. C. Effects of Pressure on the Properties of Coal Char Under Gasification Conditions at High Initial Heating Rates, Brigham Young University, 2011.

(75) Hong, J.; Hecker, W. C.; Fletcher, T. H. Modeling High-Pressure Char Oxidation Using Lamngmuir Kinetics with an Effectiveness Factor. *Proceedings of the Combusiton Institute* **2000**, *28*, 2215–2223.

(76) Navarro, M. V.; Aranda, A.; Garcia, T.; Murillo, R.; Mastral, A. M. Application of the distributed activation energy model to blends devolatilisation. *Chemical engineering journal* **2008**, *142*, 87–94.

(77) Miccio, F.; Salatino, P.; Tina, W. Modeling gasification and percolation of ash-bearing porous carbon particles. *Proceedings of the Combusiton Institute* **2000**, *28*, 2163–2170.

(78) Kajitani, S.; Tay, H.-L.; Zhang, S.; Li, C.-Z. Mechanisms and kinetic modelling of steam gasification of brown coal in the presence of volatile–char interactions. *Fuel* **2011**.

(79) Karlström, O.; Brink, A.; Hercog, J.; Hupa, M.; Tognotti, L. One-Parameter Model for the Oxidation of Pulverized Bituminous Coal Chars. *Energy & Fuels* **2012**, *26*, 968–975.

(80) Solomon, P. R.; Hamblen, D. G.; Serio, M. A.; Yu, Z.-Z.; Charpenay, S. *Can Coal Science be Predictive*.

(81) Niksa, S.; Kerstein, A. R. Interpreting coal devolatilization as a flash distillation driven by competitive kinetics for depolymerization and reattachment. In; 1989; pp. 1293–1299.

(82) Niksa, S.; Kerstein, A. R. FLASHCHAIN theory for rapid coal devolatilization kinetics. 1. Formulation. *Energy & Fuels* **1991**, *5*, 647–665.

(83) Grant, D. M.; Pugmire, R. J.; Fletcher, T. H.; Kerstein, A. R. Chemical model of coal devolatilization using percolation lattice statistics. *Energy & Fuels* **1989**, *3*, 175–186.

(84) Smith, K. L.; Smoot, L. D.; Fletcher, T. H.; Pugmire, R. J. *The Structure and Reaction Process of Coal*; 1994.

(85) Yun, Y.; Lee, G.-B. Effects of pressure in coal pyrolysis observed by high pressure TGA. *Korean Journal of Chemical Engineering* **1999**, *16*, 798–803.

(86) Duan, L.; Zhao, C.; Zhou, W.; Qu, C.; Chen, X. Investigation of Coal Pyrolysis in CO2 Atmosphere. *Energy & Fuels* **2009**, *23*, 3826–3830.

(87) Roberts, D. G.; Hodge, E. M.; Harris, D. J.; Stubington, J. F. Kinetics of char gasification with CO2 under regime II conditions: Effects of temperature, reactant, and total pressure. *Energy and Fuels* **2010**, *24*, 5300–5308.

(88) Wagner, D. R. Pyrolysis Behavior of Coal and Petroleum Coke at High Temperature and High Pressure, University of Utah, 2010.

(89) Anthony, D. B.; Howard, J. B.; Messner, H. P.; Hottel, H. C. Apparatus for determining high pressure coal-hydrogen reaction kinetics under rapid heating conditions. *Review of Scientific Instruments* **1974**, *45*, 992–5.

(90) Zeng, C. .; Chen, L. .; Liu, G. .; Li, W. .; Huang, B. .; Zhu, H. .; Zhang, B. .; Zamansky, V. . Advances in the development of wire mesh reactor for coal gasification studies. *Review of Scientific Instruments2* **2008**, *79*.

(91) Engineering, O. No Title. In *Temperature*; p. H–13–14.

(92) Wagner, D. R.; Whitty, K. J. A pulse-width modulation controlled wire-mesh heater apparatus for investigation of solid fuel pyrolysis. *Review of Scientific Instruments* **2012**, *83*, 115116–5.

(93) THermoCahn Thermax 500 User Manual.

(94) Wen, C. Y.; Chaung, T. Z. Enatrainment Coal Gasification Modeling. *Industrial & Engineering Chemistry Process Design and Development* **1979**, *18*, 684–695.

(95) Suuberg, E. M. .; Peters, W. A.; Howard, J. B. Product composition and kinetics of lignite pyrolysis. *Industrial & Engineering Chemistry Process Design and Development* **1978**, *17*, 37–46.

(96) AspenTech *Model for Entrained-flow Coal Gasifier*; 2012.

(97) Szekely, J.; Evans, J. W.; Sohn, H. Y. *Gas-Solid Reactions*; Academic Press, Inc.: New York, NY, 1976.

(98) Incropera, F. P.; Dewitt, D. P.; Bergman, T. L.; Lavine, A. S. *Fundamentals of Heat and Mass Transfer*; 6th ed.; John Wiley and Sons Inc.: Hoboken, 2007.

(99) Braun, R. L.; Mallon, R. G.; Sohn, H. Y. Analysis of Multiple Gas-Solid Reactions During the Gasification of Char in Oil Shale Blocks. In *Proceedings form the 14th Oil Shale Symposium*; 1981; pp. 289–300.

(100) Waind, T. Discussion of entrained-flow gasifier modeling **2013**.

(101) Bird, R. B.; Stewart, W. E.; Lightfoot, E. N. *Transport Phenomena*; John Wiley and Sons Inc.: Palatino, 2007.

(102) University, C. S. Chemical Equilibrium Calculation. http://navier.engr.colostate.edu/~dandy/code/code-4/.

(103) Williams, A.; Pourkashanian, M.; Jones, J. M.; Skorupska, N. *Combustion and Gasification of Coal*; Taylor and Francis: New York, NY, 2000.

(104) Hucka, V. J.; Bodily, D. M.; Huang, H. *Formation and Retention of Methane in Coal*; Salt Lake City, UT, United states, 1992.

(105) Haines, P. J. *Principles of Thermal Analysis and Calorimetry*; Haines, P. J., Ed.; Royal Society of Chemistry: Cambridge, UK, 2002.

(106) Seals, A. H. P. Seal Drawing **2012**.

(107) Manufacturing, B. Pneumatic Motion Control System Operating Manual.

(108) Carr, M. Ball Joint CAD Drawing **2012**.